

MEASUREMENT OF THE DECAY $K^+ \rightarrow \pi^+ \nu \bar{\nu}$

by Paul C. Bergbusch

M.Sc., University of British Columbia, 1995

B.Sc. (Honors), Simon Fraser University, 1993

A thesis submitted in partial fulfillment of
the requirements for the degree of

DOCTOR OF PHILOSOPHY

in the Faculty of Graduate Studies

DEPARTMENT OF PHYSICS AND ASTRONOMY

We accept this thesis as conforming to the required standard.

D.A. Bryman (supervisor), Dept. of Physics and Astronomy, UBC

J. McKenna, Dept. of Physics and Astronomy, UBC

D.F. Measday, Dept. of Physics and Astronomy, UBC

A. Zhitnitsky, Dept. of Physics and Astronomy, UBC

THE UNIVERSITY OF BRITISH COLUMBIA

October 2000

© Paul C. Bergbusch, 2000

In presenting this thesis in partial fulfilment of the requirements for an advanced degree at the University of British Columbia, I agree that the Library shall make it freely available for reference and study. I further agree that permission for extensive copying of this thesis for scholarly purposes may be granted by the head of my department or by his or her representatives. It is understood that copying or publication of this thesis for financial gain shall not be allowed without my written permission.

Department of Physics & Astronomy
The University of British Columbia
Vancouver, Canada

Date Oct. 12, 2000

Abstract

Experiment 787 at Brookhaven National Laboratory is a sensitive search for the decay of a positively-charged kaon into a positively-charged pion, a neutrino, and an anti-neutrino: $K^+ \rightarrow \pi^+ \nu \bar{\nu}$. This extremely rare decay is expected to occur in the Standard Model with a branching ratio of $(0.8 \pm 0.3) \times 10^{-10}$. It also serves as a hunting ground for new physics. Data collected between 1995 and 1997 contains one event consistent with $K^+ \rightarrow \pi^+ \nu \bar{\nu}$, with background estimated to contribute 0.08 ± 0.02 events. Because this event survives the tightest data-selection cuts which further reduce the estimated background to 0.006 ± 0.002 events, it is likely due to $K^+ \rightarrow \pi^+ \nu \bar{\nu}$. 3.24×10^{12} kaons were collected with an acceptance for $K^+ \rightarrow \pi^+ \nu \bar{\nu}$ of $(0.21 \pm 0.02)\%$, resulting in a $K^+ \rightarrow \pi^+ \nu \bar{\nu}$ branching ratio of $1.5_{-1.2}^{+3.4} \times 10^{-10}$. The weak coupling of top to down quarks, parameterized by the Cabibbo-Kobayashi-Maskawa matrix element V_{td} , is calculated to lie in the range $0.002 < |V_{td}| < 0.04$. The upper limit on the $K^+ \rightarrow \pi^+ f$ branching ratio, for massless f and for no events observed, is 1.1×10^{-10} at the 90% confidence level.

Table of Contents

Abstract	ii
Table of Contents	iii
List of Figures	vi
List of Tables	ix
Acknowledgements	xiii
Preface	xv
1 Introduction	1
2 Theory	7
2.1 Weak Interactions	7
2.2 $K^+ \rightarrow \pi^+ \nu \bar{\nu}$	12
2.3 V_{td}	16
2.4 New Physics	17
3 Experiment	20
3.1 Kaon Production and Transport	21
3.2 Detector	24
3.2.1 Beamline Detectors	24
3.2.2 Target	28
3.2.3 Drift Chamber	29
3.2.4 Range Stack	32

3.2.5	Photon Veto	34
3.2.6	Monte Carlo Simulation	38
3.3	Data Acquisition	40
4	Analysis	47
4.1	Backgrounds	47
4.1.1	$K_{\pi 2}$ and $K_{\mu 2}$ Decays	52
4.1.1.1	^{12}C Giant Dipole Resonance Background	54
4.1.2	Beam Backgrounds and Kaon Charge Exchange	63
4.2	Analysis Strategy and Techniques	66
4.3	Data Analysis and Cuts	71
4.3.1	Function Cuts	77
4.4	Background Measurement Structure	88
4.4.1	$K_{\pi 2}$ Decay	92
4.4.2	$K_{\mu 2}$ Decay	94
4.4.3	Beam Backgrounds	98
4.4.4	Kaon Charge Exchange	105
4.5	Background Measurement Results	110
4.6	Outside-the-Box Tests	113
4.7	Signal Evaluation Criteria	123
4.8	Search for Signal	125
5	Acceptance and Sensitivity	132
5.1	Counting Kaons	133
5.2	$K_{\mu 2}$ -based Acceptance	134
5.3	$K_{\pi 2}$ -based Acceptance	135
5.4	π_{scat} -based Kinematic Acceptance	137
5.5	π_{scat} -based TD Acceptance	139
5.6	μ -veto Accidental Loss	146
5.7	T · 2 Efficiency	146

5.8	UMC-based Acceptances	151
5.9	Kaon Stopping Fraction, f_s	160
5.9.1	Measurement of f_s	161
5.9.2	Measurement of the $K_{\pi 2}$ Branching Ratio	162
5.10	Summary	171
6	Final Results	175
6.1	$K^+ \rightarrow \pi^+ \nu \bar{\nu}$ Branching Ratio	175
6.2	$K^+ \rightarrow \pi^+ f$ Upper Limit	176
6.3	V_{td}	177
7	Conclusions	179
	Bibliography	187
A	BNL E787 Collaboration	192
B	Personal Contributions	193
C	Detailed Cut Descriptions	195
C.1	PASS1	195
C.2	PASS2	200
C.3	PASS3	202
C.3.1	Kinematic Pathology Cuts	202
C.3.2	Beam Pathology Cuts	208
C.3.3	Photon Veto Function	213
C.3.4	TD Function Cuts	214
C.3.5	$K_{\pi 2}$ and $K_{\mu 2}$ Kinematic Function Cuts	223
C.3.6	Beam Function Cuts	227
C.4	Data Quality Cuts	232
D	Glossary	235

List of Figures

1.1	The fundamental particles and forces.	3
2.1	Unitarity triangle in the complex (ρ, η) plane.	12
2.2	Short-distance Feynman diagrams for $K^+ \rightarrow \pi^+ \nu \bar{\nu}$	13
2.3	A long-distance Feynman diagram for $K^+ \rightarrow \pi^+ \nu \bar{\nu}$	15
2.4	Relationship between $K^+ \rightarrow \pi^+ \nu \bar{\nu}$ and $ V_{td} $ in the (ρ, η) plane.	18
3.1	Accelerator facilities at BNL.	22
3.2	Low energy separated beamline III at BNL.	23
3.3	Side view of the E787 detector.	25
3.4	Side view of the beam Čerenkov detector, and downstream views of the BWC1 and BWC2 detectors.	27
3.5	Downstream view of the target.	30
3.6	The “ultra-thin chamber” (UTC).	31
3.7	The RS shown in cross section. ϕ is the angle in the (x, y) plane about the center of the detector.	33
3.8	Pulses found in the upstream and downstream TD’s in RS layers 11-14 for a pion track stopping in layer 12.	35
3.9	The “barrel veto” (BV) and EC shown in cross section.	36
4.1	R vs. P , and kinematic categorization of events passing the $K_{\pi 2}(1)$ trigger.	49
4.2	R vs. P for the events in figure 4.1 which pass the full $\pi^+ \nu \bar{\nu}(1)$ trigger.	50
4.3	Momentum phase space of the charged track from K^+ decays.	51
4.4	t_μ vs. E for $K_{\mu 2}$ range-tail events.	58
4.5	t_μ vs. E_μ for $K_{\mu 2}$ range-tail events.	59

4.6	Momentum distribution of muon-band events.	61
4.7	t_μ vs. $E_{RS}(\text{diff})$ for muon-band events.	62
4.8	Time spectra of single counter hits in the RS.	64
4.9	A background estimate resulting from a bifurcated analysis.	68
4.10	Outside-the-box correlation study.	69
4.11	Event display of a successfully reconstructed $K_{\mu 2}$ event.	74
4.12	Close-up of the target hits for the event shown in figure 4.11.	75
4.13	Close-up of the RS hits for the event shown in figure 4.11.	76
4.14	The PV function.	82
4.15	The TD function.	84
4.16	The $K_{\pi 2}$ kinematic function.	86
4.17	The $K_{\mu 2}$ kinematic function.	87
4.18	The double-beam function.	90
4.19	The CEX function.	91
4.20	$K_{\pi 2}$ background estimation structure.	93
4.21	$K_{\mu 2}$ background estimation structure.	96
4.22	Single-beam kaon-entering background estimation structure.	99
4.23	Single-beam pion-entering background estimation structure.	101
4.24	Double-beam kaon-entering background estimation structure.	102
4.25	Double-beam pion-entering background estimation structure.	104
4.26	Target and IC displays of the "KIC" event.	106
4.27	Target and IC displays of the "TGCEO" event.	107
4.28	Target display of the "TGDEDX" event.	111
4.29	R vs. E for events in the 1995-7 $K^+ \rightarrow \pi^+ \nu \bar{\nu}$ data set passing all other cuts in the analysis.	127
4.30	R vs. E for UMC-generated $K^+ \rightarrow \pi^+ \nu \bar{\nu}$ events.	128
4.31	Display of the candidate $K^+ \rightarrow \pi^+ \nu \bar{\nu}$ event.	129
4.32	Close-up of the target and RS hits for the candidate $K^+ \rightarrow \pi^+ \nu \bar{\nu}$ event. . . .	130

5.1	T · 2 efficiency as a function of run number for $K_{\pi 2}$ and $K_{\mu 2}$ decays, and the $K_{\mu 2}/K_{\pi 2}$ ratio of efficiencies.	149
5.2	Number of T · 2-inefficient events for $K_{\pi 2}$ (top) and $K_{\mu 2}$ (bottom) decays as a function of the azimuthal angle ϕ of the track at the T counter (in π radians).	150
7.1	Constraints from astrophysics and $K^+ \rightarrow \pi^+ f$ on the masses of the axion and familon.	183
7.2	Experimental progress of the search for $K^+ \rightarrow \pi^+ \nu \bar{\nu}$	185

List of Tables

3.1	Total π^+ , ^{12}C interaction cross section, divided into 7 channels.	39
4.1	3-pulse signature in the TD of the stopping counter, for signal ($K^+ \rightarrow \pi^+\nu\bar{\nu}$) and background ($K^+ \rightarrow \mu^+\nu_\mu$).	54
4.2	Tools used to suppress background processes for $K^+ \rightarrow \pi^+\nu\bar{\nu}$	55
4.3	PASS1 cuts.	73
4.4	PASS2 cuts.	73
4.5	Definitions of the PASS2 output background data streams.	77
4.6	PASS3 kinematic pathology cuts.	78
4.7	PASS3 beam pathology cuts.	79
4.8	PASS3 data quality cuts.	80
4.9	PASS3 TD cuts.	83
4.10	PASS3 kinematic function cuts.	85
4.11	PASS3 beam function cuts.	89
4.12	Numbers of events B_j^i and C, CD_l from the normalization and rejection branches, respectively, of figures 4.20 and 4.21, and the resulting $K_{\pi 2}$ and $K_{\mu 2}$ normal- izations, rejections, and scaled background levels.	112
4.13	Numbers of events B_j^i and C, CD_l^k from the normalization and rejection branches, respectively, of figures 4.22 and 4.23, and the resulting single-beam normalizations, rejections, and scaled background levels.	114
4.14	Numbers of events B_j^i and C, CD_l from the normalization and rejection branches, respectively, of figures 4.24 and 4.25, and the resulting double-beam normal- izations, rejections, and scaled background levels.	115
4.15	Number of background events expected in the $\pi^+\nu\bar{\nu}(1)$ signal region.	116

4.16	Predicted and observed numbers of $K_{\pi 2}$ and $K_{\mu 2}$ background events.	118
4.17	Predicted and observed numbers of beam background events.	119
4.18	Complete listing of cuts applied in the analysis, divided into pathology cut classes.	120
4.19	Predicted and observed numbers of all types of background events in the 2/3 1996-7 data sample, obtained by loosening all functions at the same time. . .	121
4.20	Number of background events expected in the golden region.	124
4.21	Number of background events expected in the tight golden region.	125
5.1	K_{Blive} counting in the 1995-7 analysis. The variation in K_{Blive} with each year is primarily due to variation in the data collection time allotted to E787 each year.	133
5.2	$K_{\mu 2}$ -based acceptances of cuts.	136
5.3	SETUP cuts used in the $K_{\mu 2}$ -based acceptance measurement.	137
5.4	$K_{\pi 2}$ -based acceptances of cuts.	138
5.5	SETUP cuts used in the $K_{\pi 2}$ -based acceptance measurement.	138
5.6	π_{scat} -based acceptances of kinematic cuts.	140
5.7	SETUP cuts used in the π_{scat} -based kinematic acceptance measurement. . .	141
5.8	π_{scat} -based acceptances of TD cuts.	142
5.9	SETUP cuts used in the π_{scat} -based TD acceptance measurement.	143
5.10	Pion-nuclear absorption and decay in flight (NIDIF) contamination in the 1995 $K^+ \rightarrow \pi^+ \nu \bar{\nu}$ UMC data.	144
5.11	Accidental-induced acceptance of the trigger μ -veto.	147
5.12	Non-gap T · 2 efficiencies, $\epsilon_{T \cdot 2}^{ng}$, for $K_{\pi 2}$ and $K_{\mu 2}$ decays and kaon decays into $\pi^+ \nu \bar{\nu}$ and πf	152
5.13	UMC-based $K^+ \rightarrow \pi^+ \nu \bar{\nu}$ trigger acceptance.	153
5.14	UMC-based $K^+ \rightarrow \pi^+ f$ trigger acceptance.	154
5.15	UMC-based $\pi^+ \nu \bar{\nu}$ fiducial acceptance.	155
5.16	UMC-based πf fiducial acceptance.	155

5.17 Measured raw values of R , E , and P for the $K_{\pi 2}$ and $K_{\mu 2}$ peaks, and linear scaling factors.	157
5.18 Scaling factors which are applied to R , E , and P values from UMC-generated data.	158
5.19 Smearing factors which are applied to scaled values of R , E , and P from UMC-generated data.	158
5.20 Means and σ 's of Gaussian fits to kinematic variables from real $K_{\pi 2}$ data, and from UMC $K_{\pi 2}$ data after scaling and smearing.	159
5.21 Means and σ 's of Gaussian fits to kinematic variables from real $K_{\mu 2}$ data, and from UMC $K_{\mu 2}$ data after scaling and smearing.	159
5.22 Summary of UMC-based acceptances for $K^+ \rightarrow \pi^+ \nu \bar{\nu}$ events. The quoted uncertainties are purely statistical.	160
5.23 Summary of UMC-based acceptances for $K^+ \rightarrow \pi^+ f$ events. The quoted uncertainties are purely statistical.	160
5.24 Cuts applied to $K_{\mu 2}(1)$ monitor data in order to measure the $K_{\mu 2}$ branching ratio.	163
5.25 $K_{\mu 2}$ -based acceptance of cuts applied in the $K_{\mu 2}$ branching ratio measurement.	164
5.26 UMC-based acceptances of cuts applied in the $K_{\mu 2}$ branching ratio measurement.	165
5.27 Values of $(K_{Blive}^{eff})_{K_{\mu 2}}$ for each run period.	165
5.28 Cuts applied to $K_{\pi 2}(1)$ monitor data in order to measure the $K_{\pi 2}$ branching ratio.	167
5.29 Monitor-based acceptances of cuts applied in the $K_{\pi 2}$ branching ratio measurement.	169
5.30 UMC-based acceptances of cuts applied in the $K_{\pi 2}$ branching ratio measurement.	170
5.31 Values of $(K_{Blive}^{eff})_{K_{\pi 2}}$ for each run period.	171
5.32 $K^+ \rightarrow \pi^+ \nu \bar{\nu}$ single-event sensitivity of the 1995-7 analysis.	172
5.33 $K^+ \rightarrow \pi^+ f$ single-event sensitivity of the 1995-7 analysis.	173

6.1	Calculation of the probability that a $K^+ \rightarrow \pi^+ f$ event, for massless f , has the R , E , and P values of the candidate event.	177
C.1	Definitions of the categories of PV hits.	215
C.2	PV function cut parameters and performance at the $N_{PV} \leq 1.0$ cut position.	216
C.3	PV function.	217
C.4	TD function.	224
C.5	$K_{\pi 2}$ kinematic function.	226
C.6	$K_{\mu 2}$ kinematic function.	228
C.7	Double-beam function “inside the box”.	232
C.8	CEX function “inside the box”.	233

Acknowledgements

Back in 1995, when I decided I wanted to continue with graduate schooling and enroll as a Ph.D. candidate, I wasn't sure what I was getting into. My undergraduate degree at Simon Fraser University started in biology and chemistry, and my intention was to eventually apply to medical school. However, chemistry appealed to me more than biology, and soon I realized that I enjoyed physics the most, so I ended up with an undergraduate degree in chemical physics. In my last year of undergrad, I took some nuclear science courses which I found very interesting, especially with respect to the study of nuclear reactions that are believed to take place in stars and in the early universe, which are responsible for the materials that now make up our bodies and planet. TRIUMF was just down the road, and I figured a graduate degree was probably a good idea, so I completed a M.Sc. degree at the University of British Columbia in experimental nuclear physics with Mike Hasinoff. Mike fostered my interest in subatomic physics, and when I started looking for Ph.D. opportunities, Peter Gumplinger informed me of a particle physics experiment in New York which sounded interesting, in that it seemed to deal directly with the smallest fundamental particles that make up the matter around us. I thought the transition from nuclear to particle physics would be as natural and as smooth as my earlier transitions from biology to chemistry, atomic physics, and eventually to nuclear physics. However, I felt somewhat lost in the international, collaborative world of particle accelerators and high-energy physics, and I had to adjust to my new environment, much like other people in particle physics had to be accommodating and adjust to me. For this reason, I would like to thank Renee Poutissou, Toshio Numao, and John MacDonald for their considerable help. I'd like to thank Akira Konaka, George Redlinger, Joe Mildenerger, and Norihito Muramatsu who played a large role in my Ph.D. analysis and the completion of this dissertation. I'd like to thank the many other bright and dedicated E787 scientists

and technicians in Vancouver, New York, Princeton, and Japan who were instrumental in the acquisition and analysis of the high-quality data on which this thesis is based. I'd like to thank Doug Bryman, my Ph.D. supervisor, for his guidance and insight in helping me complete a Ph.D. degree, which, as I've come to learn, is no small feat. Over the past 5 years these people have helped me grow a lot, both as a scientist and as a person.

I'd also like to thank the many good friends I've met over the years, whether at school or elsewhere, who have supported me and made my various pursuits, including graduate school, fulfilling experiences. Last, but not most, I'd like to thank my family – John, Dawn, Dave, Aaron, Mark, and Alison – for all they have meant to me over the years. They are an integral part of who I am, and this work is as much theirs as it is mine.

Preface

This preface is designed with two purposes in mind: to give the reader some help in reading the thesis, and to outline some very basic reasons as to why one would want to pursue the topic of this thesis in the first place.

Chapter 1 is an introduction to particles and forces, which may, in part, be accessible to non-scientific readers as well as to scientific readers. Non-scientific readers will also hopefully find this preface, the abstract, and parts of chapter 7 interesting. The remainder of the thesis is quite technical. However, the thesis in its entirety is written as clearly and conceptually as possible so that particle physicists, as well as other scientists, can follow and fully understand it. Much detail is included, but hopefully not so much as to disturb textual flow. A glossary is included for aid in understanding jargon and acronyms used in the text. The following may not make much sense until much of the thesis is read, but here it is for the record: analysis “variables” and “cuts” are introduced in chapter 4, and are consistently denoted using *italicized* and CAPITALIZED text, respectively. Numbers of “events” which remain after reduction of the data are consistently denoted using the quantities B , C , CD , and M . “Scaled” numbers of events which are used as parameters in “function cuts” are consistently denoted using the quantity N . Numbers of events in the “normalization branches” of “bifurcated analyses” are denoted as B (B^*) when optional “second bifurcations” are (are not) employed in the analyses.

Now for the interesting question: why does one feel motivated to study particles and forces? A general answer, which can be used to justify scientific inquiry as a whole, is: scientific study inevitably leads to discoveries of new “phenomena”, which require the development of new ideas in order to better understand how everything in the universe interacts and evolves. The scientific process by which this knowledge is obtained can be described

very clearly in language and mathematics, and can be repeated many times in order to test the validity of the knowledge that is obtained. In this sense, one can have a lot of confidence in scientific ideas, which can then be used to solve human problems as well as to provide direction for human growth. Scientific understanding of how the world works can even bring satisfaction and peace of mind, to some people.

Most people crave some kind of knowledge, be it scientific, religious, or otherwise, in order to understand and peacefully coexist with their world. A knowledge of *why* things are the way they are aids in human survival and plays a role in social and political stability. While scientific ideas are aimed at alleviating struggle and improving quality of life through, for example, advances in medicine and engineering, religious and moral ideas are typically very personal and are aimed more at an acceptance of life's daily grind. Unlike scientific ideas, religious ideas usually cannot be tested, and are accepted more out of faith and intuition.

If one is looking for an absolute "truth" or "meaning of life" however, then both science and religion, in my opinion, have thus far failed. No single religious idea has ever united the human species with a common view of existence. And while science is adept at finding patterns in nature which give insight into the structure of the world, new questions about the patterns, and new patterns themselves, always seem to emerge, which suggests that scientific inquiry is a never-ending process which can never result in "full understanding." Perhaps, then, there is no absolute truth, or grand concept, or single principle which manifests everything. And/or perhaps conventional science and religion are intrinsically limited in scope.

Western science and religion seem to strive, somewhat, for "control" of the natural workings of the world, so that various "phenomena" can be predicted preceding, during, and after a human's life. Human beings can then exist with the least perceived amount of uncertainty and unhappiness.

Scientists try to understand and predict a pattern in nature by isolating a system, "reducing" it down to its component parts, and using these parts to model reality. For example, particle physicists build particle accelerators in order to isolate systems of particles and forces which emulate, to some degree, conditions in the early universe. They hope to be

able to construct patterns observed in the universe out of a small set of particles and forces which they observe in the laboratory. Since the advent of quantum mechanics, most scientists now realize that the very act of observing a system changes it, but the scientific approach is still largely based on “objectivity,” which aims to remove the observer from the observed. That is, while the laboratory approach of particle physics may help explain how a star evolves, it will not be able to explain how human beings interact with and “experience” the rest of the universe, because this element has been removed from the system. The universe is not like this however: we are *in* this universe, so the system studied in the lab is necessarily artificial. For this reason, increased knowledge and insight about particles and forces might be more readily obtained by observing high-energy processes which are naturally occurring elsewhere in the universe, such as in other star systems and galaxies, because these systems have not been artificially constructed. Still, the act of observing anything causes us to see what we have unconsciously decided we want to see, and the “reality” of the situation has to somehow incorporate all of the observed, the observer, and the act of observation. One would hope to avoid subject/object, conscious/unconscious, and mind/body distinctions. In fact, “A science that attends to such relationships rather than to so-called discrete entities would be a science of what has been called ‘participant observation,’ and it is this type of holistic thinking which might hold the key to future human evolution” [1].

There is a proposed theory in physics which has been labelled the “theory of *everything*” (TOE), which aims for a mathematical unification of quantum mechanics and the theory of general relativity. This theory attempts to unite the world of the very, very small (subatomic) with the world of the very, very big (cosmic). These worlds are definitely related, as is everything in the universe, because everything we can conceive of is part of the same universe. So the idea that these two worlds can both be described by the same mathematical language seems to make sense. However, the name of this theory may be an exaggeration. It’s difficult to picture a theorist sitting in a room with a pen in his/her hand, writing down some formula, and then saying “Wow – now we know *everything*.” If we truly knew everything, then we would know why we are conscious entities who exist in time. In fact, every thought, feeling, action, observation, and “phenomenon” is a process in time. The big mystery then, it seems

to me, which is difficult to address, is “what is time?”

I spend a lot of *time* thinking about this question, because it seems to be important to my own peace of mind. I believe that some sort of tangible answer can be found, but not completely via conventional scientific inquiry. This is because the question is more than an inquiry; it probes the very act of inquiry itself. Furthermore, a complete and meaningful answer to this or any question, in my opinion, should be an answer that is clear and intuitive to all. For example, Charles Darwin’s theory of “survival of the fittest” establishes an intimate and intuitive connection between the progression of time and the evolution of terrestrial “life”. Almost anyone can look at a giraffe and understand immediately that its long neck helps it to eat leaves at the tops of trees, and that this “adaptation” gives the giraffe a “survival advantage” which ensures its longevity within time. A more general connection between the progression of time and the features of the universe could be extended to incorporate not only the survival of terrestrial species, but also the structure and dynamics of galaxies, the stability of subatomic particles, and the development of human consciousness.

I believe an understanding of time can at least be approached using scientific methods. In particular, studying fundamental particles and forces in the lab brings one into direct contact with the magic and mystery of the universe, and gives one a powerful set of mental tools for trying to answer fundamental questions. Scientific tools on their own, at least for me, however, are not sufficient: pure intuition, feeling, and expression are equally valuable. I value personal interpretations of the world as much as I value scientific descriptions. Nevertheless, science is a dynamic field and it will no doubt continue to grow and evolve in positive ways. The respect I have for fundamental science and the satisfaction that it brings me provided the motivation for 12 years of scientific training and work, which includes the work described in this thesis.

Chapter 1

Introduction

All matter, energy, and every process in the observable 15-billion-year-old universe can be “reduced” to a small set of fundamental constituents. There are two classes of material particles (quarks and leptons), three families or generations of material particles (from light to heavy), and four forces (gravitational, electromagnetic, strong, and weak). The forces and material particles are similar in the sense that a force between two particles is “mediated” via exchange of another particle.

Two of the forces (gravity and electromagnetism) are “experienced” on large scales. For example, gravity keeps the earth in orbit around the sun, and keeps the atmosphere attached to the earth. Electromagnetism is responsible for the macroscopic properties of gases, liquids, and solids, including the friction between air and metal that enables flight. Conversely, the strong and weak forces are only effective at the subatomic level. For example, the strong force is responsible for the stability of the atomic nuclei that make up the earth and all living things. The weak force is responsible for the decay of the second and third generations of quarks and leptons into the lighter first generation particles. Any heavy quarks and leptons present in the early universe have long since decayed via the weak force, such that the vast majority of all matter in the universe, from the farthest, most ancient galaxies that can currently be seen, to nearby stars, planets, and people, is made out of the first generation particles.

Particles can be described in terms of their electromagnetic charge, spin, and mass. There are six quarks and six leptons, both of which are grouped into “left-handed doublets”

Chapter 1. Introduction

and “right-handed singlets”. The quark doublets consist of a charge $+2e/3$ quark and a charge $-e/3$ quark, and the lepton doublets consist of a charge 0 lepton (neutrino) and a charge $-e$ lepton, where e is the electromagnetic charge of the proton. The quarks and leptons are fermions (half-integral spin, e.g., spin = $1/2$), whereas the force particles are bosons (integral spin, e.g., the electromagnetic force particle, the photon, has spin = 1). Also associated with every particle is an anti-particle with opposite electromagnetic charge but identical spin and mass. All quarks, leptons, and force particles, except the photon, gluon (strong force particle), and maybe the neutrinos and graviton (gravity force particle), have mass. The masses are believed to arise from “spontaneous symmetry breaking” which occurs due to the existence of a massive particle known as the Higgs boson (see, for example, the review in ref. [2]). All of these particles, except the graviton and Higgs boson, have been directly observed. The quarks, leptons, and force particles are shown in figure 1.1.

Quarks interact via all four forces, whereas leptons only interact via three forces (all forces except the strong force). The forces have associated fields, and the mediating particles are the “quanta” of these fields. The electromagnetic force is mediated by the photon, and is described by a quantum field theory known as “quantum electrodynamics” (QED). The weak force is mediated by one of three particles, W^+ , W^- , Z^0 , depending on the electromagnetic charge of the particles involved in the weak process. The electromagnetic and weak forces are mathematically united in a single description known as Weinberg-Salam-Glashow $SU(2)\times U(1)$ electroweak theory [3, 4, 5]. This model has been very successful, most notably in its prediction and subsequent discovery of the W and Z bosons [6]. The strong force is mediated by gluons, and is described by a quantum field theory known as “quantum chromodynamics” (QCD). Much theoretical effort is focussed on “Grand Unified Theory” (GUT) which aims to extend the electroweak unification scheme to include strong interactions. The gravitational force is also believed to be mediated by a hypothetical particle called the graviton, but a quantum field theory of gravity has not (yet) been realized. Gravity is described by the theory of general relativity, and much theoretical effort is focussed on the so-called “Theory of Everything” (TOE) which aims to incorporate gravity into GUT.

The unification of the forces into a GUT or a TOE is desirable because it is believed

Elementary Particles

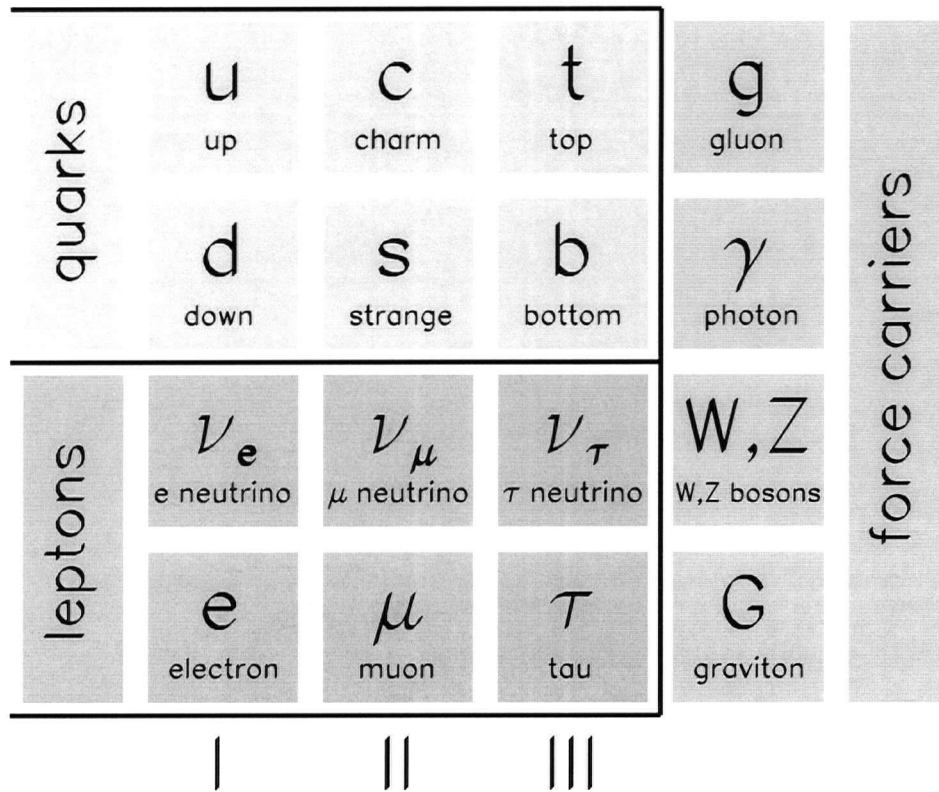


Figure 1.1: The fundamental particles and forces.

that at one time the universe was very hot and dense and essentially consisted of a single force/particle. The different forces and particles that are seen today “froze out” during the expansion and cooling of the universe caused by the “Big Bang”, which occurred roughly 15 billion years ago and gave rise to the still-expanding, still-cooling universe of today.

For example, at a few millionths of a second after the Big Bang, it is believed that quarks and gluons existed together in a hot plasma (near 2 trillion °C, evidence of which has recently been found [7]). After this point and up until the present day, the temperature of the expanding, cooling universe has been low enough such that the “charge” structure of the strong force is apparent. The strong force has three charges (named red, green, and blue), whereas the electromagnetic force has only a single charge (positive, and its opposite negative). Furthermore, the long-distance, low-temperature behaviour of the strong force is such that particles can only exist in chargeless states (e.g., red + anti-red, or all “colours” together: red + green + blue). That is, quarks are not directly detected as individual quarks (at least not with current technology operating below the quark-gluon plasma temperature). They are detected as quark + anti-quark pairs (mesons), or as three quarks bound together (baryons). Mesons and baryons are collectively called “hadrons”.

Also, the strong, electromagnetic, and weak forces are described by “renormalizable” quantum field theories [8], which predict that the strengths of the forces are functions of energy. The strong coupling decreases with energy, whereas the electromagnetic and weak couplings increase with energy. Just as the electromagnetic and weak forces have the same intrinsic coupling at “electroweak” energy scales (> 80 GeV), one expects the strong, electromagnetic, and weak forces to have the same intrinsic coupling at “GUT” energy scales ($> 10^{16}$ GeV – see, for example, ref. [9]). The matching of the strong, electromagnetic, and weak couplings can be made exact by invoking “supersymmetry” (SUSY), which predicts that each fundamental spin 1/2 fermion has a companion spin 0 boson, and each fundamental spin 1 or spin 2 boson has a companion spin 1/2 or spin 3/2 fermion. SUSY particles have not (yet) been observed, perhaps due to their large masses predicted as a consequence of supersymmetry “breaking”. Formulation of a successful GUT has also not yet been achieved.

Formulation of a TOE requires compatibility of the two fundamental theories in physics:

general relativity and quantum mechanics. At very small distance scales, quantum-mechanical energy fluctuations (“quantum foam”) are incompatible with the smooth, continuous space-time of general relativity. “String theory” [9] attempts to resolve this problem, and has credibility as a TOE because it naturally incorporates SUSY, and accounts for the weakness of gravity relative to the other forces via introduction of “extra dimensions”. These extra dimensions are not observed beyond the usual 3+1 spatial dimensions plus time due to “compactification”.

Other hypothetical particles (in addition to the Higgs boson and SUSY particles) are “axions” and “familons”, which are predicted to arise due to the spontaneous breaking of certain symmetries in nature. These particles may have non-zero mass, in which case they may be part of the “dark matter” of the universe. Most of the matter in the universe is believed to be dark matter, because the amount of visible matter in the universe is not sufficient to account for the observed rotation curves of galaxies and the dynamics of galaxy clusters and superclusters (as predicted by classical mechanics).

While searches for hypothetical particles and development of a GUT and a TOE continue, the $SU(3) \times SU(2) \times U(1)$ “Standard Model” (SM) of particles and interactions is composed of three generations of quarks and leptons, together with electroweak theory and QCD. The SM accounts for all of the observed particles and describes a wide variety of processes with great precision. However, some basic questions still remain. For example, why are there three generations of quarks and leptons? Is there a pattern to the specific masses of the fundamental particles? And why are quarks and leptons different? One can probe the SM and look for answers to the above questions in two ways: (1) observe interactions in an energy regime that has not yet been explored (i.e., at very high energies), and (2) observe very rare, low-energy electroweak processes, because the SM allows for precise predictions of low-energy electroweak processes, and non-SM contributions to a rare process could be relatively large. The search for the decay $K^+ \rightarrow \pi^+ \nu \bar{\nu}$ utilizes the latter of these two approaches. In chapter 2, the SM theory of electroweak interactions, and its prediction for $K^+ \rightarrow \pi^+ \nu \bar{\nu}$, are presented. The experimental method for measuring $K^+ \rightarrow \pi^+ \nu \bar{\nu}$ is discussed in chapter 3. The analysis of data taken between 1995 and 1997 is described in chapters 4 and 5, and the

Chapter 1. Introduction

results given in chapter 6. Conclusions are drawn in chapter 7.

Chapter 2

Theory

This chapter continues the theoretical discussion of particle physics from the previous chapter, with emphasis on weak interactions and the decay $K^+ \rightarrow \pi^+ \nu \bar{\nu}$.

2.1 Weak Interactions

As mentioned in the previous chapter, quarks interact via all four forces, whereas leptons only interact via three forces (all forces except the strong force). Put another way, the strong force operates only on the quarks, not on the leptons, because only the quarks carry strong “charge”. Each quark carries one of the three strong charges (red, green, or blue).

The electromagnetic force operates on both quarks and leptons, but not on the lepton neutrinos because these do not carry electromagnetic charge. The pair of quarks or leptons in a given generation differs by exactly one unit of electromagnetic charge. The two quarks in each generation carry $+2/3$ and $-1/3$ units of electromagnetic charge, respectively, and the two leptons in each generation carry 0 and -1 units of electromagnetic charge, respectively.

The weak force operates on all quarks and leptons (as does the gravitational force). That is, all quarks and leptons carry weak “charge”. Furthermore, the weak force mediators themselves (W^+, W^-, Z^0) can carry one unit of electromagnetic charge, unlike the strong, electromagnetic, and gravitational mediators which do not carry electromagnetic charge ($g, \gamma,$ and G). The weak force can transform a quark or lepton in a given generation into the other (lighter) quark or lepton from the same generation, while still conserving

electromagnetic charge. The strong, electromagnetic, and gravitational forces cannot do this, and in fact are observed to also conserve particle “flavour”. That is, a specific quark or lepton is stable and remains that specific quark or lepton regardless of whether or not it undergoes a strong, electromagnetic, or gravitational interaction. One might expect, however, that the weak force, similar to the other forces, at least conserves generation. This too is not the case. Both kaon decay (which involves decay of second-generation quark into a first-generation quark, $s \rightarrow u$) and neutron decay (which involves decay of a first-generation quark into the other, lighter first-generation quark, $d \rightarrow u$) are observed to occur, albeit at different rates. Recent evidence for neutrino oscillations and masses [10] suggests that the weak force also does not conserve generation in the lepton sector.

However, inter-generational weak processes which involve decay of a second-generation quark into the the first-generation quark with the same electromagnetic charge (e.g., $K_L^0 \rightarrow \mu^+ \mu^-$, and $K^0 - \bar{K}^0$ mixing, both of which involve $s \rightarrow d$ decay) are observed to occur at extremely low rates. That is, “neutral” weak interactions seem to conserve generation, whereas “charged” weak interactions do not. One can account for this behaviour, as well as maintain a general quark-generation-conserving structure for the weak force, by “rotating” the physical, massive quarks which undergo strong, electromagnetic, and gravitational interactions, into an analogous set of quarks which undergo weak interactions. This “change of basis” was originally performed via a unitary rotation matrix of rank 2, which “mixes” the quarks in terms of a single parameter, the Cabibbo angle θ_C [11], or as the sine of this angle, $\lambda = \sin \theta_C = 0.22$. At this time, only three species of quarks were known (u, d, s) and the rank 2 rotation matrix required a fourth quark (c) which was subsequently discovered. The rotation of the physical, massive quark “eigenstates” into the weak quark eigenstates is referred to as the “GIM” (Glashow, Iliopoulos, Maiani) mechanism [12], and results in a cancellation of decay amplitudes such that “flavour-changing neutral currents” (FCNC), i.e., weak processes which involve a quark changing into a different quark with the same electromagnetic charge (e.g., $K_L^0 \rightarrow \mu^+ \mu^-$), are not allowed.

Later, the four-quark rotation matrix was generalized to the six-quark case. This rank 3 rotation matrix, called the “CKM” (Cabibbo, Kobayashi, Maskawa) matrix [13], naturally

incorporates CP violation which had previously been discovered in neutral kaon decays [14]. Furthermore, the fifth and sixth quarks, b and t , which are the third-generation quarks, have since been found experimentally. Conventionally, one performs the CKM mixing by rotating the charge $-e/3$ quark mass eigenstates (d, s, b) relative to the charge $+2e/3$ quark mass eigenstates (u, c, t). That is, the weak eigenstates d', s', b' are related to the mass eigenstates d, s, b via the unitary CKM matrix:

$$\begin{pmatrix} d' \\ s' \\ b' \end{pmatrix} = \begin{pmatrix} V_{ud} & V_{us} & V_{ub} \\ V_{cd} & V_{cs} & V_{cb} \\ V_{td} & V_{ts} & V_{tb} \end{pmatrix} \begin{pmatrix} d \\ s \\ b \end{pmatrix}. \quad (2.1)$$

The CKM matrix has four independent parameters which, in the leading order of the Wolfenstein parameterization [15], are A, λ, ρ, η :

$$\begin{pmatrix} V_{ud} & V_{us} & V_{ub} \\ V_{cd} & V_{cs} & V_{cb} \\ V_{td} & V_{ts} & V_{tb} \end{pmatrix} \simeq \begin{pmatrix} 1 - \lambda^2/2 & \lambda & A\lambda^3(\rho - i\eta) \\ \lambda & 1 - \lambda^2/2 & A\lambda^2 \\ A\lambda^3(1 - \rho - i\eta) & -A\lambda^2 & 1 \end{pmatrix}. \quad (2.2)$$

In this parameterization, the CKM matrix elements are written in powers of $\lambda = \sin \theta_C = 0.22$. The parameter η describes CP violation in the SM in that non-zero values of η break CP invariance for weak interactions. Current experimental ranges of the magnitudes of the CKM matrix elements are [16]

$$\begin{pmatrix} |V_{ud}| & |V_{us}| & |V_{ub}| \\ |V_{cd}| & |V_{cs}| & |V_{cb}| \\ |V_{td}| & |V_{ts}| & |V_{tb}| \end{pmatrix} = \begin{pmatrix} [0.9742, 0.9757] & [0.219, 0.226] & [0.002, 0.005] \\ [0.219, 0.225] & [0.9734, 0.9749] & [0.037, 0.043] \\ [0.004, 0.014] & [0.035, 0.043] & [0.9990, 0.9993] \end{pmatrix}. \quad (2.3)$$

Knowledge of the CKM matrix elements comes from measurement of first-order and second-order weak processes. Those determined “directly” using first-order processes include [16]:

- $|V_{ud}|$ — determined from superallowed nuclear β decay and from decay of the neutron, both of which involve $d \rightarrow u$ decay.
- $|V_{us}|$ — determined from $K^+ \rightarrow \pi^0 e^+ \nu_e$ decay and from Λ decays, which involve $s \rightarrow u$ decay.
- $|V_{cd}|$ — determined from “inverse charm decay”, i.e., neutrino or anti-neutrino production of c quarks off of valence d quarks.

- $|V_{cs}|$ — determined using semi-leptonic $D \rightarrow K$ decay and hadronic W decays.
- $|V_{cb}|$ — determined using semi-leptonic $B \rightarrow D$ decays.
- $|V_{ub}|$ — determined from inclusive semi-leptonic decay of B mesons via $b \rightarrow ul\bar{\nu}_l$, by measuring the lepton energy spectrum above the endpoint of $b \rightarrow cl\bar{\nu}_l$ decay. The result is interpreted in terms of $|V_{ub}/V_{cb}|$, and is strongly model dependent. $|V_{ub}|$ can also be extracted from exclusive semi-leptonic $B \rightarrow \pi$ and $B \rightarrow \rho$ decay, but again there is significant theoretical model dependence of the result.
- $|V_{tb}|$ — from measurement of the fraction of t quarks that decay semi-leptonically into b quarks as opposed to s or d quarks, one measures $|V_{tb}|^2/(|V_{td}|^2 + |V_{ts}|^2 + |V_{tb}|^2)$.

Further information on CKM matrix elements (particularly those involving coupling to t quarks) can be determined “indirectly” from flavour-changing second-order weak processes which involve an internal “loop” (e.g., $K^+ \rightarrow \pi^+ \nu \bar{\nu}$, as described in section 2.2 and shown in figure 2.2). One predicts values for CKM matrix elements by assuming that the dominant contribution to the process comes from the t -quark loop and not from non-SM physics. Conversely, the agreement of predicted and measured quantities can be used to put constraints on new physics. Quantities measured using one-loop processes include:

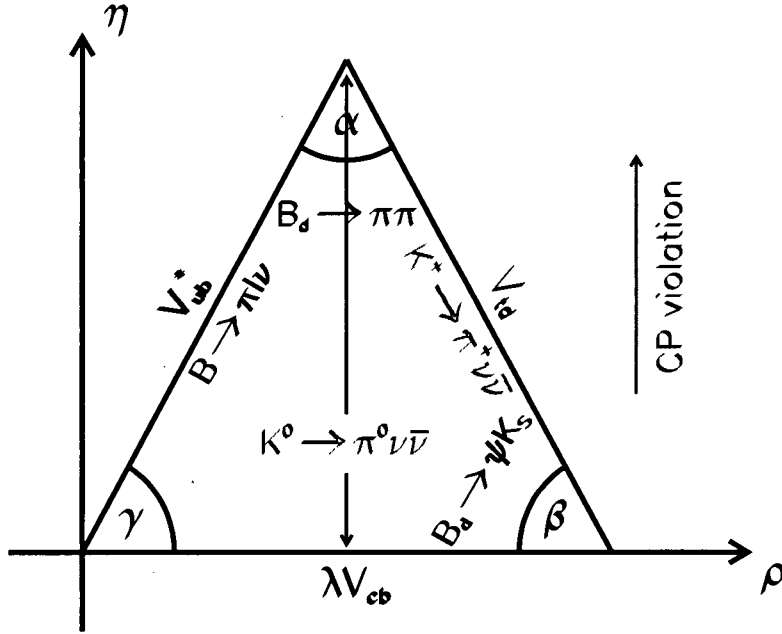
- $|V_{tb}^* \cdot V_{td}|$ — from $B_d^0 - \bar{B}_d^0$ mixing.
- $|V_{td}|/|V_{ts}|$ — an upper limit on this quantity comes from the lower limit of the B_s^0, \bar{B}_s^0 mass difference as determined from a limit on $B_s^0 - \bar{B}_s^0$ mixing, and the ratio of hadronic matrix elements for $B_s^0 - \bar{B}_s^0$ mixing and $B_d^0 - \bar{B}_d^0$ mixing as calculated using lattice QCD.
- $|V_{ts}|/|V_{cb}|$ — from observation of $b \rightarrow s\gamma$ decays.
- $|V_{td}|$ — assuming three generations of quarks, $|V_{ts}| \simeq |V_{cb}|$, so $|V_{td}|$ can be extracted from the $|V_{td}|/|V_{ts}|$ ratio above measured using B physics. As shown in section 2.3, $|V_{td}|$ can also be extracted from $K^+ \rightarrow \pi^+ \nu \bar{\nu}$ decay, which is theoretically precise, but difficult to observe due to the rarity of this K decay channel (see section 2.2).

The CKM matrix elements (in particular, V_{cs} and V_{td}) can also be constrained using the assumption of unitarity of the quark mixing matrix (independent of the “rank” of this matrix, which is the number of quark generations). In fact, all of the above direct and indirect information on the CKM matrix elements can be summarized in terms of the “unitarity triangle”. A matrix V is unitary if $V^\dagger V = 1$, which implies that if the complex conjugate of elements in one row (column) of a unitary matrix are multiplied by the corresponding elements in a different row (column), the products sum to zero. Applied to the first and third columns of the rank 3 CKM matrix in Eq. (2.2), this means that

$$V_{ub}^* V_{ud} + V_{cb}^* V_{cd} + V_{tb}^* V_{td} \simeq V_{ub}^* + \lambda V_{cb}^* + V_{td} = 0 \quad (2.4)$$

where the approximation $V_{ud} \simeq V_{tb} \simeq 1$ has been made. This triangle in the complex (ρ, η) plane is shown in figure 2.1. Because η parameterizes CP violation in the SM, the altitude or area of this triangle gives the SM contribution to CP violation. The location of the $\eta \neq 0$ vertex is currently constrained by measurement of $|V_{ub}|$, B mixing, and the CP -violating parameter ϵ from neutral kaon decays. The altitude of the triangle may eventually be determined, given V_{ts} , from the CP -violating process $K_L^0 \rightarrow \pi^0 \nu \bar{\nu}$, which offers a high-precision measurement of the imaginary part of $V_{ts}^* \cdot V_{td}$. Also, in neutral B decays to CP eigenstates, e.g., $B_d(\bar{B}_d) \rightarrow \pi\pi$ and $B_d(\bar{B}_d) \rightarrow \psi K_S$, there is a direct relationship between CP -violating asymmetries and $\sin 2\phi$, where ϕ is one of the angles of the unitarity triangle, denoted by α, β, γ in figure 2.1. Twice the area of this triangle, or any of 5 other unitarity triangles, is given by the Jarlskog invariant [17], whose non-zero value is a necessary and sufficient condition for CP violation with three generations.

Measurement of the unitarity triangle is therefore a test of the SM, in that non-unitarity of the 3×3 CKM matrix could imply more than three generations of quarks. Furthermore, measurement of η constrains the SM contribution to CP violation. The motivation for the search for $K^+ \rightarrow \pi^+ \nu \bar{\nu}$ stems from the desire to measure the small, imprecisely-determined CKM matrix element $|V_{td}|$. Another goal is to search for non-SM physics.

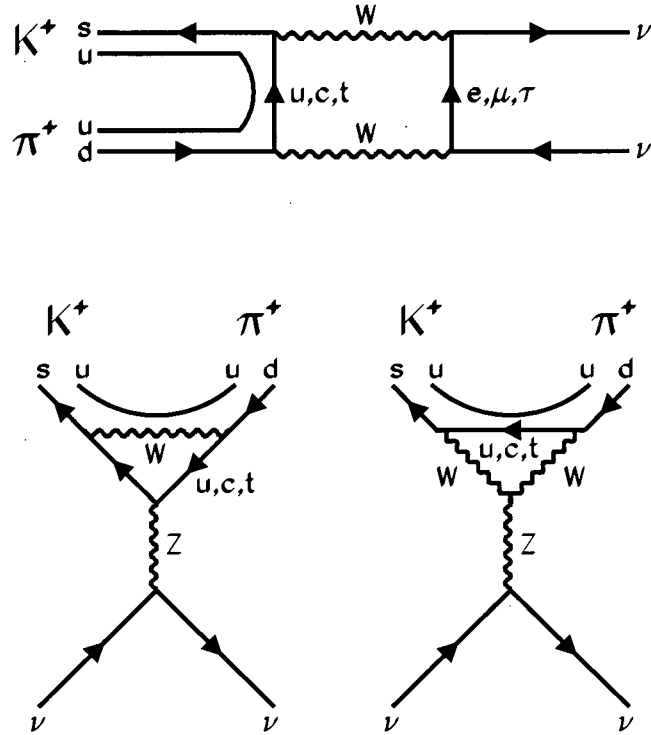

 Figure 2.1: Unitarity triangle in the complex (ρ, η) plane.

2.2 $K^+ \rightarrow \pi^+ \nu \bar{\nu}$

$K^+ \rightarrow \pi^+ \nu \bar{\nu}$ is a second-order FCNC which is highly suppressed in the SM. The Feynman diagrams for $K^+ \rightarrow \pi^+ \nu \bar{\nu}$ are shown in figure 2.2, and consist of a “W-box” diagram and two “Z-penguin” diagrams. The weak amplitude for this process goes as

$$\mathcal{M} \sim \sum_{i=u,c,t} V_{is}^* V_{id} \frac{\gamma^\mu q_\mu + m_i}{q^2 - m_i^2} \quad (2.5)$$

where the V_{ij} are CKM matrix elements, the γ^μ are Dirac matrices, q_μ is the momentum transfer, and the m_i are quark masses. As stated in the previous section, if the complex conjugate of elements in one row (column) of a unitary matrix are multiplied by the corresponding elements in a different row (column), the products sum to zero. Applied to the first and second columns of the CKM matrix in Eq. (2.2), this means that $V_{us}^* V_{ud} + V_{cs}^* V_{cd} + V_{ts}^* V_{td} = 0$. So if the quark masses, m_i , are equal, the assumed unitarity of the CKM matrix causes \mathcal{M} to vanish. However, the breaking of flavour symmetry, which results in the different quark masses, means that \mathcal{M} is non-zero and that $K^+ \rightarrow \pi^+ \nu \bar{\nu}$ can proceed at a very small rate.


 Figure 2.2: Short-distance Feynman diagrams for $K^+ \rightarrow \pi^+ \nu \bar{\nu}$.

The greatest violator of quark mass equality is the top quark, which means that of the up, charm, and top-quark contributions to $K^+ \rightarrow \pi^+ \nu \bar{\nu}$, the top-quark contribution is the greatest, and the decay is sensitive to the weak coupling of top to down quarks, given by the CKM matrix element V_{td} .

The up-quark contribution to $K^+ \rightarrow \pi^+ \nu \bar{\nu}$ is negligible, and the effective Hamiltonian for $K^+ \rightarrow \pi^+ \nu \bar{\nu}$ is given by [18]

$$\mathcal{H}_{eff} = \frac{G_F}{\sqrt{2}} \frac{\alpha}{2\pi \sin^2 \theta_W} \sum_{l=e,\mu,\tau} [V_{cs}^* V_{cd} X_{NL}^l + V_{ts}^* V_{td} X(x_t)] (\bar{s}d)_{V-A} (\bar{\nu}_l \nu_l)_{V-A} \quad (2.6)$$

where G_F is the Fermi weak coupling constant, α is the electromagnetic fine structure constant, and θ_W is the Weinberg or weak mixing angle. The dependence on the charged lepton masses, resulting from the W -box diagram in figure 2.2, is negligible for the top-quark but not the charm-quark contribution to $K^+ \rightarrow \pi^+ \nu \bar{\nu}$, because the mass of the top quark is much greater than that of all three charged leptons, whereas the mass of the charm quark is similar to that of the τ lepton.

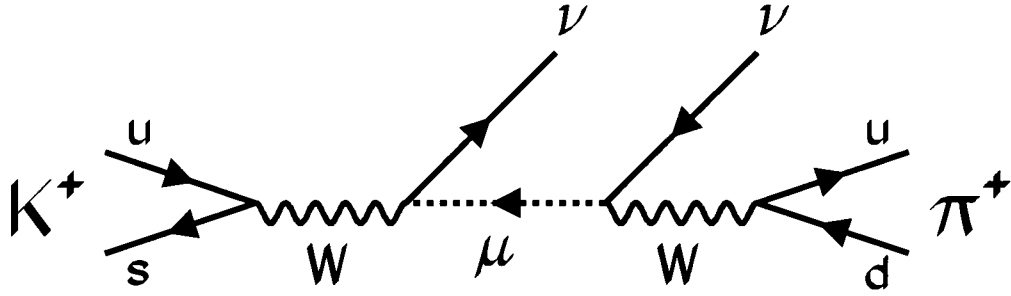
QCD corrections to the quark loops are treated perturbatively and are contained in the GIM functions $X(\alpha_s, x_i, \ln x_i)$, where α_s is the strong coupling constant and x_i is the square of the relative mass of quark i and the W boson, $x_i = m_i^2/M_W^2$. The logarithmic terms, $\ln x_i$, enter into $X(\alpha_s, x_i, \ln x_i)$ at order α_s^n as $\ln^m x_i$, where $m = 0, 1, 2, \dots, n + 1$ [19]. For the top-quark loop, x_t is of order 1 (2.17), so $\ln x_t$ is small (0.774). Furthermore, the strong coupling $\alpha_s(\mu)$ is small ($\ll 1$) at energy scales $\mu = \mathcal{O}(m_t)$. Therefore, $X(\alpha_s, x_t, \ln x_t)$ need only be calculated to leading order in α_s , but all orders in x_t must be kept. The GIM function for the top-quark loop is calculated in the “leading-order logarithmic approximation” (LLA) [19] and denoted simply as $X(x_t)$, which is given by [18]

$$X(x_t) = \eta_X \cdot X_0(x_t) \quad (2.7)$$

$$X_0(x_t) = \frac{x_t}{8} \left[-\frac{2+x_t}{1-x_t} + \frac{3x_t-6}{(1-x_t)^2} \ln x_t \right] \quad (2.8)$$

where $\eta_X = 0.994$ summarizes QCD corrections. Conversely, for the charm-quark loop, x_c is small (0.0155), so $|\ln(x_c)|$ is large (4.16). Furthermore, QCD perturbation theory is less accurate for the smaller energy scales $\mu = \mathcal{O}(m_c)$ at which $\alpha_s(\mu)$ is larger. Therefore, $X(\alpha_s, x_c, \ln x_c)$ need only be calculated to leading order in x_c , but non-leading orders in α_s must be kept. The GIM function for the charm-quark loop comes from a renormalization group calculation in the “next-to-leading-order logarithmic approximation” (NLLA) [18, 19], and is denoted simply as X_{NL}^l . Theoretical uncertainty in this term comes from the choice of renormalization scale and the charm quark mass, and is about 5%.

Long-distance contributions to $K^+ \rightarrow \pi^+ \nu \bar{\nu}$, where a light meson or lepton is exchanged (e.g., see figure 2.3), are three orders of magnitude smaller than the short-distance diagrams of figure 2.2 which have heavy quarks in intermediate states [20, 21, 22]. Furthermore, the matrix element of the weak hadronic current, $\langle \pi^+ | J_H^W | K^+ \rangle$, is related via weak isospin to the well-measured first-order weak decay $K^+ \rightarrow \pi^0 e^+ \nu_e$, which has a branching ratio of $(4.82 \pm 0.06)\%$ [16]. $K^+ \rightarrow \pi^+ \nu \bar{\nu}$ is therefore theoretically “clean” and the branching ratio is given by [18]


 Figure 2.3: A long-distance Feynman diagram for $K^+ \rightarrow \pi^+ \nu \bar{\nu}$.

$$B(K^+ \rightarrow \pi^+ \nu \bar{\nu}) = \kappa_+ \left[\left(\frac{\Im \lambda_t}{\lambda^5} X(x_t) \right)^2 + \left(\frac{\Re \lambda_c}{\lambda} P_0(X) + \frac{\Re \lambda_t}{\lambda^5} X(x_t) \right)^2 \right] \quad (2.9)$$

$$\kappa_+ = r_{\kappa_+} \frac{3\alpha^2 B(K^+ \rightarrow \pi^0 e^+ \nu_e)}{2\pi^2 \sin^4 \theta_W} \lambda^8 = 4.11 \times 10^{-11} \quad (2.10)$$

where λ is the Wolfenstein λ from Eq. (2.2), $\lambda_i = V_{is}^* V_{id}$, and λ_c is real to an accuracy of better than 10^{-3} . $\Im \lambda_t$ is proportional to the Jarlskog invariant [17]. $r_{\kappa_+} = 0.901$ is the isospin-breaking correction for $K^+ \rightarrow \pi^0 e^+ \nu_e$ relative to $K^+ \rightarrow \pi^+ \nu \bar{\nu}$. $P_0(X) = 0.42 \pm 0.06$, defined for the charm sector, is a function of QCD renormalization scale and m_c . The SM prediction for the $K^+ \rightarrow \pi^+ \nu \bar{\nu}$ branching ratio is

$$B(K^+ \rightarrow \pi^+ \nu \bar{\nu}) = (0.82 \pm 0.32) \times 10^{-10} \quad (2.11)$$

where the uncertainty is dominated by the measurement uncertainty in the CKM matrix elements $|V_{cb}|$ and $|V_{ub}/V_{cb}|$ which are used to constrain λ_t . The total theoretical uncertainty in the $K^+ \rightarrow \pi^+ \nu \bar{\nu}$ branching ratio, resulting from the choice of QCD renormalization scale in the charm sector, charm quark mass, weak isospin-breaking and two-loop electroweak corrections, is about 7%. Because the predicted rate is so low and lies in a narrow range, $K^+ \rightarrow \pi^+ \nu \bar{\nu}$ serves as a sensitive probe of the quantum structure of SM flavour dynamics.

2.3 V_{td}

The measured value of the $K^+ \rightarrow \pi^+ \nu \bar{\nu}$ branching ratio can be used to extract the magnitude of the CKM matrix element V_{td} . Rewriting Eq. (2.9) using an ‘‘improved’’ Wolfenstein parameterization gives [18]

$$B(K^+ \rightarrow \pi^+ \nu \bar{\nu}) = \kappa_+ A^4 X^2(x_t) \frac{1}{\sigma} [(\sigma \bar{\eta})^2 + (\rho_0 - \bar{\rho})^2]. \quad (2.12)$$

ρ_0 is defined as

$$\rho_0 = 1 + \frac{P_0(X)}{A^2 X(x_t)}. \quad (2.13)$$

$\bar{\rho}$, $\bar{\eta}$ and σ are defined by

$$\bar{\rho} = \rho \left(1 - \frac{\lambda^2}{2}\right), \quad (2.14)$$

$$\bar{\eta} = \eta \left(1 - \frac{\lambda^2}{2}\right), \quad (2.15)$$

$$\sigma = \left(\frac{1}{1 - \frac{\lambda^2}{2}}\right)^2. \quad (2.16)$$

Eq. (2.12) defines an ellipse in the $(\bar{\rho}, \bar{\eta})$ plane centered at $(\rho_0, 0)$. In the leading order of the Wolfenstein parameterization,

$$\sigma \rightarrow 1, \quad \bar{\eta} \rightarrow \eta, \quad \bar{\rho} \rightarrow \rho \quad (2.17)$$

and Eq. (2.12) becomes

$$B(K^+ \rightarrow \pi^+ \nu \bar{\nu}) = \kappa_+ A^4 X^2(x_t) [\eta^2 + (\rho_0 - \rho)^2] \quad (2.18)$$

which defines a circle in the (ρ, η) plane centered at $(\rho_0, 0)$ with radius r_0 given by

$$r_0^2 = \frac{1}{A^4 X^2(x_t)} \frac{B(K^+ \rightarrow \pi^+ \nu \bar{\nu})}{\kappa_+}. \quad (2.19)$$

From Eq. (2.2), the Wolfenstein parameterization of the CKM matrix defines

$$V_{td} = A\lambda^3(1 - \rho - i\eta). \quad (2.20)$$

So

$$|V_{td}| = A\lambda^3 R_t \quad (2.21)$$

where, in the leading-order Wolfenstein parameterization,

$$R_t^2 = (1 - \rho)^2 + \eta^2 \quad (2.22)$$

which defines a circle in the (ρ, η) plane centered at $(1,0)$.

Because Eqs. (2.18) and (2.19) define a circle in the (ρ, η) plane with radius r_0 centered at $(\rho_0, 0)$, and Eq. (2.22) defines a circle in the (ρ, η) plane with radius R_t centered at $(1,0)$, V_{td} may be extracted by building a triangle with sides of length $\rho_0 - 1$, r_0 and R_t . As shown in figure 2.4, a third circle from B physics provides a unique third vertex to the triangle: this circle has radius $R_b = \frac{|V_{ub}/V_{cb}|}{V_{us}}$ and is centered at $(0,0)$. No one side of the triangle can be longer than the sum of the two other sides, nor smaller than the absolute value of the difference between those sides, so

$$||\rho_0 - 1| - r_0| < R_t < ||\rho_0 - 1| + r_0|. \quad (2.23)$$

These limits on R_t define the limits on $|V_{td}|$ according to Eq. (2.21). $|\rho_0 - 1|$ and r_0 come from a combination of theoretical prediction and experimental measurement of quantities in Eqs. (2.13) and (2.19), respectively. Calculations of ρ_0 , r_0 , R_t , and $|V_{td}|$ are described in section 6.3.

2.4 New Physics

Observation of a rate for $K^+ \rightarrow \pi^+ \nu \bar{\nu}$ which is different from the SM prediction, or a π^+ momentum spectrum different from that for massless neutrinos and pure $V - A$ couplings, could indicate physics beyond the SM. Possible extensions to the SM include:

- $K^+ \rightarrow \pi^+ X^0$, where X^0 is a Nambu-Goldstone boson, e.g., an axion, familon, or majoron [16, 20, 23], which arises when a global continuous symmetry is spontaneously broken in the vacuum. The boson's coupling to SM particles, or, equivalently, its mass, is suppressed by (i.e., is inversely proportional to) the energy scale of the symmetry breaking.
- intermediate-state supersymmetric particles [20].

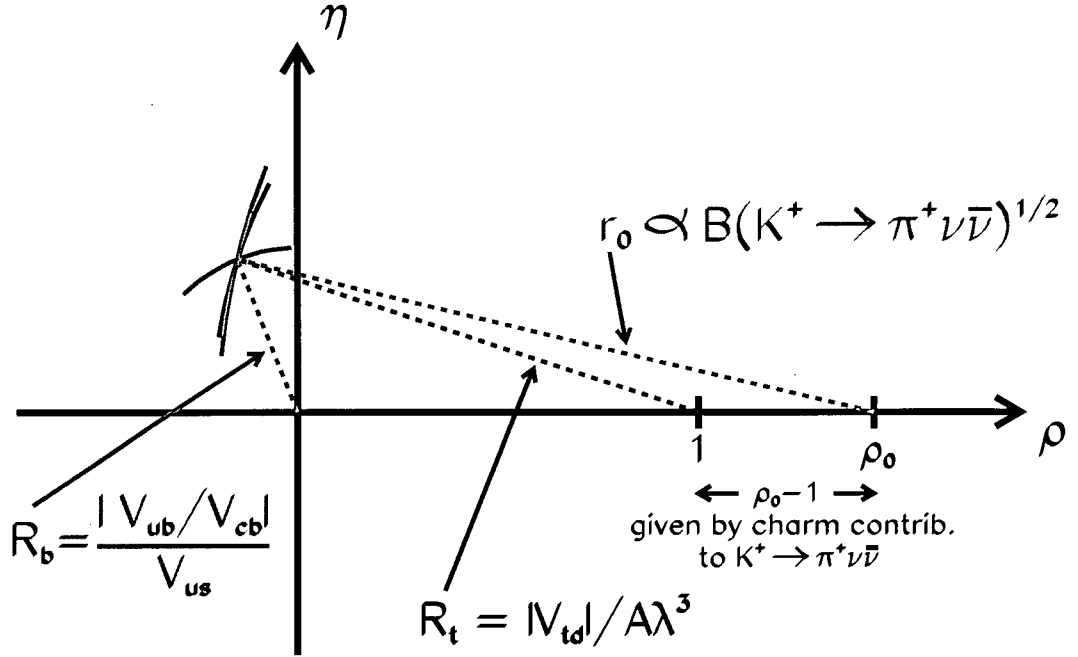


Figure 2.4: Relationship between $K^+ \rightarrow \pi^+ \nu \bar{\nu}$ and $|V_{td}|$ in the (ρ, η) plane.

- a fourth generation of quarks, which could interfere constructively or destructively with the top and charm contributions, or a fourth generation of leptons which would increase the number of channels available for $K^+ \rightarrow \pi^+ \nu \bar{\nu}$.
- an enhanced effective $\bar{s}dZ$ vertex [24], which is currently constrained by measurement of direct CP violation, ϵ'/ϵ [16].
- right-handed neutrinos (associated with the majoron), which would alter the π^+ momentum spectrum.
- lepton flavour violation $K^+ \rightarrow \pi^+ \nu_l \nu_l$.
- a “fifth” force [20].
- $K^+ \rightarrow \pi^+ XX$, where X is any neutral weakly-interacting particle.

Note that the $K \rightarrow \pi$ decay system is well-suited to the search for massless Goldstone bosons ($K^+ \rightarrow \pi^+ X^0$). The kaon and the pion are the lightest SM pseudoscalar (spin 0) particles so, by conservation of angular momentum, the other particle in a two-body $K \rightarrow \pi$ decay

must also have spin 0. This means that, in the search for Goldstone bosons (which are scalar or pseudoscalar), there is no interference in the final state from massless SM scalar or non-scalar particles (e.g., the photon).

Chapter 3

Experiment

As shown in the previous chapter, $K^+ \rightarrow \pi^+ \nu \bar{\nu}$ is theoretically clean and sensitive to top physics. The challenge then is to make $K^+ \rightarrow \pi^+ \nu \bar{\nu}$ experimentally clean, such that it can be measured and utilized as a sensitive probe of the SM. Because neutrinos are weakly-interacting neutral particles, the experimental signature for $K^+ \rightarrow \pi^+ \nu \bar{\nu}$ is simply $K^+ \rightarrow \pi^+$, with nothing else observed. Potential backgrounds are the decays $K^+ \rightarrow \pi^+ \pi^0$ (referred to as $K_{\pi 2}$ decay) and $K^+ \rightarrow \mu^+ \nu_\mu$ (referred to as $K_{\mu 2}$ decay), which have branching ratios of 0.2116 ± 0.0014 and 0.6351 ± 0.0018 , respectively [16]. These two-body decays, monochromatic in the kaon rest frame, are suppressed kinematically by limiting the search for $K^+ \rightarrow \pi^+ \nu \bar{\nu}$ to the region between the $K_{\pi 2}$ and $K_{\mu 2}$ kinematic peaks, called the “ $\pi^+ \nu \bar{\nu}(1)$ ” region, or the region just below the $K_{\pi 2}$ kinematic peak, called the “ $\pi^+ \nu \bar{\nu}(2)$ ” region (see figure 4.3 of the next chapter). $K_{\pi 2}$ decays are further suppressed via photon detection of $\pi^0 \rightarrow \gamma\gamma$, and $K_{\mu 2}$ decays are further suppressed via π^+/μ^+ particle identification (PID). Other potential backgrounds include scattering of beam pions and kaon charge-exchange (CEX): $K^+ n \rightarrow K^0 p$ followed by $K_L^0 \rightarrow \pi^+ l^- \bar{\nu}_l$, where l^- is a muon or an electron. K^+/π^+ PID and timing in the beam, and PID of the kaon decay product can be used to suppress these backgrounds. Because the branching ratio for $K^+ \rightarrow \pi^+ \nu \bar{\nu}$ is on the order of 10^{-10} , suppression of each type of background must be at least 10^{10} for a signal/background ratio > 1 . These considerations motivate beamline and detector design. More details on the backgrounds to $K^+ \rightarrow \pi^+ \nu \bar{\nu}$ and the methods used to suppress and estimate their contamination are given in chapter 4.

The experiment was carried out at Brookhaven National Laboratory (BNL), Upton, Long Island, New York, under the auspices of experiment 787 (E787). A total of 3.2 trillion kaons were collected in the detector over 3 separate run periods in 1995, 1996, and 1997.

3.1 Kaon Production and Transport

The major accelerator facilities at BNL are shown in figure 3.1. Production of kaons begins with a volume of hydrogen gas. An electrical arc is applied to the hydrogen in order to produce negatively-charged hydrogen ions (H^- ions), which are accelerated to 200 MeV in a linear accelerator (LINAC). The electrons are removed from the H^- ions by thin carbon foils in order to produce H^+ ions (protons), which are accelerated to a momentum of 24 GeV/c in a pair of synchrotrons: a “booster” and the “alternating gradient synchrotron” (AGS). 60 trillion protons (60 Tp) are extracted in 1.6-second “spills” once every 3.6 seconds from the AGS via resonant extraction [25, 26]. This beam, called “slow extracted beam” (SEB), is split in a “switchyard” into 4 beams via 3 electrostatic wire splitters. The beams are then transported to 4 target stations: A, B, C and D. The C target is composed of platinum which extends 6 cm in the beam direction. Typical AGS running conditions have 15 Tp per 1.6-second spill at 24 GeV/c incident on the C target, which directly produce positively-charged kaons and pions. “Low energy separated beamline III” (LESBIII, shown in figure 3.2) [27] collects and focusses the kaons produced at the C target for use by E787. The raw content of the beam emerging from the C target contains about 500 pions and 500 protons for every kaon, which are momentum-selected by a dipole magnet (C2D1 in figure 3.2). Kaons, pions, and protons of equal momenta have different velocities, so they arrive at the first electrostatic separator (C2BS-1 in figure 3.2) at different times. The separator applies an alternating voltage across the beam with amplitude, frequency, and phase such that kaons pass through the separator undeflected, but pions and protons are swept out of the beam. A second separator (C2BS-2 in figure 3.2) sweeps pions and muons out of the beam which arise from kaon and pion decay in the region between the two separators. The resulting beam is again momentum-selected by a second dipole magnet (C2D2 in figure 3.2). LESBIII also

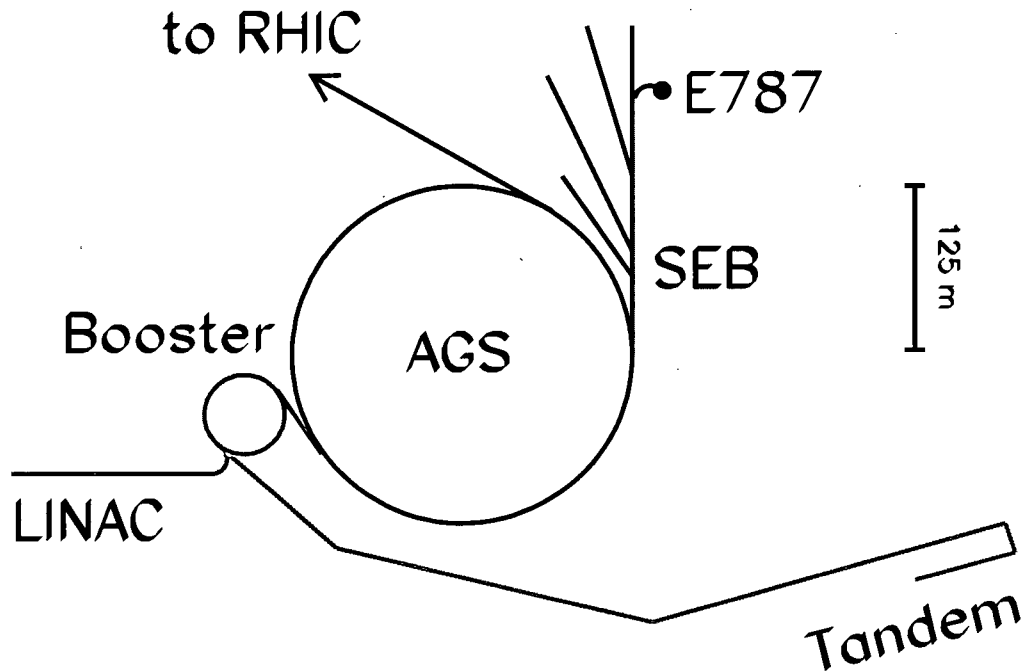


Figure 3.1: Accelerator facilities at BNL.

contains a number of focussing quadrupole, sextupole, and octupole magnets and collimating slits, and has a total length of 19.6 m from the C target to the E787 target. The angular acceptance of LESBIII is 12 msr and the momentum acceptance is 4.5% FWHM. LESBIII provides the world's best kaon beam, with a flux of about $5 \times 10^5 K^+$ per Tp incident on the C target, and $K^+ : \pi^+$ and $K^+ : \mu^+$ ratios of about 4:1. Proton contamination is negligible due to the large deflection of protons by the separators. For comparison, the previous best kaon beam (provided by LESBI) had a $K^+ : \pi^+$ ratio of about 2:5. At typical AGS running conditions of 15 Tp per spill incident on the C target, about $7 \times 10^6 K^+$ emerge from LESBIII per spill. These kaons were selected at 790 MeV/c in 1995, 730 MeV/c in 1996, 710 MeV/c in the first half of 1997 (1997a), and 670 MeV/c in the latter half of 1997 (1997b). The kaon beam momentum was successively lowered in order to improve the fraction of kaons which stop inside the E787 detector, which is mounted at the end of LESBIII inside a solenoidal magnet (C2D3 in figure 3.2). The kaons are slowed in degrader materials before entering the E787 target, so after kaon decay in flight, disappearance interactions, and scattering out of the beam, about $1.3 \times 10^6 K^+$ enter the E787 target per spill.

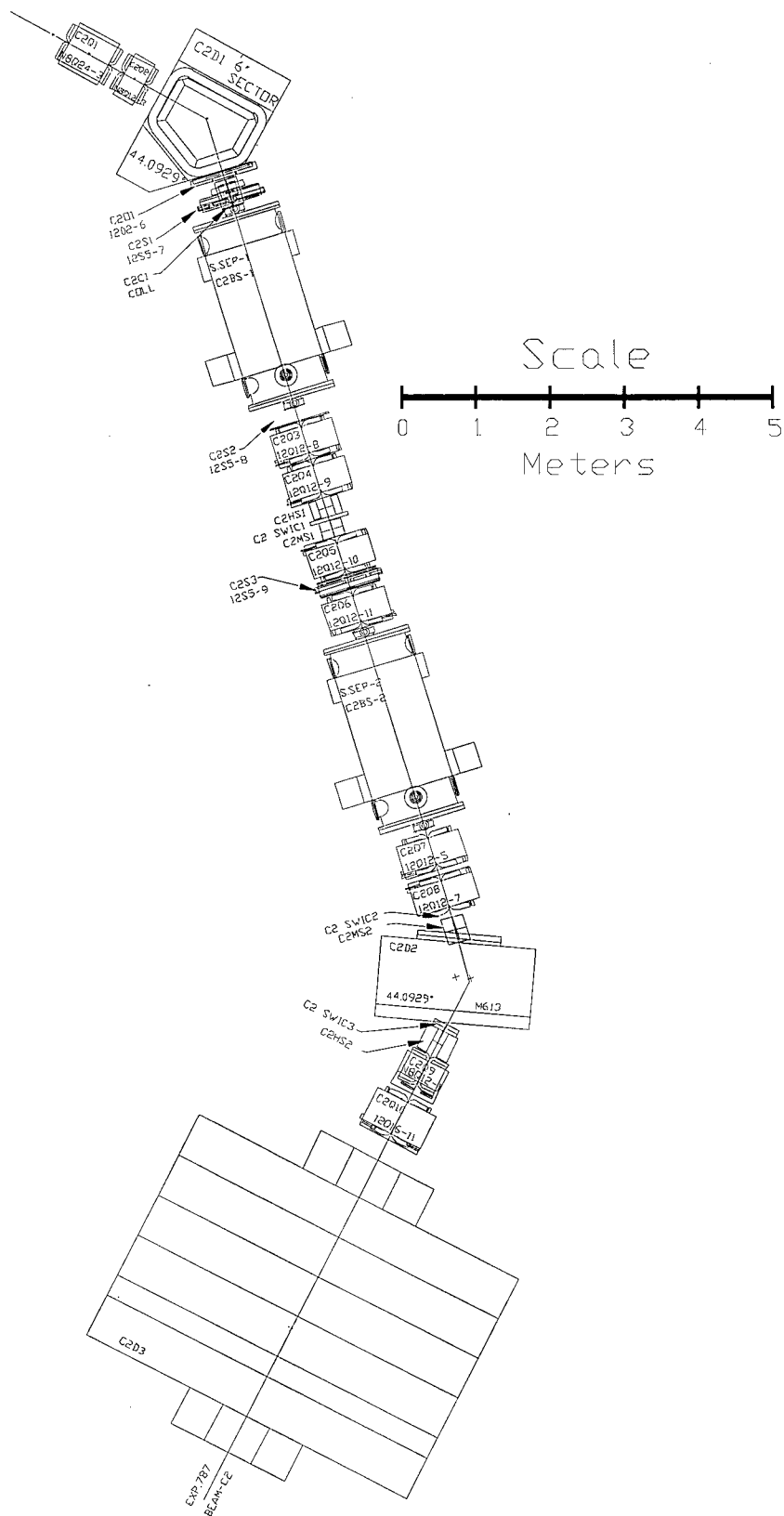


Figure 3.2: Low energy separated beamline III at BNL.

3.2 Detector

A global view of the E787 detector is shown in figure 3.3. The basic components of the detector are:

- beamline detectors for individual detection of beam kaons;
- a scintillating fiber target for reconstruction of the kaon decay vertex and tracking of charged decay product(s);
- a drift chamber for track-finding and measurement of momentum;
- a range stack for energy and range measurements and PID of the track; and
- a system of photon detectors.

In the discussion below, “upstream”/”downstream” refers to the direction opposite/along the kaon beam momentum. The coordinate system is defined such that z lies along the beam axis, with z increasing downstream. x is in the horizontal direction, increasing to the right, and y is in the vertical direction, increasing upwards, as viewed from downstream of the detector. The point (0,0,0) is defined as the geometric center of the drift chamber.

3.2.1 Beamline Detectors

The function of the various detectors in the beam is to identify single kaons entering the target. The kaon beam passes through (in order) a Čerenkov counter, a “hole” counter, 2 wire chambers, a degrader and a hodoscope before entering the target.

The Čerenkov counter, shown in figure 3.4, is located about 2 m upstream of the target center and independently detects beam kaons and pions based on the scheme of Fitch and Motley [28]. The Čerenkov light is directed into a ring of 14 photo-multiplier tubes (PMT’s) at large radius for (slow) kaons, or a ring of 14 PMT’s at smaller radius for (faster) pions of the same momentum. The PMT’s are read out by time-to-digital converters (TDC’s), and are multiplexed into an analog-to-digital converter (ADC) and a 500 MHz transient digitizer

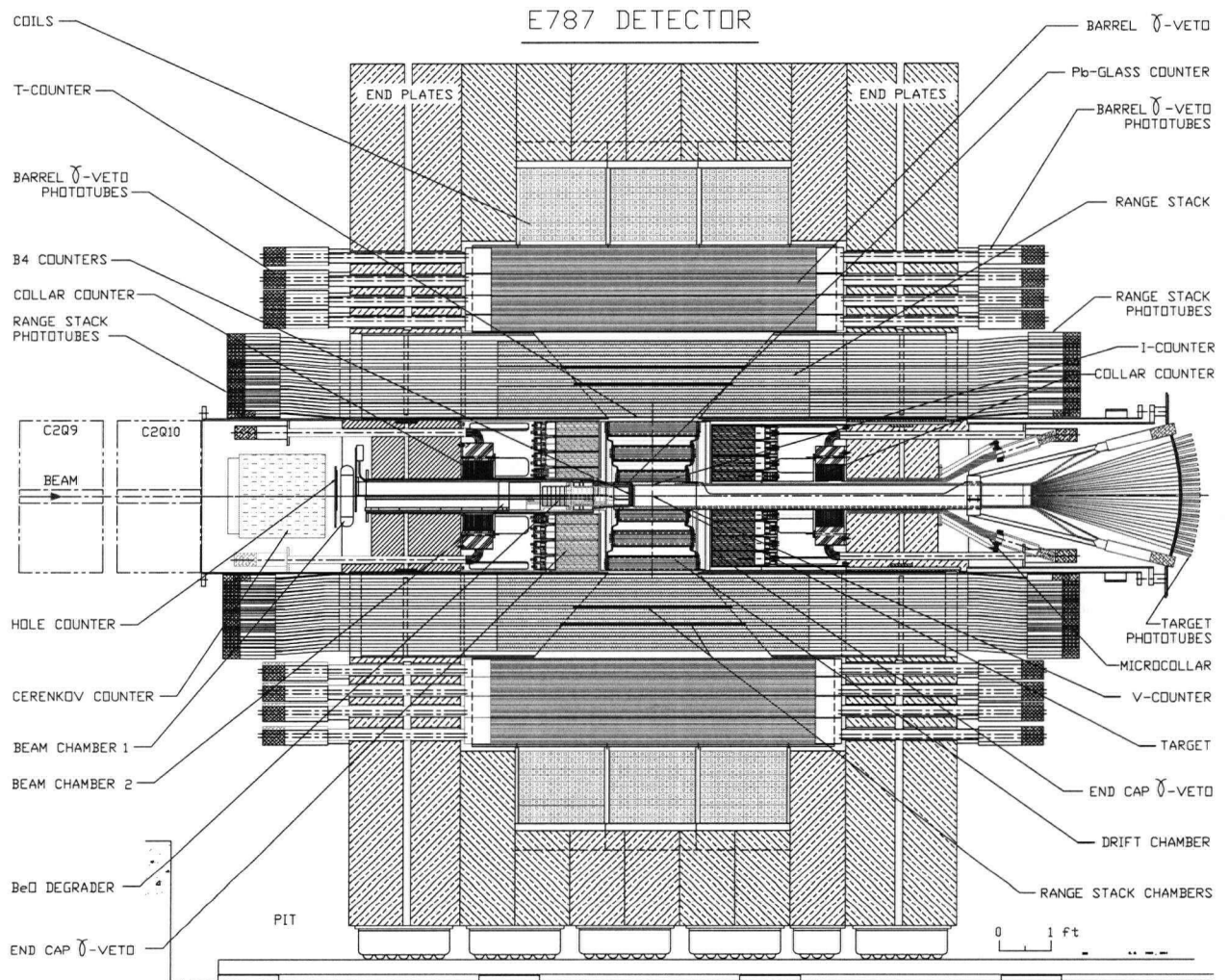


Figure 3.3: Side view of the E787 detector.

based on flash ADC's (hereafter referred to as a TD). The TD's sample voltage in 2 ns intervals [29] to provide information on the time development of a pulse. A kaon or pion is identified by a specified minimum number of PMT's that register pulses within a specified time window.

The hole counter is located at the upstream face of the first beam wire chamber, and is composed of two L-shaped plastic scintillators which join to form a rectangle. The rectangular hole defines the acceptance region in the (x, y) plane for kaons in the beam. Each scintillator is instrumented with a PMT which is read out by an ADC and a TDC.

The beam wire chambers are used for precision measurements of the (x, y) coordinate and time of beam particles so that multiple coincident beam particles can be detected. The first beam wire chamber (BWC1), shown in figure 3.4, is located about 1.7 m upstream of the target center, and has 3 planes $(X, U1, U2)$ of 12- μm -diameter gold-plated tungsten anode wires strung 1.27 mm apart. The X -plane has 144 wires strung vertically, and the $U1$ - and $U2$ -planes each have 120 wires strung at $\pm 45^\circ$ to the vertical. Each pair of 2 adjacent wires is read out by a single TDC. The second beam wire chamber (BWC2), shown in figure 3.4, is located about 90 cm downstream from BWC1, and has 3 planes $(X, U1, U2)$ of 12.7- μm -diameter gold-plated tungsten anode wires strung 0.79 mm apart. The X -, $U1$ -, and $U2$ -planes each have 96 wires strung vertically and at $\pm 120^\circ$ to the vertical, respectively. The middle 72 wires of each plane are read out by TDC's in groups of 3 adjacent wires, while the outer 24 wires on each end are read out in groups of 6 adjacent wires. The "fast" gas in the chambers is a 4:1 mixture of CF_4 :isobutane, and the anode wires are held at approximately 3 kV (gain = 10^4).

The degrader slows kaons down such that they stop in the target, and is composed of a cylinder of roughly 35 cm of BeO followed by 10 cm of PbO (called "lead glass"). The exact length of BeO is varied depending on the momentum of the kaon beam. The high density of BeO combined with its low atomic number provide good slowing power while minimizing the effects of multiple Coulomb scattering. The lead glass is active and was primarily designed to detect kaon-decay photons which travel back upstream from the target. However, it is also used to detect beam pions via Čerenkov light. The downstream face of the 11.2-cm-

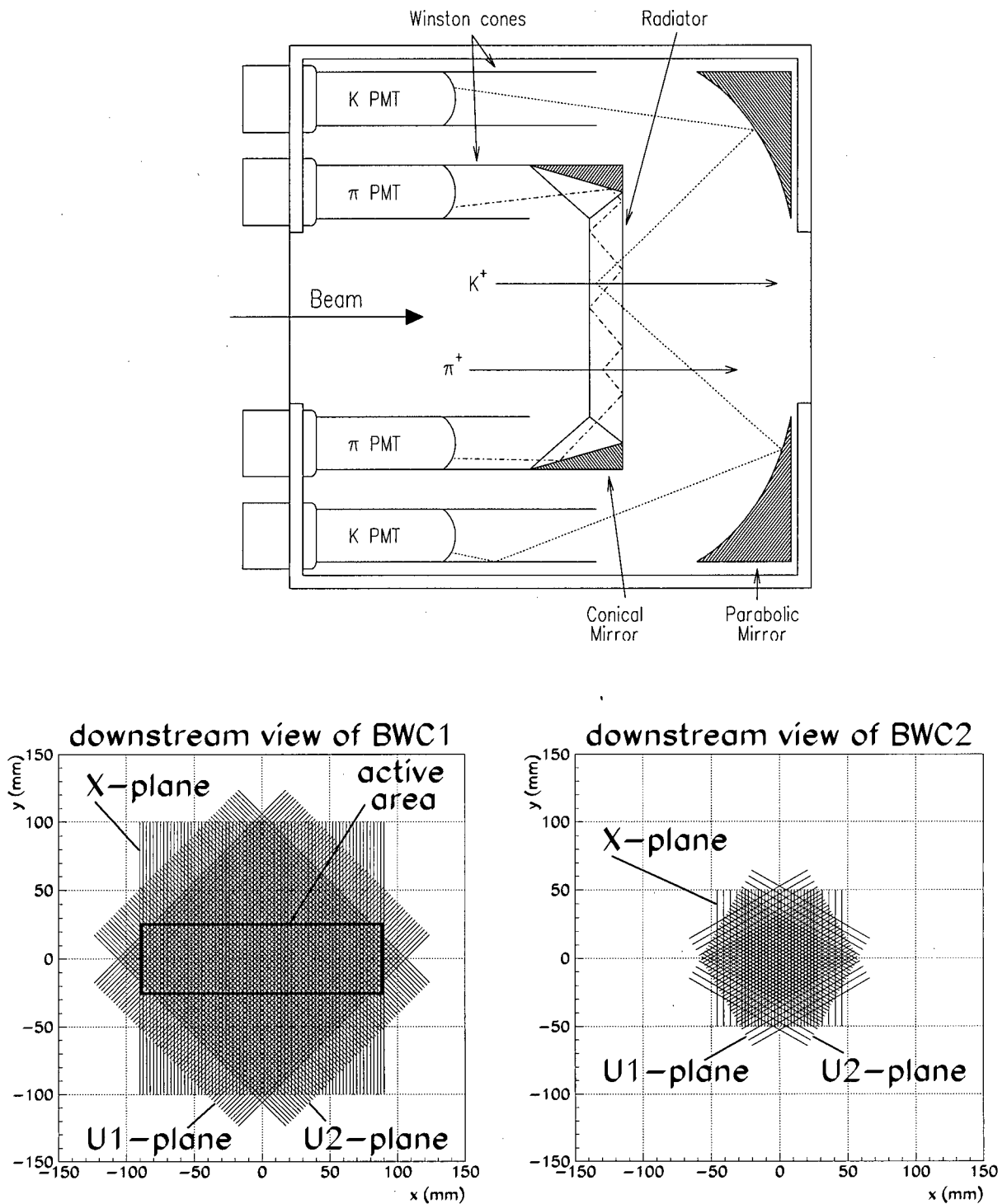


Figure 3.4: Top: Side view of the beam Čerenkov detector. Bottom: Downstream views of the BWC1 and BWC2 detectors. Multiplexed wires are shown as a single wire. The “active area” of BWC1 is the area defined by the hole counter.

diameter lead glass cylinder is located about 12 cm upstream of the target center. Light is collected from the sides of the cylinder by a 1.0-cm-thick lucite sleeve coupled with silicone gel. The lucite sleeve is glued on the upstream side to a lead glass sleeve, which is glued to 16 azimuthally-segmented trapezoidal lead glass pieces. Each of these pieces is instrumented with a fine-mesh PMT which can operate in the 1 T magnetic field immersing the detector (see section 3.2.3). The PMT's are located in a ring surrounding the BeO degrader and are read out by TDC's. Two PMT's were defective during the 1996 data-taking period, resulting in a decrease in beam pion detection power.

The B4 hodoscope provides an (x, y) coordinate for particles which pass through the degrader, and is placed up against the upstream face of the target (10 cm upstream of the target center) for matching with the (x, y) coordinate of the kaon detected in the target. It consists of 2 0.25-inch-thick planes (U, V) of 8 plastic scintillating fingers each. Starting from the central pair of fingers and moving outwards in pairs, the dimensions of the fingers are 120 mm \times 10.0 mm, 120 mm \times 12.5 mm, 110 mm \times 17.5 mm, and 80 mm \times 20.0 mm, respectively. The long dimension of the fingers in the U, V planes is mounted at $\pm 55^\circ$ to the vertical, respectively. The fingers are instrumented with PMT's which are read out by ADC's, TDC's, and TD's.

More information on the Čerenkov counter, BWC1, BWC2, the degrader and the B4 hodoscope can be found elsewhere [30].

3.2.2 Target

The target is used to locate the kaon decay vertex and to track charged kaon decay products. It is also sensitive to photons. The target is located immediately downstream of the B4 hodoscope and consists of 413 5.0-mm-square, 28 3.5-mm-square, 72 2.0-mm-square, and 104 1.0-mm-square 3.1-m-long plastic scintillating fibers, packed axially to form a circular target roughly 12 cm in diameter (see figure 3.5). The 3.5-mm, 2.0-mm and 1.0-mm fibers are inserted in the gaps near the outer edge of the target. The 5.0-mm fibers are each connected to PMT's, whereas the 3.5-mm, 2.0-mm and 1.0-mm fibers are connected in groups to 8,

4, and 4 PMT's, respectively. The PMT's are read out by ADC's, TDC's, and 500 MHz transient digitizers based on GaAs charge-coupled devices (hereafter referred to as CCD's). The CCD's, similar to the TD's, sample voltage in 2 ns intervals [31]. Kaons travel along the fibers, leaving up to 80 MeV per fiber and typically exciting < 5 fibers. Fiducially-accepted pions from kaon decay travel perpendicular to the fibers, leaving about 1 MeV per fiber and exciting up to 25 fibers, depending on the location of the kaon decay vertex in the target. The fiducial region of the target is defined by two layers of 6 plastic scintillator counters arranged cylindrically around the target (see figure 3.5). The inner scintillators, called the I-counters (IC's), define an acceptable z -region by tagging charged decay products after a kaon stops in the target and before decay products enter the drift chamber. The IC's are 6.4 mm thick at an inner radius of 6.0 cm and extend 24 cm downstream from the upstream face of the target. They are instrumented with PMT's which are read out by ADC's, TDC's, and TD's. The outer scintillators, called the V-counters (VC's), overlap the downstream edge of the IC's by 6 mm, and serve to detect particles which are downstream of the fiducial region of the target. The VC's are 5 mm thick and 1.96 m long, and are staggered with respect to the IC's. They are instrumented with PMT's which are read out by ADC's and TDC's.

3.2.3 Drift Chamber

The "ultra-thin chamber" (UTC), and the E787 detector as a whole, are immersed in a 1 T axial magnetic field, where the magnetic field lines point downstream. Due to the Lorentz force, a charged particle has a curved trajectory in a magnetic field, where the radius of curvature is proportional to the component of the particle's momentum which is perpendicular to the magnetic field. For a uniform field in the z direction then, the (x, y) component of a particle's momentum is given by

$$p(\text{MeV}/c) \simeq 3 \cdot |q| \cdot B(\text{Tesla}) \cdot r(\text{cm}) \quad (3.1)$$

where $|q|$ is the magnitude of the particle's charge in units of the proton charge e . The UTC's primary functions are therefore to provide momentum measurements of charged tracks with

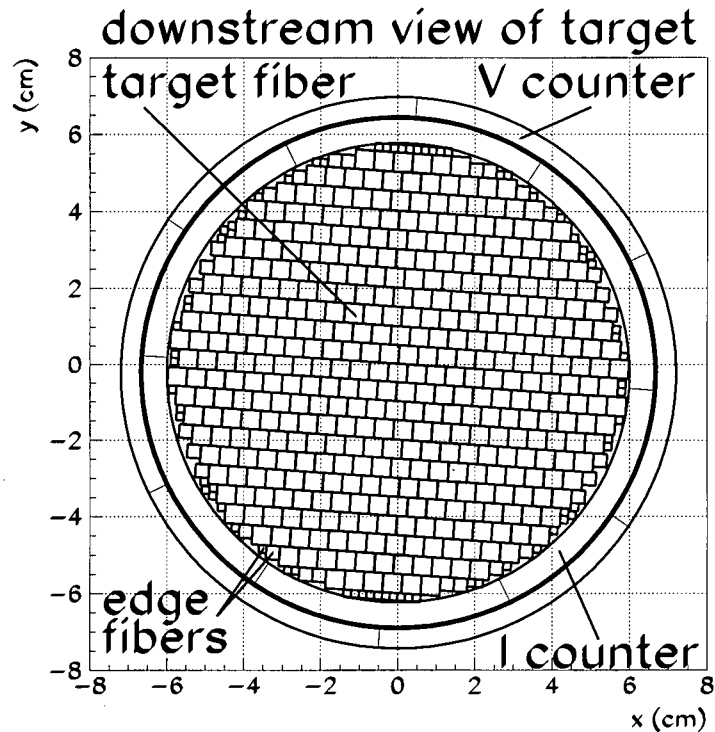


Figure 3.5: Downstream view of the target. The 104 1.0-mm-square fibers in the target are not drawn.

a resolution on the order of 1%, and to provide good tracking between the target and range stack.

The UTC, shown in figure 3.6, is located just outside the IC at an inner radius of 7.85 cm and an outer radius of 43.31 cm. It consists of 12 layers of drift cells, grouped into 3 superlayers: 4 layers \times 48 cells in the inner superlayer, 4 layers \times 96 cells in the middle superlayer, and 4 layers \times 144 cells in the outer superlayer. The cells have dimensions of between 11 and 19 mm, and are composed of 9 wires strung axially: a single 20- μm -diameter gold-plated tungsten anode sense wire surrounded by 8 100- μm -diameter gold-plated aluminum cathode wires arranged in a “square”. Cathode wires are shared at the boundaries between cells. Cells in each layer are staggered by one-half cell with respect to neighbouring layers in order to resolve the left-right ambiguity. The gas in the superlayers is a 49.6%:49.6%:0.8% mixture of argon:ethane:ethanol ($v_{drift} = 5 \text{ cm}/\mu\text{s}$). The cathode wires are grounded and the anode wires are held at 2 kV (gain = 8×10^4). Each anode wire is instrumented with an ADC and a TDC. The drift times to the anode wires provide (x, y)

E787 Central Tracking Drift Chamber

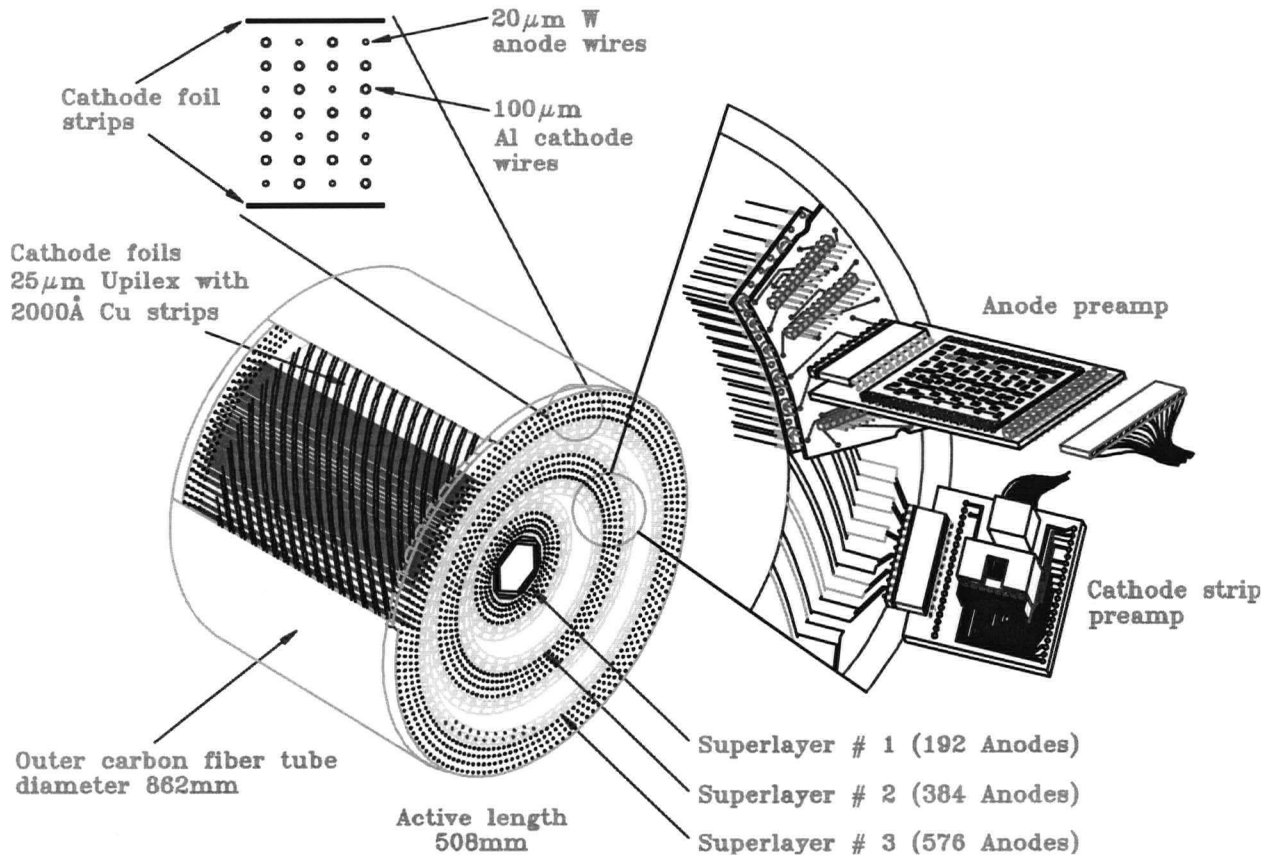


Figure 3.6: The “ultra-thin chamber” (UTC).

coordinates for tracks.

At the inner and outer radii of each superlayer are a helical array of cathode strips at a pitch angle of 45° . The 7-mm-wide strips are 1200 \AA copper coated with 300 \AA nickel, are separated by 1 mm, and are mounted on 25- μm -thick Kapton foil. There are 48, 72, 108, 144, 180, and 216 strips on the 6 foils, from inner to outer, respectively. The centroid of induced charge on a cluster of strips provides a z coordinate with a resolution of about 1 mm. Each cathode strip is instrumented with an ADC and a TDC.

Between the 3 superlayers are 2 inactive regions of nitrogen gas. Differential pressure in the 5 gas volumes supports the cathode foils (excluding the innermost and outermost foils, which are held in place by support tubes). The active length of the UTC is 50.8 cm for a solid angle acceptance of about 2π sr as seen by the target. The total mass in the measurement

region (excluding the inner and outer support tubes and innermost and outermost foils) amounts to 2×10^{-3} radiation lengths.

More information on the UTC can be found elsewhere [32].

3.2.4 Range Stack

The primary functions of the range stack (RS) are energy and range measurements of charged tracks, and PID. The RS, shown in figure 3.7, is located immediately outside the UTC at an inner radius of 45.1 cm and an outer radius of 89.6 cm. It is composed of 21 layers of plastic scintillator, each azimuthally segmented into 24 sectors. The innermost layer, called the T layer, is 6.35 mm thick and 52.0 cm long, and is used in the trigger to define the approximately 2π -sr solid angle acceptance of the range stack (RS), which roughly coincides with the solid angle acceptance of the UTC. The outer 20 layers are 19.05 mm thick and 1.82 m long, and are used for energy, range, and decay-sequence measurements of charged tracks, as well as detection of photons. Each end of each RS counter is instrumented with a PMT which is read out by an ADC. Groups of 4 PMT signals from the same end (upstream or downstream) of RS counters from 4 adjacent sectors in the same layer are multiplexed together and read out by a TD. The 4 multiplexed PMT signals are also input separately into the TD boards and read out as “flags” so that the pulse information in a TD channel can be assigned to 1 or more of the 4 multiplexed counters. The times of TD pulses on each of the upstream and downstream ends are found with respect to an electronically-generated reference pulse, called the “fiducial” pulse. The time of a hit in a RS counter is found from the average of the upstream and downstream TD times. The z location of a hit is found from the difference of the upstream and downstream TD times.

The detector is designed such that pion tracks from $K^+ \rightarrow \pi^+ \nu \bar{\nu}$ stop in the RS, so that the $\pi \rightarrow \mu \rightarrow e$ decay sequence can be observed in the TD corresponding to the counter where the charged pion track came to rest (the “stopping counter”). An example of TD pulses in and around the stopping counter for a pion track is shown in figure 3.8. The pion pulse can be anywhere between 1 and 30 MeV in the stopping counter, the muon from pion

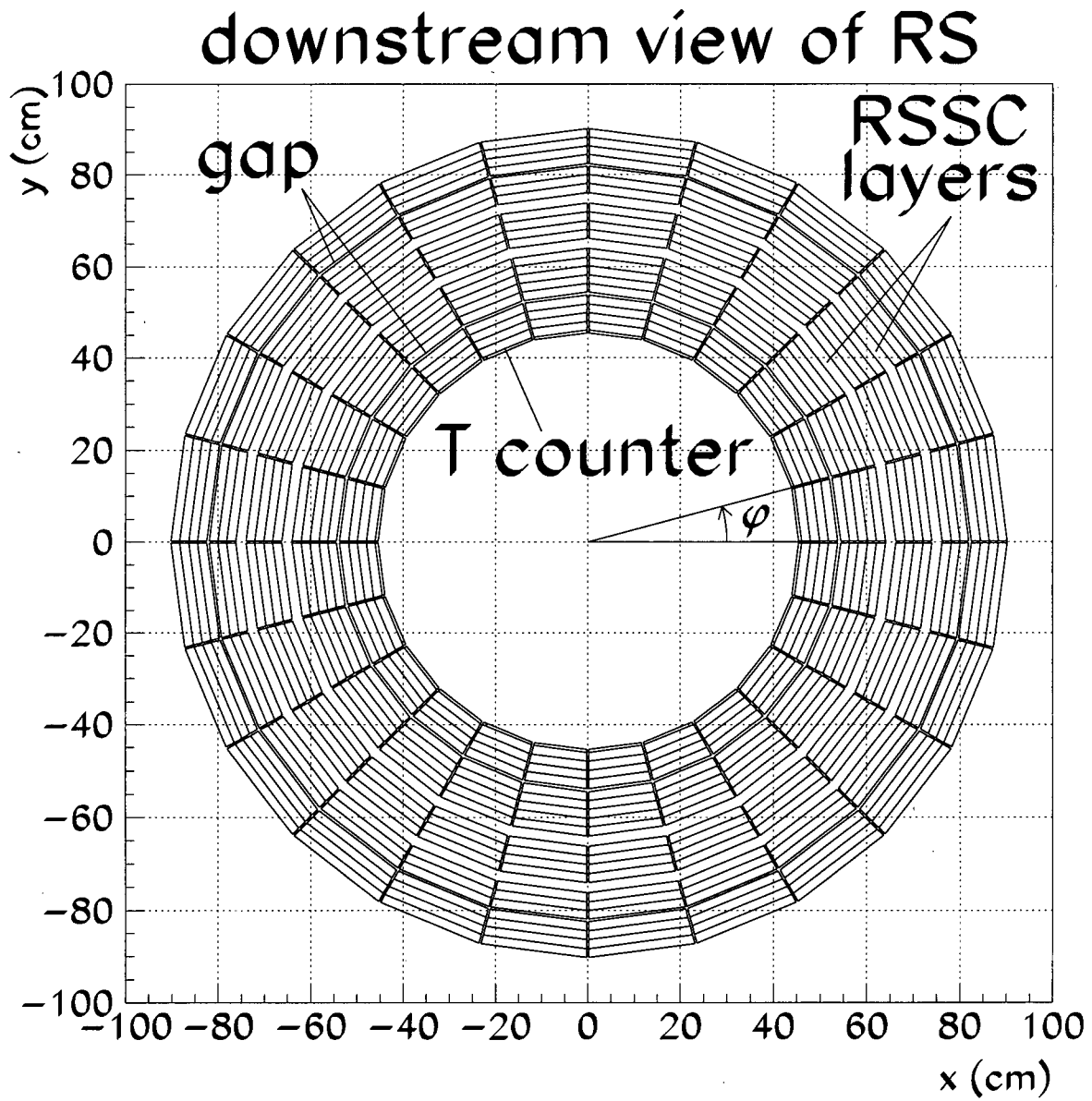


Figure 3.7: The RS shown in cross section. ϕ is the angle in the (x, y) plane about the center of the detector.

decay at rest is 4.1 MeV confined to the stopping counter, and the positron from muon decay is up to 52 MeV and can be spread over several RS counters (up to 10 MeV per RS counter). These energies define the required dynamic range of the TD's. Pion pulses are typically 30 – 40 ns in width, so the TD sampling rate of 500 MHz (once every 2 ns) allows reconstruction of the pulse shapes so that double-pulse $\pi \rightarrow \mu$ decays can be detected for pion decay times earlier than 10 ns (the π^+ mean lifetime is 26 ns). The μ^+ mean lifetime is 2.2 μ s, so a memory depth of between 5 and 7 μ s is used to detect Michel positrons, which results in a large TD data volume. The readout time of the TD data is the limiting readout time in data acquisition (see section 3.3). More information on the RS and TD's can be found elsewhere [29, 33].

Located after layer 10 and layer 14 are range stack straw chambers (RSSC's). They provide (x, y) and z coordinates of the track in the RS. The inner RSSC's consist of 2 layers of 24 straws per sector, and the outer RSSC's consist of 2 layers of 28 straws per sector, for a total of 2496 straws. Each straw is 3.4 mm in radius, and has a 38- μ m-thick Kapton skin, coated on the inside with Cu/Ni cathode, enclosing a gas volume of 25%:74.5%:0.5% argon:isobutane:water and a 50- μ m-diameter gold-coated tungsten anode wire. The anode wires are held at about 3 kV, and the straw chambers are operated in "limited streamer" mode where ionizing particles cause a spark between the anode and cathode. Pairs of straws in the same layer and separated azimuthally by half a sector are connected by a "jumper card" at one end, and read out by TDC's at the other end. The time difference between the early pulse and the late pulse from the two connected straws gives the z position of the hit. More information on the RSSC's can be found elsewhere [34].

3.2.5 Photon Veto

A roughly 4π -sr array of photon detectors is used to suppress $K_{\pi 2}$ decays and any other radiative processes. The primary photon veto consists of a barrel, upstream and downstream endcaps (EC's), an upstream and downstream collar (CO), and a downstream microcollar (CM). The barrel and endcap are shown in figure 3.9.

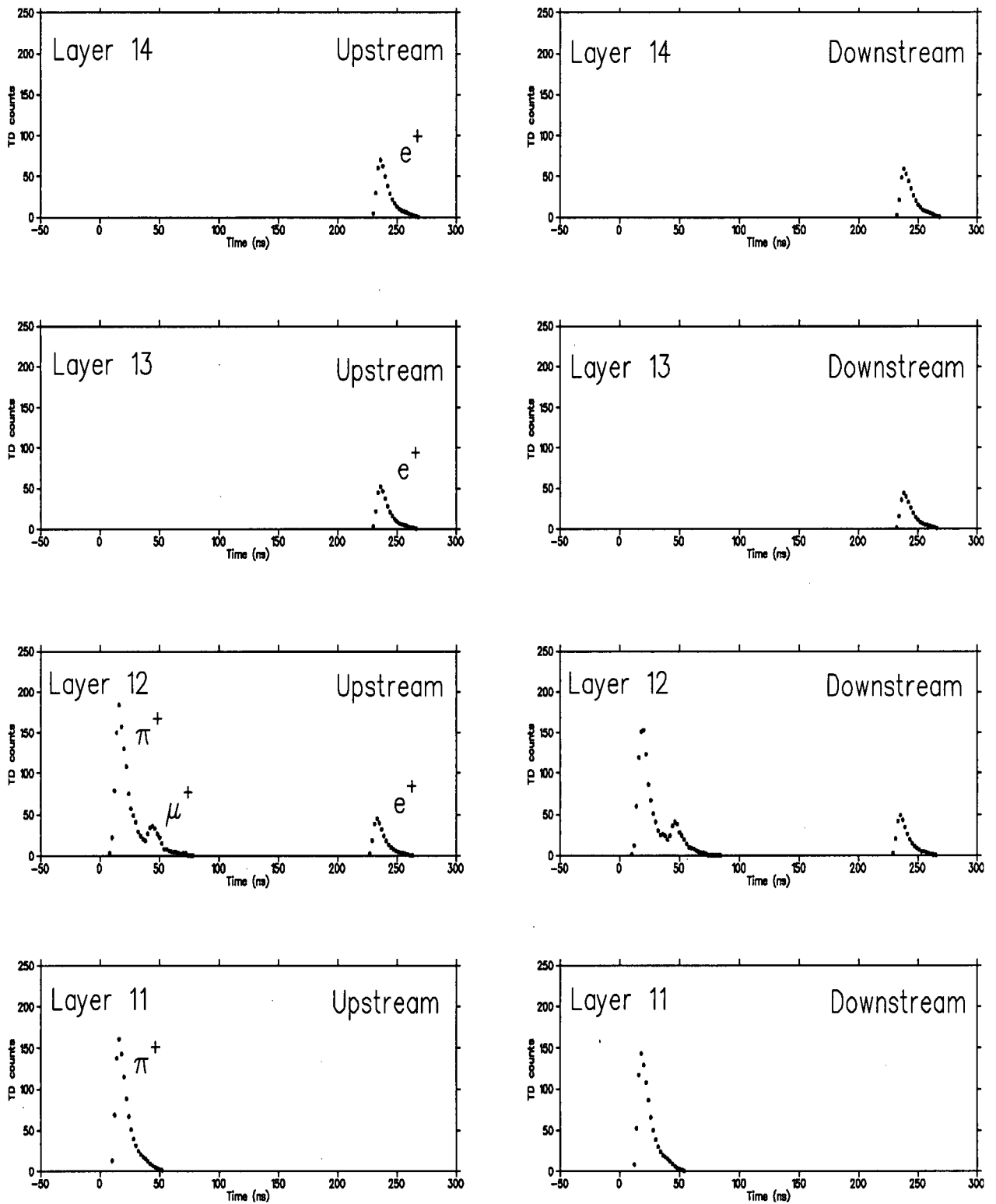


Figure 3.8: Pulses found in the upstream and downstream TD's in RS layers 11-14 for a pion track stopping in layer 12.

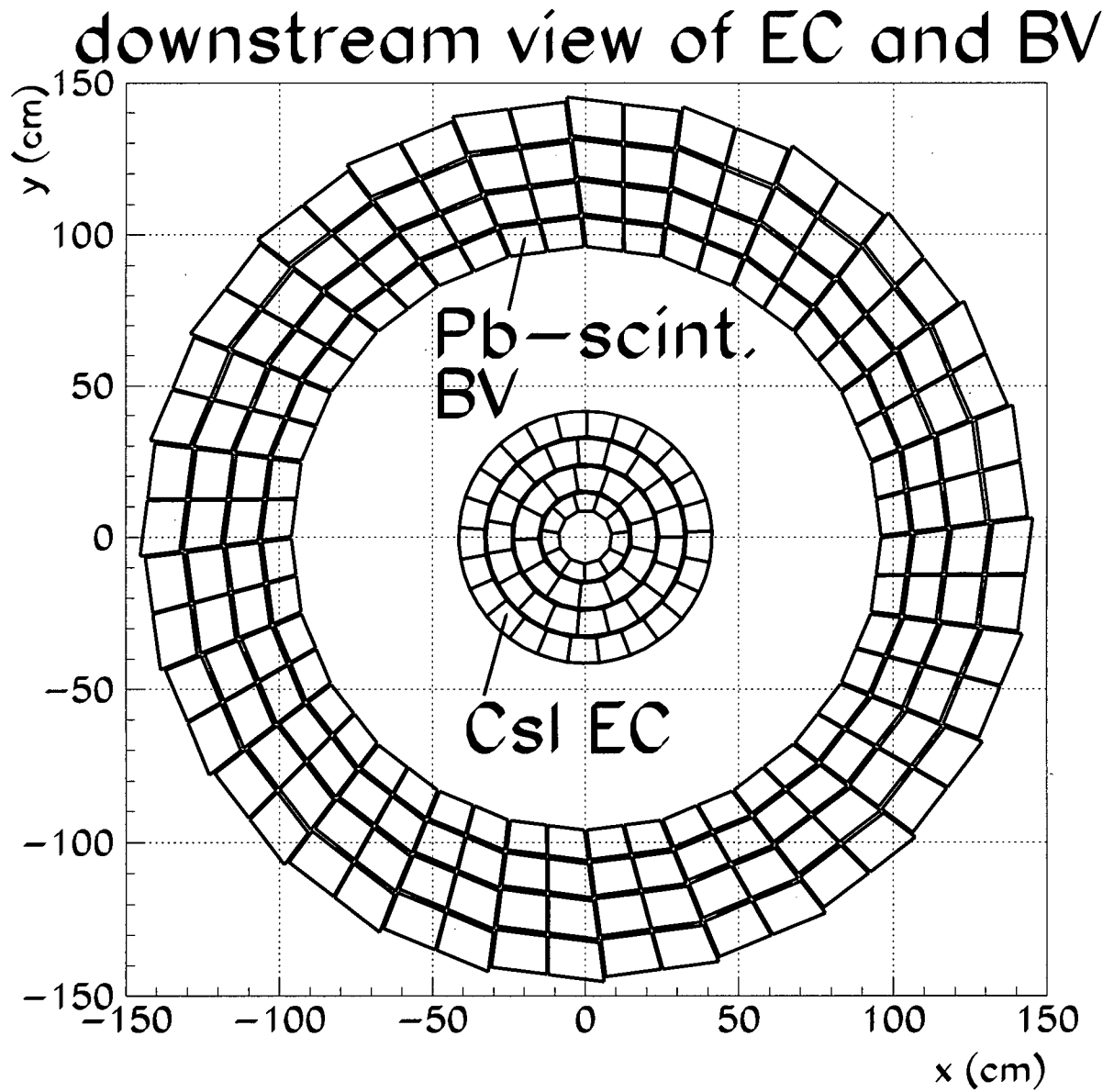


Figure 3.9: The “barrel veto” (BV) and EC shown in cross section.

Chapter 3. Experiment

The barrel is 1.90 m long and accounts for roughly $2/3$ of the 4π -sr photon coverage. It surrounds the range stack at a minimum radius of 94.5 cm and a maximum radius of 145.3 cm, and consists of 24 azimuthal sectors each containing 8 modules. The 8 modules in each sector are split into 4 radially and 2 azimuthally, for a total azimuthal segmentation of 48. The azimuthal boundaries of each sector are tilted so that the inert inter-sector gaps do not project back to any part of the target. Each radial module, from inner to outer, consists of 16, 18, 20, and 21 layers of 1-mm-thick lead plus 5-mm-thick scintillator, respectively, for a total of 14.3 radiation lengths in the barrel. Each end of each module is instrumented with a PMT, which is read out by an ADC and a TDC. The fraction of total photon energy seen by the active regions (scintillator) of the barrel is about 28%. More information on the barrel can be found elsewhere [29].

The upstream and downstream endcaps are composed of 4 rings of undoped CsI crystals, where each crystal is pentagonal in cross section. The rings extend from an inner radius of 10 cm to an outer radius of 43 cm (similar to the UTC) with a length of 25 cm (13.5 radiation lengths), and are mounted at the upstream and downstream ends of the UTC. The upstream EC has 13, 14, 21, and 27 crystals in the 4 rings, from inner to outer, and the downstream EC has 11, 13, 19, and 25 crystals, for a total of 143 crystals. The radial segmentation is staggered from ring to ring to minimize photon escape through the radial cracks. Fine-mesh PMT's are attached directly to the crystals (i.e., inside the magnetic field of the detector) for efficient light collection. The PMT's are read out by ADC's, TDC's, and CCD's. More information on the EC's and the fine-mesh PMT's can be found elsewhere [35, 36].

The collars and microcollar are used to detect photons which travel at small angles relative to the beamline and therefore miss the barrel and EC. The upstream and downstream collars are composed of 25 layers of 5-mm-thick plastic scintillator alternating with 24 layers of 1-mm-thick lead, stacked axially. They are located about 34 cm "behind" the back edge of the corresponding CsI EC crystals (with respect to the detector origin) and are 15 cm in length. They surround the beam line, extending from an inner radius of 10 cm to an outer radius of 25 cm, and are azimuthally segmented into 12 sectors, each instrumented with a PMT read out by an ADC and a TDC. The microcollar is composed of 8 layers

of plastic scintillating fibers alternating with 7 layers of lead foil, stacked radially around the beamline and located just downstream of the downstream collar. Starting at an inner radius of 15.6 cm and extending to an outer radius of 20.0 cm (including air gaps between successive layers), the 8 layers of fibers contain 30, 31, 32, 33, 34, 35, 36, and 37 fibers each 2 mm in diameter, and the intervening 7 layers of lead are 0.41, 0.61, 0.61, 0.61, 0.61, 0.61, and 0.41 mm thick. The microcollar fibers lie parallel to the beamline, and are grouped into 4 azimuthal quadrants, each instrumented with a PMT which is read out by an ADC and a TDC.

3.2.6 Monte Carlo Simulation

The detector, and various physical processes occurring within the detector, are modelled by a Monte Carlo simulation called “UMC” [37]. UMC includes all detector elements except the beam counters (i.e., it includes everything except that which is upstream of the target), and generates all types of data except for TD and CCD data. Propagation of kaon decay products begins at the position of stopped kaons in the target. The kaon stopping distribution is found using real $K_{\mu 2}$ decays (from $K_{\mu 2}(1)$ monitor data: see section 3.3), where the muon track is within $\pm 10^\circ$ of the vertical. Corrections to the stopping distribution are applied for geometrical differences between the real detector and that simulated by UMC, and for $K_{\mu 2}(1)$ trigger bias. The kaon decay point in x, y, z , along with other information about the $K_{\mu 2}$ decay, are written to a “beam file”. Beam files are made for the 4 different kaon beam momenta (see section 3.1): 790 MeV/ c (1995), 730 MeV/ c (1996), 710 MeV/ c (1997a), and 670 MeV/ c (1997b).

Multiple Coulomb scattering of charged muons and pions off various nuclei in the detector is calculated according to the theory of Molière [16], with corrections for the spin of the scattered particle and the form factor of the scattering nucleus [38].

Hadronic interactions of positively-charged pions in plastic scintillator are calculated using a combination of data and phenomenological modelling [39]. The well-measured $\pi^+, ^{12}\text{C}$ total cross section is divided into 7 channels, shown in table 3.1: elastic, “pseudo-elastic”,

channel	process	$\sigma(125 \text{ MeV})$
elastic	$\pi^+ {}^{12}\text{C} \rightarrow \pi^+ {}^{12}\text{C}$	214 mb
pseudo-elastic	$\pi^+ {}^{12}\text{C} \rightarrow \pi^+ {}^{12}\text{C}^*$	11 mb
quasi-elastic	$\pi^+ {}^{12}\text{C} \rightarrow \pi^+ p {}^{11}\text{B}^\Delta$	52 mb
	$\pi^+ {}^{12}\text{C} \rightarrow \pi^+ n {}^{11}\text{C}^\Delta$	31 mb
	$\pi^+ {}^{12}\text{C} \rightarrow \pi^0 N X$	16 mb
absorption	$\pi^+ {}^{12}\text{C} \rightarrow X \text{ (no } \pi)$	194 mb
spallation	$\pi^+ {}^{12}\text{C} \rightarrow \pi^+ X$	120 mb

Table 3.1: Total $\pi^+, {}^{12}\text{C}$ interaction cross section, divided into 7 channels, for π^+ kinetic energy of 125 MeV. The meaning of Δ in ${}^{11}\text{B}^\Delta$ and ${}^{11}\text{C}^\Delta$ is that the product nucleus can be in either the ground or an excited state. * denotes an excited state, N denotes either p or n , and X denotes any nuclear or particle product or combination of products. Excited states in ${}^{12}\text{C}$ are typically the 4.4 and 9.6 MeV states, but levels up to 20 MeV have been observed.

3 quasi-elastic, absorption, and “spallation”. The cross sections for each channel increase roughly linearly with π^+ kinetic energy, starting from 0 mb at about 0 MeV and peaking near 165 MeV, above which they decrease roughly linearly up to 200 MeV. The cross sections at 125 MeV (i.e., near the midpoint of the $\pi^+ \nu \bar{\nu}(1)$ signal region) are shown in table 3.1.

Individual measurements of the elastic cross section at specific π^+ kinetic energies between 60 and 205 MeV are about 10% uncertain; a fit is made to 5 data points in this range. Data on the pseudo-elastic cross section above 100 MeV indicates that it is at most a few percent of the elastic cross section, so it is arbitrarily assumed to be 5% of the elastic cross section over the entire energy range. The quasi-elastic cross sections are found using the well-measured inclusive $\pi^+, {}^{12}\text{C}$ and $\pi^-, {}^{12}\text{C}$ processes: $\pi {}^{12}\text{C} \rightarrow \pi n(p) {}^{11}\text{C}^\Delta({}^{11}\text{B}^\Delta)$, where Δ means that the product nucleus can be in either the ground or an excited state. These 2 processes can each be approximated by a linear combination of 3 “elementary” processes: (1) $\pi^\pm n \rightarrow \pi^\pm n$, (2) $\pi^{+(-)} n(p) \rightarrow \pi^0 p(n)$, and (3) $\pi^\pm p \rightarrow \pi^\pm p$. The well-measured $\pi^\pm, {}^{12}\text{C}$ cross sections then give 2 independent ratios of the 3 elementary cross sections. These 2 ratios, combined with the well-measured $\pi^+ p \rightarrow \pi^+ p$ cross section, are used to get approximate values of the 3 quasi-elastic cross sections. These underestimate the available data, but individual measurements of the quasi-elastic cross sections at energies between 60 and 205 MeV have large uncertainties (up to 50%). Individual measurements of the absorption

cross section at energies between 60 and 205 MeV are about 10% uncertain; a fit is made to 5 data points in this range. Individual measurements of the total cross section at energies between 50 and 205 MeV are about 1% uncertain; a fit is made to 9 data points in this range. The spallation cross section is then the difference between the total cross section and the other 6 channels.

Photon and electron interactions are calculated using the EGS electromagnetic shower simulation package [40].

The accuracy of UMC in modelling the detector is verified by comparing various geometric and kinematic variables for $K_{\pi 2}$ and $K_{\mu 2}$ decays as calculated using UMC-generated and real data [41]. The accuracy of UMC in modelling $\pi^+, {}^{12}\text{C}$ interactions is verified by measuring the $K_{\pi 2}$ branching ratio (see section 5.9.2).

3.3 Data Acquisition

As mentioned in section 3.1, roughly 1.3×10^6 kaons enter the E787 target per spill. A single kaon entering the target and decaying into the fiducial region of the detector defines an “event”. ADC, TDC, CCD, and TD data from a $K^+ \rightarrow \pi^+ \nu \bar{\nu}$ event typically totals between 70 and 90 kbytes. To accommodate data transfer speeds of about 14 – 17 Mbytes/s between digitizing hardware and the main computer, the number of events per spill must be reduced to about 100. This is done by a “trigger” which is designed to minimize the number of background events (e.g., $K_{\pi 2}$ and $K_{\mu 2}$ decays) while maximizing the number of potential $K^+ \rightarrow \pi^+ \nu \bar{\nu}$ events.

The trigger is composed of a fast level 0 trigger, and slower level 1.1 and level 1.2 triggers. The level 0 trigger must make decisions faster than the rate of kaons entering the target (i.e., sub- μs), so it is composed entirely of logic pulses from fast detectors. The level 0 trigger for $K^+ \rightarrow \pi^+ \nu \bar{\nu}$ rejects events by a factor of about 550 – 750, and introduces 38 ns of deadtime for every coincident hit in the first and second layers of the RS (i.e., per T · 2 signal – see below). The level 1.1 and 1.2 triggers involve arithmetic processing of ADC and TD data, and operate on the lower-rate events that pass the level 0 trigger. The level 1.1 trigger has

a rejection factor of about 13 after level 0, and introduces about 10 – 20 μs of deadtime per level 0 trigger. The level 1.2 trigger has a rejection factor of about 2 after level 1.1, and introduces a deadtime of about 100 μs per level 1.1 trigger. The $K^+ \rightarrow \pi^+\nu\bar{\nu}$ trigger therefore has a rejection of about 14000 – 19000, and reduces the 1.3×10^6 kaons entering the detector to about 100 events per spill.

The level 0 trigger is based on two timing strobes which are used to issue gate signals to various detector subsystems. The “beam strobe” is defined by the time of a kaon detected by the Čerenkov counter (the \check{C}_K signal) or the B4 hodoscope, whichever is later, and the “detector strobe” is defined by the time of coincident hits in the first and second layers of the RS (the T · 2 signal). The detector strobe is formed from a logical OR of T · 2 signals from each RS sector, so T · 2 cable lengths are trimmed to keep sector-to-sector timing differences to < 1 ns. Kaon decay triggers use both strobes, but are initiated by the detector strobe. That is, signals which form the level 0 trigger are latched onto a bus which is updated with every new T · 2 signal. Up to 16 different level 0 triggers can be implemented based on the information on the trigger bus. For example, as mentioned at the beginning of chapter 3, $K^+ \rightarrow \pi^+\nu\bar{\nu}$ events of interest are in the $\pi^+\nu\bar{\nu}(1)$ and $\pi^+\nu\bar{\nu}(2)$ regions. The $K^+ \rightarrow \pi^+\nu\bar{\nu}$ trigger is therefore defined as a logical OR of two different triggers, named $\pi^+\nu\bar{\nu}(1)$ and $\pi^+\nu\bar{\nu}(2)$. The level 0 and level 1.n components of these triggers are given by

$$\begin{aligned} \pi^+\nu\bar{\nu}(1) = & K_B \cdot \text{IC} \cdot \text{DC} \cdot \text{T} \cdot 2 \cdot (6_{ct} + 7_{ct}) \cdot \overline{(19_{ct} + 20_{ct} + 21_{ct})} \\ & \cdot \overline{\text{BV+EC}} \cdot (\text{L0rr1}(1) \cdot \text{US} + \text{L0rr1}(2) \cdot \text{DS}) \cdot \text{HEX} \cdot \text{L1.1} \cdot \text{L1.2} \end{aligned} \quad (3.2)$$

$$\begin{aligned} \pi^+\nu\bar{\nu}(2) = & K_B \cdot \text{IC} \cdot \text{DC} \cdot \text{T} \cdot 2 \cdot 3_{ct} \cdot 4_{ct} \cdot 5_{ct} \cdot 6_{ct} \cdot \overline{(13_{ct} + \dots + 18_{ct})} \\ & \cdot \overline{(19 + 20 + 21)} \cdot \overline{\text{BV+EC}} \cdot \text{L0rr2}(1) \cdot \text{HEX} \cdot \text{L1.1} \cdot \text{L1.2} \end{aligned} \quad (3.3)$$

where

- K_B : a coincidence between \check{C}_K (the definition of \check{C}_K changed over 1995-7, varying between 5 and 9 kaon PMT's hit out of a total of 14), a hit in either plane of the B4 hodoscope, an energy sum of fiber hits in the target (at least 10 – 20 MeV summed), and a signal identifying the spill from the AGS. In 1995 (1996-7), the B4 signal had to

fall within about ± 20 ns (± 6 ns) of \check{C}_K , and the target signal had to fall within about ± 20 ns (± 30 ns) of \check{C}_K . The K_B signal identifies kaons entering the target, and has a 50 ns width as input into the trigger transmitter. This is to ensure that K_B is active when a T · 2 hit, arising from a kaon decay product, updates the trigger bus. The mean kaon lifetime is $\tau_{K^+} = 12.386$ ns, so $1 - e^{-50/12.386} = 98.2\%$ of all kaon decays are potentially accepted by the trigger.

- IC: a hit in any I-counter within about ± 5 ns of the detector strobe. This selects kaon decay products leaving the target and entering the fiducial region of the detector.
- DC: delayed coincidence. An IC hit must be present some minimum time after \check{C}_K , typically set between 1.4 and 1.8 ns. This selects kaons which stop in the target and decay at rest.
- T · 2: a hit in a layer 2 counter in the same sector and in coincidence with (within ± 20 ns of) a hit in the T layer. This selects charged tracks which have entered the RS. The T · 2 time is defined as the average of the times from each end of the layer 2 counter. In 1996 and subsequent years, the IC signal was added to T · 2 in order to reduce the rate of detector strobos arising from kaon interactions and production of secondaries in the degrader, which subsequently hit the first and second layers of the RS. Reducing the rate of detector strobos reduces the deadtime associated with the trigger. This is also the reason for making the T counters so thin: to reduce the probability of photon conversion in the T counters, so that detector strobos are more likely to arise only from charged tracks. Thin T counters coupled to thin light guides also reduce the probability of photon conversion in the (inactive) light guides, so that photons associated with a kaon decay are less likely to be “hidden”.
- $6_{ct} + 7_{ct}$: a “charged-track” (*ct*) hit in layer 6 or layer 7 of the RS within ± 20 ns of the detector strobe. *ct* refers to the T · 2 sector or within 2 sectors clockwise of the T · 2 sector (i.e., in the direction of curvature of the positively-charged track, as viewed from downstream of the detector). The *ct* label only applies to RS counters which

are sector-adjacent to at least one other ct hit earlier in the RS track. This trigger condition rejects low-range tracks (e.g., $K^+ \rightarrow 3\pi$).

- $\overline{19_{ct} + 20_{ct} + 21_{ct}}$: “online μ -veto”. There can be no ct hits in layers 19, 20, or 21 within ± 20 ns of the detector strobe. This rejects high-range tracks, such as μ^+ tracks from $K_{\mu 2}$ decays.
- $\overline{BV+EC}$: “online photon veto”. Photon energy in the barrel and in the EC must be below a threshold value. This rejects $K_{\pi 2}$ decays. The summed energy of hits in the barrel within ± 10 ns of the detector strobe must be below 5.0 MeV visible energy (corresponding to a 17 MeV photon, due to “invisible” energy loss in the lead of the barrel). The energy of hits within ± 3 ns of the detector strobe in each EC crystal must be less than 20 MeV. (Due to the proximity of the EC to the beam, the EC time windows must be small and energy thresholds high in order to maintain high trigger acceptance).
- $L0rr1(1) \cdot US + L0rr1(2) \cdot DS$: “refined range” for tracks, which rejects (a) low-range tracks that fail to reach RS layer 11, and (b) high-range tracks that pass the μ -veto, because the track propagates at a small angle with respect to the beam axis and doesn’t reach RS layer 19. $L0rr1(1)$ and $L0rr1(2)$ are refined range “masks” applied independently to tracks tagged as being in the upstream (US) half or downstream (DS) half of the RS, respectively. The range of a track is found from the range in the target (from the number of target fibers hit), plus the range outside of the target (from the polar angle and termination point of the track). The polar angle is estimated from the z of track hits (from the end-to-end time difference) in RS layers 11, 12, and 13. The termination of the track in the RS is found by the online “stopping counter finder” (SCF), which defines the stopping counter as the outermost ct hit in the RS within ± 20 ns of the detector strobe.
- HEX: “hextant cut”. The 24 sectors of the range stack are grouped into 6 hextants of 4 sectors each (i.e., the same grouping as the RS TD multiplexing). Only 1 hextant

can have hits within ± 10 ns of the detector strobe, or 2 hextants if they are adjacent. This rejects multiple track events, and $K_{\pi 2}$ decays where the photon converts away from the track in the RS.

- L1.1: level 1.1 trigger (all requirements above are part of the level 0 trigger). The L1.1 trigger looks at the pulse height (PH) and pulse area (PA) of the pulse(s) in the TD of the stopping counter, and rejects events if the signature for $\pi \rightarrow \mu$ decay is missing. For example, if there appears to be only a single pulse at track time (defined as a range of TD bins where the TD value is always > 0), then the PH/PA ratio of this “non-detached” pulse must be smaller than a certain value which is set by comparing PH/PA ratios for single and non-detached double pulses. The PH/PA ratio is smaller for double pulses than for single pulses because the PA increases whereas the PH remains the same when a second (muon) pulse is present on the tail of the first (pion) pulse. The L1.1 requirement therefore rejects muon tracks in the RS. Events are also rejected if the PH of the non-detached pulse exceeds a maximum value. For events with “detached” pulses, where the first and second pulses are well separated in time, the first pulse is required to satisfy a minimum PA and maximum PH, and the second pulse must satisfy a minimum and maximum PA and occur before a maximum time relative to the first pulse. The “cut parameters” (PH and PA requirements) were found using pion tracks from $K_{\pi 2}$ decays in 1995, but from beam pion scattering events in subsequent years, because beam pions, unlike $K_{\pi 2}$ pions, populate all layers in the RS with good statistics. The net effect of this change was that the L1.1 requirement was loosened in 1996. It was tightened in 1997 by also requiring a minimum PH/PA ratio for non-detached pulses.
- L1.2: level 1.2 trigger. This trigger was implemented roughly midway through the 1997 run, and rejects events with more than 1 MeV ADC energy in any RS counter in the same hextant and layer as the stopping counter (excluding the stopping counter itself), and/or the counter in the layer above and in the same sector as the stopping counter. The ADC gate is about 100 ns wide starts about 10 ns before $T \cdot 2$ time. The

L1.2 trigger therefore rejects $K_{\mu 2}$ decays which pass L1.1 due to “accidental” energy in and around the stopping counter providing the second pulse of the double-pulse $\pi \rightarrow \mu$ decay signature. Also, a refinement to the HEX requirement is made by requiring events with two adjacent hit hextants to have different T · 2 and stopping hextants. L1.2 also removes events with invalid SCF assignments.

In addition to collecting $K^+ \rightarrow \pi^+ \nu \bar{\nu}$ triggers, various “monitor” triggers are collected for use in data quality assessment, detector calibrations, and acceptance and background measurements. For example, four triggers used in the acceptance calculations of chapter 5 are the $K_{\pi 2}(1)$, $K_{\pi 2}(2)$, $K_{\mu 2}(1)$, and π_{scat} triggers:

- $K_{\pi 2}(1) = K_B \cdot T \cdot 2 \cdot (6_{ct} + 7_{ct}) \cdot \overline{(19_{ct} + 20_{ct} + 21_{ct})}$
- $K_{\pi 2}(2) = K_B \cdot IC \cdot DC \cdot T \cdot 2 \cdot (6_{ct} + 7_{ct}) \cdot \overline{(19_{ct} + 20_{ct} + 21_{ct})} \cdot HEX \cdot L1.1 \cdot L1.2$
- $K_{\mu 2}(1) = K_B \cdot T \cdot 2 \cdot (6_{ct} + 7_{ct}) \cdot (19_{ct} + 20_{ct} + 21_{ct})$
- $\pi_{scat} = \pi_B \cdot \overline{DC} \cdot IC \cdot T \cdot 2 \cdot (6_{ct} + 7_{ct}) \cdot \overline{(20 + 21)} \cdot \overline{BV+EC} \cdot HEX$

where π_B is the same as K_B , but with the \check{C}_K signal replaced by the \check{C}_π signal for a beam pion detected by the Čerenkov counter. The monitor triggers are prescaled to reduce online deadtime and to create suitably-sized data samples. The $\pi^+ \nu \bar{\nu}(1)$, $\pi^+ \nu \bar{\nu}(2)$, and prescaled monitor triggers together form the “standard mix” trigger which is used for E787 data acquisition.

ADC, TDC, CCD, and TD data is accumulated by up to 19 SLAC Scanner Processors (SSP’s) [42] during the spill. A trigger SSP notifies the secondary SSP’s when an event of interest has occurred, at which time the secondary SSP’s independently read their data into memory. This occurs during the spill, and is the largest source of online deadtime (about 2 ms per event). The total online deadtime is therefore roughly

$$1.3 \times 10^6 \cdot [0.038 \mu s + 15 \mu s / 650 + 100 \mu s / (650 \cdot 13)] + 100 \cdot 2000 \mu s = 0.29 \text{ seconds,}$$

which is about 18% of the 1.6-second spill length. In the period between spills (typically about 2 seconds), a master SSP collects the data from each secondary SSP, assembles events,

and sends the events to a Silicon Graphics Irix computer for online processing [43] and long-term storage. Part of the online processing involves analysis of events in order to quickly identify failures in the detector, electronics, and/or data acquisition systems. This analysis is referred to as the “quality of data” (QOD) assessment.

The master SSP also collects data from the trigger SSP (e.g., monitor prescale factors) and the “scalers”, which count various signals such as \check{C}_K , K_B , and $T \cdot 2$ during the spill.

Events are written to one of several 8-mm data-quality tapes, which are written in parallel in order to reduce the I/O time per event. Roughly 10300 tapes [33, 44, 45] of $K^+ \rightarrow \pi^+ \nu \bar{\nu}$ data (about 30 Tbytes) were written during the 1995, 1996, and 1997 run periods combined.

Chapter 4

Analysis

The $K^+ \rightarrow \pi^+\nu\bar{\nu}$ data-taking hardware and online trigger were discussed in the previous chapter. In this chapter, the characteristics of background events which satisfy the trigger, and the offline techniques and tools used to suppress the background are presented. Measurements of background and signal for the 1995-7 data set are described.

The 1995 data has previously been analyzed twice [46, 47], giving rise to the observation of a single $K^+ \rightarrow \pi^+\nu\bar{\nu}$ event and the following published results [46]:

- $B(K^+ \rightarrow \pi^+\nu\bar{\nu}) = 4.2_{-3.5}^{+9.7} \times 10^{-10}$
- $B(K^+ \rightarrow \pi^+X^0) < 3.0 \times 10^{-10}$ at 90% confidence level
- $0.006 < |V_{td}| < 0.06$

As will be shown in chapter 5, the current analysis and the full 1995-7 data set have a $K^+ \rightarrow \pi^+\nu\bar{\nu}$ single-event sensitivity which is a factor of 2.8 greater than the published 1995 analysis and the 1995 data set alone.

4.1 Backgrounds

Plots of range (in scintillator) vs. momentum for charged tracks which pass the $K_{\pi_2}(1)$ and $\pi^+\nu\bar{\nu}(1)$ triggers are shown in figures 4.1 and 4.2, respectively. From the definitions given in section 3.3, the $K_{\pi_2}(1)$ trigger is a loose version of the $\pi^+\nu\bar{\nu}(1)$ trigger (for example,

the $K_{\pi 2}(1)$ trigger does not include the online photon veto: $\overline{BV+EC}$). These figures show potential backgrounds for $K^+ \rightarrow \pi^+\nu\bar{\nu}$, which are kinematically categorized as $K_{\mu 2}$ peak, $K_{\mu 2}$ range tail, $K_{\pi 2}$ peak, $K_{\pi 2}$ range tail, muon band, and pion band. Note that after online application of the $\pi^+\nu\bar{\nu}(1)$ trigger (and before offline application of data-selection requirements), the major background is muon background.

Events in the $K_{\pi 2}$ peak are due to π^+ tracks which have the expected values of range, energy, and momentum for a kaon decaying at rest into a π^+ and a π^0 ($R = 30$ cm, $E = 108$ MeV, $P = 205$ MeV/c). Events in the $K_{\mu 2}$ peak are due to μ^+ tracks which have the expected values of range, energy, and momentum for a kaon decaying at rest into a μ^+ and a ν_μ ($R = 54$ cm, $E = 152$ MeV, $P = 236$ MeV/c). Events in the $K_{\pi 2}$ and $K_{\mu 2}$ range tails have smaller values of range (and also energy) than the peak values due to elastic (inelastic) scattering in the RS. The scattering occurs after the track has passed through the UTC because the momenta of events in the range tail are the same as those in the peak. Muon-band events can arise from $K^+ \rightarrow \mu^+\nu_\mu\gamma$ (referred to as radiative $K_{\mu 2}$, or $K_{\mu\nu\gamma}$ decay), $K^+ \rightarrow \pi^0\mu^+\nu_\mu$ (referred to as $K_{\mu 3}$ decay), $K_{\mu 2}$ decay in flight, and/or $K_{\mu 2}$ decay with inelastic scattering in the target, such that range, energy, and momentum are smaller than the $K_{\mu 2}$ peak values. Pion-band events are mainly due to pions in the beam which scatter into the detector (called π_{scat} background). Pion-band events with range, energy, and momentum smaller than the $K_{\pi 2}$ peak values can also arise from inelastic scattering of $K_{\pi 2}$ pions in the target.

The backgrounds for $K^+ \rightarrow \pi^+\nu\bar{\nu}$ can be loosely grouped into two categories: K^+ -decay and non- K^+ -decay backgrounds. The major K^+ -decay backgrounds are shown in figure 4.3. The present $K^+ \rightarrow \pi^+\nu\bar{\nu}$ analysis focusses on the region between the $K_{\pi 2}$ and $K_{\mu 2}$ kinematic peaks which, as mentioned at the beginning of chapter 3, is referred to as the $\pi^+\nu\bar{\nu}(1)$ region. Because the experimental signature for $K^+ \rightarrow \pi^+\nu\bar{\nu}$ is a single π^+ track with nothing else observed, and because most kaon decays involve multiple charged tracks and/or photons and have small branching ratios and small fractions of final state phase space in the $\pi^+\nu\bar{\nu}(1)$ region, the only decays which contribute significantly as background in the $\pi^+\nu\bar{\nu}(1)$ region are the $K_{\pi 2}$ and $K_{\mu 2}$ decays. The major non- K^+ -decay backgrounds come from pions in the beam which scatter into the detector, and from kaon charge exchange.

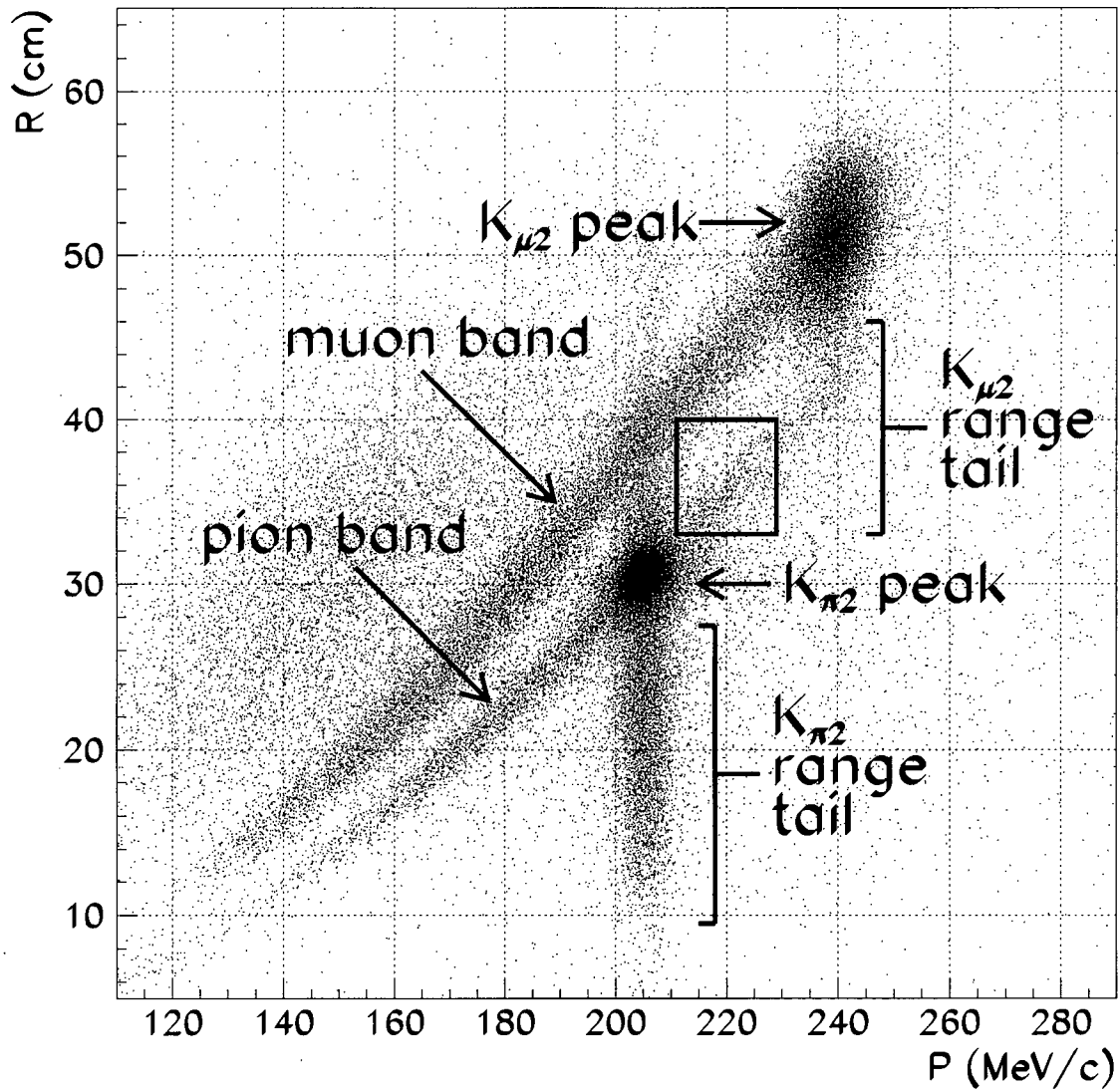


Figure 4.1: Range in scintillator (R) vs. momentum (P), and kinematic categorization of events passing the $K_{\pi 2}(1)$ trigger. The $\pi^+\nu\bar{\nu}(1)$ signal region is shown as a box. The production mechanisms for the listed categories of events are described in section 4.1 of the text. The $K_{\mu 2}$ peak momentum is reconstructed higher than the accepted value of 236 MeV/c [16] because a “pion hypothesis” has been used to calculate the momentum loss in the target (see section C.1).

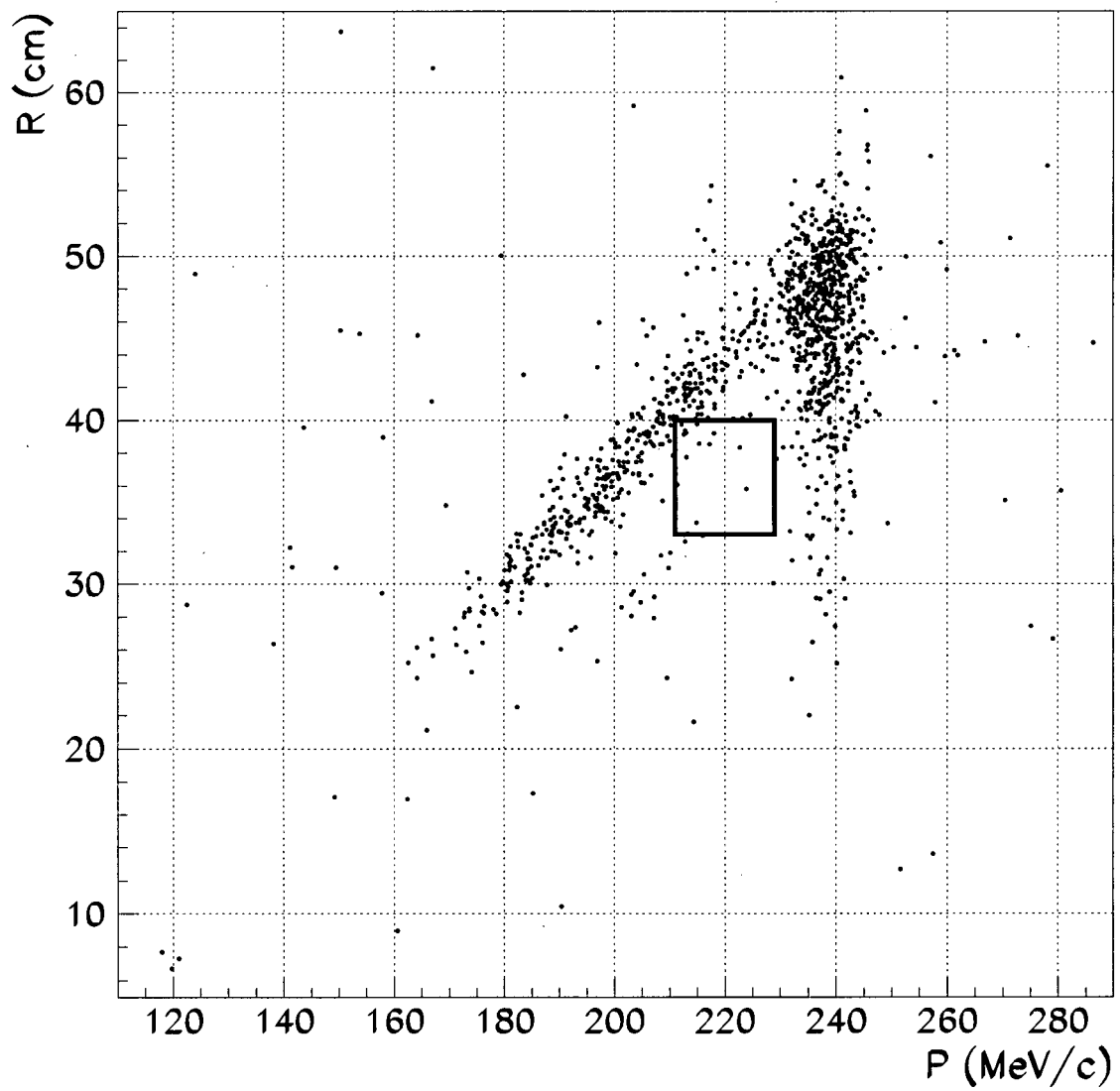


Figure 4.2: Range in scintillator (R) vs. momentum (P) for the events in figure 4.1 which pass the full $\pi^+\nu\bar{\nu}(1)$ trigger.

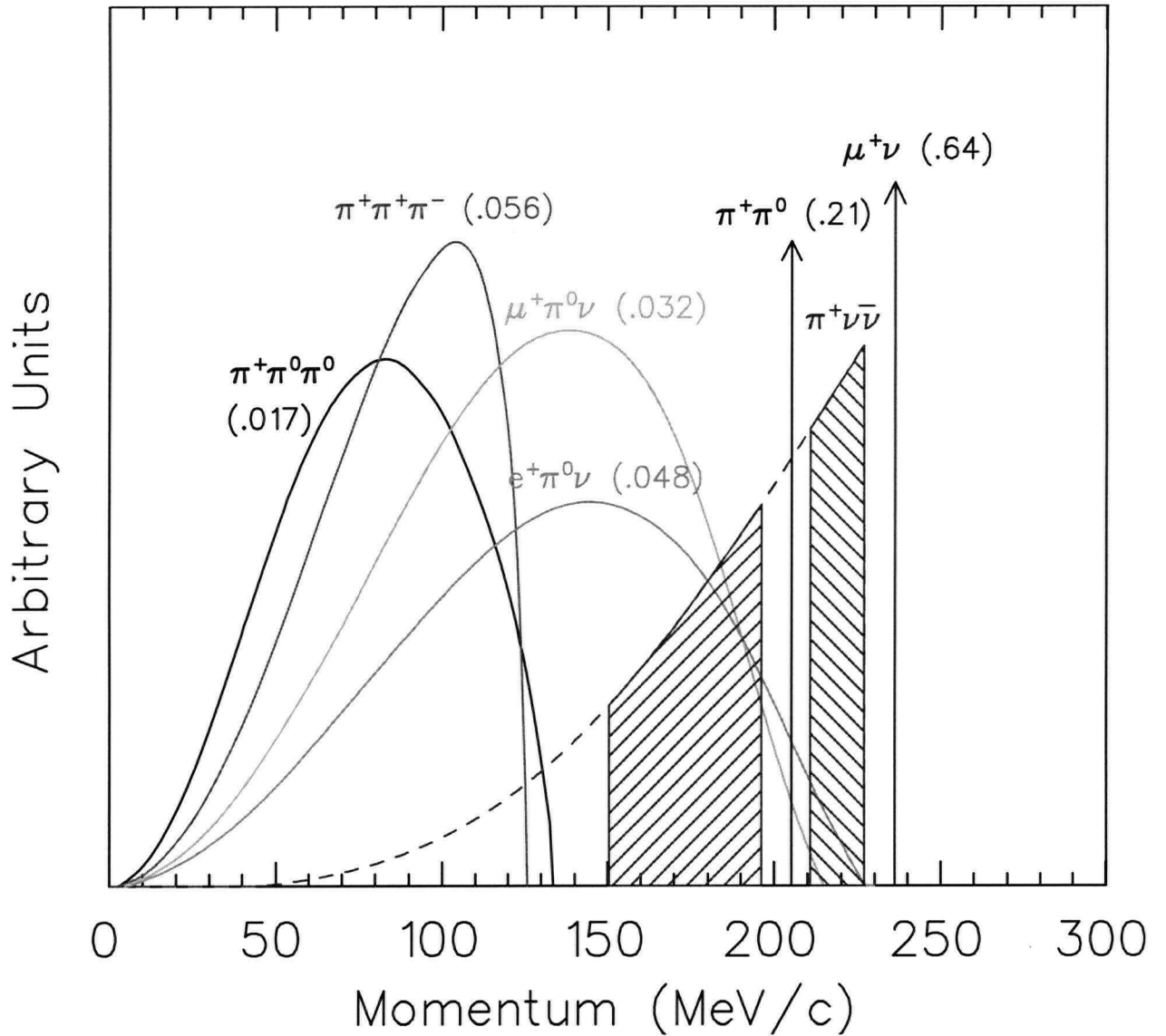


Figure 4.3: Momentum phase space of the charged track from K^+ decays. The number in brackets next to the final state of each kaon decay channel is the branching ratio of that decay. The upper and lower shaded regions are the momentum components of the $\pi^+\nu\bar{\nu}$ (1) and $\pi^+\nu\bar{\nu}$ (2) signal regions, respectively. The present analysis is concerned with the $\pi^+\nu\bar{\nu}$ (1) region, which is defined as the signal region between the $K_{\pi 2}$ ($K^+ \rightarrow \pi^+\pi^0$) and $K_{\mu 2}$ ($K^+ \rightarrow \mu^+\nu_{\mu}$) kinematic peaks.

4.1.1 $K_{\pi 2}$ and $K_{\mu 2}$ Decays

Because the $K_{\pi 2}$ and $K_{\mu 2}$ decays are two-body decays, they are monochromatic in the K^+ rest frame. Therefore, they are suppressed kinematically by (1) imposing a “delayed coincidence,” i.e., requiring that the kaon decay product be detected later than the kaon, such that the kaon decays from rest, and (2) cutting out the $K_{\pi 2}$ and $K_{\mu 2}$ kinematic peaks. This results in a large loss in “acceptance” (i.e., a loss of potential $K^+ \rightarrow \pi^+ \nu \bar{\nu}$ events): the kaon mean lifetime is 12 ns and $K^+ \rightarrow \pi^+ \nu \bar{\nu}$ decays are only accepted (after online + offline data-selection requirements) for kaons which decay at least about 5 ns after being detected. Furthermore, only the range, energy, and momentum phase space between the $K_{\pi 2}$ and $K_{\mu 2}$ kinematic peaks (i.e., the $\pi^+ \nu \bar{\nu}(1)$ region) is retained for $K^+ \rightarrow \pi^+ \nu \bar{\nu}$. This region is shown as the high-momentum shaded region in figure 4.3, and only accounts for about 16% of the total $K^+ \rightarrow \pi^+ \nu \bar{\nu}$ phase space. Additional kinematic suppression comes from requirements on the energy loss rate (dE/dx) and range-momentum correlation of charged tracks, which serve to separate pion from muon tracks and therefore to suppress $K^+ \rightarrow \mu^+$ decays. $K_{\pi 2}$ decays are additionally suppressed via high-efficiency photon detection in the barrel, EC, RS, target, CO, CM, IC, and VC. $K_{\mu 2}$ decays are further suppressed by requiring observation of the 3-pulse $\pi \rightarrow \mu \rightarrow e$ decay signature in the RS, given that muon tracks have a much different 2-pulse $\mu \rightarrow e$ decay signature.

$K^+ \rightarrow \pi^+ \pi^0$ can imitate $K^+ \rightarrow \pi^+ \nu \bar{\nu}$ if (1a) the $K_{\pi 2}$ kaon decays in flight, boosting the charged pion into the $\pi^+ \nu \bar{\nu}(1)$ region, or (1b) the $K_{\pi 2}$ range (R), energy (E) and momentum (P) are “upshifted” into the $\pi^+ \nu \bar{\nu}(1)$ region due to Gaussian resolution or non-Gaussian tails, and (2) the 25 – 225 MeV photons from $\pi^0 \rightarrow \gamma\gamma$ are missed. For (1a) to happen, the event has to fool the delayed coincidence. This can happen if the decay-in-flight kaon is missed in the beamline, and an earlier kaon, whose decay products are missed, is misidentified as the kaon responsible for the decay. The second kaon can overlap the first kaon and decay in the target, or decay earlier in the beamline (e.g., in the degrader) with the decay-pion overlapping the first kaon in the target and scattering into the detector. Contributions from (1b) should be rare, unless the high-side non-Gaussian tails of R , E , and P are correlated.

(2) is also rare as photon detection provides a measured π^0 suppression of about 1.7×10^6 (at an acceptance of 80%).

$K^+ \rightarrow \mu^+ \nu_\mu$ can imitate $K^+ \rightarrow \pi^+ \nu \bar{\nu}$ if (1a) the kaon decays in flight, reverse-boosting the muon into the $\pi^+ \nu \bar{\nu}(1)$ region, or (1b) the $K_{\mu 2}$ muon inelastically scatters in the target, causing a “downshift” in R , E , and P , or (1c) the $K_{\mu 2}$ muon inelastically scatters in the RS, causing a downshift in R and E , plus an independent downshift in P due to Gaussian resolution or a non-Gaussian tail, and (2) the muon is misidentified as a pion. For (2) to happen, the dE/dx of the muon in the target and RS must be similar to that of a pion, and there must be a correlated or simultaneous downshift in R and P . Furthermore, the 3-pulse $\pi \rightarrow \mu \rightarrow e$ decay sequence must be faked in the RS. For a real $\pi \rightarrow \mu \rightarrow e$ decay, the first pulse, arising from termination of the pion track in the stopping counter, is expected to be between about 1 and 30 MeV; the second pulse is 4.1 MeV, confined to the stopping counter, and is due to the muon from pion decay; and the third pulse is due to the 0 – 52 MeV electron shower from muon decay, typically spread over several RS counters. A muon track can fake the 3-pulse $\pi \rightarrow \mu \rightarrow e$ signature if, in addition to the 2-pulse $\mu \rightarrow e$ decay, there is a third pulse due to an accidental hit. Various combinations of these pulses are possible: the accidental hit may be responsible for the first (π) or second (μ) pulse in the TD data of the stopping counter, or the third (e) pulse in the TD data of the stopping and neighbouring counters. These “TD backgrounds” are referred to as pion-time accidental, muon-time accidental, and electron-time accidental (or early muon decay) background, respectively. The 3-pulse signature can also be faked if only 2 pulses are present ($\mu \rightarrow e$), but the first pulse is very large or very small or irregularly shaped, such that it fits better to a double pulse than to a single pulse. This type of TD background is referred to as “tail-fluctuation” background. Finally, muons from $K_{\mu 2}$ decay can inelastically scatter in the RS, exciting the giant dipole resonance (GDR) in ^{12}C which can de-excite by emitting a neutron. This neutron can travel slowly and unnoticed to the stopping counter, where it can provide the second pulse in the 3-pulse decay sequence (the first and third pulses coming from $\mu \rightarrow e$ decay). This type of TD background is referred to as GDR background. The different TD backgrounds are summarized in table 4.1. The GDR background is discussed

	1st pulse	2nd pulse	3rd pulse
signal: $K^+ \rightarrow \pi^+ \nu \bar{\nu}$	π	μ	e
background:			
early muon decay	μ	e from μ decay	accidental
muon-time accidental	μ	accidental	e from μ decay
pion-time accidental	accidental	μ	e from μ decay
tail-fluctuation		2-pulse fit to a μ pulse	e from μ decay
GDR	μ	n emission from GDR-excited ^{12}C	e from μ decay

Table 4.1: 3-pulse signature in the TD of the stopping counter, for signal ($K^+ \rightarrow \pi^+ \nu \bar{\nu}$) and background ($K^+ \rightarrow \mu^+ \nu \mu$).

in more detail in section 4.1.1.1.

Radiative $K_{\mu 2}$ decay, $K^+ \rightarrow \mu^+ \nu \mu \gamma$, is also a potential background because a photon with as little energy as 20 MeV can result in a muon with energy and momentum in the $\pi^+ \nu \bar{\nu}(1)$ signal region (i.e., in the muon band at $P = 215 \text{ MeV}/c$ in figure 4.1). $K^+ \rightarrow \mu^+ \nu \mu \gamma$ can therefore imitate $K^+ \rightarrow \pi^+ \nu \bar{\nu}$ if (1) the muon is downshifted in range due to Gaussian resolution or a non-Gaussian tail, (2) the photon is missed, and (3) the muon is misidentified as a pion (as described for $K_{\mu 2}$ decays above). A range tail associated with events in the muon band may be significant (similar to the range tail associated with events in the $K_{\mu 2}$ momentum peak), and low energy photons are detected less efficiently than high-energy photons, so although the branching ratio for $K_{\mu \nu \gamma}$ decay is small (less than 0.01 of the branching ratio for $K_{\mu 2}$ decay), radiative $K_{\mu 2}$ may be a significant source of background.

The tools used to suppress $K_{\pi 2}$, $K_{\mu 2}$, and other K^+ -decay backgrounds are shown in table 4.2. The “software cuts” which attack K^+ -decay and non- K^+ -decay backgrounds are outlined in section 4.3.

4.1.1.1 ^{12}C Giant Dipole Resonance Background

Giant Dipole Resonance (GDR) background is a particular case of $K_{\mu 2}$ background where both the $\pi \rightarrow \mu \rightarrow e$ decay sequence in the RS is faked, and the muon track is kinematically shifted into the $\pi^+ \nu \bar{\nu}(1)$ region. This correlation between TD and kinematic quantities can

Background	BR	kinematics	PV	PID	mult. tracks	$\check{C}_{K,\pi}$	DC
$K^+ \rightarrow \mu^+ \nu_\mu$	0.64	✓		✓			
$K^+ \rightarrow \pi^+ \pi^0$	0.21	✓	✓				
$K^+ \rightarrow \pi^0 l^+ \nu_l$	0.08		✓	✓			
$K^+ \rightarrow 3\pi$	0.07	✓	✓		✓		
$K^+ \rightarrow \mu^+ \nu_\mu \gamma$	5×10^{-3}	✓	✓	✓			
$K^+ \rightarrow \pi^+ \gamma \gamma$	1×10^{-6}		✓				
beam π^+						✓	✓
$K_L^0 \rightarrow \pi^+ l^- \bar{\nu}_l$				✓	✓		✓

Table 4.2: Tools used to suppress background processes for $K^+ \rightarrow \pi^+ \nu \bar{\nu}$. “BR” (branching ratio) is the probability for a kaon to decay to a specific final state, “kinematics” refers to kinematic selection ($R, E, P, dE/dx, R$ vs. P), “PV” (photon veto) refers to detection of photons, “PID” (particle identification) refers to detection of the $\pi \rightarrow \mu \rightarrow e$ decay sequence in the stopping counter, “mult. tracks” refers to detection of multiple charged tracks, “ $\check{C}_{K,\pi}$ ” refers to identification of kaons in the beam Čerenkov detector, and “DC” (delayed coincidence) refers to the online and offline requirements that the kaon’s decay products be detected at least about 5 ns after the kaon is detected, such that the kaon decays from rest.

lead to poor rejection for GDR background. Experimental evidence for the GDR background mechanism in the E787 $K^+ \rightarrow \pi^+ \nu \bar{\nu}$ data is, at present, suggestive but not conclusive.

GDR background can arise as follows: the 152-MeV muon from $K_{\mu 2}$ decay inelastically scatters in the plastic target or RS, exciting the giant dipole resonance in ^{12}C via a virtual photon. The muon thereby loses the energy of the resonance (23.2 MeV, $\Gamma = 6$ MeV [48]), which can place it in or near the $\pi^+ \nu \bar{\nu}(1)$ kinematic signal region. The excited ^{12}C can de-excite by emitting a neutron, which can travel slowly and unnoticed to the stopping counter where it leaves a second pulse some time after the first track pulse, with energy similar to that of the muon from pion decay. If the electron from decay of the track muon is detected later than the neutron hit, then the 3-pulse pion decay sequence in the stopping counter can appear to be satisfied.

More specifically, the ^{12}C photonuclear cross section with single neutron emission (photon-neutron cross section) is significant at the GDR (about 7 mb [49]), and is significant for larger energies up to at least 37 MeV (between 1 and 4 mb for $n, np,$ and $2n$ emission combined [48, 49]). Convolution of the photon-neutron cross section near the GDR with the virtual

photon distribution emitted by muons gives the muon inelastic cross section associated with single neutron emission from ^{12}C . This cross section is about 0.02 mb, and has modest energy dependence for muons with energy between 50 and 300 MeV [41]. The inelastic scattering can occur early in the muon track (e.g., at low layers in the RS), such that both range and energy are downshifted, placing the muon in the $K_{\mu 2}$ range tail. The muon energy loss can also occur in the target, in which case range, energy, and momentum are all downshifted, placing the muon in the muon band. Single neutrons are emitted from GDR-excited ^{12}C with between 1 and 23 MeV, peaking near 4 MeV [41]. A 10 MeV neutron has an interaction length of about 12 cm in plastic scintillator, and travels slowly ($0.14c = 4.3 \text{ cm/ns}$). In low-energy (n, p) scattering, the energy transfer distribution is flat, so half the protons get more than half of the neutron energy. A 10 MeV neutron can therefore give rise to a proton with between 6 and 10 MeV, which can leave between 2.5 and 5 MeV of visible energy (due to saturation of ionizing energy in the scintillator [50]) in the stopping counter a small time after the first track pulse. The mean pion lifetime is small (26 ns), and pion decay at rest gives rise to a muon with 4.1 MeV (3.0 MeV visible in the scintillator), so, with the track muon and its decay-electron providing the first and third pulses in the stopping counter, the GDR mechanism can give rise to a 3-pulse signature similar to $\pi \rightarrow \mu \rightarrow e$ decay.

The evidence first found for GDR background is shown in figure 4.4. In the top row of figure 4.4, the time of the second pulse in the stopping counter relative to the first pulse, t_{μ} , is plotted vs. the kinetic energy of the $K_{\mu 2}$ muon, E , for higher-range (left) and lower-range (right) $K_{\mu 2}$ range-tail events. Two vertical bands are seen in each plot. The right band corresponds to the full energy $K_{\mu 2}$ muon (152 MeV); the left band is about 22 MeV lower at 130 MeV. The right band is flat in t_{μ} for both plots (i.e., independent of range), but the left band is concentrated at small t_{μ} . Furthermore, the left band is wider (extending to lower energies) and is more heavily populated in the plot of lower-range events. $K_{\mu 2}$ range-tail events in the low-energy band likely arise from muon inelastic scattering in the RS, and pulses at small t_{μ} (close to track time) are more likely to be related to the track than those at large t_{μ} . Therefore, the range-tail events in the low-energy band which have small t_{μ} are suspected to be GDR background events. In contrast, the events in the full-energy

band likely arise from muons which have undergone an elastic scatter, and the fact that the full-energy band is flat in t_μ suggests that the second pulse in the stopping counter is coming from accidental hits. The rejection of the “cuts” used to suppress TD background (see section 4.3) is about a factor of 10 smaller for $K_{\mu 2}$ range-tail events with small t_μ than it is for full-range $K_{\mu 2}$ peak events with large t_μ . This factor of 10 difference may be the difference in rejection between GDR and muon-time accidental background, which suggests that GDR background is the limiting $K_{\mu 2}$ background.

The bottom 4 plots of figure 4.4 are projections of the top 2 plots onto the energy axis, for large (middle row) and small (bottom row) t_μ . The lower-range plots (right) have a much higher concentration of events in the low-energy band than the higher-range plots (left), especially at small t_μ . Note in the lower-range plots (right) that the population of events in the low-energy band shifts to lower energies for smaller t_μ . This can also be seen in the top right plot of figure 4.4 in that the suspected GDR events (i.e., the events clustered at small t_μ in the low-energy band) seem to have a correlation between t_μ and energy. As the muon energy gets smaller (i.e., as the energy that the muon loses due to inelastic scattering gets larger), t_μ seems to get smaller. In figure 4.5, t_μ is plotted vs. the second-pulse energy in the stopping counter, E_μ , for the same $K_{\mu 2}$ range-tail events from the top right plot of figure 4.4. A correlation between t_μ and E_μ may be present, because the suspected GDR events (i.e., the events at small t_μ) seem to move to smaller t_μ with increasing E_μ . Both the t_μ correlation with E in figure 4.4 and the t_μ correlation with E_μ in figure 4.5 can be understood in terms of the GDR mechanism: the more energy that the muon loses to excite ^{12}C , the larger the energy and velocity that the de-excitation neutron can have, leading to shorter travel times to the stopping counter (smaller values of t_μ) and larger energy deposits in the stopping counter (larger values of E_μ).

However, the experimental evidence for GDR background shown in figures 4.4 and 4.5 is merely suggestive. If GDR background is significant, then there should also be GDR background arising from muons scattering in the target, which would result in a momentum shift from the $K_{\mu 2}$ peak value of 236 MeV/c to ≤ 211 MeV/c (for a loss of ≥ 22 MeV), placing the muons in the muon band. As shown in figure 4.6, the momentum distribution of

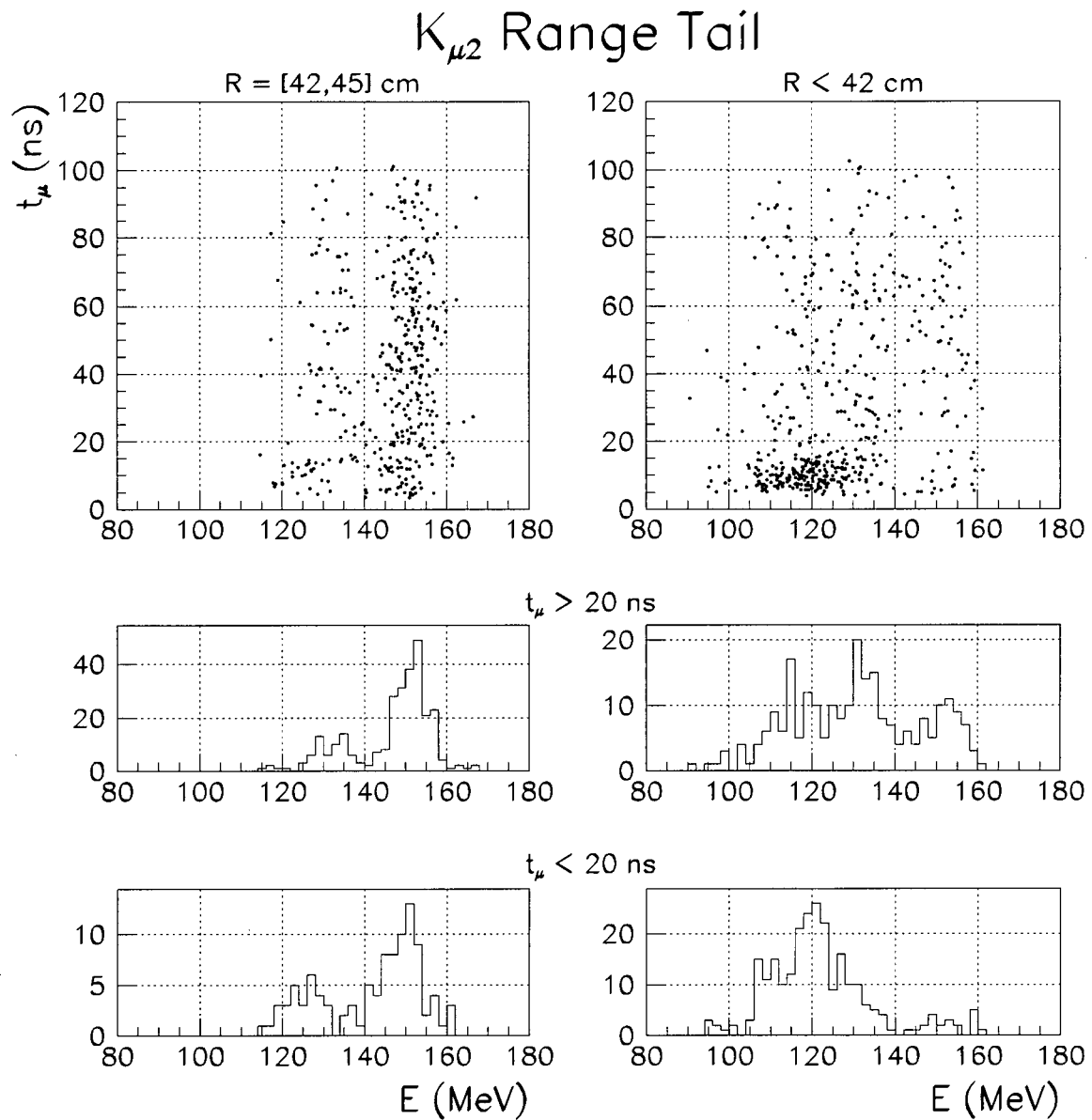


Figure 4.4: Top: Second-pulse time relative to first-pulse time in the stopping counter, t_μ , vs. μ^+ track energy for $K_{\mu 2}$ range-tail events at $R = [42, 45]$ cm (left) and $R < 42$ cm (right), after non-GDR TD backgrounds have been largely removed. The events clustered at $t_\mu < 20$ ns and $E < 130$ MeV are suspected to be due to GDR background.

Middle: Energy projection of the top plots for $t_\mu > 20$ ns.

Bottom: Energy projection of the top plots for $t_\mu < 20$ ns.

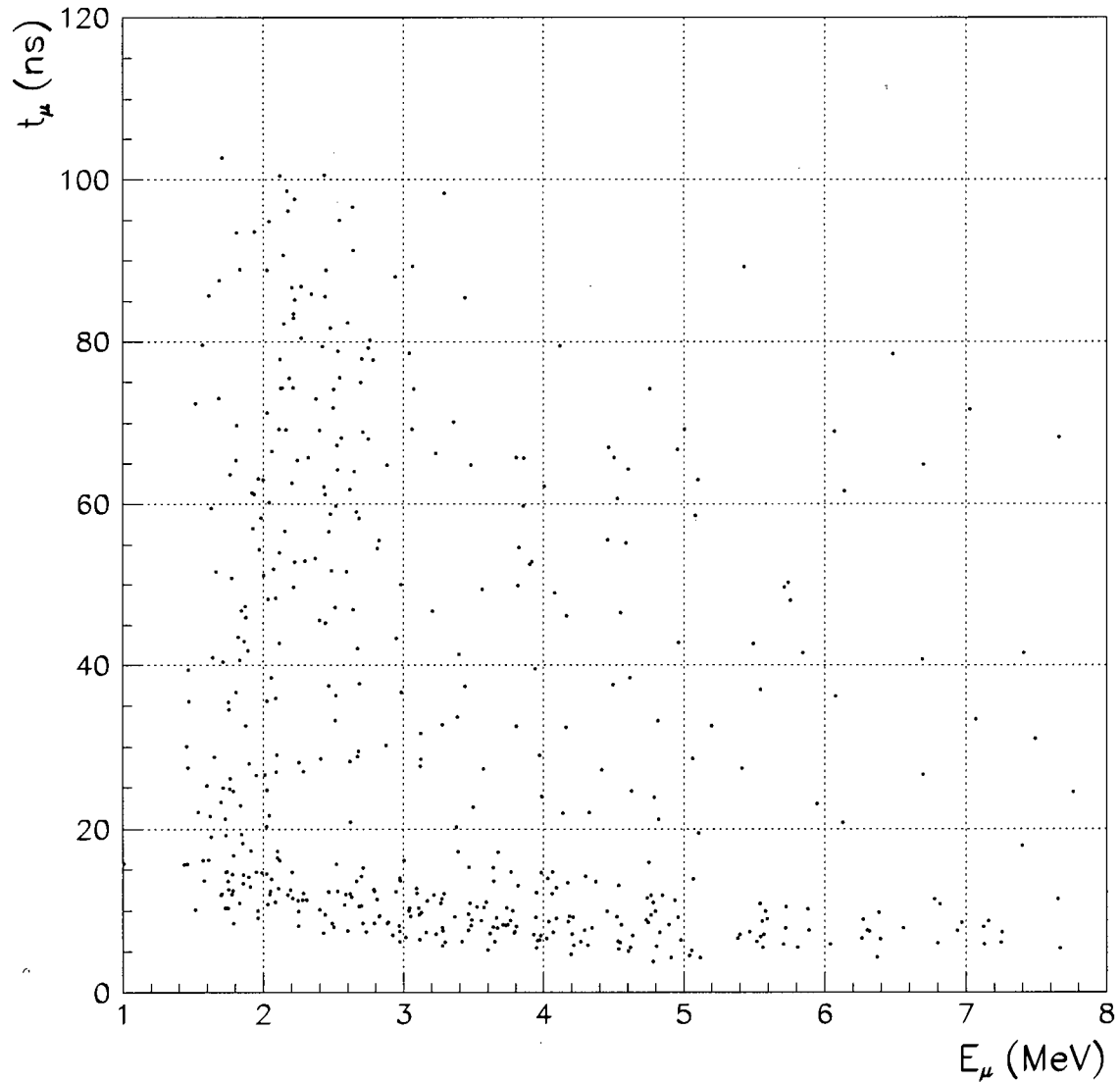
$K_{\mu 2}$ Range Tail

Figure 4.5: Second-pulse time relative to first-pulse time in the stopping counter, t_{μ} , vs. second-pulse energy, E_{μ} , for $K_{\mu 2}$ range-tail events, after non-GDR TD backgrounds have been largely removed. The triangular region at $E_{\mu} = [1, 5]$ MeV and $t_{\mu} < 10$ ns is devoid of events due to application of TD tail-fluctuation “cuts” (see section 4.3) and the difficulty in finding a low-energy second pulse buried under the large-energy first pulse at small t_{μ} .

muon-band events does in fact peak near 211 MeV/ c , though the decrease in the number of events for $P > 211$ MeV/ c may be partly due to the fact that the $K_{\mu 2}$ data sample used to make this plot contains only events which have $R < 45$ cm (see figures 4.1 and 4.2 for the range-momentum correlation of muon-band events). Also, the momentum distribution of muon-band events, while peaking near 211 MeV/ c , is very broad. However, the distribution may be broad because the GDR in ^{12}C is broad. From figure 4.4, it appears that inelastic scattering of muons can result in $K_{\mu 2}$ energy shifts down to 105 MeV. If this loss occurs in the target, then the $K_{\mu 2}$ peak momentum can shift down to 182 MeV/ c . On the other hand, if muon-band events are mainly due to radiative $K_{\mu 2}$ decay, $K_{\mu 3}$ decay, and/or $K_{\mu 2}$ decay in flight, then the muon-band events themselves should have missing energy in the RS ≥ 22 MeV if muon inelastic scattering is occurring. In figure 4.7, t_{μ} is plotted vs. $E_{RS}(\text{diff})$ for the same muon-band events from figure 4.6, where $E_{RS}(\text{diff})$ is the expected muon energy in the RS based on the momentum measured in the UTC, minus the measured muon energy in the RS. A band at 0 MeV is seen, but no band at $E_{RS}(\text{diff}) \geq 22$ MeV is seen, which is where radiative $K_{\mu 2}$, $K_{\mu 3}$, and $K_{\mu 2}$ decay-in-flight events with an inelastic scatter in the RS should show up. The events seen at negative values of $E_{RS}(\text{diff})$ are due to radiative $K_{\mu 2}$ or $K_{\mu 3}$ decay where a photon leaves energy on the charged track.

Independent of whether the muon band arises from $K_{\mu 2}$ muons scattering inelastically in the target or from radiative $K_{\mu 2}$ decay, $K_{\mu 3}$ decay, and/or $K_{\mu 2}$ decay in flight: if there is a large component of GDR background present in the muon band, then the muon-band events should be concentrated at small t_{μ} , and the TD rejection of muon-band events at small t_{μ} should be similar to the TD rejection of $K_{\mu 2}$ range-tail events at small t_{μ} . The muon-band events may not be concentrated at t_{μ} as small as that for range-tail events however, because the neutron from muon-band GDR background (muon scattering in the target) has more distance to travel to the stopping counter than the neutron from range-tail GDR background (muon scattering in the RS). Comparing the t_{μ} distribution of events in the low-energy band of the top right plot in figure 4.4 with the t_{μ} distribution in figure 4.7, the muon-band distribution of t_{μ} is much flatter than the low-energy range-tail distribution. However, the TD rejection in the muon band at small t_{μ} , similar to that in the $K_{\mu 2}$ range tail at small t_{μ} ,

Muon Band

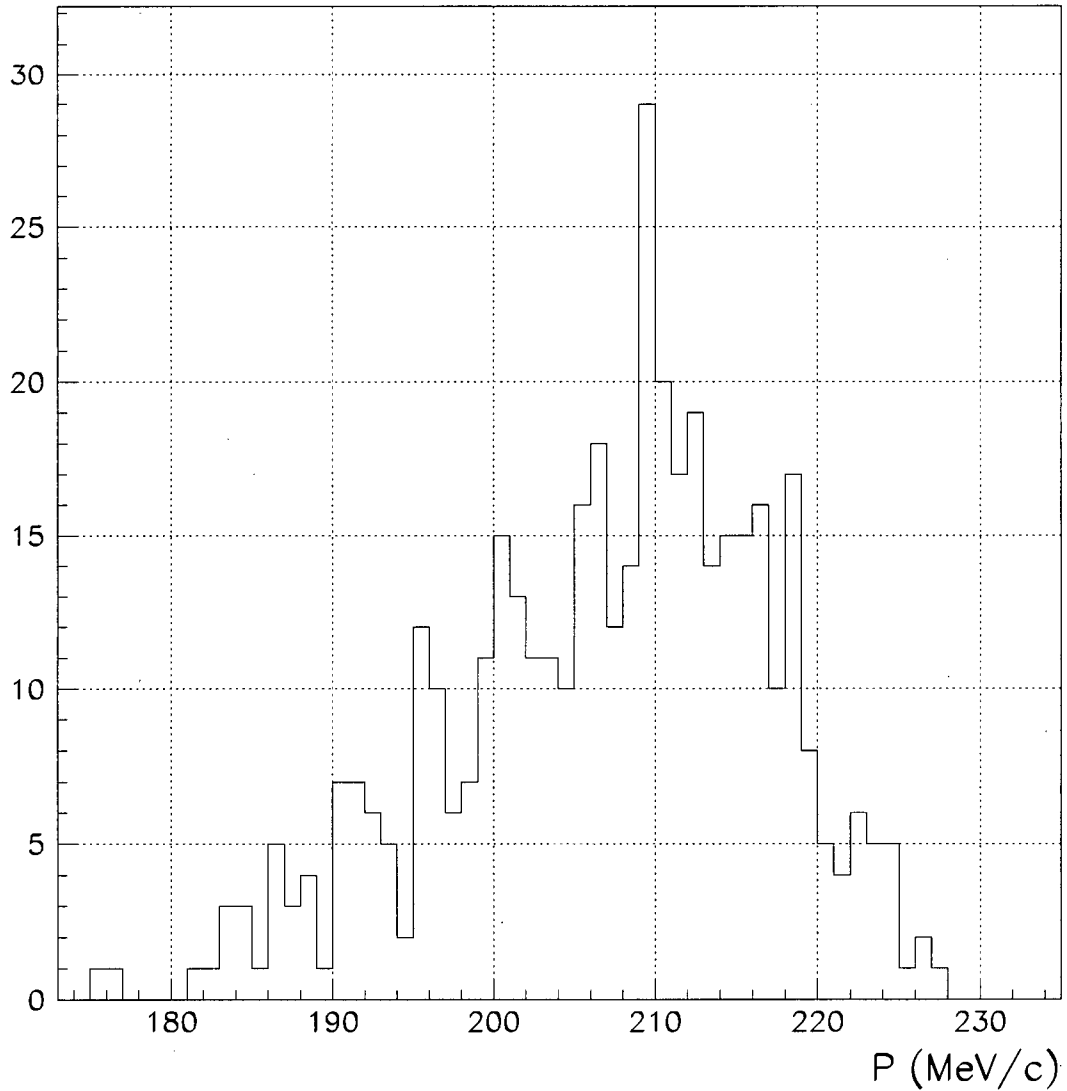


Figure 4.6: Momentum distribution of muon-band events, after non-GDR TD backgrounds have been largely removed. Events are required to have $R < 45$ cm, $E < 150$ MeV, and $P < 228$ MeV/c.

Muon Band

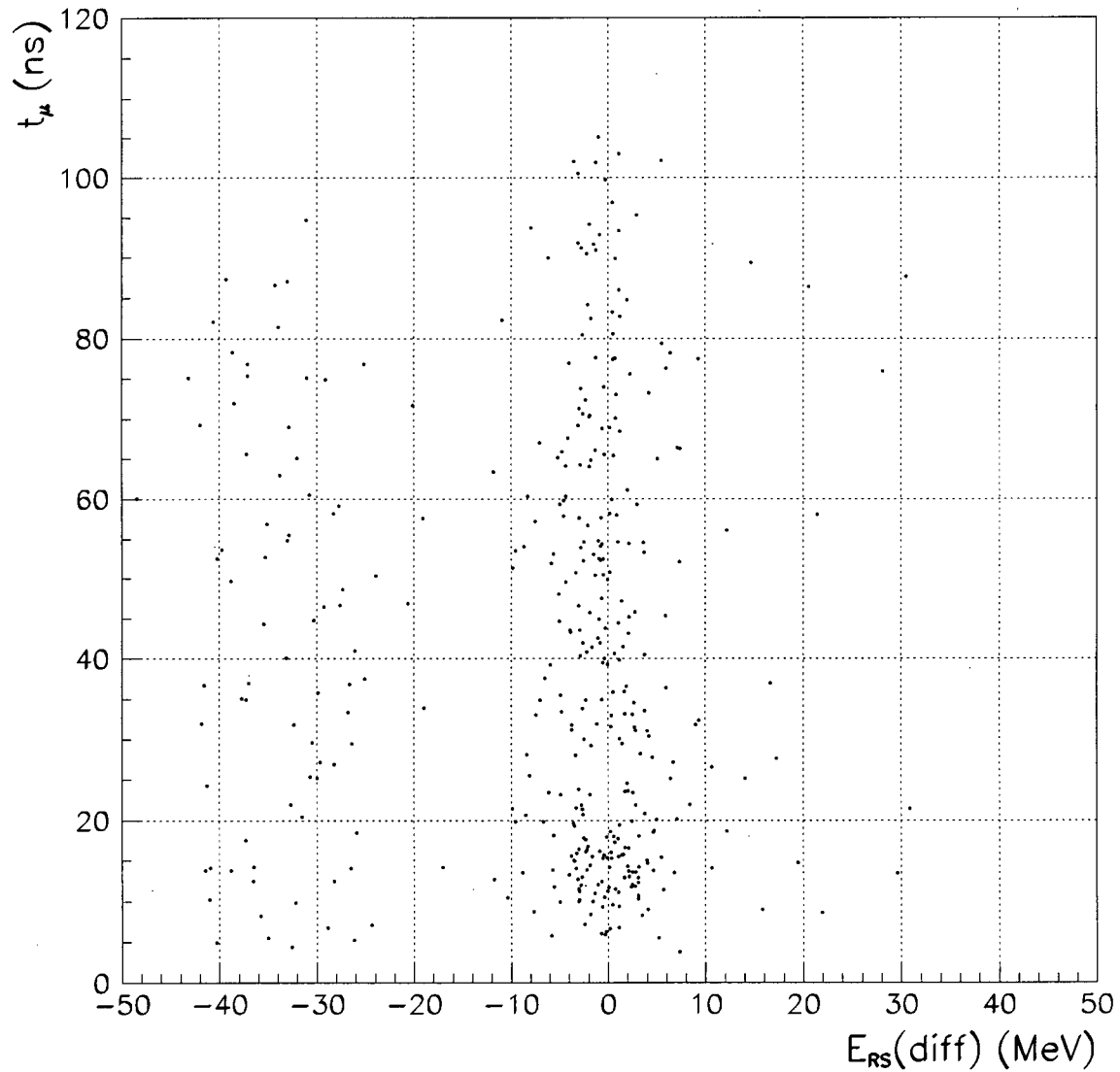


Figure 4.7: Second-pulse time relative to first-pulse time in the stopping counter, t_μ , vs. $E_{RS}(\text{diff})$ for muon-band events after non-GDR TD backgrounds have been largely removed. $E_{RS}(\text{diff})$ is the expected RS track energy (using momentum measured in the UTC) minus the measured RS track energy. The events at negative values of $E_{RS}(\text{diff})$ are due to radiative $K_{\mu 2}$ or $K_{\mu 3}$ decay where a photon leaves energy on the charged track.

is about a factor of 10 worse than that in the $K_{\mu 2}$ peak, which perhaps suggests that both the muon band and range tail have some component of TD background which is difficult to reject that is not present in the $K_{\mu 2}$ peak, e.g., GDR background.

Also, $K_{\mu 2}$ events have been examined for neutron activity in RS counters other than the stopping counter, where the neutrons may arise due to de-excitation of GDR-excited ^{12}C . There is clear evidence of excess near-track-time activity off the track in low-range, low-energy $K_{\mu 2}$ range-tail events, shown as a peak near $t = 0$ ns in the rightmost plot in the middle row of figure 4.8. However, the expected difference in TD rejection between $K_{\mu 2}$ peak and range-tail events, based on this activity, is only about 4.9 [41]. However, any neutrons leaving energy in the same hexant and layer of a track counter were ignored in this study (because their TD times, due to multiplexing, tend to be shifted to 0 ns), and this is precisely where the neutron rate could be highest.

Finally, a prediction of the relative number of $K_{\mu 2}$ peak and range-tail events, assuming that the range tail arises from the GDR mechanism, has been attempted by convoluting the virtual photon distribution emitted by muons with the photoneutron cross section for ^{12}C [41]. The predicted number of range-tail events relative to peak events is about 10^{-5} , which is consistent with what is observed. So, based on all of the above evidence, it is indeed possible that a large component of the limiting background from the $K_{\mu 2}$ range-tail and muon-band is due to GDR background. However, more data which is enhanced in this particular background mechanism is needed, and Monte Carlo modelling of the process needs to be attempted before the GDR background can be unambiguously identified.

4.1.2 Beam Backgrounds and Kaon Charge Exchange

Beam background is grouped into 4 categories: “single beam” kaon- and pion-entering, and “double-beam” kaon- and pion-entering. Single-beam kaon-entering events are kaon decay-in-flight events, which are suppressed by requiring a delayed coincidence of the kaon and its decay product. Single-beam pion-entering events are events where a beam pion scatters into the detector. These are suppressed by requiring a delayed coincidence of the

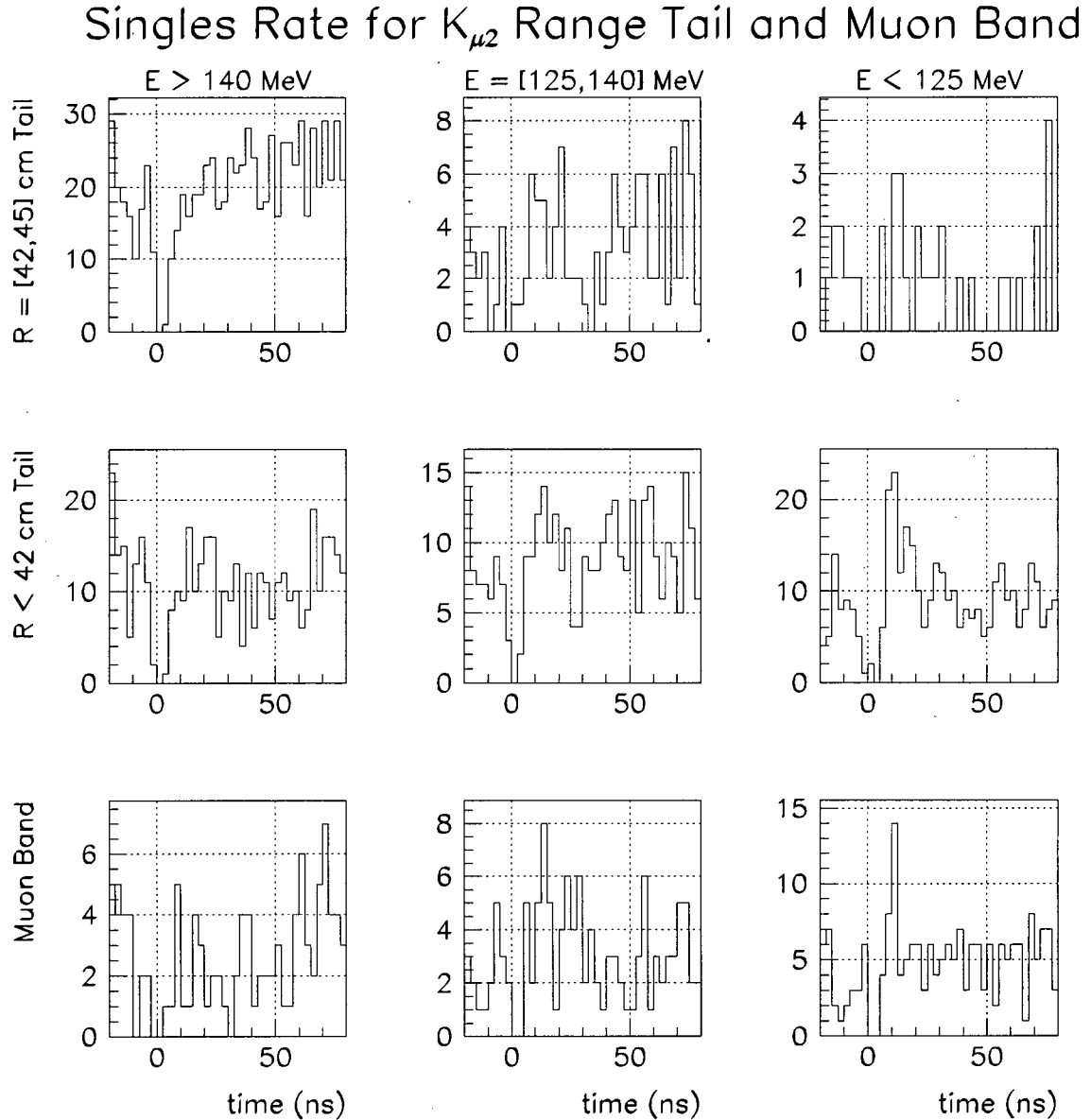


Figure 4.8: Time spectrum of single counter hits in the RS (all energies), for $K_{\mu 2}$ range-tail events with $R = [42, 45]$ cm (top row), $R < 42$ cm (middle row), and muon-band events (bottom row), with track energy $E > 140$ MeV (left column), $E = [125, 140]$ MeV (middle column), and $E < 125$ MeV (right column) MeV. The deficiency of events around $t = 0$ ns is due to the online and offline photon vetos. Hits in the track hexant have been ignored. An excess of near-track-time hits (near $t = 0$ ns) is observed for low-range $K_{\mu 2}$ range-tail events with $E < 125$ MeV (rightmost plot in the middle row), which is possibly a result of neutrons emitted from GDR-excited ^{12}C .

beam particle and the track particle, and by high-efficiency detection of beam pions in the Čerenkov detector (99.84% [30]). Single-beam background can imitate $K^+ \rightarrow \pi^+\nu\bar{\nu}$ if the beam and/or track timing is poorly reconstructed such that the delayed coincidence requirements are satisfied.

Double-beam events are the same as single-beam events, except that an earlier kaon is present such that the delayed coincidence is fooled. These events are suppressed by looking for coincident activity in the beamline detectors and RS. Double-beam background can imitate $K^+ \rightarrow \pi^+\nu\bar{\nu}$ if the decay-in-flight kaon or scattering pion is missed in the beam, and the earlier kaon's decay products are missed.

Kaon charge-exchange background arises from kaon charge-exchange, $K^+n \rightarrow K^0p$ (e.g., in the target), followed by $K_L^0 \rightarrow \pi^+l^-\bar{\nu}_l$. The cross section for kaon charge exchange in carbon is estimated to increase rapidly from 0 to 11 mb between K^+ energies of about 20 and 60 MeV, then increase more slowly to 15 mb at a K^+ energy of about 100 MeV (see, for example, ref. [51]). The K^0 in the final state is a 1:1 linear combination of the short-lived K_S^0 ($\tau = 0.08934$ ns) and the long-lived K_L^0 ($\tau = 51.7$ ns). Neutral kaons are not slowed in the target, so potential background arising from prompt K_S^0 decay is effectively removed by requiring a delayed coincidence of the kaon and its decay product. However, K_L^0 particles are long-lived, and can decay into the fiducial volume of the detector if they travel slowly in the target. Also, the phase space of $K_L^0 \rightarrow \pi^+l^-\bar{\nu}_l$ is such that the final state π^+ (l^-) can be in the $\pi^+\nu\bar{\nu}(1)$ signal region if the final state l^- (π^+) is of low energy, or the K_L^0 decays in flight. Detection of both of the final-state charged tracks, and the kinematics (dE/dx and R vs. P) and PID (via detection of $\pi \rightarrow \mu \rightarrow e$ in the stopping counter) of the l^- track can be used to suppress this process. CEX background can therefore imitate $K^+ \rightarrow \pi^+\nu\bar{\nu}$ if (1a) $K^+n \rightarrow K^0p$ occurs after the K^+ has traversed the beamline detectors, or (1b) $K^+n \rightarrow K^0p$ occurs earlier in the beamline, and the K^+ signal comes from a different kaon whose decay products are missed; (2) the K_L^0 travels slowly such it decays, satisfying the delayed coincidence, into the fiducial volume of the detector; and (3a) the l^- from $K_L^0 \rightarrow \pi^+l^-\bar{\nu}_l$ is missed, or (3b) the π^+ is missed, and the l^- is misidentified as a pion as described in section 4.1.1.

The tools used to suppress beam and CEX background are shown in table 4.2. The “software cuts” which attack K^+ -decay and non- K^+ -decay backgrounds are outlined in section 4.3.

4.2 Analysis Strategy and Techniques

The number of $K^+ \rightarrow \pi^+\nu\bar{\nu}$ events expected in the combined 1995-7 data is on the order of 1 event, based on the number of collected kaons and the acceptance of data-selection requirements (see chapter 5), and the predicted $K^+ \rightarrow \pi^+\nu\bar{\nu}$ branching ratio (see section 2.2). Therefore, the goal in the offline analysis is to suppress the backgrounds in the $\pi^+\nu\bar{\nu}(1)$ signal region to an expected value of $\ll 1$ background event, such that any events observed in this region can be unambiguously assigned to signal. This large suppression of backgrounds (by at least 10^{10}) makes estimation of the background in the signal region difficult, because any measurement involving low statistics is subject to large statistical fluctuations. Furthermore, the sequential development of data-selection requirements (i.e., “cuts”) using smaller and smaller numbers of events can result in “bias”, because it is difficult to ascertain whether or not a small number of pathological events is drawn from a larger population on which the cuts are supposed to be effective. For the same reason, the definition of a signal event based on examination of a single event is biased because it is always possible to invent some cut which will reject a single event.

To avoid bias, this analysis is a “blind” analysis. That is, background sources are identified *a priori*, and a signal region is defined (the $\pi^+\nu\bar{\nu}(1)$ region, often referred to as the “box”) where the signal/background ratio is expected to be highest. Cuts to suppress background are developed using events which lie outside the box. Events in the box are not counted or examined until the cuts and the background estimates are final.

To enhance the statistical power of the analysis, background measurements are made via “bifurcated” analyses. Each background is addressed by at least two uncorrelated cuts or groups of cuts, which can be independently “inverted” to create high-statistics background samples from the data. That is, background data samples can be created by selecting events

which fail a specific cut. Wherever possible, background is extracted from the real data (as opposed to modelling the background with Monte Carlo simulations) so that all possible background event pathologies are taken into account. The performance of other, uncorrelated cuts can then be tested on these data samples.

A pictorial representation of a bifurcated analysis is shown in figure 4.9. The validity of this method relies on the assumption that the bifurcated cuts are uncorrelated. This assumption can be tested by loosening the bifurcated cuts simultaneously, re-measuring the background levels at these looser cut positions, and (after masking out the box) observing the numbers of events in these “outside-the-box” regions. If the number of events observed is greater than that predicted close to the box, a correlation between cuts may be present, which invalidates the bifurcated background estimate for the box. The outside-the-box correlation study is shown pictorially in figure 4.10.

To detect any bias in the cuts, background measurements are performed on independent data samples. The data is partitioned into 1/3 and 2/3 samples, and cuts are designed and the background level measured using the 1/3 data samples. The background level is then re-measured using the independent 2/3 data sample. If the cuts are unbiased, the 1/3 and 2/3 data samples should give the same result (within statistical uncertainty). If the 2/3 measurement gives an anomalously high result which exceeds a predetermined acceptable level, then a predetermined contingency cut or cut-tightening is applied to reduce the background to the acceptable level. If this level is not met, then the 1/3 study and 2/3 test is repeated, although there is no longer a truly independent data sample available for testing the cuts. In either case, new cuts may be designed and applied purely as “safety cuts” (defined in section 4.3) based on the results from the 2/3 test.

In the present analysis, cuts are initially designed and the background level first measured using the 1/3 1995 data (the 1995 data has previously been examined [46, 47]). After testing on the 2/3 1995 data, the cuts are recalibrated for 1996-7 data using the 1/3 1996-7 data with high statistics (at least 100 events remaining after application of each cut, to minimize bias). New cuts (if necessary) are developed and the background level is measured using the 1/3 1996-7 data, followed by background measurement on the 2/3 1996-7 data. The 1996

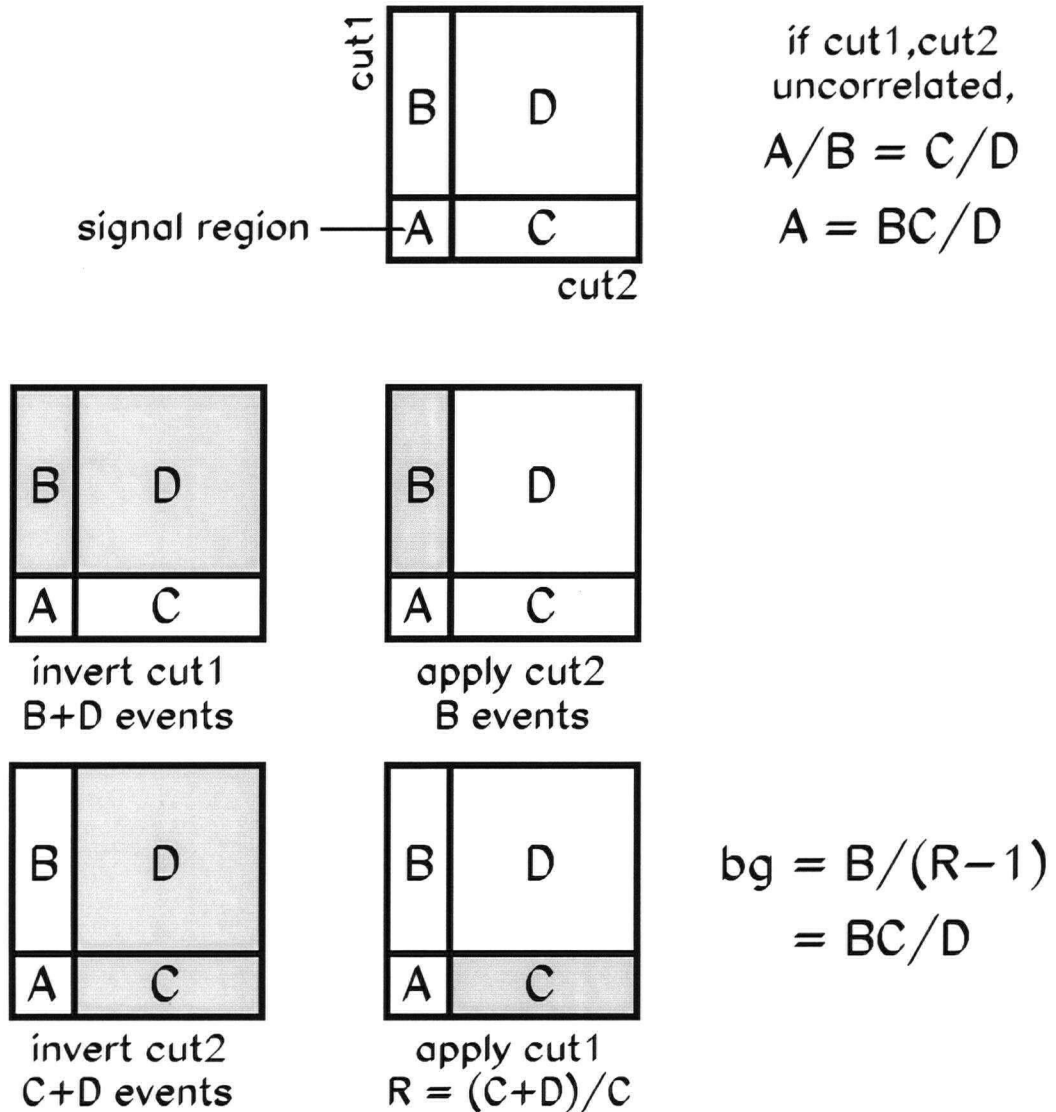


Figure 4.9: A background estimate resulting from a bifurcated analysis.

Top: If the amount of background is linear in some cut parameters cut1 and cut2, and these parameters are uncorrelated, then the number of background events in region A of the cut1,cut2 parameter space relative to that in B is equal to that in C relative to D.

Middle: Count events that fail cut1 and pass cut2 to get the “normalization” B.

Bottom: Select events that fail cut2, and measure the “rejection” of cut1 via $R = (C+D)/C$, where C and D are the numbers of events in regions C and D, respectively. Region A is never examined in this procedure. The background estimated to be present in region A is given by $B/(R-1) = BC/D$.

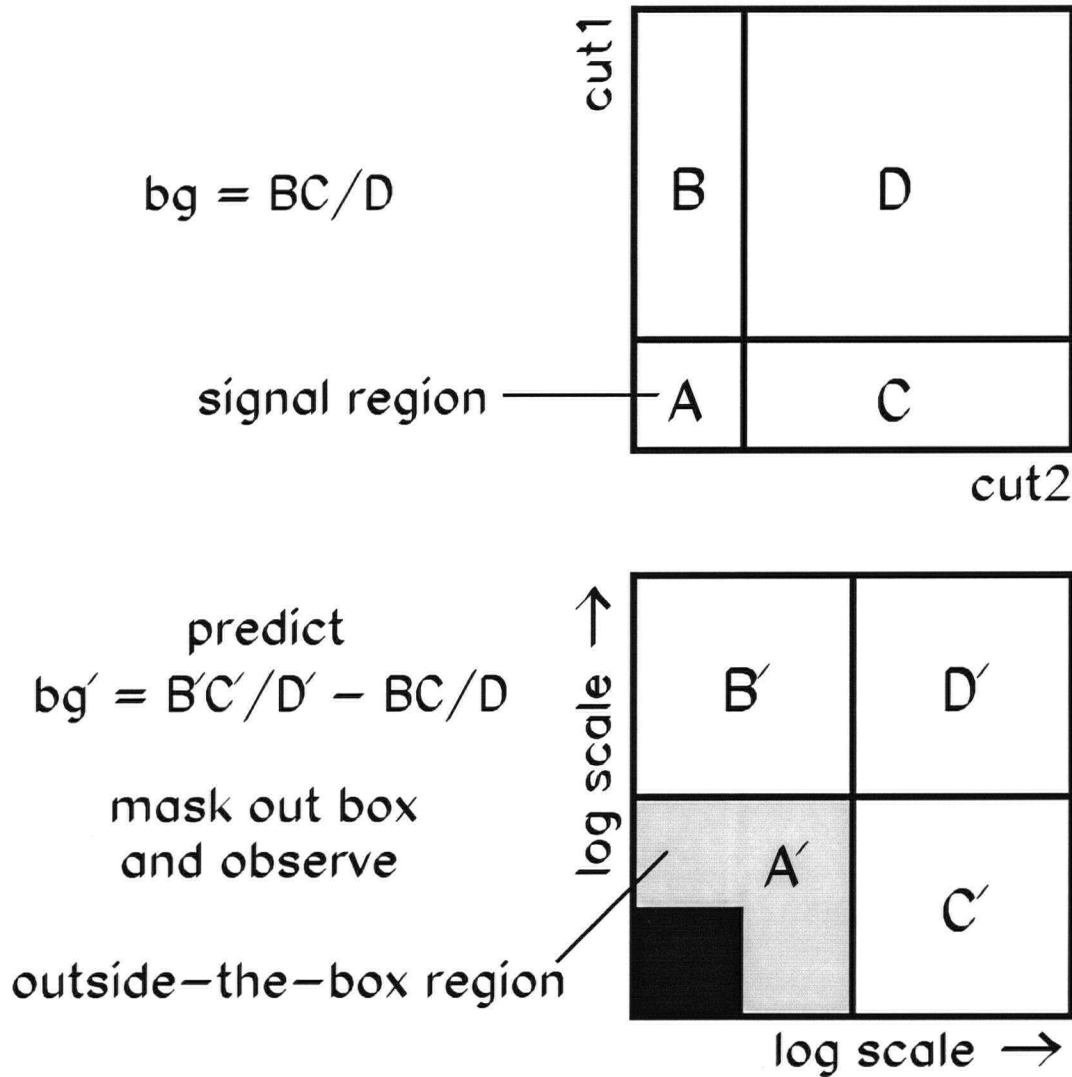


Figure 4.10: Outside-the-box correlation study. The validity of the bifurcated background measurement procedure (see figure 4.9) relies on the assumption that cut1 and cut2 are uncorrelated. To test this, the background measurement can be made using larger and larger A regions, formed by loosening cut1 and cut2 by the same amount (in the above figure, by a factor of 10 for a total loosening of $10 \times 10 = 100$). The predicted number of events in the looser box can be compared to the observed number (after masking out the final box, which is only 1% of the loose box in this example) which should agree if no correlations are present.

and 1997 data sets are combined into a single data set, because together they have roughly the same statistics as the 1995 data set.

Finally, the bifurcated cuts are designed to have additional rejection beyond that which defines the background level in the box, so that a cut-tightening (box-shrinking) procedure can be used to evaluate candidate $K^+ \rightarrow \pi^+ \nu \bar{\nu}$ events. The specific procedure by which cuts are tightened is defined before examining any (small number of) events which lie in the box, in order to avoid bias. This cut tightening, and the cut loosening for the outside-the-box correlation test mentioned above, is performed using functions of the bifurcated cuts associated with each background type. The functions are defined in terms of a parameter $N \geq 0$ which is linear in background [52]. For example, a specific level of background can be achieved by requiring events to have $N \leq 1$. The requirement $N \leq 2$ then corresponds to a cut which lets in a factor of 2 more background events, and the requirement $N \leq 0.33$ corresponds to a cut which reduces the number of background events by a factor of 3. Effective cuts are those which reject background while keeping signal, so signal events are not linear in N , but rather concentrated at small values of N . Values of N are therefore a measure of the likelihood of an event to be signal: an event with a small N value is more likely to be signal than an event with a large N value. Equivalent functions can be defined in terms of a parameter $A \geq 0$ which is linear in signal. For example, if the requirement $A \leq 1$ corresponds to a cut which has a certain acceptance for signal, then the requirement $A \leq 0.5$ corresponds to a cut which reduces the number of signal events by a factor of 2. Again, effective cuts are those which reject background while keeping signal, so background events are not linear in A , but rather concentrated at large values of A . Values of A are therefore a measure of the likelihood of an event to be background: an event with a large A value is more likely to be background than an event with a small A value. N and A values are scaled such that the requirements $N \leq 1$ and $A \leq 1$ roughly correspond to the cut positions which give the background level and acceptance, respectively, of a previous analysis of 1995 data [46]. Because there is roughly a factor of 3 more data in the combined 1995-7 data set, events in the current analysis will be required to have $N \leq 0.33$ in order to maintain the same background level as the 1995 analysis. Kaon-rate-independent cuts (e.g.,

kinematic cuts on the total range, energy, and momentum of a charged track) typically have less acceptance loss per gain in rejection than rate-dependent cuts (e.g., cuts on activity in the photon detectors, or the RS counter in which in the charged track comes to rest), so for a given background which is addressed by both rate-independent and rate-dependent cuts, the current analysis will typically proceed with the rate-independent function cut set near $N \leq 0.33$, while the rate-dependent function cut remains set near $N \leq 1$.

Once the cuts and signal evaluation functions have been defined, and achieve a background level in the signal region of $\ll 1$ event, the box is “opened”. That is, all the cuts are applied and the surviving events (which, by definition, are signal events) are counted and examined.

4.3 Data Analysis and Cuts

Mechanically, the analysis is performed by analyzing the data on tape with a computer program which consists of a number of software routines linked together. The routines unpack the data on an event-by-event basis, and calculate quantities associated with each event. Specific requirements on the values of these quantities are known as “cuts” because they serve to cut or remove background events from the $K^+ \rightarrow \pi^+ \nu \bar{\nu}$ data.

The cuts can be loosely grouped into “reconstruction cuts”, “pathology cuts”, “function cuts”, and “safety cuts”. The reconstruction cuts require that a charged track be reconstructed in the target, UTC, and RS, such that the event is worthy of further analysis. The pathology cuts are typically applied at the initial stages of a bifurcated analysis in order to remove events which can contaminate the bifurcated data samples with correlations. A function cut is inverted to define one of these data samples, on which the performance of another, uncorrelated function cut is evaluated in order to make a background estimate. Safety cuts, like all cuts, are used to suppress background, but they are not used in the background estimates because their performance is difficult to evaluate. This is usually because some event pathology was recognized only after background estimates were made using both the 1/3 and 2/3 data samples, so there is no independent data sample on which to test the cut

designed to address this pathology. The reconstruction, pathology, and safety cuts are all “binary” cuts in that events either “pass” or “fail” these cuts. The function cuts are designed on a sliding scale, so that they can be loosened to perform the outside-the-box correlation test (see sections 4.2 and 4.6), and tightened to estimate the “likelihood” of an event to be a signal or background event (see sections 4.2 and 4.7).

To reduce the 30 Tbytes of raw data into a volume suitable for timely development of cuts and background estimation, the analysis is performed in three “passes”. In the first pass (PASS1), basic event reconstruction is performed, some general, loose cuts are applied to reject the most obvious of the $K_{\pi 2}$, $K_{\mu 2}$ and beam backgrounds, and the data is compacted such that the volume of raw data is reduced by a factor of about 10 while maintaining high acceptance for $K^+ \rightarrow \pi^+ \nu \bar{\nu}$ events. This creates a manageable number of output data tapes to be analyzed during the second pass (PASS2). The PASS1 cuts are listed and briefly described in table 4.3. An event display of a successfully reconstructed $K_{\mu 2}$ event is shown in figures 4.11, 4.12 and 4.13. This event is viewed from downstream of the detector, such that a positively charged track curves clockwise in the magnetic field of the detector. These figures are also used for reference in the detailed description of all cuts found in Appendix C.

The PASS2 cuts are loose versions of some pathology and function cuts which are developed further at the third pass (PASS3). The PASS2 cuts are listed and briefly described in table 4.4. They are used in various combinations to define 3 background data streams, referred to as SKIM1, SKIM2, and SKIM3, shown in table 4.5. The SKIM1, SKIM2, and SKIM3 data streams are used at PASS3 for study of $K_{\pi 2}$, $K_{\mu 2}$, and beam background, respectively. Note that each of these streams also serves as a “signal” stream in that no cuts are inverted (at this stage) to define a background data sample.

The PASS3 analysis involves calculation of many quantities for each SKIM1, SKIM2, and SKIM3 event, which are stored (grouped by event) in “ntuples”. The ntuples are created, filled, and read by the Physics Analysis Workstation (PAW) program [53]. With PAW one can loop through the events in the ntuples fairly quickly, filling histograms for the development of cuts, and/or applying cuts to measure background. To speed up the analysis even further, “summary” ntuples which contain only the information pertinent to making

cut	pass condition
TRBIT	the online trigger is satisfied
RD_TRK	a track is (crudely) reconstructed in the RS
STLAY	the online stopping counter and hexant agree with those found offline
RSHEX	there are no hits in the stopping layer and hexant which are not part of the track
TRKTIM	an average track time is found in the RS
INTIME	the non-track hits in the RS at track time sum to less than 10 MeV (e.g., no photons from $K_{\pi 2}$ decay are found in the RS)
FITPI	the 2-pulse $\pi \rightarrow \mu$ decay signature is found in the stopping counter
UTC/RANGE/TARGET	a track is reconstructed in the UTC which lines up with the track in the RS, and the energy and range of the track in the RS are accurately calculated
PDC	the track particle does not arise from a high-momentum beam particle ($> 280 \text{ MeV}/c$ in the UTC)
LAY14	the track does not exit the RS and enter the RS support structure

Table 4.3: PASS1 cuts.

cut	pass condition
PVCUT	no above-threshold photon energy is detected in the barrel, EC, or RS
TGPVCUT	no above-threshold photon energy is detected in the target
TGPVTR	no above-threshold photon energy is detected in the target
TGRECON	a kaon cluster and a pion track are reconstructed in the target
TGCUT	the kaon times in the target and B4 hodoscope are consistent, and the pion times in the target, IC, and RS are consistent within measurement uncertainties; the energy deposit in the IC is consistent with that of a charged pion track
PSCUT	a pion is not present in the beamline at the same time as the track in the RS, based on B4 and \check{C}_{π} information, which means that the RS track is not likely to have arisen from a beam pion
RSHEX2	the track does not cross sectors in the stopping layer
TDCUT	there are no hits within ± 1 sector of the stopping counter which occur at the same time as the second pulse in the stopping counter

Table 4.4: PASS2 cuts.

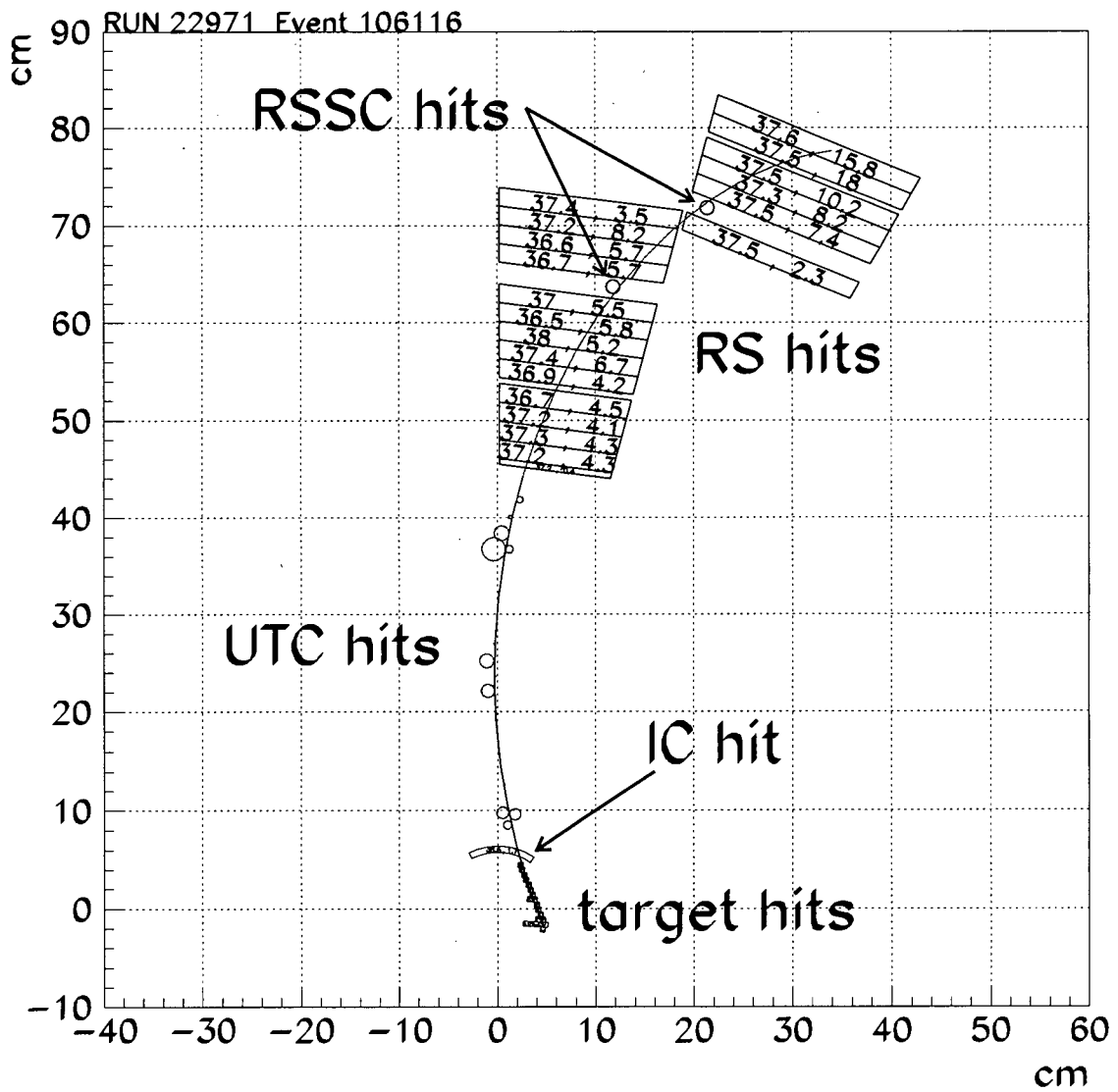


Figure 4.11: Event display of a successfully reconstructed $K_{\mu 2}$ event.

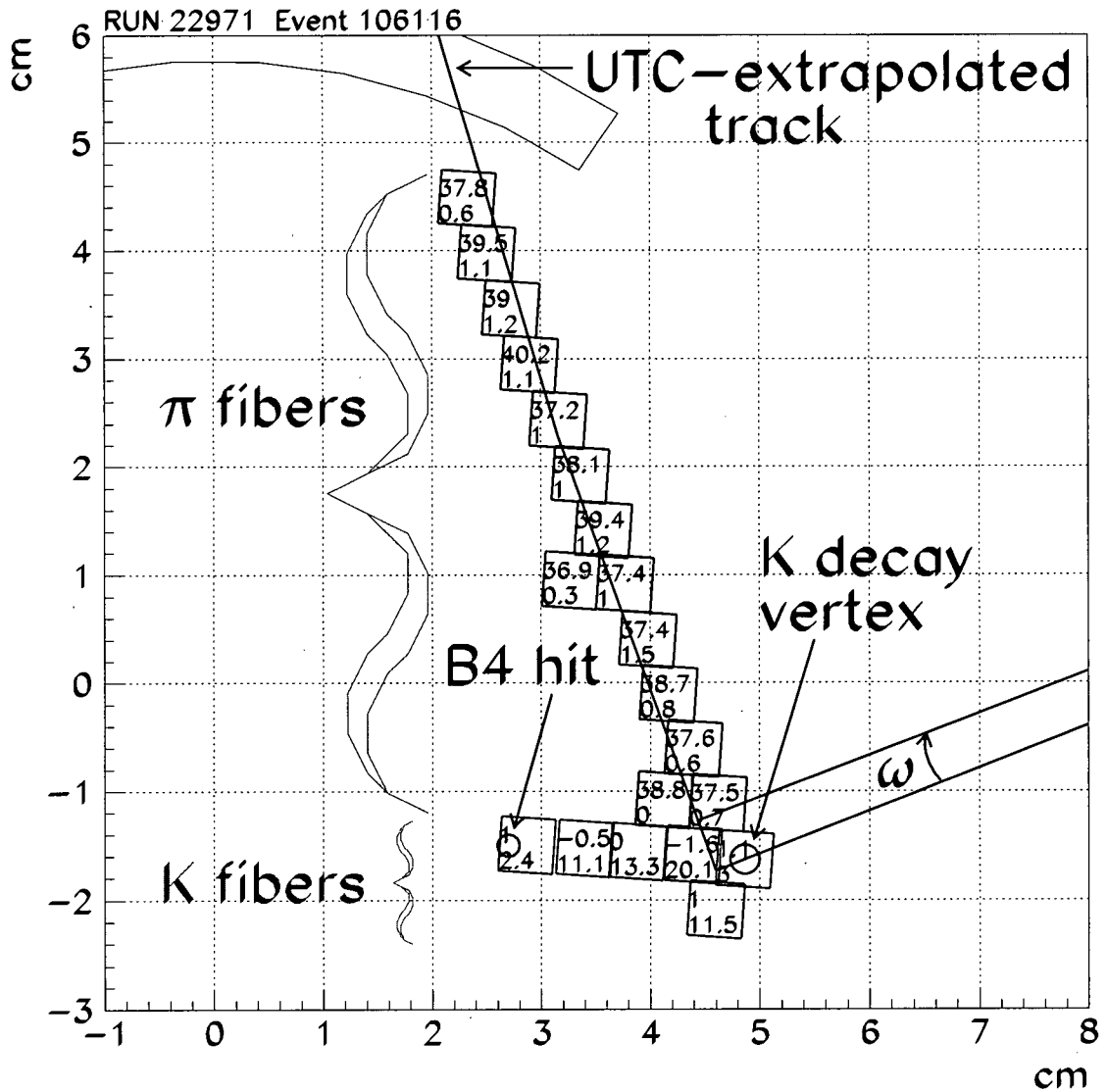


Figure 4.12: Close-up of the target hits for the event shown in figure 4.11. The top and bottom numbers in each fiber are the time (ns) and energy (MeV) of each hit, respectively. The kaon fibers have hits close to $t = 0$ ns, whereas the pion fibers have hits about 38 ns later, ensuring that the kaon decayed from rest. ω is the angle in the (x, y) plane along the circular UTC track.

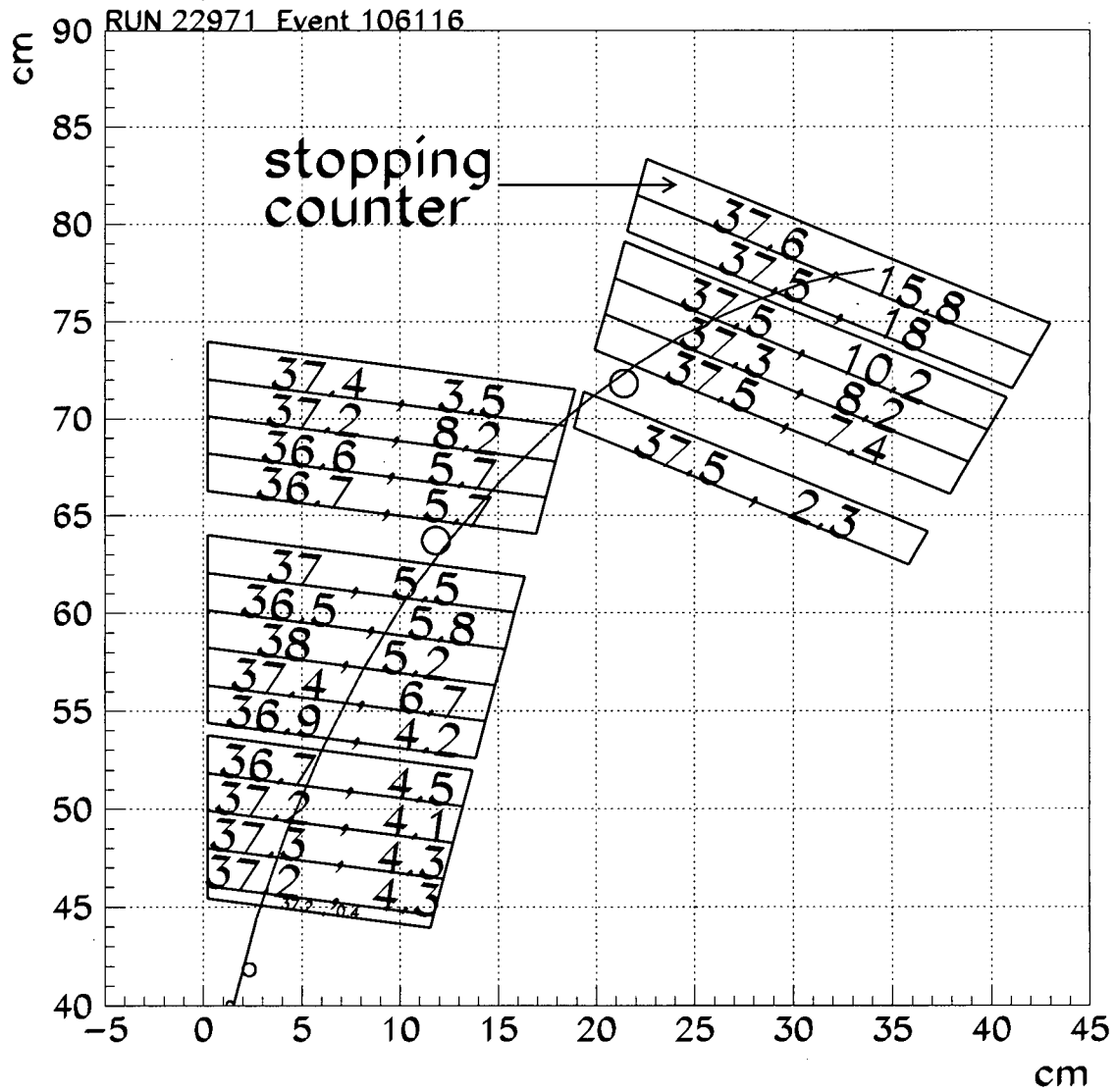


Figure 4.13: Close-up of the RS hits for the event shown in figure 4.11. The left and right numbers in each counter are the time (ns) and energy (MeV) of each hit, respectively.

SKIM1 ($K_{\pi 2}$)	SKIM2 ($K_{\mu 2}$)	SKIM3 (beam)
TGRECON	TGRECON	TGRECON
TGCUT	TGCUT	TGCUT
RSHEX2	RSHEX2	RSHEX2
TGPVCUT	TGPVCUT	TGPVTR
—	PVCUT	PVCUT
TDCUT	—	TDCUT
PSCUT	PSCUT	—

Table 4.5: Definitions of the PASS2 output background data streams.

the background estimates are created from the “full-record” ntuples. The PASS3 cuts are grouped into kinematic and beam pathology cuts, and PV, TD, kinematic, and beam function cuts. The kinematic and beam pathology cuts are listed and briefly described in tables 4.6 and 4.7, respectively. The function cuts are described in section 4.3.1. Some data quality cuts are also applied at PASS3 which are listed in table 4.8. Note, from sections C.3.1, C.3.2, and C.3.4, that some PASS3 cuts are modified from the 1995 versions for application to 1996-7 data (CHIRF), and that some PASS3 cuts are applied only to the 1996-7 data (PROBZ, CHIRF_NHZ, MASS, OPSVETO_LKB, TDDFA1, TDECON, and TDVEL), mainly because of an increase in $K_{\mu 2}$ background observed in the 1996-7 data set (see sections 5.10 and C.3.4). Additional technical information on the PASS3 cuts is available elsewhere [41].

4.3.1 Function Cuts

As shown in figure 4.9 and stated in sections 4.2 and 4.3, a bifurcated background estimate involves “inversion” of a “function cut” in order to define a background data sample, on which the performance of another, uncorrelated function cut is evaluated. The two, uncorrelated function cuts associated with a particular background type are called the “normalization” and “rejection” function cuts, respectively. As stated in section 4.2, each function cut is designed on a sliding scale in terms of a parameter N , which is the scaled number of events remaining in a background data sample after the cut has been applied. Each function cut may also be defined in terms of a parameter A , which is the scaled accep-

cut	pass condition
UTCQUAL	the UTC track fit in the (x, y) plane is of high quality
PROBZ	the UTC track fit in the (r, z) plane is of high quality
ZUTOOUT	the track does not exit the side of the UTC
LAYV4	the track stops in one of RS layers 11 through 18 inclusive
COS3D	the track propagates within $\pm 30^\circ$ of the vertical
ZFRF	the track does not exit or stop near the side of the RS
LAYER14	the track does not stop or curl over in the outer RSSC
CHIRF	the track particle does not scatter in the RS as inferred from RS (x, y) and z and UTC z track hit coordinates
CHIRF_NHZ	the track particle does not scatter in the RS as inferred from RSSC and UTC z information
RSDEX	the energy deposit of the track particle in each RS counter is consistent with that of a pion
TGDEX	the energy deposit of the track particle in the target is consistent with that of a pion
PIGAP	there are no gaps in the pion track in the target
TGLIKE	the target track fit is of high quality
TGB4	the B4 hit position and target kaon fiber hit positions are consistent with propagation of a kaon
EICKIN	the measured IC energy is not greater than the energy loss expected from a charged pion track
MASS	the mass of the particle which created the charged track is $\leq 153 \text{ MeV}/c^2$, such that the charged track does not arise from low-energy (high mass) muons which have inelastically scattered in the RS

Table 4.6: PASS3 kinematic pathology cuts.

cut	pass condition
TGCCDPF	significant energy from the track particle is not hidden in target kaon fibers, as inferred from CCD information
EPITG	accidental energy does not overlap any target pion fibers
EPIMAXK	kaon energy does not spill into target pion fibers
PHIVTX	no back-to-back tracks are found in the target
PHIVTX2	no back-to-back tracks are found in the target
OPSVETO	no back-to-back energy from the π^+ and π^0 from $K_{\pi 2}$ is detected in the target
OPSVETO_LKB	no back-to-back energy from the charged pion and the charged lepton from K_L^0 decay is detected in the target
TGEDGE	significant energy from the track particle is not hidden in target edge fibers
TGQUALT	a kaon cluster and a pion track are reconstructed in the target
TGER	the energy and range of the track in the target are consistent with a pion (not a muon)
TARGF	no gap between the kaon cluster and the pion track
DTGTTP	the track in the target is well-matched to the track in the UTC
RTDIF	the uncertainty in the range of the track in the target is small
DRP	the track particle does not scatter in the target
TIMCON	the kaon times in the target and B4 hodoscope are consistent, and the pion times in the target and RS are consistent within measurement uncertainties
TIC	the times of the track in the IC and RS are consistent within measurement uncertainties
TGCCD	kaon fibers are assigned correctly (from CCD information)
EIC	the energy deposit in the IC is consistent with that of a charged pion track
KIC	a second beam particle does not enter an IC and overlap the first beam particle which stops in the same IC
TGGEO	a second beam particle does not enter an IC and overlap either the first beam particle which stops in the same IC, or the decay product of the first beam particle which enters the same IC
B4EKZ	the energy in the B4 hodoscope, UTC-extrapolated z in the target, and energy in the target are all consistent with that of a kaon stopping in the target
B4EKZ_IC	if there are no pion fibers in the target, then the B4EKZ cut requirement is made more stringent
TGZFOOL	the kaon must decay from inside the target
BHTRS	the track in the RS does not arise from a beam particle, based on the fact that there is no activity in the beam hole counter at track time

Table 4.7: PASS3 beam pathology cuts.

cut	pass condition
BAD_RUN	all hardware involved in data-taking was operational
BAD_STC	the TD pulse-area-to-MeV calibration is valid for the stopping counter

Table 4.8: PASS3 data quality cuts.

tance of the applied cut. A function cut can be loosened to define large N and A values, and tightened to define small N and A values (see sections C.3.3, C.3.4, C.3.5 and C.3.6). The N and A values are scaled such that the requirements $N \leq 1$ and $A \leq 1$ roughly correspond to the cut position(s) which gives the background level and acceptance, respectively, of a previous analysis of 1995 data [46]. For $K_{\pi 2}$ background, the $K_{\pi 2}$ kinematic function cut and the PV function cut (both described below) are the (uncorrelated) normalization and rejection function cuts, respectively. For $K_{\mu 2}$ background, the $K_{\mu 2}$ kinematic function cut and the TD function cut (both described below) are the (uncorrelated) normalization and rejection function cuts, respectively. Backgrounds need to be suppressed by an additional factor of 3 over the previous analysis, because there is roughly a factor of 3 more data in the combined 1995-7 data set. As stated in section 4.2, the rate-independent function cuts (e.g., the $K_{\pi 2}$ and $K_{\mu 2}$ kinematic function cuts) are therefore tightened by a factor of 3, whereas the rate-dependent function cuts (e.g., the PV and TD function cuts) stay at the same level of background suppression as the previous analysis, because the rate-dependent cuts have more loss in acceptance per gain in rejection than the rate-independent cuts. That is, events in the current analysis will be required roughly to have $K_{\pi 2}$ and $K_{\mu 2}$ kinematic function values $N \leq 0.33$, and PV and TD function values $N \leq 1.0$. Beam background and CEX functions are constructed somewhat differently, due to overlap between the 4 different types of beam background (single-beam kaon- and pion-entering, and double-beam kaon- and pion-entering), and the fact that the CEX background estimate is based on Monte Carlo data (see section 4.4.4). Finally, note that if a function has $A > 1.0$ at the $N = 1.0$ cut point, this corresponds to an “improvement” in the analysis, in that the current analysis has more acceptance than the previous analysis at the same level of background suppression.

The PV function is shown in figure 4.14 and tabulated in table C.3. It is plotted as N_{PV}

vs. A_{PV} , where N_{PV} is a measure of background level and A_{PV} is a measure of acceptance. Each point on the function corresponds to a set of time windows (around track time) and energy thresholds (minimum energy) in the barrel, EC, RS, target, IC, VC, CO, and CM for detection of individual photon hits (see section C.3.3). Events with $N_{PV} \leq 1.0$ are defined to pass the PV function cut, whereas events with $N_{PV} > 1.0$ fail. The cut can be made looser or tighter by varying the value of N_{PV} at which events are rejected (recall from section 4.2 that background is linear in N). Events can also be assigned a likelihood of having photon energy based on the value of N_{PV} .

The collection of PASS3 cuts identifying $\pi \rightarrow \mu \rightarrow e$ decays in the TD data of the stopping counter, referred to as the PASS3 TD cuts, are all used to construct the TD function. The PASS3 TD cuts are divided into “fixed” and “variable” cuts, where the fixed cuts are applied at one specific level of rejection to define a discrete range of function values $N_{TD} > 10$, and the variable cuts can be loosened or tightened in order to define a continuous range of function values $N_{TD} < 10$. Each TD cut is designed to attack one of the five types of TD background listed in table 4.1. The TD cuts and the backgrounds they attack are summarized in table 4.9. The TD function at $N_{TD} < 10$ is shown in figure 4.15 and tabulated in table C.4. Each point on the function for $N_{TD} < 10$ corresponds to a different value of the “pion likelihood”, as defined by a combination of the TDLIK2, TDLIK3, and TDDFA2 cuts (see section C.3.4). Events with $N_{TD} \leq 1.003$ are defined to pass the TD function cut, whereas events with $N_{TD} > 1.003$ fail.

The PASS3 $K_{\pi 2}$ and $K_{\mu 2}$ kinematic function cuts are listed and briefly described in table 4.10. The $K_{\pi 2}$ kinematic function is shown in figure 4.16 and tabulated in table C.5, where each point on the function corresponds to a specific lower limit on range, energy, and momentum values. Function values $N_{kin, K_{\pi 2}}$ decrease (become more signal-like) as range, energy, and momentum values increase away from the $K_{\pi 2}$ peak. Events with $N_{kin, K_{\pi 2}} \leq 0.3358$ are defined to pass the $K_{\pi 2}$ kinematic function cut (i.e., pass the BOX and BOX' cuts), whereas events with $N_{kin, K_{\pi 2}} > 0.3358$ fail. The $K_{\mu 2}$ kinematic function is shown in figure 4.17 and tabulated in table C.6, where each point on the function corresponds to a specific upper limit on values of momentum and $\chi(RP)$, where $\chi(RP)$ is the measured

N vs. A for the PV function

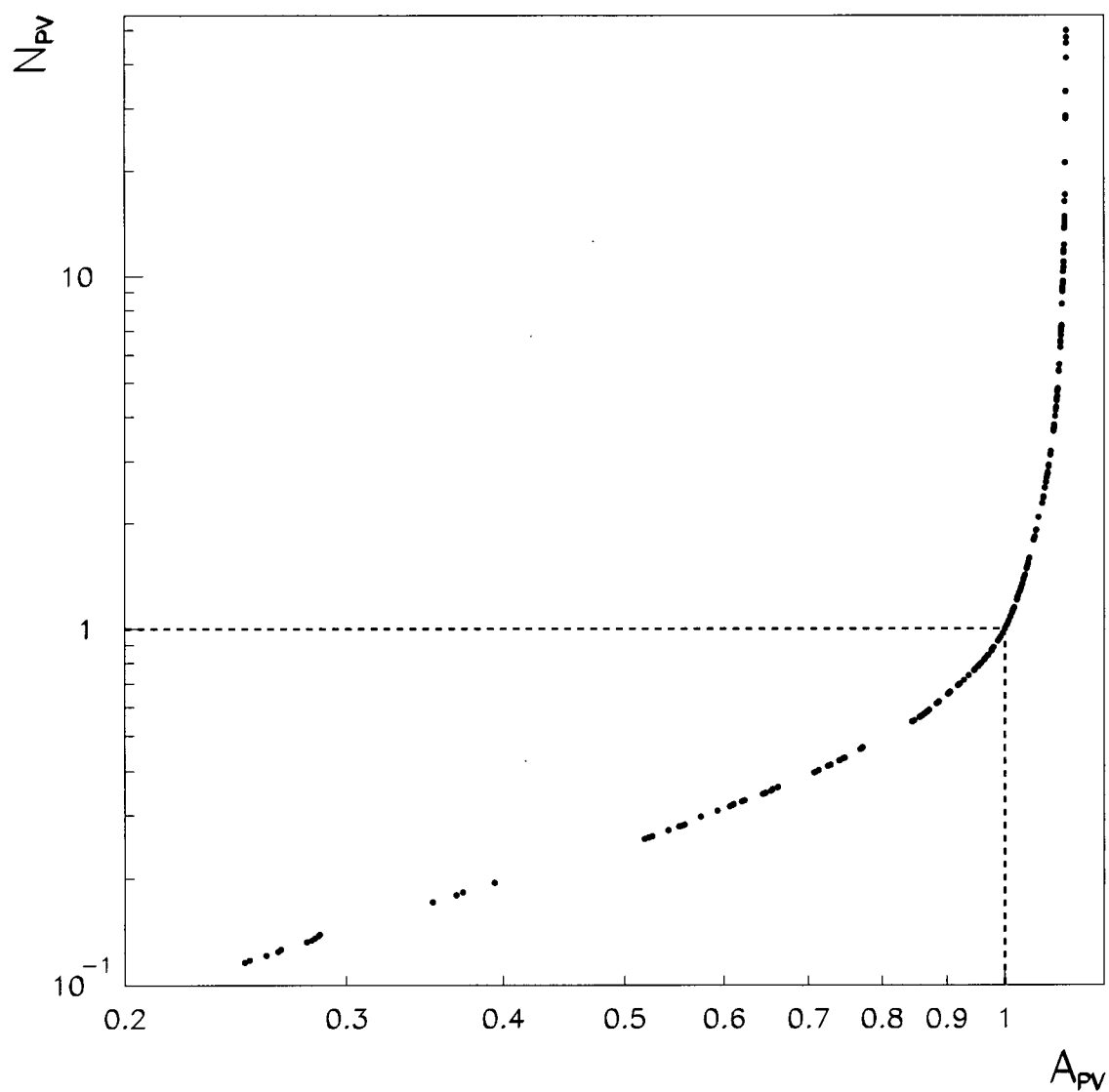


Figure 4.14: The PV function drawn as N_{PV} vs. A_{PV} . Events with $N_{PV} \leq 1.0$ (indicated by the dashed line) pass the PV function cut.

cut	background addressed	pass condition
fixed cuts:		
TDTCON	π -time accidental	the average RS track time is consistent with track time in the stopping counter
TDDFA1	tail-fluctuation	the $\pi \rightarrow \mu$ double-pulse fit in the stopping counter is of good quality
EV5	early μ decay	no accidental activity in the RS at e time
ELVETO	μ -time accidental	no accidental activity in RS or barrel at μ time
TDFOOL	μ -time accidental	no accidental activity along the RS track at μ time
TDECON	μ -time accidental	the TD and ADC stopping-counter π energies are consistent
TDVEL	GDR	the μ time vs. energy, i.e., "velocity" is not indicative of a GDR de-excitation neutron
variable cuts:		
TDLIK2	μ -time accidental	the μ pulse is unlikely to have arisen from an accidental
TDLIK3	early μ decay	the e pulse is unlikely to have arisen from an accidental
TDDFA2	tail-fluctuation	the $\pi \rightarrow \mu$ double-pulse fit in the stopping counter is of good quality

Table 4.9: PASS3 TD cuts.

N vs. A for the TD function

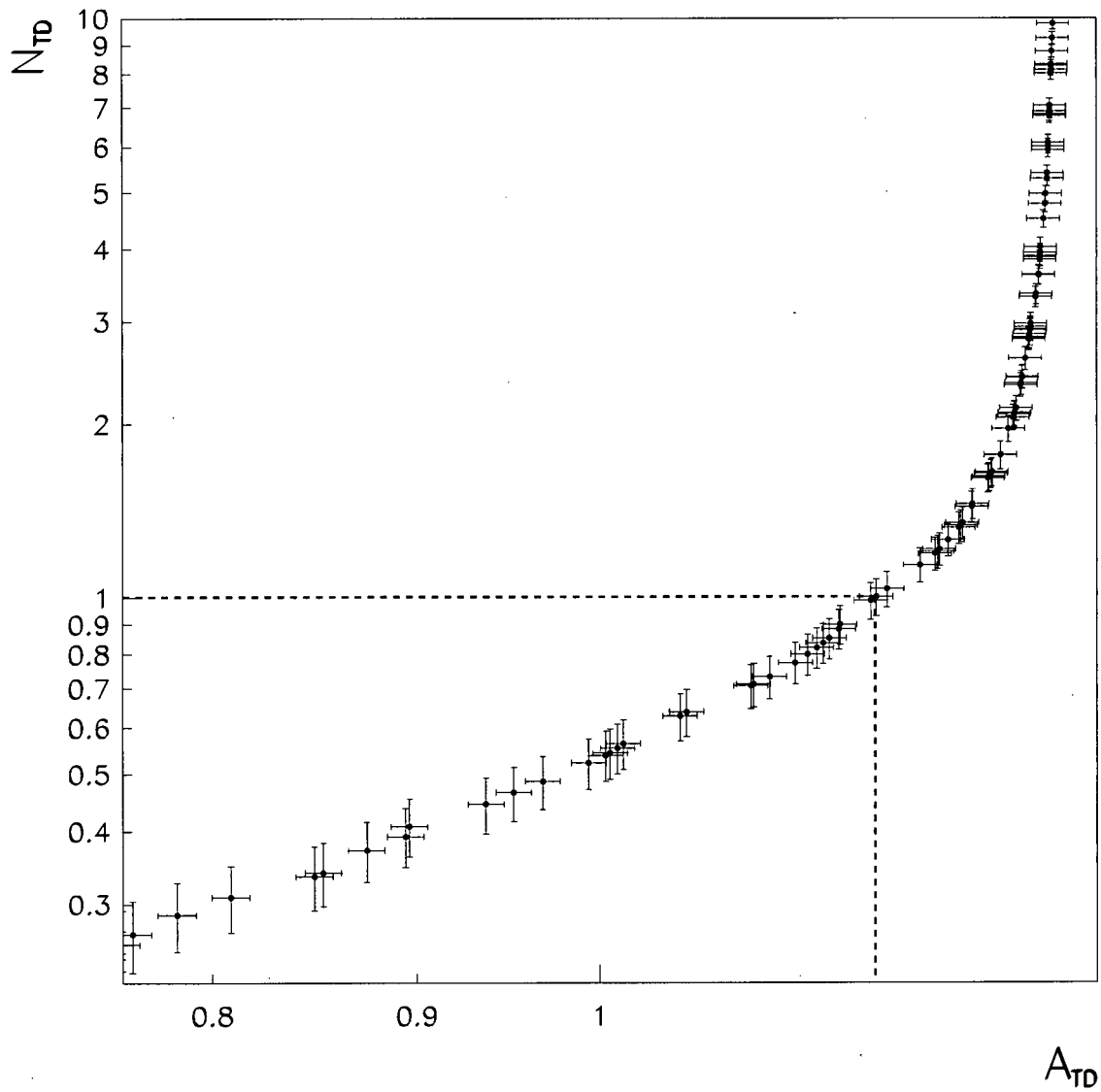


Figure 4.15: The TD function drawn as N_{TD} vs. A_{TD} . Events with $N_{TD} \leq 1.003$ (indicated by the dashed line) pass the TD function cut.

cut	pass condition
RNGMOM	the range-momentum correlation of the event places it outside the muon band (i.e., in the pion band)
BOX	range, energy, and momentum of the track fall between the $K_{\pi 2}$ and $K_{\mu 2}$ peaks (i.e., the RBOX, EBOX, and PBOX cuts combined)
RBOX	range of the track falls between the $K_{\pi 2}$ and $K_{\mu 2}$ peaks
EBOX	energy of the track falls between the $K_{\pi 2}$ and $K_{\mu 2}$ peaks
PBOX	momentum of the track falls between the $K_{\pi 2}$ and $K_{\mu 2}$ peaks
BOX'	range, energy, and momentum of the track, corrected for the polar angle, are larger than those of $K_{\pi 2}$ peak events (i.e., the RBOX', EBOX', and PBOX' cuts combined)
RBOX'	range of the track, corrected for the polar angle, is larger than that of $K_{\pi 2}$ peak events
EBOX'	energy of the track, corrected for the polar angle, is larger than that of $K_{\pi 2}$ peak events
PBOX'	range of the track, corrected for the polar angle, is larger than that of $K_{\pi 2}$ peak events

Table 4.10: PASS3 kinematic function cuts.

minus expected range in the RS, divided by the range resolution (see the description of the RNGMOM cut in section C.3.5). Function values $N_{kin,K_{\mu 2}}$ decrease (become more signal-like) as momentum values decrease away from the $K_{\mu 2}$ peak and $\chi(RP)$ values decrease away from the muon band towards the pion band. Events with $N_{kin,K_{\mu 2}} \leq 0.2681$ are defined to pass the $K_{\mu 2}$ kinematic function cut (i.e., pass the BOX and RNGMOM cuts), whereas events with $N_{kin,K_{\mu 2}} > 0.2681$ fail.

The PASS3 beam function cuts are listed and briefly described in table 4.11. For the single- and double-beam kaon- and pion-entering normalization and rejection functions, as well as the CEX function described below, the $N = 1.0, A = 1.0$ point is defined to give the standard level of background suppression in the current analysis (i.e., N and A are not scaled to the previous 1995 analysis like they are for the PV, TD, $K_{\pi 2}$ and $K_{\mu 2}$ kinematic functions). So events are defined to have $N \leq 1.0$ if they satisfy the requirements of the beam and CEX function cuts described in section C.3.6). The looser points ($N > 1.0$) on the single-beam kaon- and pion-entering normalization functions are found by loosening the requirements of the CKTRS, CKTAIL and CPITRS, CPITAIL cuts, respectively; the looser points on

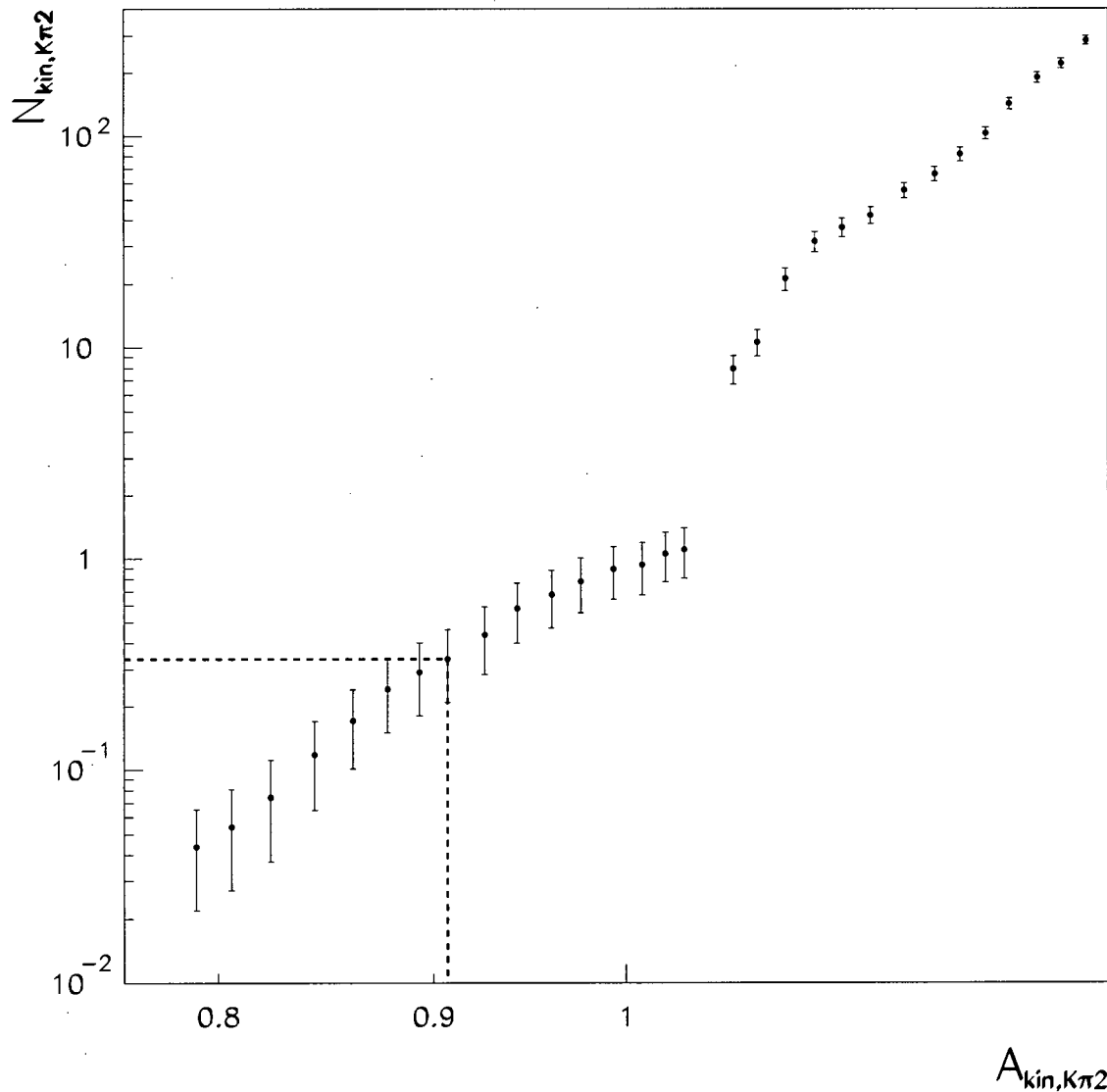
N vs. A for the $K_{\pi 2}$ kinematic function

Figure 4.16: The $K_{\pi 2}$ kinematic function drawn as $N_{kin,K\pi 2}$ vs. $A_{kin,K\pi 2}$. The “discontinuity” near $N_{kin,K\pi 2} = 1$ is due to the fact that $N_{kin,K\pi 2}$ values from 285.1 down to 0 are defined by tightening the BOX’ cut, which is a cut on R , E , and P corrected for polar angle of the track. Near $N_{kin,K\pi 2} = 1.0$ the BOX cut is also applied, in order to enforce hard cuts on R , E , and P independent of polar angle (see section C.3.5). Events with $N_{kin,K\pi 2} \leq 0.3358$ (indicated by the dashed line) pass the $K_{\pi 2}$ kinematic function cut.

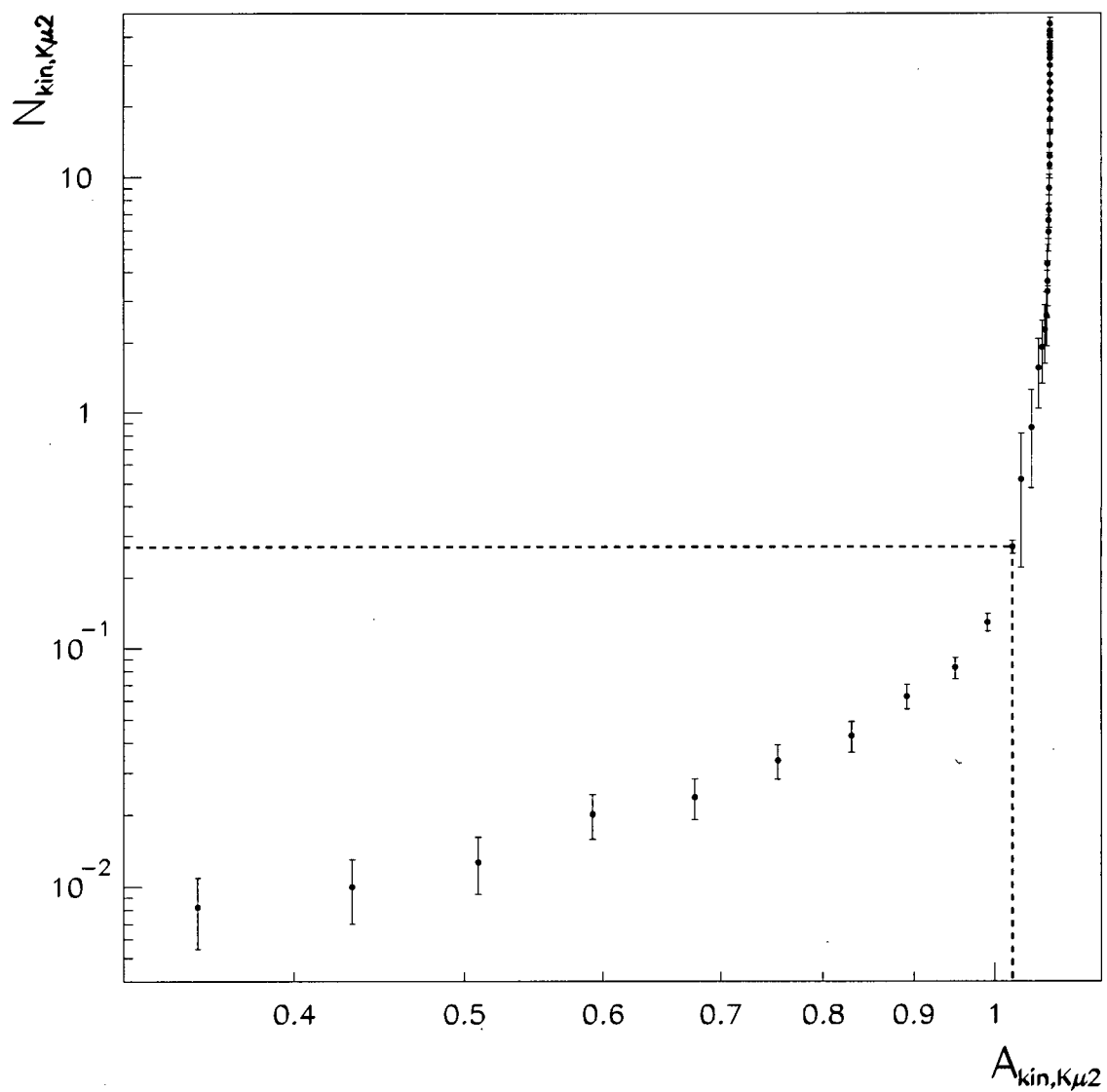
N vs. A for the $K_{\mu 2}$ kinematic function

Figure 4.17: The $K_{\mu 2}$ kinematic function drawn as $N_{kin,K\mu 2}$ vs. $A_{kin,K\mu 2}$. Events with $N_{kin,K\mu 2} \leq 0.2681$ (indicated by the dashed line) pass the $K_{\mu 2}$ kinematic function cut.

the single-beam kaon- and pion-entering rejection functions are both found by loosening the requirements of the DELC cut; the looser points on the double-beam kaon- and pion-entering normalization functions are found by loosening the requirements of the B4TRS, B4TD and B4TRS, B4TD, PBNRS cuts, respectively; and the looser points on the double-beam kaon- and pion-entering rejection functions are found by loosening the requirements of the BWTRS, CKTRS, CKTAIL and BWTRS, CPITRS, CPITAIL cuts, respectively (see section C.3.6). There is clearly some overlap in the cuts which are loosened to define the $N > 1.0$ range of function values, which makes definition of independent N values for each beam function difficult. The functions are loosened for the purposes of the outside-the-box correlation study (see sections 4.2 and 4.6), in which case all 4 types of beam background are re-measured and totalled each time a single beam function is loosened. The single-beam background is very small (see section 4.5), so it is not necessary to define tight single-beam function values in the range $N < 1.0$. The double-beam kaon- and pion-entering functions are combined into one function in order to define tight double-beam function values in the range $N_{BM2} < 1.0$. This function is shown in figure 4.18 and tabulated in table C.7, where each point on the function corresponds to a specific lower limit on the minimum absolute time of all BWC1 and BWC2 hits (excluding those associated with the event kaon) relative to track time in the RS (see the description of the BWTRS cut in section C.3.6). Function values decrease (become more signal-like) as the lower limit is raised. One CEX function is also defined at tight function values in the range $N_{CEX} < 1.0$, shown in figure 4.19 and tabulated in table C.8, where each point on the function corresponds to a specific lower limit on the kaon likelihood and decay time (see the descriptions of the B4EKZ and DELC cuts in sections C.3.2 and C.3.6, respectively). Function values decrease (become more signal-like) as the lower limit is raised.

4.4 Background Measurement Structure

As shown in figure 4.9, a bifurcated background estimate is given by $B/(R-1)$, where B is a “normalization” (the number of events which remain after application of all cuts except

cut	pass condition
DELC	the kaon decays from rest
BWTRS	the track in the RS does not arise from a beam particle, based on the fact that there is no activity in the beam wire chambers at track time
BWHRS	the track in the RS does not arise from a beam particle, based on the fact that there is no activity in the beam wire chambers at track time
CKTRS	the track in the RS does not arise from a kaon decaying in flight, based on the fact that there is no activity in the kaon Čerenkov counter at track time
CKTAIL	the track in the RS does not arise from a kaon decaying in flight, based on the fact that there is no activity in the kaon Čerenkov counter at track time
CPITRS	the track in the RS does not arise from a beam pion, based on the fact that there is no activity in the pion Čerenkov counter at track time
CPITAIL	the track in the RS does not arise from a beam pion, based on the fact that there is no activity in the pion Čerenkov counter at track time
PBNRS	the track in the RS does not arise from a beam pion, based on the fact that there is no activity in the active degrader at track time
B4DEDX	the energy deposit in the B4 hodoscope is consistent with a kaon (not a pion)
B4TRS	the track in the RS does not arise from a beam particle, based on the fact that there is no activity in the B4 hodoscope at track time
B4TD	the track in the RS does not arise from a beam particle, based on the fact that there is no activity in the B4 hodoscope at track time (from multiple-pulse TD information)

Table 4.11: PASS3 beam function cuts.

N vs. A for the BM2 function

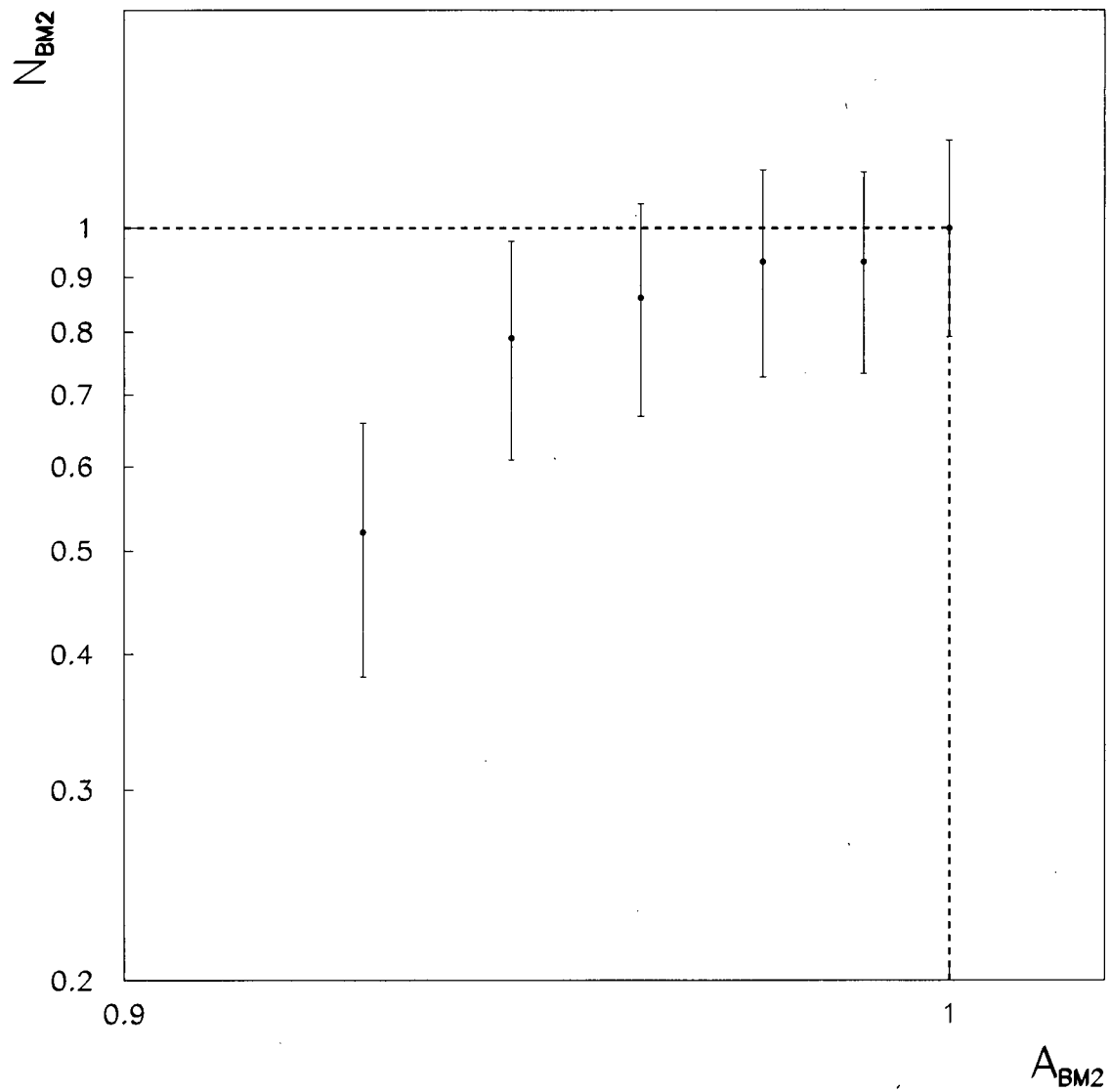


Figure 4.18: The double-beam function at $N_{BM2} \leq 1.0$, drawn as N_{BM2} vs. A_{BM2} . Events with $N_{BM2} \leq 1.0$ (indicated by the dashed line) pass the double-beam function cut.

N vs. A for the CEX function

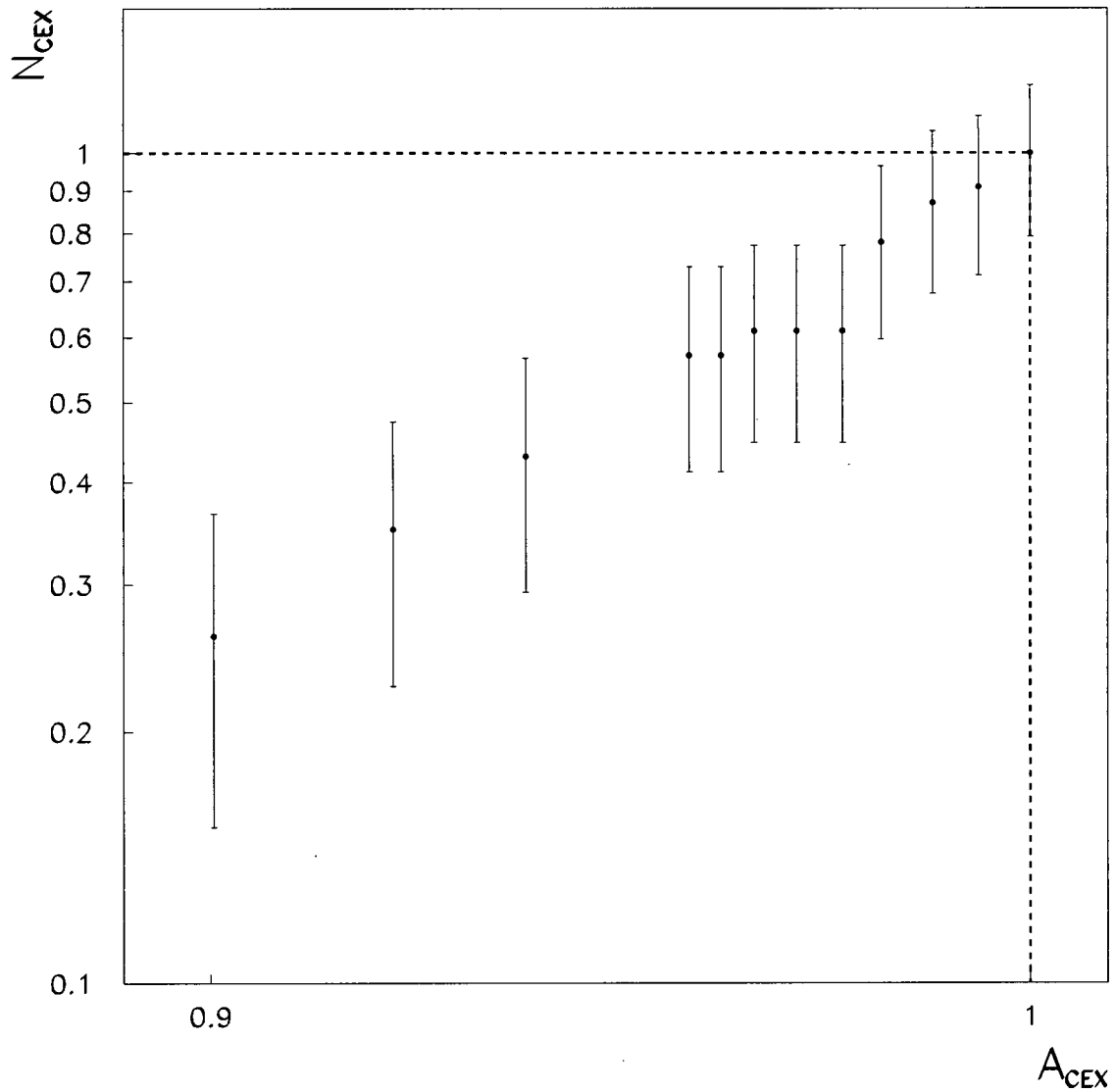


Figure 4.19: The CEX function at $N_{CEX} \leq 1.0$, drawn as N_{CEX} vs. A_{CEX} . Events with $N_{CEX} \leq 1.0$ (indicated by the dashed line) pass the CEX function cut.

one, which is inverted) and R is a “rejection” (the measured rejection of the inverted cut). The sequence of cuts applied to get the normalization is referred to as the “normalization branch”, and the sequence of cuts applied to measure the rejection is referred to as the “rejection branch” of a bifurcated analysis. It should be clear from figure 4.9 that the choice of which of the two bifurcated cuts is inverted to get the normalization and which is inverted to measure the rejection is arbitrary. The structures of the $K_{\pi 2}$, $K_{\mu 2}$, beam, and CEX background estimates are given below.

4.4.1 $K_{\pi 2}$ Decay

The structure of the PV-kinematic bifurcation used to estimate the $K_{\pi 2}$ background is shown in figure 4.20. The normalization is found by inverting the PV function cut and applying the $K_{\pi 2}$ kinematic function cut, and the measured rejection is that of the PV function cut. The validity of the bifurcated $K_{\pi 2}$ background measurement relies on the assumption that the PV and kinematic function cuts are uncorrelated. One potential mechanism of correlation is a photon from the π^0 “hiding” on the charged π^+ track. This would simultaneously make photons harder to find and upshift the energy of the π^+ track into the $\pi^+\nu\bar{\nu}(1)$ signal region. However, these correlated events are removed by applying the RSDEDX cuts (part of the kinematic pathology cuts described in section C.3.1) before the bifurcation is made (see figure 4.20), so that tracks with energy loss in the RS inconsistent with that of a single pion are completely removed from the analysis. In fact, the $K_{\pi 2}$ background estimation structure shown in figure 4.20 is designed so that, for events which survive to the bottoms of the normalization and rejection branches, any correlations between the detection of photons and kinematic upshifting of the π^+ should be small.

Note that in the normalization branch a second bifurcation is employed in order to enhance statistics. The PV function cut is inverted, all other cuts in the analysis are applied except for the low-side EBOX and EBOX' cuts, and the number of events remaining in the SKIM1 data sample, $B_{K_{\pi 2}}^{RP}$, is counted. The rejection of the low-side EBOX and EBOX' cuts is determined separately, by measuring the energy lineshape for events which pass loose

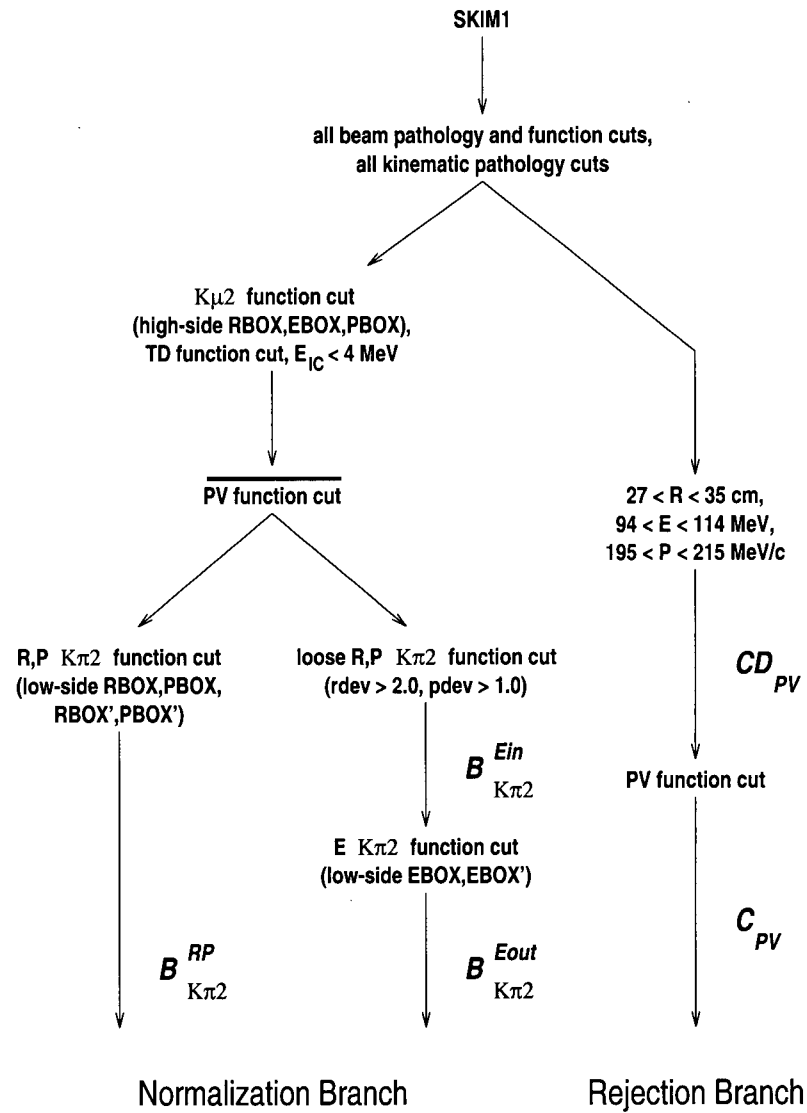


Figure 4.20: $K_{\pi 2}$ background estimation structure. The $B_{K_{\pi 2}}^i$ and C, CD_{PV} quantities refer to numbers of events remaining at various stages in the $K_{\pi 2}$ normalization and rejection branches, respectively, and correspond to the numbers of events in regions B, C, and C+D in figure 4.9, which are used to estimate the $K_{\pi 2}$ background level (see section 4.5). The TD function cut does not include TDECON or TDVEL (these cuts were developed late in the analysis). Note that some of the beam and kinematic pathology cuts and TD cuts are only applied to the 1996-7 data (see sections C.3.1, C.3.2 and C.3.4).

RBOX' and EBOX' cuts, namely, $rdev > 2.0$ and $pdev > 1.0$ (see section C.3.5). These cuts on R and P must be tight enough (i.e., near the box) such that correlations between energy and the other two kinematic quantities (mainly range) do not invalidate the second bifurcation. The $K_{\pi 2}$ kinematic normalization is then given by $B_{K_{\pi 2}}^{RP}$ divided by the rejection minus 1 of the EBOX and EBOX' cuts: $B_{K_{\pi 2}}^{Ein}/B_{K_{\pi 2}}^{Eout} - 1$.

The PV rejection is found using $K_{\pi 2}$ peak events in the SKIM1 data sample which fail the $K_{\pi 2}$ kinematic function cut. The PV rejection is found during optimization of the PV function as described in section C.3.3.

4.4.2 $K_{\mu 2}$ Decay

The structure of the TD-kinematic bifurcation used to estimate the $K_{\mu 2}$ background is shown in figure 4.21. Similar to the $K_{\pi 2}$ bifurcation, the normalization is found by inverting the TD function cut and applying the $K_{\mu 2}$ kinematic function cut, and the measured rejection is that of the TD function cut. The validity of the bifurcated $K_{\mu 2}$ background measurement relies on the assumption that the TD and kinematic function cuts are uncorrelated. One potential source of correlation is the GDR background mechanism described in section 4.1.1.1, which simultaneously creates a second pulse in the stopping counter consistent with $\pi \rightarrow \mu$ decay and downshifts the range and energy of the μ^+ track into the $\pi^+\nu\bar{\nu}(1)$ signal region. This correlation mechanism was found late in the analysis via the outside-the-box correlation study (see section 4.6), and appears to be significant only in the 1996-7 data, possibly due to the use of narrower TD pulse shapes for the $\pi \rightarrow \mu$ double-pulse fitting in the stopping counter (see section C.3.4). These correlated events are difficult to remove from the $K_{\mu 2}$ background estimation structure without a substantial loss of statistics, so they are suppressed to a negligible level by applying the MASS cut as a safety cut (see section C.3.1) and the TDVEL cut as part of the TD function cut (see section C.3.4). Another potential source of correlation is μ^+ tracks which exit the side of the RS, such that range and energy of the μ^+ track are downshifted into the $\pi^+\nu\bar{\nu}(1)$ signal region and, at the same time, an accidental "hidden" in the support structure of the RS leaves an isolated second pulse in

the apparent stopping counter. These correlated events are located at large z in the RS and/or have polar angles far from 90° (see Appendix D), so they are removed from the $K_{\mu 2}$ background estimation structure by applying the COS3D, ZFRF, and LAYER14 cuts (see section C.3.1). Moreover, the $K_{\mu 2}$ background estimation structure shown in figure 4.21 is designed so that, for events which survive to the bottoms of the normalization and rejection branches, any correlations between the detection of the second pulse in the stopping counter and kinematic downshifting of the μ^+ should be small.

The number of events at the bottom of the normalization branch in figure 4.21, $B_{K_{\mu 2}}^*$, is the number of $K_{\mu 2}$ background events which fail the TD function cut but pass all other cuts in the analysis (except the MASS cut, which is a safety cut for $K_{\mu 2}$ background). Most of these events have R and E values much smaller than, but P values very close to, the $K_{\mu 2}$ peak values. That is, these events appear to be $K_{\mu 2}$ range-tail events which have slightly small values of momentum. The small momentum values may be due to Gaussian resolution and/or non-Gaussian mismeasurement. $K_{\mu 2}$ background in the box is expected to arise from both the $K_{\mu 2}$ range tail and the muon band, so to estimate the contribution from the muon band, the PV function cut is removed from the normalization branch and the number of surviving muon-band events, $B_{\mu band}^{PVoff}$, is counted. The enhancement of the muon band due to non-application of the PV is measured using muon-band events with R , E , and P in the box, but failing the RNGMOM cut, and is found to be a factor of 2.3. The estimated number of muon band events at the bottom of the normalization branch is then $B_{\mu band} = B_{\mu band}^{PVoff} / 2.3$. The muon-band contribution was found to be small in the 1995 data, and no evidence of enhanced muon-band background was found in the 1996-7 data, so it was not explicitly measured for the 1996-7 data. The 1995 $K_{\mu 2}$ normalization is therefore given by $B_{K_{\mu 2}} = B_{K_{\mu 2}}^* + B_{\mu band}$, whereas the 1996-7 $K_{\mu 2}$ normalization is simply $B_{K_{\mu 2}}^*$.

For the 1/3 1995 $K_{\mu 2}$ normalization, statistics for range-tail events were enhanced by using a second bifurcation. This enhancement is achieved by not applying the high-side PBOX cut in the normalization branch of figure 4.21. Instead, $K_{\mu 2}(1)$ monitor events, which are composed almost entirely of $K_{\mu 2}$ peak events, are used to find the rejection of the high-side PBOX cut (similar to the measurement of the $K_{\mu 2}$ kinematic function – see section C.3.5).

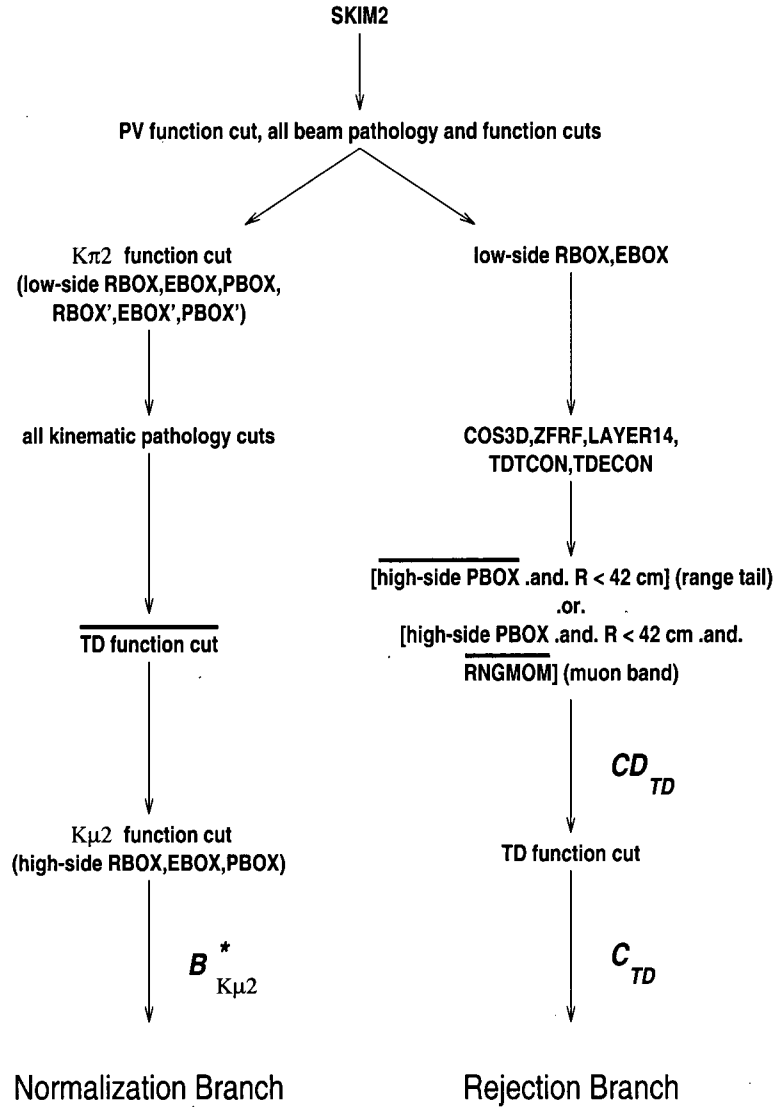


Figure 4.21: $K_{\mu 2}$ background estimation structure. The $B_{K_{\mu 2}}^*$ and C, CD_{TD} quantities refer to numbers of events remaining at various stages in the $K_{\mu 2}$ normalization and rejection branches, respectively, and correspond to the numbers of events in regions B, C, and C+D in figure 4.9, which are used to estimate the $K_{\mu 2}$ background level (see section 4.5). For the 1/3 1995 background estimate, a second bifurcation is employed in the normalization branch. For the 1/3 and 2/3 1995 and 1/3 1996-7 background estimates, $R < 45$ cm is used in the definition of $K_{\mu 2}$ range-tail and muon-band events; the PV function cut is not applied to the rejection branch; and the beam cuts do not include CKTRS or CKTAIL, and involve a loose DELC. More details can be found in section 4.4.2 of the text. The rejection of the TD function cut (as measured in the rejection branch) does not include the TDTCON and TDECON cuts: these are applied as pathology cuts, higher up in the rejection branch, because events failing these cuts can correlate TD and kinematic cuts which are bifurcated here to estimate the $K_{\mu 2}$ background. Note that some of the beam and kinematic pathology cuts and TD cuts are only applied to the 1996-7 data (see sections C.3.1, C.3.2 and C.3.4).

This second bifurcation gives a valid normalization because the momentum lineshape of $K_{\mu 2}$ range-tail events is not correlated with range (see figures 4.1 and 4.2) nor energy. The $K_{\mu 2}$ range-tail normalization for the 1/3 1995 data is then given by the number of events at the bottom of the normalization branch in figure 4.21 without the high-side PBOX cut applied, divided by the rejection of the high-side PBOX cut as found using $K_{\mu 2}(1)$ monitor data.

The rejection of the TD cuts is found by inverting the high-side PBOX cut and the RNGMOM cut on the SKIM2 data sample. The low-side RBOX and EBOX cuts are applied to remove $K_{\pi 2}$ events while maintaining statistics for muon-band events. The rejection measurements on 1/3 1995, 2/3 1995 and 1/3 1996-7 data were performed with all beam cuts applied except CKTRS and CKTAIL, and using a loose version of the DELC cut ($t_{\pi} - t_K \geq 1$ ns – see section C.3.6) in order to enhance statistics. $K_{\mu 2}$ range-tail and muon-band events were defined to have $R < 45$ cm. After the initial measurement of the TD rejection on the 1/3 1996-7 data sample, it was found that the TD rejection in the $K_{\mu 2}$ momentum peak is a strong function of range, varying from over 2000 for $R > 45$ cm to about 800 for $34 < R < 40$ cm (possibly due in part to the GDR background mechanism – see section 4.1.1.1). Also, after the TD rejection measurement on the 2/3 1996-7 data, the muon-band rejection was found to be a strong function of PV (roughly a factor of 2 worse rejection for events with E and R in the box if the PV function cut is applied). The TD rejection in the box is most accurately given by the rejection of $K_{\mu 2}$ range-tail events close to the box, and the rejection of muon-band events (radiative $K_{\mu 2}$ decays, $K_{\mu 3}$ decays, $K_{\mu 2}$ decay in flight, and/or $K_{\mu 2}$ decay with inelastic scattering in the target) after the full PV has been applied, so $K_{\mu 2}$ range-tail and muon-band events were re-defined to have $R < 42$ cm, and the PV function cut as well as the complete set of beam cuts were applied. For the reduced number of events which satisfy these criteria, the TD rejection for muon-band events is slightly worse than that for $K_{\mu 2}$ range-tail events [41], so the TD rejection in 1996-7 is estimated as the rejection of muon-band events with energy and range in the box, using muon-band events from both the 1/3 and 2/3 1996-7 SKIM2 data samples.

4.4.3 Beam Backgrounds

The structure of the bifurcation used to estimate the single-beam kaon-entering background is shown in figure 4.22. Many cuts are applied to select a pure sample of kaons decaying in flight. The normalization is found by inverting the DELC cut and applying the CKTRS, CKTAIL cuts, and the measured rejection is that of the DELC cut. However, the rejection of the DELC cut is measured using beam pions which scatter into the detector (selected by inverting the B4DEDX cut), not using kaons which decay in flight. This is because a sample of beam pion scatters is easy to define without using time information, and the time structure in various detector elements of a beam pion scatter should be similar to that of a kaon decaying in flight. The normalization and rejection branches therefore use completely different data samples and are believed to be uncorrelated. However, a second bifurcation between the CKTRS, CKTAIL and TD, PV function cuts is present in the normalization branch in order to enhance statistics, and to specifically select kaons in the beam which decay in flight. Therefore, the validity of the bifurcated single-beam kaon-entering background measurement relies on the assumption that the CKTRS, CKTAIL cuts are uncorrelated with the TD, PV function cuts with respect to single-beam kaon-entering background. This is expected to be the case because the CKTRS, CKTAIL cuts use beam-particle information from the Čerenkov counter, whereas the TD, PV function cuts mainly use decay-particle information from the RS, barrel, and EC. Note that the rejection of the DELC cut is measured 4 ways (in an attempt to enhance statistics): with and without the TD and kinematic cuts applied, each of these conditions with and without the BOX cut applied. The rejection of the DELC cut is taken as the most conservative (minimum) value of the 4 measurements.

The structure of the bifurcation used to estimate the single-beam pion-entering background is shown in figure 4.23. Many cuts are applied to select a pure sample of beam pions scattering into the detector. The normalization is found by inverting the DELC cut and applying the CPITRS, CPITAIL cuts, and the measured rejection is that of the DELC cut. The rejection of the DELC cut is measured using beam pions selected not by inverting the CPITRS, CPITAIL cuts, but rather by inverting the B4DEDX cut (similar to the single-

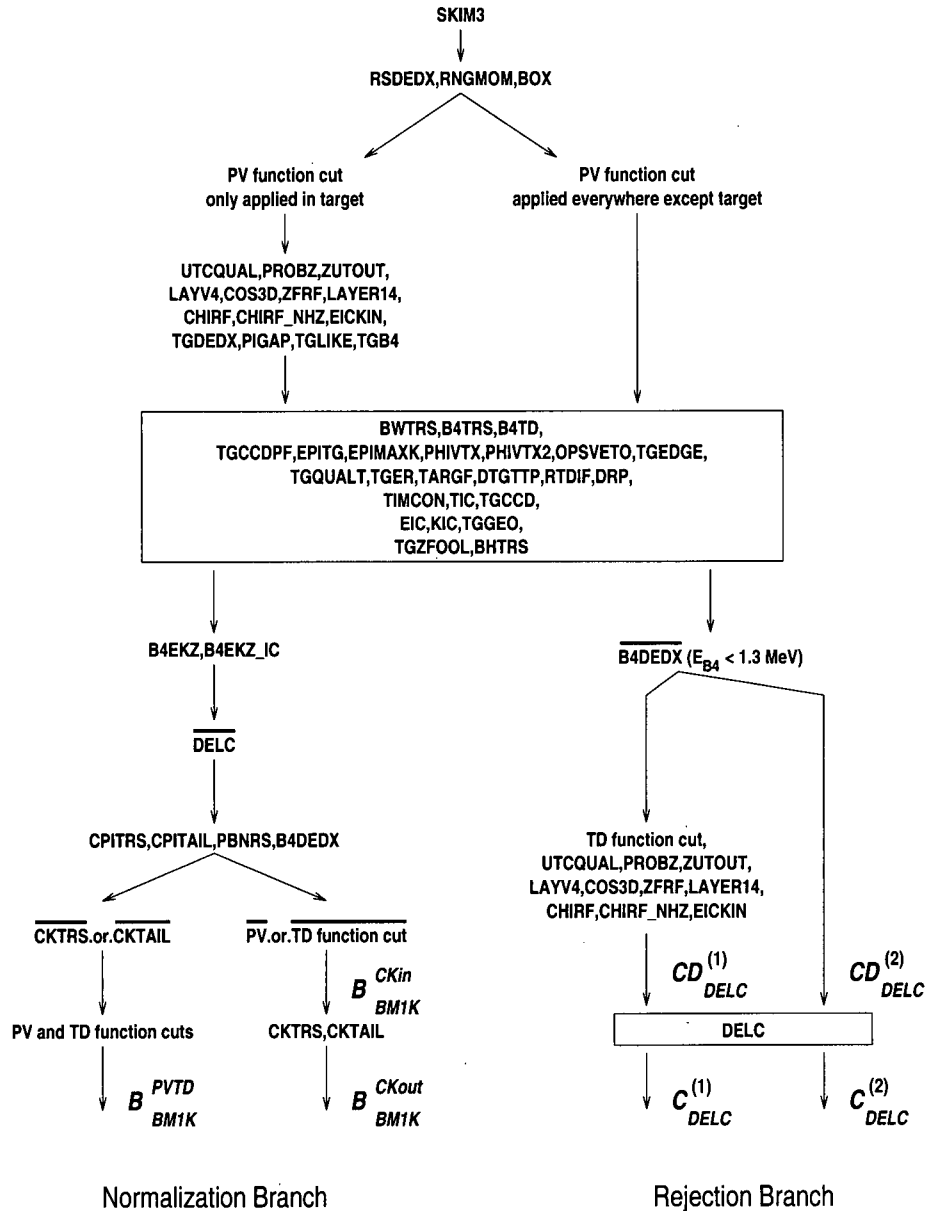


Figure 4.22: Single-beam kaon-entering background estimation structure. The B_{BM1K}^i and $C, CD_{DEL C}^k$ quantities refer to numbers of events remaining at various stages in the single-beam kaon-entering normalization and rejection branches, respectively, and correspond to the numbers of events in regions B, C, and C+D in figure 4.9, which are used to estimate the single-beam kaon-entering background level (see section 4.5). The TD function cut does not include TDECON or TDVEL (these cuts were developed late in the analysis). Note that some of the beam and kinematic pathology cuts and TD cuts are only applied to the 1996-7 data (see sections C.3.1, C.3.2 and C.3.4).

beam kaon-entering rejection branch), so the normalization and rejection branches would appear to be uncorrelated. However, a second bifurcation between the CPITRS, CPITAIL and PBNRS, B4DEDX cuts is present in the normalization branch in order to enhance statistics, and to specifically select pions in the beam which scatter into the detector. Therefore, the validity of the bifurcated single-beam pion-entering background measurement relies somewhat on the assumption that the CPITRS, CPITAIL cuts are uncorrelated with the DELC cut, as well as on the assumption that the CPITRS, CPITAIL cuts are uncorrelated with the PBNRS, B4DEDX cuts, with respect to single-beam pion-entering background. This is expected to be the case because the CPITRS, CPITAIL cuts use information from the Čerenkov counter, whereas the DELC, PBNRS, and B4DEDX cuts use information from the target, lead glass, and B4 counters, respectively, all of which are located downstream of the BeO degrader far from the Čerenkov counter. Note that the rejection of the DELC cut is measured 4 ways, similar to the measurement for single-beam kaon-entering background.

The structure of the bifurcation used to estimate the double-beam kaon-entering background is shown in figure 4.24. Many cuts are applied to select a pure sample of events which have a kaon detected in the beam not only at the kaon detection time, but also at kaon decay time. The normalization is found by inverting the CKTRS, CKTAIL, BWTRS cuts and applying the B4TRS, B4TD cuts, and the measured rejection is that of the CKTRS, CKTAIL, BWTRS cuts. The validity of the bifurcated double-beam kaon-entering background measurement relies on the assumption that the CKTRS, CKTAIL, BWTRS cuts are uncorrelated with the B4TRS, B4TD cuts with respect to double-beam kaon-entering background. This is expected to be the case because the CKTRS, CKTAIL, BWTRS cuts use information from the Čerenkov and beam wire counters, whereas the B4TRS, B4TD cuts use information from the B4 counter, which is located downstream of the BeO degrader far from the Čerenkov and beam wire counters.

The structure of the bifurcation used to estimate the double-beam pion-entering background is shown in figure 4.25. Many cuts are applied to select a pure sample of events which have a kaon detected in the beam, followed by a pion detected in the beam at kaon decay time. Similar to the double-beam kaon-entering background estimation structure, the normaliza-

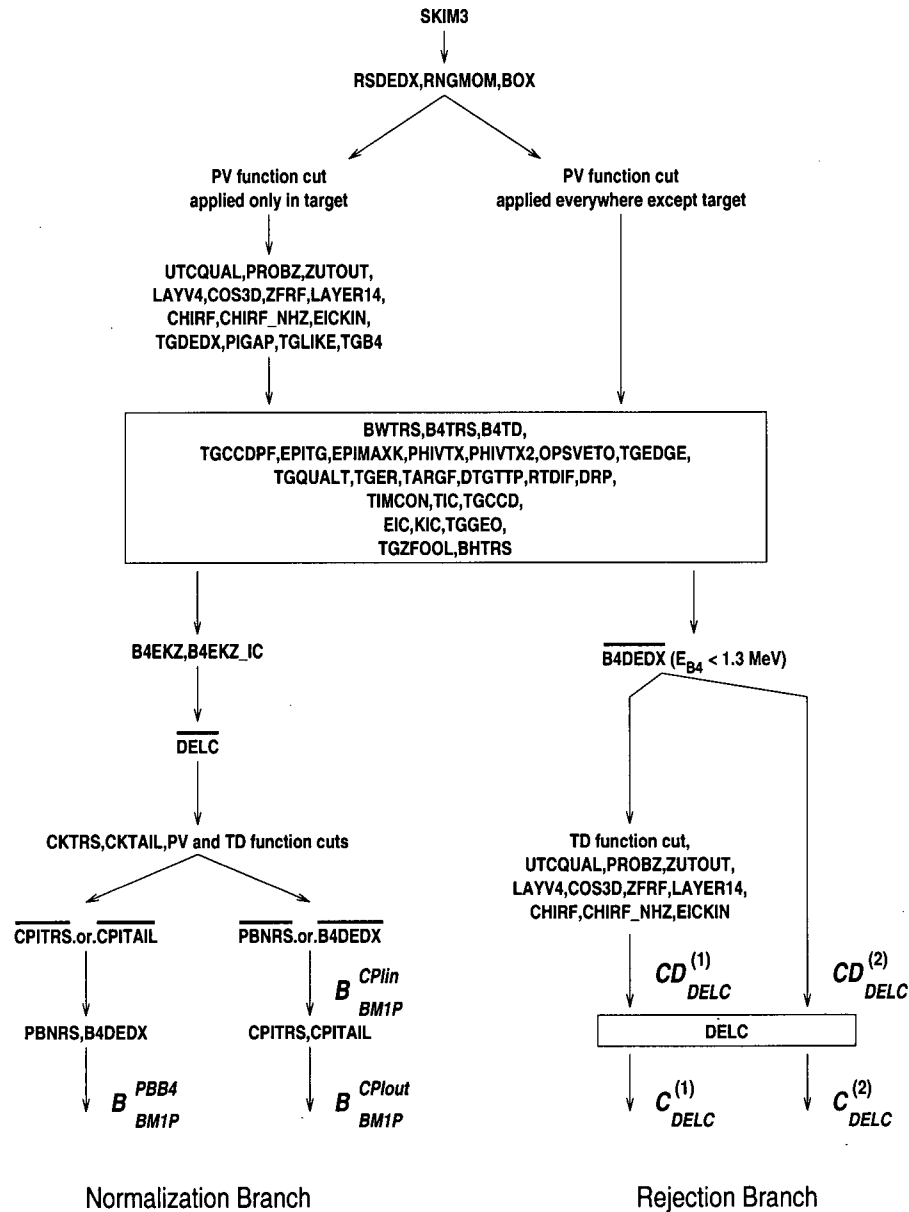


Figure 4.23: Single-beam pion-entering background estimation structure. The B^i_{BM1P} and $C, CD^k_{DEL C}$ quantities refer to numbers of events remaining at various stages in the single-beam pion-entering normalization and rejection branches, respectively, and correspond to the numbers of events in regions B, C, and C+D in figure 4.9, which are used to estimate the single-beam pion-entering background level (see section 4.5). The TD function cut does not include TDECON or TDVEL (these cuts were developed late in the analysis). Note that some of the beam and kinematic pathology cuts and TD cuts are only applied to the 1996-7 data (see sections C.3.1, C.3.2 and C.3.4).

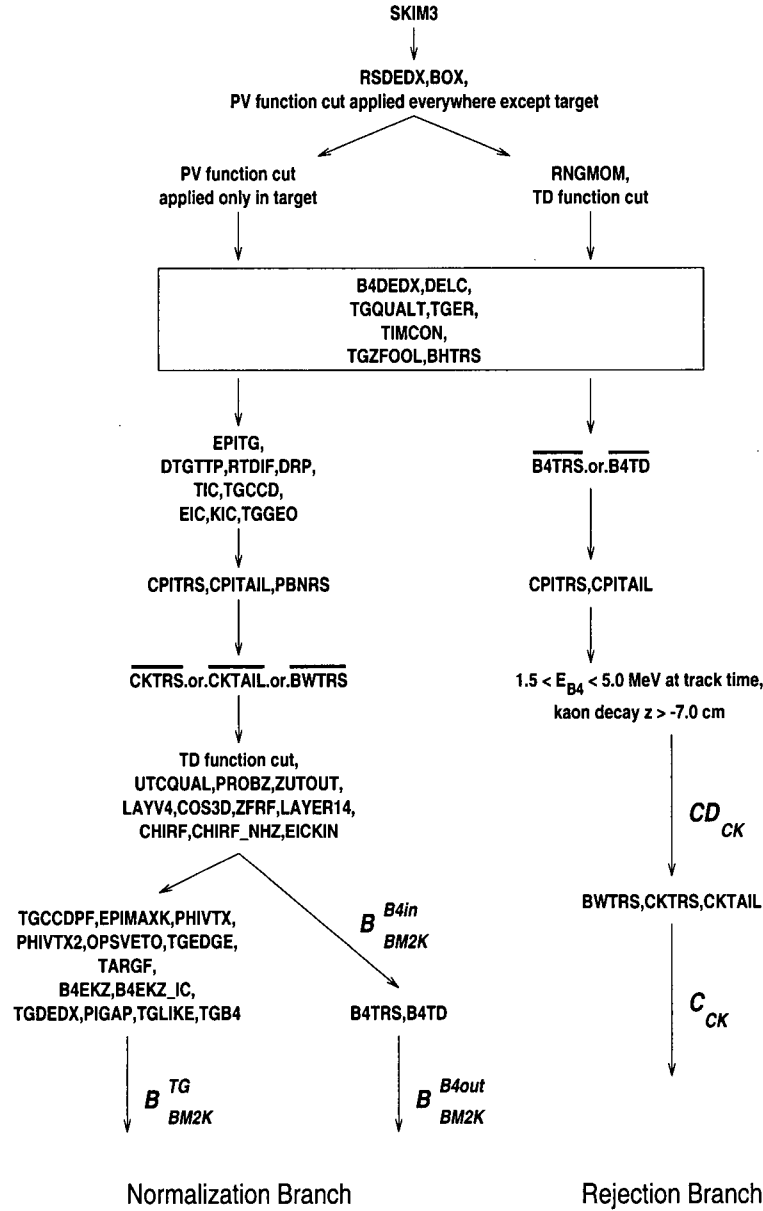


Figure 4.24: Double-beam kaon-entering background estimation structure. The B_{BM2K}^i and C, CD_{CK} quantities refer to numbers of events remaining at various stages in the double-beam kaon-entering normalization and rejection branches, respectively, and correspond to the numbers of events in regions B, C, and C+D in figure 4.9, which are used to estimate the double-beam kaon-entering background level (see section 4.5). The second bifurcation between target and B4 cuts in the normalization branch, and the requirement that the UTC-extrapolated kaon-decay z be more downstream than -7.0 cm in the rejection branch, are only used for the 1996-7 background estimates. More details can be found in section 4.4.3 of the text. The TD function cut does not include TDECON or TDVEL (these cuts were developed late in the analysis). Note that some of the beam and kinematic pathology cuts and TD cuts are only applied to the 1996-7 data (see sections C.3.1, C.3.2 and C.3.4).

tion is found by inverting the CPITRS, CPITAIL, BWTRS cuts and applying the B4TRS, B4TD, PBNRS cuts, and the measured rejection is that of the CPITRS, CPITAIL, BWTRS cuts. The validity of the bifurcated double-beam pion-entering background measurement relies on the assumption that the CPITRS, CPITAIL, BWTRS cuts are uncorrelated with the B4TRS, B4TD, PBNRS cuts with respect to double-beam pion-entering background. This is expected to be the case because the CPITRS, CPITAIL, BWTRS cuts use information from the Čerenkov and beam wire counters, whereas the B4TRS, B4TD, PBNRS cuts use information from the B4 and lead glass counters, which are located downstream of the BeO degrader far from the Čerenkov and beam wire counters.

A second bifurcation between target cuts and B4 timing cuts is used in the double-beam kaon- and pion-entering normalization branches in order to enhance statistics. This bifurcation is valid only if the KIC and TGCEO cuts (see section C.3.2) are applied earlier in the normalization branches in order to remove events which potentially correlate target and B4 cuts. For example, a “KIC” event is shown in figure 4.26, where a beam particle stops in an IC at $t = 1.6$ ns, leaving a large energy pulse (27 MeV) which, after discrimination, can be up to 80 ns wide. This initial beam particle therefore “masks out” the IC TDC hit of a second beam particle which enters the target 49 ns later through the same IC and propagates or decays in flight out the other side of the target. A “TGCEO” event is shown in figure 4.27. IC TD and target CCD information indicate that the first kaon stops at the target edge leaving a large energy pulse in a target fiber (39 MeV), then decays at 19 ns with the decay product leaving a large energy pulse in an IC (23 MeV). TDC hits in the kaon stopping fiber and IC are masked out for up to 80 ns, so that a second particle which enters the target at 46 ns near the decay point of the first kaon is not detected. These types of events tend to pass both target and B4 cuts, because only one particle plus apparent decay product can be seen in the target, and the second beam particle enters the target near the target edge, thereby missing the B4 hodoscope. Events in the double-beam kaon- and pion-entering normalization branches which fail the TGCEO cut were discovered after the 1/3 and 2/3 1995 background estimates had already been made, so the TGCEO cut is applied as a pathology cut in the beam background estimate only for 1996-7 data. It is

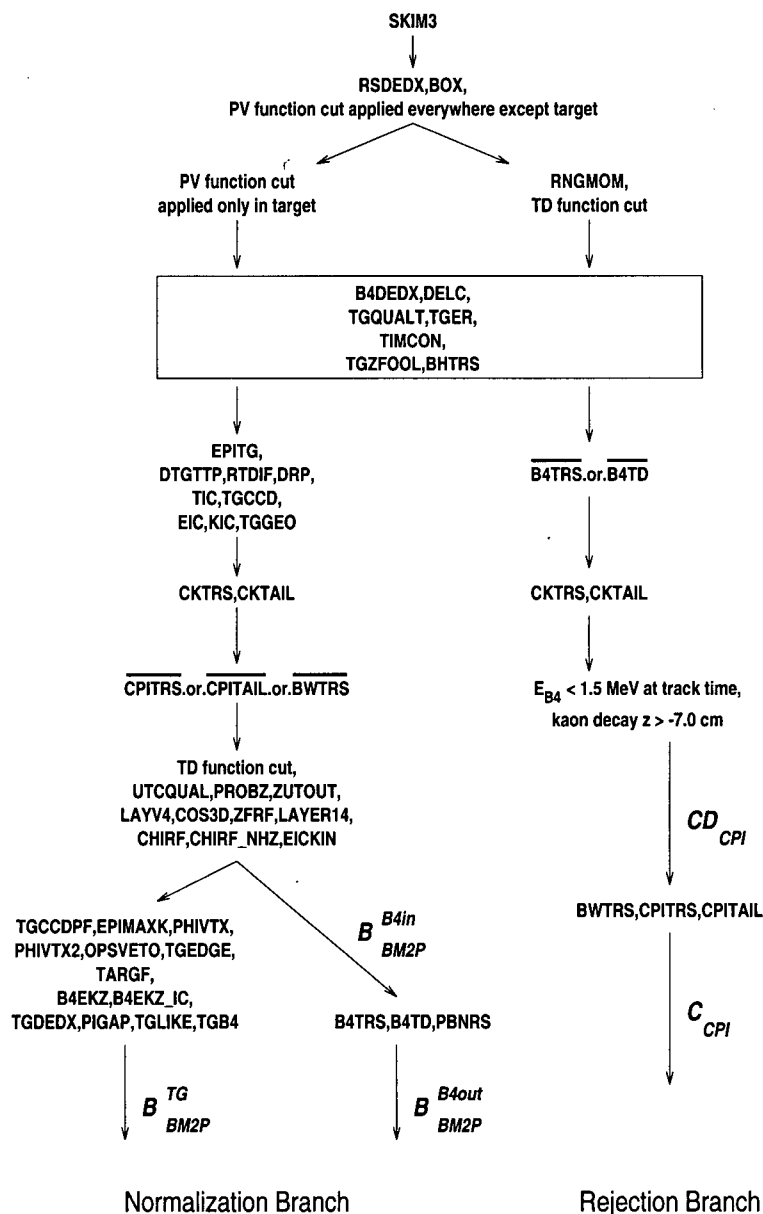


Figure 4.25: Double-beam pion-entering background estimation structure. The B_{BM2P}^i and C, CD_{CPI} quantities refer to numbers of events remaining at various stages in the double-beam pion-entering normalization and rejection branches, respectively, and correspond to the numbers of events in regions B, C, and C+D in figure 4.9, which are used to estimate the double-beam pion-entering background level (see section 4.5). The second bifurcation between target and B4 cuts in the normalization branch, and the requirement that the UTC-extrapolated kaon-decay z be more downstream than -7.0 cm in the rejection branch, are only used for the 1996-7 background estimates. More details can be found in section 4.4.3 of the text. The TD function cut does not include TDECON or TDVEL (these cuts were developed late in the analysis). Note that some of the beam and kinematic pathology cuts and TD cuts are only applied to the 1996-7 data (see sections C.3.1, C.3.2 and C.3.4).

applied as a safety cut to the 1995 data. Therefore, the second bifurcation is skipped in 1995: the target and B4 cuts are applied sequentially, and the number of surviving events counted to get the double-beam normalization directly. Note however that the TGCEO cut is ultimately applied to the 1995 data, so the actual beam background level in 1995 may be lower than estimated, i.e., closer to the second-bifurcated result than to the non-second-bifurcated result. Furthermore, with only KIC applied, correlations between target and B4 cuts appear to be small [41]. Nevertheless, the more conservative (no second bifurcation) result is used for the 1995 beam background estimate.

The double-beam kaon-entering rejection of the CKTRS, CKTAIL, BWTRS cuts and pion-entering rejection of the CPITRS, CPITAIL, BWTRS cuts are measured in 2 ways: with the BOX cut, and with only the low-side BOX cut applied in an attempt to enhance statistics. The more conservative (minimum) value of rejection is used. The events which remain at the bottom of the rejection branch appear to arise from B4 “splashes”, where the kaon decays near the upstream edge of the target and leaves photon or delta-ray energy in the B4 counter, thereby causing the event to fail the B4TRS or B4TD cut but pass the BWTRS, CKTRS/CPITRS, CKTAIL/CPITAIL cuts. Because this contamination was only discovered after the 1/3 and 2/3 1995 background estimates had already been made, these events are partially removed only from the 1996-7 background estimation structure, while maintaining good statistics, by requiring that the UTC-extrapolated z position of kaon decay in the target be more downstream than -7.0 cm. Roughly 1/3 of the events which otherwise survive the rejection branch are removed by this requirement.

4.4.4 Kaon Charge Exchange

The kaon charge exchange background estimate does not involve a bifurcation like the $K_{\pi 2}$, $K_{\mu 2}$, and beam background estimates above, because a sample of $K_L^0 \rightarrow \pi^+ l^- \bar{\nu}_l$ decays is difficult to extract from the data. Instead, Monte Carlo data is generated with arbitrary statistics, to which all cuts are applied in order to estimate the remaining CEX background level.

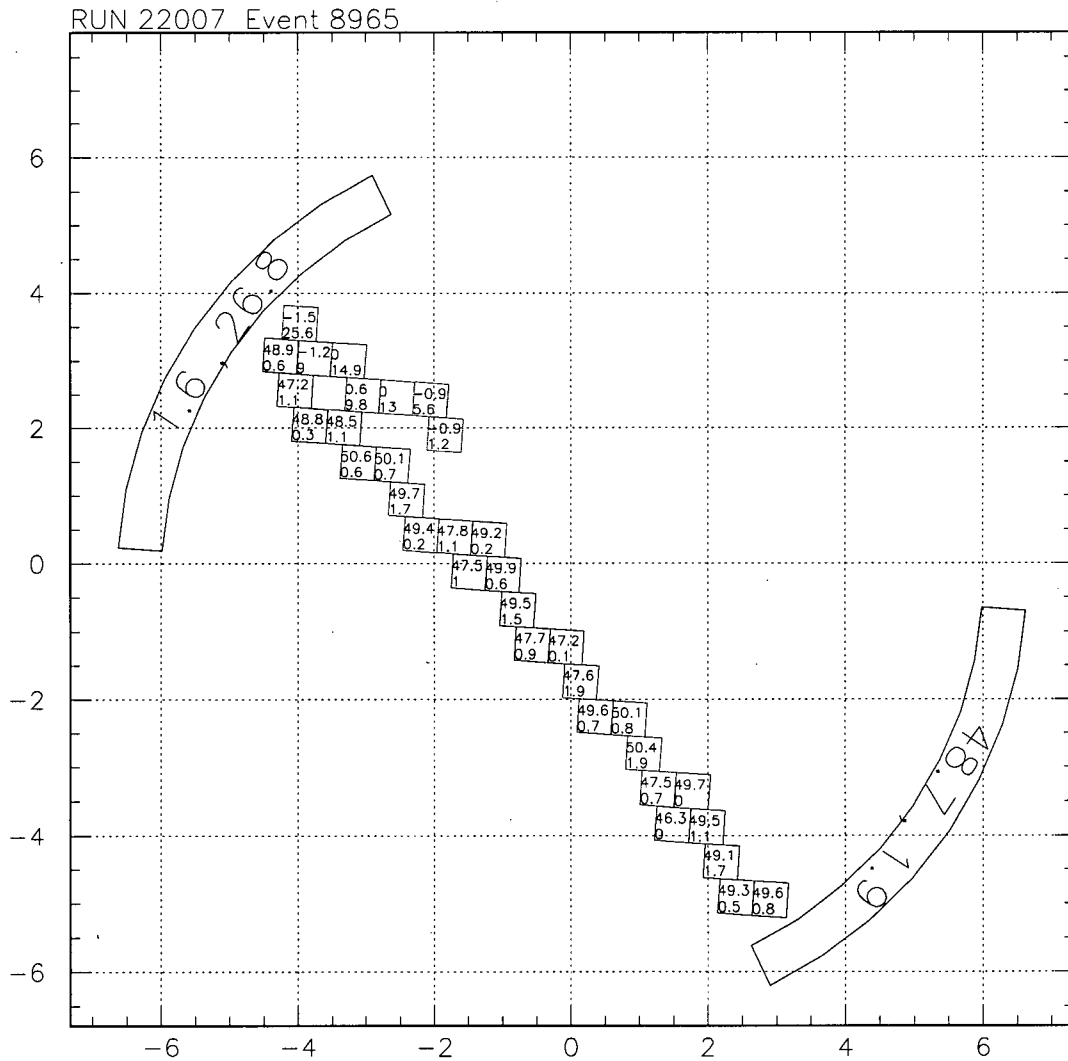


Figure 4.26: Target and IC displays of the “KIC” event. The top and bottom numbers in each target fiber, and the left and right numbers in each IC, are the time (ns) and energy (MeV) of each hit, respectively.

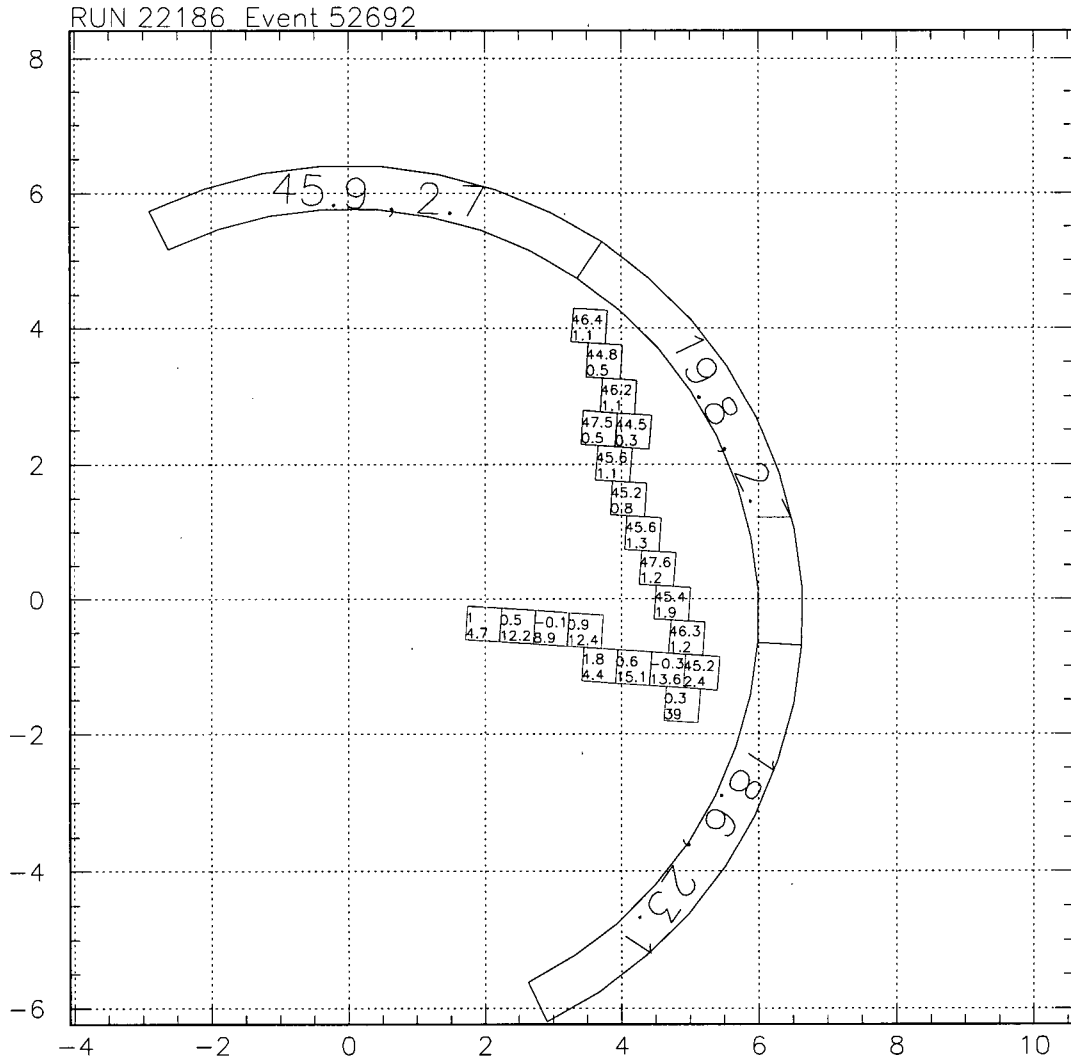


Figure 4.27: Target and IC displays of the “TGCEO” event. The top and bottom numbers in each target fiber, and the left and right numbers in each IC, are the time (ns) and energy (MeV) of each hit, respectively.

$K_S^0 \rightarrow \pi^+\pi^-$ decay, with its two-body final state, has a clearly identifiable signature (unlike $K_L^0 \rightarrow \pi^+\nu\bar{\nu}$ decay), so the K_L^0 production rate, momentum spectrum, decay vertex distribution, and pattern of target kaon fiber times and energies is taken from the measured K_S^0 quantities, found using data collected with a K_S^0 trigger [54]. This trigger is similar to the $K_{\pi_2}(2)$ trigger shown in section 3.3, but with the DC requirement inverted, two T · 2 coincidences required, and the online PV applied. Background from K_L^0 is expected only to be significant for “slow” K_L^0 ’s ($P < 100$ MeV/c), and the production rate for these K_L^0 ’s is approximated by

$$R_{K_L^0} = \frac{M_{K_S^0}(P < 100\text{MeV}/c)}{\epsilon_{K_S^0} \cdot A_{PV} \cdot B(K_S^0 \rightarrow \pi^+\pi^-) \cdot K_{Blive}/PS} \quad (4.1)$$

where $M_{K_S^0}(P < 100\text{MeV}/c)$ is the number of reconstructed $K_S^0 \rightarrow \pi^+\pi^-$ decays passing the $K^+ \rightarrow \pi^+\nu\bar{\nu}$ trigger with $P < 100$ MeV/c; $\epsilon_{K_S^0}$ is the $K_S^0 \rightarrow \pi^+\pi^-$ reconstruction efficiency (online + offline cuts) for K_S^0 ’s produced with $P < 100$ MeV/c (0.082); A_{PV} is the acceptance of the online PV due to accidentals (0.75); $B(K_S^0 \rightarrow \pi^+\pi^-)$ is the $K_S^0 \rightarrow \pi^+\pi^-$ branching ratio (0.686); K_{Blive} is K_B from section 3.3, corrected by the online trigger deadtime; and PS is the online K_S^0 trigger prescale. This production rate is measured to be $R_{K_L^0} = 4.51 \times 10^{-5}$ [54].

The above quantities measured using K_S^0 data are input into a Monte Carlo simulation which generates $K_L^0 \rightarrow \pi^+\mu^-\bar{\nu}_\mu$ ($K_{\mu 3}^0$) and $K_L^0 \rightarrow \pi^+e^-\bar{\nu}_e$ ($K_{e 3}^0$) decays. To increase the speed of UMC event generation, (1) events are discarded where the K_L^0 leaves the target before decaying; (2) only semi-leptonic K_L^0 decays with a π^+ in the final state are accepted; (3) the final state π^+ must have $P > 190$ MeV/c, and the final state μ^- or e^- must have $P > 100$ MeV/c or $P > 30$ MeV/c, respectively. The equivalent UMC K_{Blive} is then the number of K_L^0 events generated, multiplied by the rejection of conditions (1), (2) and (3), divided by the production rate $R_{K_L^0}$. Only the final cuts that are meaningful for UMC data (i.e., all cuts except for TD cuts and some beam cuts – see section 3.2.6) are applied to the UMC CEX data [41], and the number of remaining events normalized to K_{Blive} of the $K^+ \rightarrow \pi^+\nu\bar{\nu}$ data. The CEX background for the 1995 data is therefore calculated as follows:

$$\begin{aligned}
bg_{CEX}(1995) &= \left(M_{pass}^{K_{e3}^0} \times \frac{K_{Blive}(1995) \times 0.588}{K_{Blive}(UMC, K_{e3}^0)} + \right. \\
&\quad \left. M_{pass}^{K_{\mu 3}^0} \times \frac{K_{Blive}(1995) \times 0.412}{K_{Blive}(UMC, K_{\mu 3}^0)} \right) \times \frac{A_{tot}^{data}}{A_{trig} \times A_{\pi^+\nu\bar{\nu}}^{umc}} \\
&= \left(18 \times \frac{1.53 \times 10^{12} \times 0.588}{7.8821 \times 10^{14}} + \right. \\
&\quad \left. 5 \times \frac{1.53 \times 10^{12} \times 0.412}{1.6592 \times 10^{14}} \right) \times \frac{0.00256}{0.1197 \times 0.1886} \\
&= 0.0045 \text{ events}
\end{aligned} \tag{4.2}$$

where $M_{pass}^{K_{e3}^0}$ and $M_{pass}^{K_{\mu 3}^0}$ are the numbers of UMC-generated K_{e3}^0 and $K_{\mu 3}^0$ events, respectively, that pass all applied cuts; $K_{Blive}(UMC, K_{e3}^0)$ and $K_{Blive}(UMC, K_{\mu 3}^0)$ are the “equivalent” K_{Blive} quantities for UMC-generated K_{e3}^0 and $K_{\mu 3}^0$ events, respectively, as described above; $K_{Blive}(1995)$ is K_{Blive} from the 1995 $K^+ \rightarrow \pi^+\nu\bar{\nu}$ data; 0.588 and 0.412 represent the relative branching ratios for $K_L^0 \rightarrow \pi^+e^-\bar{\nu}_e$ and $K_L^0 \rightarrow \pi^+\mu^-\bar{\nu}_\mu$; A_{trig} is the UMC-measured $K^+ \rightarrow \pi^+\nu\bar{\nu}$ trigger acceptance; $A_{\pi^+\nu\bar{\nu}}^{umc}$ is the combined acceptance of the cuts which are applied to the CEX UMC data, as measured using $K^+ \rightarrow \pi^+\nu\bar{\nu}$ UMC data; and A_{tot}^{data} is the total acceptance for the $K^+ \rightarrow \pi^+\nu\bar{\nu}$ analysis. The factor $A_{tot}^{data}/(A_{trig} \times A_{\pi^+\nu\bar{\nu}}^{umc})$ is simply a correction for $K^+ \rightarrow \pi^+\nu\bar{\nu}$ acceptance loss which is not modelled by UMC (TD cuts, PV accidental loss, beam cuts, etc.). The values of A_{tot}^{data} , A_{trig} , and $A_{\pi^+\nu\bar{\nu}}^{umc}$ in the above equation for $bg_{CEX}(1995)$ are taken from a previous analysis [46].

The CEX background level for 1996-7 data is calculated by normalizing the 1995 result to the 1996-7 K_{Blive} :

$$bg_{CEX}(1996-7) = 0.0045 \times \frac{1.7 \times 10^{12}}{1.5 \times 10^{12}} = 0.0051 \text{ events.} \tag{4.3}$$

An event which fails only the TGDEDX cut was found after examination of the entire 1996-7 data sample (as part of the outside-the-box tests – see section 4.6). The target display of this event is shown in figure 4.28. Because the pion track appears to originate away from the kaon stopping position, the event could be interpreted as a K^+ entering the target and undergoing CEX near $t = 0$ ns, followed by invisible propagation of K_L^0 and subsequent $K_L^0 \rightarrow \pi^+l^-\bar{\nu}_l$ decay near $t = 6$ ns. The existence of this event could

indicate a loophole in the CEX background estimate, because the CEX background estimate is $\ll 1$ event in the box even if the TGDEDX cut is turned off. To check whether or not a serious loophole exists, several cuts effective for CEX background are removed or loosened (to enhance statistics), and the number of events remaining in UMC and real data are compared. No serious discrepancies are found [41]. Nevertheless, the OPSVETO_LKB safety cut (see section C.3.2) is added to suppress the CEX background further.

4.5 Background Measurement Results

The $K_{\pi 2}$ and $K_{\mu 2}$ background estimates, and the numbers of events B_j^i and C, CD_l from figures 4.20 and 4.21, are shown in table 4.12 for each of the 1/3 and 2/3 1995 and 1996-7 data sets. As shown in figure 4.9, the $K_{\pi 2}$ and $K_{\mu 2}$ background levels are given by $bg_{K_{\pi 2}} = B_{K_{\pi 2}}/(R_{PV} - 1)$ and $bg_{K_{\mu 2}} = B_{K_{\mu 2}}/(R_{TD} - 1)$, respectively, where the $K_{\pi 2}$ normalization is given by $B_{K_{\pi 2}} = B_{K_{\pi 2}}^{RP}/(B_{K_{\pi 2}}^{E_{in}}/B_{K_{\pi 2}}^{E_{out}})$ (see section 4.4.1 and figure 4.20) and the $K_{\mu 2}$ normalization is given by $B_{K_{\mu 2}} = B_{K_{\mu 2}}^* (+B_{\mu band}^{PVoff}/2.3)$ for 1996-7 (1995) data. $B_{K_{\mu 2}}$ for the 1/3 1995 data set also involves a second bifurcation of kinematic quantities (cuts on P are bifurcated with cuts on R and E) in order to enhance statistics from the $K_{\mu 2}$ range tail (see section 4.4.2 and figure 4.21). The rejection of the PV function cut was estimated with high statistics using the 1/3 1995 data, and confirmed on the 2/3 1995 and 1/3 1996-7 data samples. It is listed as $R_{PV} = 50.1 \pm 1.1$ in table 4.12. The rejection of the TD function cut is given by $R_{TD} = CD_{TD}/C_{TD}$ (see section 4.4.2 and figure 4.21). If any B_j^i or C, CD_l quantity is 0, it is taken to be 1 when calculating the background level. The $K_{\pi 2}$ and $K_{\mu 2}$ background levels, listed as $bg_{K_{\pi 2}}$ and $bg_{K_{\mu 2}}$ in table 4.12, for the 1/3 and 2/3 data sets are scaled up by 3 and 3/2 (10/3 and 10/7 in 1995), respectively, to account for the fractions of the full data sets that they represent. The $K_{\pi 2}$ background level for the 2/3 1996-7 data set is not scaled up, however, because the $K_{\pi 2}$ normalization, $B_{K_{\pi 2}}$, for the 2/3 1996-7 data set is actually that from the 1/3 and 2/3 1996-7 data sets combined. The $K_{\pi 2}$ normalization for the 2/3 1996-7 data set fluctuated down relative to that for 1/3 1996-7 (although the results are within statistical uncertainty), and the 1/3 1996-7 measurement was performed

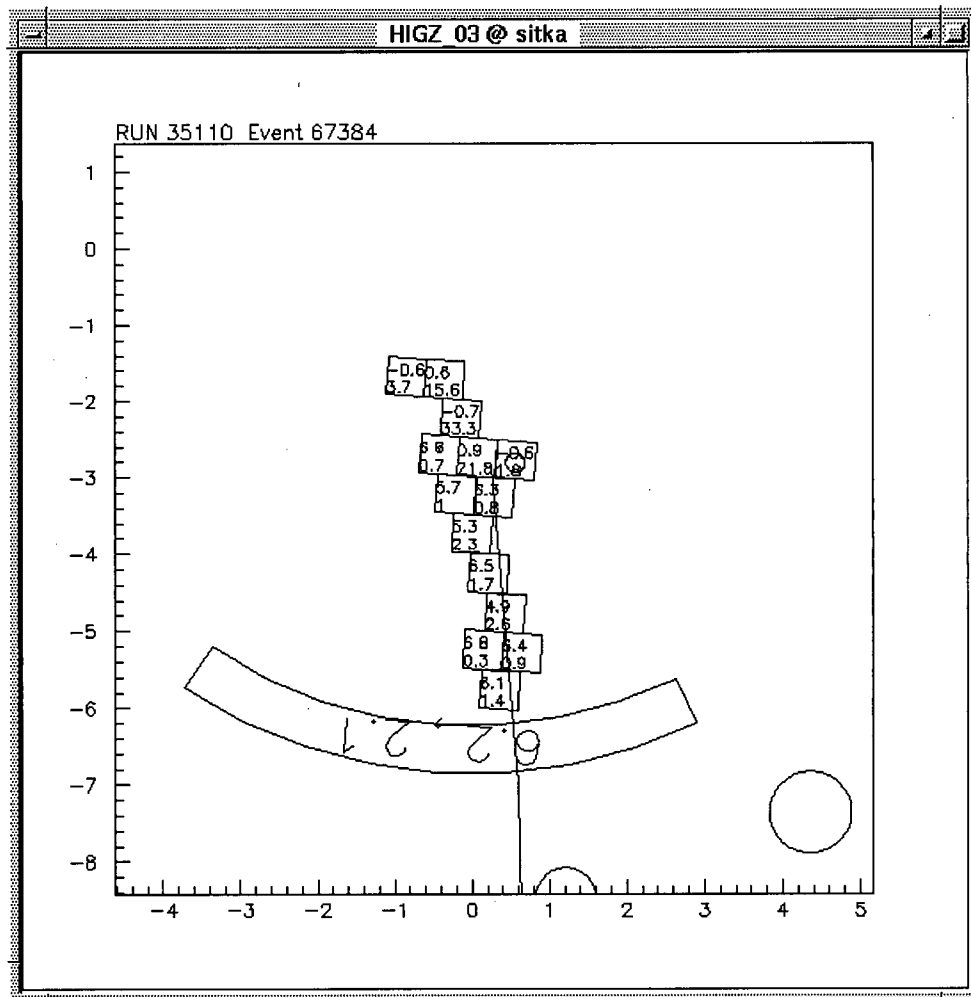


Figure 4.28: Target display of the “TGDEDX” event. The top and bottom numbers in each target fiber, and the left and right numbers in the IC, are the time (ns) and energy (MeV) of each hit, respectively. The kaon decay product appears to originate two fibers to the left of the kaon decay fiber.

	1995		1996-7	
	using 1/3	using 2/3	using 1/3	using 2/3
$B_{K\pi_2}^{RP}$	8	23	9	17 (full)
$B_{K\pi_2}^{Ein}$	443	1031	517	1374 (full)
$B_{K\pi_2}^{Eout}$	9	24	12	24 (full)
$B_{K\pi_2}$	0.16 ± 0.08	0.54 ± 0.16	0.21 ± 0.09	0.30 ± 0.11 (full)
R_{PV}	50.1 ± 1.1			
$bg_{K\pi_2}$	0.0110 ± 0.0053	0.0156 ± 0.0045	0.0128 ± 0.0056	0.0060 ± 0.0022
$B_{K\mu_2}^*$	$\frac{231}{34903/234}$	4	6	8
$B_{\mu band}^{PVoff}$	0	2	—	—
$B_{K\mu_2}$	2.0 ± 0.5	4.9 ± 2.1	6.0 ± 2.4	8.0 ± 2.8
CD_{TD}	71130	136180	79173	8113 (full)
C_{TD}	86	146	95	14 (full)
R_{TD}	827 ± 89	933 ± 77	833 ± 85	580 ± 155 (full)
$bg_{K\mu_2}$	0.0080 ± 0.0020	0.0075 ± 0.0033	0.0216 ± 0.0091	0.0207 ± 0.0092

Table 4.12: Numbers of events B_j^i and C, CD_l from the normalization and rejection branches, respectively, of figures 4.20 and 4.21 for each of the 1/3 and 2/3 1995 and 1996-7 data sets, and the resulting K_{π_2} and K_{μ_2} normalizations $B_{K_{\pi_2}, K_{\mu_2}}$, rejections $R_{PV, TD}$, and scaled background levels $bg_{K_{\pi_2}, K_{\mu_2}}$ as defined in the text of section 4.5. Note that the K_{π_2} normalization, $B_{K_{\pi_2}}$, and the TD rejection, R_{TD} , quoted for the 2/3 1996-7 data set are actually those from the “full” 1996-7 data set (1/3 + 2/3). All quoted uncertainties are purely statistical.

in a completely unbiased way (any new cuts introduced for 1996-7 that are part of the K_{π_2} normalization were designed by studying K_{μ_2} background), so a less-statistically-uncertain and more conservative result for the 1996-7 K_{π_2} normalization is obtained using the full 1996-7 data set. The rejection of the TD function cut, R_{TD} in table 4.12, for the 2/3 1996-7 data set is also calculated using the 1/3 and 2/3 1996-7 data sets combined (see section 4.4.2).

The single-beam background estimates, and the numbers of events B_j^i and C, CD_l^k from figures 4.22 and 4.23, are shown in table 4.13 for each of the 1/3 and 2/3 1995 and 1996-7 data sets. As shown in figure 4.9, the single-beam kaon- and pion-entering background levels are given by $bg_{BM1K} = B_{BM1K}/(R_{DEL C} - 1)$ and $bg_{BM1P} = B_{BM1P}/(R_{DEL C} - 1)$, respectively, where the single-beam kaon- and pion-entering normalizations are given by $B_{BM1K} = B_{BM1K}^{PVT D}[(B_{BM1K}^{CKin}/B_{BM1K}^{CKout}) - 1]$ (see section 4.4.3 and figure 4.22) and $B_{BM1P} = B_{BM1P}^{PBB4}[(B_{BM1P}^{CPIin}/B_{BM1P}^{CPIout}) - 1]$ (see section 4.4.3 and figure 4.23). The rejection of the DELC cut, $R_{DEL C}$, is taken from the minimum of four different $CD_{DEL C}/C_{DEL C}$ values (see sec-

tion 4.4.3 and figures 4.22 and 4.23).

The double-beam background estimates, and the numbers of events B_j^i and C, CD_l from figures 4.24 and 4.25, are shown in table 4.14 for each of the 1/3 and 2/3 1995 and 1996-7 data sets. As shown in figure 4.9, the double-beam kaon- and pion-entering background levels are given by $bg_{BM2K} = B_{BM2K}/(R_{CK} - 1)$ and $bg_{BM2P} = B_{BM2P}/(R_{CPI} - 1)$, respectively, where the double-beam kaon- and pion-entering normalizations are given by $B_{BM2K} = \frac{B_{BM2K}^{TG}}{B_{BM2K}^{B4in}/B_{BM2K}^{B4out}}$ and $B_{BM2P} = \frac{B_{BM2P}^{TG}}{B_{BM2P}^{B4in}/B_{BM2P}^{B4out}}$ (i.e., using the second bifurcation – see section 4.4.3 and figures 4.24 and 4.25). If the second bifurcation is not used, then the double-beam kaon- and pion-entering normalizations are given by $B_{BM2K} = B_{BM2K}^*$ and $B_{BM2P} = B_{BM2P}^*$, where B_{BM2K}^* and B_{BM2P}^* are the numbers of events left at the bottom of the normalization branches in figures 4.24 and 4.25 after all cuts in these branches have been applied sequentially. The double-beam rejections, R_{CK} and R_{CPI} , are taken from the minima of two different $(CD/C)_{CK}$ values and two different $(CD/C)_{CPI}$ values (see section 4.4.3 and figures 4.24 and 4.25).

The CEX background estimates for the 1995 and 1996-7 data sets are given in section 4.4.4.

The background levels at the final cut positions are summarized in table 4.15. The total number of background events expected in the $\pi^+\nu\bar{\nu}(1)$ signal region for the complete 1995-7 data set is 0.080 ± 0.020 , based on the measurements using the 2/3 data sets in 1995 and 1996-7. This estimate does not include the second-bifurcation result for the 1995 double-beam background estimate. If the second bifurcation is used for all years, then the expected number of background events for 1995-7 is 0.067 ± 0.014 .

4.6 Outside-the-Box Tests

After making background estimates for a particular data sample (e.g., 2/3 1995), and before moving on to analysis of the next data sample (e.g., 1/3 1996-7), two “outside-the-box” tests are performed in order to gain confidence that all potential backgrounds have been measured and that the background estimates (see section 4.5) are accurate:

	1995		1996-7	
	using 1/3	using 2/3	using 1/3	using 2/3
B_{BM1K}^{PVTD}	11	25	5+3	22+8
B_{BM1K}^{CKin}	32	87	36+11	78+18
B_{BM1K}^{CKout}	6	28	1+2	7+1
B_{BM1K}	2.54 ± 1.21	11.86 ± 3.01	0.81 ± 0.59	2.64 ± 1.03
$CD_{DEL C}^{(1)}$	2093	5079	2055	4062
$C_{DEL C}^{(1)}$	0	0	0	0
$CD_{DEL C}^{(2)}$	4127	10191	4498	9130
$C_{DEL C}^{(2)}$	0	1	0	0
$CD_{DEL C}^{(1)}$ (BOX off)	3389	8328	3377	6650
$C_{DEL C}^{(1)}$ (BOX off)	0	0	0	1
$CD_{DEL C}^{(2)}$ (BOX off)	6788	16849	7461	15105
$C_{DEL C}^{(2)}$ (BOX off)	0	3	1	2
$R_{DEL C}^{(1)}$	2093 ± 2092	5079 ± 5078	2055 ± 2054	4062 ± 4061
$R_{DEL C}^{(2)}$	4127 ± 4126	10191 ± 10190	4498 ± 4497	9130 ± 9129
$R_{DEL C}^{(1)}$ (BOX off)	3389 ± 3388	8328 ± 8327	3377 ± 3376	6650 ± 6649
$R_{DEL C}^{(2)}$ (BOX off)	6788 ± 6787	5616 ± 3242	7461 ± 7460	7553 ± 5340
bg_{BM1K}	0.0040 ± 0.0045	0.0033 ± 0.0034	0.0012 ± 0.0015	0.0010 ± 0.0010
B_{BM1P}^{PBBA}	9	33	34+3	80+2
B_{BM1P}^{CPin}	76	201	29+29	47+77
B_{BM1P}^{CPout}	5	8	1+1	1+2
B_{BM1P}	0.63 ± 0.35	1.37 ± 0.53	1.32 ± 1.22	1.79 ± 1.73
bg_{BM1P}	0.0010 ± 0.0012	0.0004 ± 0.0004	0.0019 ± 0.0026	0.0007 ± 0.0009

Table 4.13: Numbers of events B_j^i and C, CD_i^k from the normalization and rejection branches, respectively, of figures 4.22 and 4.23 for each of the 1/3 and 2/3 1995 and 1996-7 data sets, and the resulting single-beam normalizations $B_{BM1K, BM1P}$, rejections $R_{DEL C}$, and scaled background levels $bg_{BM1K, BM1P}$ as defined in the text of section 4.5. All quoted uncertainties are purely statistical. As shown in the table, the single-beam kaon- and pion-entering normalizations are calculated separately for the 1996 and 1997 data sets, and then added. The rejection of the DELC cut, $R_{DEL C}$, is taken from the minimum of four different values: $R_{DEL C}^{(1)}$ and $R_{DEL C}^{(2)}$ with and without the BOX cut applied (see section 4.4.3 and figures 4.22 and 4.23).

Background	1995		1996-7	
	using 1/3	using 2/3	using 1/3	using 2/3
B_{BM2K}^{TC}	0	2	0	1
B_{BM2K}^{4in}	11	26	25	36
B_{BM2K}^{4out}	3	2	0	0
B_{BM2K}^* (no 2nd bif.)	0	1	—	—
B_{BM2K}	0.273 ± 0.304	0.154 ± 0.151	0.040 ± 0.056	0.0278 ± 0.039
B_{BM2K} (no 2nd bif.)	1.0 ± 1.0	1.0 ± 1.0	—	—
CD_{CK}	276	810	237	461
C_{CK}	2	7	0	2
CD_{CK} (low-side BOX)	577	1409	381	762
C_{CK} (low-side BOX)	4	14	0	7
R_{CK}	138 ± 97	116 ± 44	237 ± 236	231 ± 163
R_{CK} (low-side BOX)	144 ± 72	101 ± 27	381 ± 380	109 ± 41
bg_{BM2K}	0.0066 ± 0.0088	0.0022 ± 0.0022	0.0005 ± 0.0009	0.0004 ± 0.0006
bg_{BM2K} (no 2nd bif.)	0.0243 ± 0.0298	0.0143 ± 0.0148	—	—
B_{BM2P}^{TC}	2	2	4	5
B_{BM2P}^{4in}	67	163	141	283
B_{BM2P}^{4out}	2	1	0	5
B_{BM2P}^* (no 2nd bif.)	0	0	—	—
B_{BM2P}	0.060 ± 0.059	0.012 ± 0.015	0.028 ± 0.032	0.088 ± 0.056
B_{BM2P} (no 2nd bif.)	1.0 ± 1.0	1.0 ± 1.0	—	—
CD_{CPI}	3812	9148	5108	9921
C_{CPI}	4	4	0	6
CD_{CPI} (low-side BOX)	6248	15149	8780	17425
C_{CPI} (low-side BOX)	7	9	3	10
R_{CPI}	953 ± 476	2287 ± 1143	5108 ± 5107	1654 ± 675
R_{CPI} (low-side BOX)	893 ± 337	1683 ± 561	2927 ± 1689	1743 ± 551
bg_{BM2P}	0.00022 ± 0.00024	0.00001 ± 0.00001	0.00003 ± 0.00004	0.00008 ± 0.00006
bg_{BM2P} (no 2nd bif.)	0.00374 ± 0.00400	0.00085 ± 0.00090	—	—

Table 4.14: Numbers of events B_j^i and C, CD_i from the normalization and rejection branches, respectively, of figures 4.24 and 4.25 for each of the 1/3 and 2/3 1995 and 1996-7 data sets, and the resulting double-beam normalizations $B_{BM2K, BM2P}$, rejections $R_{CK, CPI}$, and scaled background levels $bg_{BM2K, BM2P}$ as defined in the text of section 4.5. All quoted uncertainties are purely statistical. The double-beam normalizations, B_{BM2K} and B_{BM2P} , and the resulting double-beam background levels, bg_{BM2K} and bg_{BM2P} , are calculated with and without the second bifurcation. The double-beam rejections, R_{CK} and R_{CPI} , are taken from the minima of two different values: with the BOX cut applied, and with only the low-side BOX cut applied (see section 4.4.3 and figures 4.24 and 4.25).

bkgd	1995		1996-7		1995-7
	using 1/3	using 2/3	using 1/3	using 2/3	
$K_{\pi 2}$	0.0110 ± 0.0053	0.0156 ± 0.0045	0.0128 ± 0.0056	0.0060 ± 0.0022	0.0216 ± 0.0050
$K_{\mu 2}$	0.0080 ± 0.0020	0.0075 ± 0.0033	0.0216 ± 0.0091	0.0207 ± 0.0092	0.0282 ± 0.0098
BM1	0.0051 ± 0.0054	0.0037 ± 0.0038	0.0031 ± 0.0037	0.0016 ± 0.0018	0.0054 ± 0.0042
BM2	0.0281 ± 0.0300 (0.0069 ± 0.0088)	0.0152 ± 0.0149 (0.0022 ± 0.0022)	0.0005 ± 0.0009	0.0005 ± 0.0006	0.0157 ± 0.0149 (0.0027 ± 0.0023)
CEX	0.0045 ± 0.0045	0.0045 ± 0.0045	0.0051 ± 0.0051	0.0051 ± 0.0051	0.0096 ± 0.0068
total	0.0567 ± 0.0314 (0.0355 ± 0.0126)	0.0465 ± 0.0169 (0.0335 ± 0.0084)	0.0431 ± 0.0124	0.0340 ± 0.0109	0.0804 ± 0.0201 (0.0675 ± 0.0138)

Table 4.15: Number of background events expected in the $\pi^+\nu\bar{\nu}(1)$ signal region for the 1995 and 1996-7 data using estimates based on the 1/3 and 2/3 data samples. All quoted uncertainties are purely statistical. “BM1” and “BM2” refer to the sum of the kaon- and pion-entering single- and double-beam backgrounds, respectively. The 1995 BM2 background estimates using the second bifurcation are shown in parentheses. The total background for 1995-7 is calculated using the 2/3 estimates.

- a correlation study, performed by loosening the bifurcated branches of a background estimate and comparing predicted and observed numbers of events;
- a search for events which fail only 1 of 16 possible “cut classes”.

The outside-the-box correlation study is described in section 4.2. Backgrounds are estimated using the bifurcation technique shown in figures 4.20 through 4.25 and the calculations described in section 4.5, but with the two function cuts associated with the normalization and rejection branches of each background estimate loosened at the same time. The number of events in each outside-the-box region, as defined by the looser cuts, is then counted and compared with the prediction. Results for various loosening of the $K_{\pi 2}$, $K_{\mu 2}$, single-beam and double-beam background normalization and rejection function cuts, as a function of pathology cuts applied (grouped into classes), are shown in tables 4.16 and 4.17 for the 2/3 1996-7 data sample. Background predictions and observations are made with each pathology cut class (defined in table 4.18) turned off, so that any discrepancies between predicted and observed numbers of events may be more readily assigned to a particular correlation mechanism. For example, in table 4.16, the discrepancy at the $K_{\mu 2}$ 10×10 outside-the-box cut position with the MASS cut turned off (5 $K_{\mu 2}$ background events observed when 0.63 events were predicted) stimulated further study of correlations between TD and kinematic

cuts, which led to the GDR background hypothesis (see section 4.1.1.1) and development of the TDVEL and MASS cuts (see section C.3.4). Otherwise, predictions of the outside-the-box correlation study are consistent with observations in all cases, except perhaps at the loosest single-beam kaon-entering cut positions in table 4.17, where slightly more events are observed than predicted. However, this discrepancy is occurring very far from the final cut positions (possibly due to some breakdown in the background estimation structure for very loose cuts), so it is not worrisome.

Background predictions and observations, as a function of pathology cuts applied, from a global loosening of all function cuts at the same time on the 2/3 1996-7 data sample, are shown in table 4.19. Predictions are somewhat higher than observations, possibly due to correlations among background types. These correlations are partially taken into account by re-calibrating the functions every time a cut class is turned off and/or functions associated with other background types are loosened. For example, in figure 4.21, the ZUTOUT, COS3D, ZFRF, LAYER14 kinematic pathology cuts are turned off, and the $K_{\pi 2}$ kinematic, PV, and beam function cuts are all loosened when estimating the $K_{\mu 2}$ component of the background for the global loosening with the “kinz” cut class turned off (i.e., the second row in table 4.19). This is done so that additional $K_{\mu 2}$ background introduced by loosening the beam function cuts, above and beyond that introduced by loosening the TD and $K_{\mu 2}$ kinematic function cuts, is accounted for. However, it’s possible that loosening the beam function cuts can introduce the same additional $K_{\mu 2}$ background that loosening the TD and $K_{\mu 2}$ kinematic function cuts does (e.g., $K_{\mu 2}$ decay in flight events). This additional background is then predicted twice (in both the $K_{\mu 2}$ and beam background estimates), whereas it is observed in the outside-the-box region only once, making predictions higher than observations. In any case, observations are not larger than predictions, which gives confidence in the background estimates.

Note that when a function is loosened, the inverted function (in the other branch of the bifurcation) is kept at the standard cut position, so that the tagging efficiency of the inverted cut for background events remains high. This tagging efficiency must be high so that events which correlate the bifurcated cuts (e.g., are more likely to pass a cut if they pass its

cuts turned off		$K_{\pi 2}$: PV \times kin.			$K_{\mu 2}$: TD \times kin.		
		10×10	50×50	50×300	10×10	159×134	1000×134
none	predict:	1.04	10	47	0.42	13.7	119
	observe:	1	10	48	2	12	111
mass	predict:	1.04	10	48	0.63	34.9	295
	observe:	1	10	49	5	37	272
kinz	predict:	1.25	11	59	2.10	65.7	536
	observe:	1	11	61	4	74	511
kqual	predict:	1.46	14	56	1.43	46.8	388
	observe:	2	14	58	3	63	357
kintg	predict:	1.67	15	61	0.55	16.5	143
	observe:	1	15	63	2	16	134
kdedx	predict:	1.04	11	52	1.66	127.9	1026
	observe:	1	11	54	4	131	953
epitg	predict:	1.24	12	59	0.50	16.5	143
	observe:	1	12	61	2	13	132
tgtr	predict:	1.05	11	49	0.41	13.8	119
	observe:	1	11	50	2	12	111
timcon	predict:	1.05	11	48	0.43	14.2	123
	observe:	1	11	49	2	12	115
ic	predict:	1.46	12	51	0.44	15.7	133
	observe:	2	12	57	2	14	124
b4ekz	predict:	1.04	10	47	0.46	14.1	121
	observe:	1	10	48	2	12	112
bhtrs	predict:	1.04	10	47	0.42	13.8	119
	observe:	1	10	48	2	12	111

Table 4.16: Predicted and observed numbers of $K_{\pi 2}$ and $K_{\mu 2}$ background events in the 2/3 1996-7 data sample, obtained by loosening the PV and $K_{\pi 2}$ kinematic function cuts, and the TD and $K_{\mu 2}$ kinematic function cuts, respectively, by the factors shown. Background predictions and observations are made with various pathology cuts, grouped into classes (see table 4.18), turned off. The actual loosening factors given in the head of the table are only approximate, because the events introduced by turning off pathology cut classes may not be distributed evenly in the function values N . The different functions are defined for different ranges in N (see sections C.3.3, C.3.4, and C.3.5), which is why the maximal loosening for each function cut is different in the head of the table. Note that predicted and observed numbers of events agree almost exactly at the maximal loosening for the PV (factor of 50) and TD (factor of 1000) function cuts. This is because these loosest cut positions correspond to turning the cuts off, which is essentially equivalent to inverting the cuts, and it is on the inverted-cut data samples that the kinematic functions are calibrated.

cuts turned off		single-beam kaon-entering			single-beam pion-entering		
		loose1	loose2	loose3	loose1	loose2	loose3
none	predict:	0.057	0.94	8.9	0.029	0.31	1.9
	observe:	0	0	14	0	0	2
kinz	predict:	0.073	1.15	10.8	0.042	0.42	2.5
	observe:	0	1	16	0	0	2
kqual	predict:	0.058	0.91	9.3	0.029	0.29	1.8
	observe:	0	0	14	0	0	2
kintg	predict:	0.070	1.13	11.3	0.038	0.41	2.5
	observe:	0	0	16	0	0	2
kdedx	predict:	0.062	1.04	9.5	0.038	0.42	2.6
	observe:	0	0	14	0	0	2
epitg	predict:	0.145	1.57	13.4	0.079	0.58	3.2
	observe:	0	0	20	0	0	4
tgtr	predict:	0.073	1.05	9.6	0.036	0.32	1.9
	observe:	0	0	15	0	0	2
timcon	predict:	0.128	1.65	16.7	0.062	0.44	2.5
	observe:	0	0	22	0	0	3
ic	predict:	0.077	1.00	9.0	0.035	0.29	1.7
	observe:	0	0	14	0	0	2
b4ekz	predict:	0.095	1.70	17.2	0.050	0.53	3.2
	observe:	0	1	18	0	0	4
bhtrs	predict:	0.067	1.07	9.8	0.037	0.41	2.5
	observe:	0	0	14	0	0	2
cuts turned off		double-beam kaon-entering			double-beam pion-entering		
		loose1	loose2	loose3	loose1	loose2	loose3
none	predict:	0.0037	0.036	0.31	0.020	0.16	1.2
	observe:	0	0	0	0	0	1
kinz	predict:	0.0046	0.036	0.30	0.019	0.16	1.2
	observe:	0	0	0	0	0	1
kqual	predict:	0.0033	0.031	0.30	0.020	0.16	1.2
	observe:	0	0	0	0	0	1
kintg	predict:	0.0044	0.037	0.32	0.026	0.24	1.8
	observe:	0	0	0	0	0	3
kdedx	predict:	0.0039	0.037	0.31	0.024	0.19	1.4
	observe:	0	0	0	0	0	2
epitg	predict:	0.0039	0.035	0.31	0.047	0.53	4.3
	observe:	0	0	0	0	0	4
tgtr	predict:	0.0036	0.033	0.30	0.023	0.19	1.4
	observe:	0	0	0	0	0	1
timcon	predict:	0.0052	0.039	0.35	0.030	0.28	2.2
	observe:	0	0	0	0	0	1
ic	predict:	0.0069	0.042	0.31	0.030	0.30	2.3
	observe:	0	0	0	0	1	2
b4ekz	predict:	0.0064	0.045	0.36	0.068	0.78	6.3
	observe:	0	0	0	0	0	6
bhtrs	predict:	0.0044	0.036	0.30	0.022	0.17	1.2
	observe:	0	0	0	0	0	1

Table 4.17: Predicted and observed numbers of beam background events in the 2/3 1996-7 data sample, obtained by loosening the single-beam kaon-entering (DELC, CKTRS, CKTAIL) and pion-entering (DELC, CPITRS, CPITAIL) function cuts, and the double-beam kaon-entering (BWTRS, CKTRS, CKTAIL, B4TRS, B4TD) and pion-entering (BWTRS, CPITRS, CPITAIL, B4TRS, B4TD, PBNRS) function cuts. Background predictions and observations are made with various pathology cuts, grouped into classes (see table 4.18), turned off. Because the single-beam functions involve cuts which are also used by the double-beam functions, it is difficult to define the individual single- and double-beam N values at the outside-the-box cut positions, which is why they are labelled as “loose1, loose2, loose3” in the table. The functions are loosened such that loose1, loose2, and loose3 correspond to increases in the predicted amount of beam background by about 1, 2, and 3 orders of magnitude, respectively.

cut class	cut members
1. pv	PV function
2. kp2	$K_{\pi 2}$ kinematic function (low-side RBOX,EBOX,PBOX, and RBOX',EBOX',PBOX')
3. td	TD function (TDTCON,TDDFA1,EV5,ELVETO,TDFOOL,TDVEL,TDLIK2,TDLIK3,TDDFA2)
4. km2	$K_{\mu 2}$ kinematic function (high-side RBOX,EBOX,PBOX, and RNGMOM)
5. bmfn	DELC,BWTRS,CKTRS,CKTAIL,CPITRS,CPITAIL,PBNRS,B4DEDX,B4TRS,B4TD
6. mass	MASS
7. kinz	ZUTOOUT,COS3D,ZFRF,LAYER14
8. kqual	UTCQUAL,PROBZ,CHIRF,CHIRF_NHZ
9. kintg	TGDEDX,PIGAP,TGLIKE,TGB4
10. kdedx	CHIMAX_RSDEDX,CL_RSDEDX,RSLIKE,TDECON
11. epitg	TGCCDPF,EPITG,EPIMAXK,PHIVTX,PHIVTX2,OPSVETO,OPSVETO.LKB,TGEDGE
12. tgtr	TGQUALT,TGER,TARGF,DTGTTP,RTDIF,DRP
13. timcon	TIMCON,TIC,TGCCD
14. ic	EICKIN,EIC,KIC,TGGEO
15. b4ekz	B4EKZ,B4EKZ_IC,TGZFOOL
16. bhtrs	BHTRS

Table 4.18: Complete listing of cuts applied in the analysis, divided into pathology cut classes. Classes 6 – 16 are turned off one by one in the outside-the-box correlation study. Classes 1 – 16 are used in the single-class-failure study. Note that some cuts are applied only to the 1996-7 data (see sections C.3.1, C.3.2 and C.3.4).

bifurcated partner cut) are not eliminated by inverted cuts from the bifurcated background estimation structure.

The outside-the-box correlation tests are very effective at detecting correlations between bifurcated cuts. For example, early in the analysis when designing the $K_{\pi 2}$ kinematic function on the 1/3 1995 data, a correlation was discovered between kinematic quantities which are part of the second bifurcation in the $K_{\pi 2}$ background estimation structure (cuts on E are bifurcated with cuts on R and P). This correlation was discovered via observation of roughly a factor of 3 more events than predicted at the $K_{\pi 2}$ outside-the-box cut positions (e.g., 20 events observed at the 50×50 cut position when 7.1 were expected). This was found to be mainly due to (1) a problem with the IC energy calculation, which affects all of E , R , and P , and (2) a problem in the position of target fibers relative to the UTC (the “target rotation bug”), which resulted in a non-Gaussian high P tail to the $K_{\pi 2}$ peak. Possible problems with the IC were also suggested by more events observed than predicted (9 vs. 4) at the “loose3” double-beam kaon-entering outside-the-box cut position, when the cuts in the “ic” pathology class were turned off. The $K_{\pi 2}$ correlations were removed by introducing the EICKIN cut, and by using tighter cuts on R and P when measuring the rejection of the low-side EBOX cut. Possible correlations in the double-beam kaon-entering background

cuts turned off		loosening factor			
		4	25	100	2500
none	predict:	0.276	2.59	9.74	62.9
	observe:	0	2	7	38
kinz	predict:	0.548	5.04	20.78	110.7
	observe:	0	3	14	69
kqual	predict:	0.349	3.75	17.07	97.7
	observe:	0	2	12	52
kintg	predict:	1.004	4.76	16.08	93.8
	observe:	0	3	10	62
kdedx	predict:	0.592	4.83	20.65	131.2
	observe:	0	3	14	62
epitg	predict:	0.899	7.40	19.79	139.3
	observe:	0	9	19	112
tgtr	predict:	0.612	4.67	14.20	60.8
	observe:	0	3	8	41
timcon	predict:	0.470	4.31	14.36	77.3
	observe:	0	2	8	55
ic	predict:	0.771	6.02	20.77	127.0
	observe:	0	2	10	49
b4ekz	predict:	0.810	6.51	30.80	331.5
	observe:	0	3	18	201
bhtrs	predict:	0.784	6.32	23.05	206.5
	observe:	0	2	7	38

Table 4.19: Predicted and observed numbers of all types of background events in the 2/3 1996-7 data sample, obtained by loosening all functions at the same time. Background predictions and observations are made with various pathology cuts, grouped into classes (see table 4.18), turned off. The contributions from each of the $K_{\pi 2}$, $K_{\mu 2}$, and beam backgrounds are increased over the final background levels in the $\pi^+ \nu \bar{\nu}(1)$ signal region by the approximate factors shown in the head of the table.

estimate were removed by tightening the KIC cut, and by introducing the B4EKZ_IC and TGCEO cuts.

Late in the analysis, a potential correlation was found between TD and kinematic cuts in the 2/3 1996-7 data, via 5 events observed when 0.73 were expected at the $10 \times 10 K_{\mu 2}$ outside-the-box cut position. This apparent correlation was eventually attributed to GDR background [41], and the TDVEL and MASS cuts were introduced to attack it. The $K_{\pi 2}$ and $K_{\mu 2}$ outside-the-box correlation results shown in table 4.16 are those after the TDVEL and MASS cuts were added, whereas the beam and global results in tables 4.17 and 4.19 do not include these cuts.

The single-event failure study consists of a search for events which fail only one of the cut classes listed in table 4.18. Events which fail a single cut may be “close to the box”, and may indicate an event pathology which has not been properly accounted for in the background estimates.

For each of the 1/3 and 2/3 1995 and 1996-7 data sets, there are hundreds of events which fail just the $K_{\pi 2}$ kinematic function cut. However, the vast majority of these events fail badly, and are well outside the range of meaningful function values (i.e., they are far from the box). The small number (between 1 and 3 for each data set) which have meaningful function values each fail at least two of the low-side R , E , and P BOX cuts. Furthermore, the number observed is consistent with the number expected from the $K_{\pi 2}$ background estimate in the box and assumption of a linear increase in background with $N_{kin, K_{\pi 2}}$. For each data set there are also typically a few events which fail just the TD function cut, a few events which fail just the $K_{\mu 2}$ kinematic function cut, and up to roughly 10 events which fail just the beam function cuts. The TD failures always fail at least 2 of the fixed TD cuts, and therefore have maximal TD function values and are located far from the box. The $K_{\mu 2}$ failures either fail badly (are well outside the range of meaningful function values, far from the box), or are consistent with the number expected from the $K_{\mu 2}$ background estimate in the box and assumption of a linear increase in background with $N_{kin, K_{\mu 2}}$. The beam function cut failures always fail multiple cuts which come from at least 2 different branches of either the single-beam or double-beam background estimation structures.

The only potentially troubling event, which might indicate a problem in the background estimates, is in the 2/3 1996-7 data. This event fails only the “kintg” pathology class, and in fact fails only the TGDEDX cut. This event is discussed in section 4.4.4 and is believed to be a CEX background event. Further study of the CEX background did not indicate any loopholes in the CEX background estimate [41]. The OPSVETO_LKB safety cut introduced to deal with this event was designed late in the analysis, and is not part of the beam and global outside-the-box correlation results shown in tables 4.17 and 4.19.

4.7 Signal Evaluation Criteria

Prior to “opening the box” and examining any candidate events in the $\pi^+\nu\bar{\nu}(1)$ signal region, a “golden region” is defined where the background level is about a factor of 10 smaller than that estimated in section 4.5, such that candidate events can be assigned a likelihood to be signal based on whether or not they fall in this region. Given that the $K_{\mu 2}$ and $K_{\pi 2}$ backgrounds are large compared to the beam backgrounds (see table 4.15), only the PV, TD, and $K_{\pi 2}$ and $K_{\mu 2}$ kinematic function cuts are tightened by a factor of $\sqrt{10}$, so that the $K_{\pi 2}$ and $K_{\mu 2}$ backgrounds are each reduced by a factor of $\sqrt{10} \cdot \sqrt{10} = 10$. The acceptance loss of the tighter PV cut reduces the $K_{\mu 2}$ background further. Likewise the acceptance loss of the tighter TD cut reduces the $K_{\pi 2}$ background further. The acceptance loss of the tighter PV, TD, and $K_{\pi 2}$ and $K_{\mu 2}$ kinematic function cuts combined reduces the single-beam, double-beam, and CEX backgrounds.

The background rejection and signal acceptance of the golden region relative to the signal region are estimated as follows. The final PV cut requires $N_{PV} \leq 1.0$, so the cut which is a factor of $\sqrt{10}$ tighter requires $N_{PV} \leq 1/\sqrt{10}$. From table 4.14, this corresponds to the requirement $N_{PV} \leq 0.3093$ which has $1.0000/0.3177 = 3.15$ rejection and $0.6065/1.000 = 0.606$ acceptance relative to the final cut position. The final TD cut requires $N_{TD} \leq 1.003$. From table C.4, the cut which is a factor of $\sqrt{10}$ tighter requires $N_{TD} \leq 0.308$, which has $1.003/0.308 = 3.26$ relative rejection and $0.808/1.171 = 0.690$ relative acceptance. The final $K_{\pi 2}$ kinematic cut requires $N_{kin, K_{\pi 2}} \leq 0.3358$. From ta-

bkgd	cuts	extra rej.	no. of events	relative acc.
$K_{\pi 2}$	$N_{PV} \leq 0.3177, N_{kin, K_{\pi 2}} \leq 0.1175$	13.06	0.00166 ± 0.00038	0.564
$K_{\mu 2}$	$N_{TD} \leq 0.308, N_{kin, K_{\mu 2}} \leq 0.0828$	17.43	0.00162 ± 0.00056	0.640
BM1	—	2.771	0.00193 ± 0.00152	1.0
BM2	—	2.771	0.00097 ± 0.00083	1.0
CEX	—	2.771	0.00346 ± 0.00246	1.0
total		7.00	0.00964 ± 0.00308	0.36

Table 4.20: Number of background events expected in the golden region for the 1995-7 data. The “no. of events” for each background type is obtained by dividing the final background levels in table 4.15 by the “extra rejection”. The extra rejection comes from tighter cuts which have additional background suppression and acceptance loss. More details can be found in section 4.7 of the text.

ble C.5, the cut which is a factor of $\sqrt{10}$ tighter requires $N_{kin, K_{\pi 2}} \leq 0.1175$, which has $0.3358/0.1175 = 2.86$ relative rejection and $0.8433/0.9069 = 0.930$ relative acceptance. The final $K_{\mu 2}$ kinematic cut requires $N_{kin, K_{\mu 2}} \leq 0.2681$. From table C.6, the cut which is a factor of $\sqrt{10}$ tighter requires $N_{kin, K_{\mu 2}} \leq 0.0828$, which has $0.2681/0.0828 = 3.24$ relative rejection and $0.9500/1.0237 = 0.928$ relative acceptance.

In the golden region, the $K_{\pi 2}$ background is therefore reduced by a factor of $3.15 \cdot 2.86/0.690 = 13.06$ with $0.606 \cdot 0.930 = 0.564$ acceptance. The $K_{\mu 2}$ background is reduced by a factor of $3.26 \cdot 3.24/0.606 = 17.43$ with $0.690 \cdot 0.928 = 0.640$ acceptance. The single-beam, double-beam, and CEX backgrounds are reduced by a factor of $1/(0.606 \cdot 0.690 \cdot 0.930 \cdot 0.928) = 2.771$ with no acceptance loss. As shown in table 4.20, a total of 0.00964 ± 0.00308 background events is expected in the golden region for the complete 1995-7 data set (note that the second bifurcation result for the 1995 double-beam background estimate is used here, in order to define and achieve high rejections inside the box). This is a factor of 7.00 less than the background in the signal region (0.0675 ± 0.0138), at $0.564 \cdot 0.640 = 36\%$ of the signal region acceptance.

As shown in table 4.20, the CEX background dominates in the golden region. In a previous analysis [46], the golden region was defined as having a factor of 10 less background than the signal region. This can be done here (although it was done after signal event examination) by tightening the CEX function by a factor of 4. The final CEX cut

bkgd	cuts	extra rej.	no. of events	relative acc.
$K_{\pi 2}$	$N_{PV} \leq 0.3177, N_{kin, K_{\pi 2}} \leq 0.1175$	14.50	0.00149 ± 0.00035	0.564
$K_{\mu 2}$	$N_{TD} \leq 0.308, N_{kin, K_{\mu 2}} \leq 0.0828$	19.36	0.00146 ± 0.00050	0.640
BM1	—	3.078	0.00174 ± 0.00137	1.0
BM2	—	3.078	0.00087 ± 0.00075	1.0
CEX	$N_{CEX} \leq 0.26$	10.66	0.00090 ± 0.00064	0.9004
total		10.4	0.00646 ± 0.00180	0.33

Table 4.21: Number of background events expected in the tight golden region for the 1995-7 data. The “no. of events” for each background type is obtained by dividing the final background levels in table 4.15 by the “extra rejection”. The extra rejection comes from tighter cuts which have additional background suppression and acceptance loss. More details can be found in section 4.7 of the text.

requires $N_{CEX} \leq 1.0$. From table C.8, the cut which is a factor of about 4 tighter requires $N_{CEX} \leq 0.26$, which has $1.0/0.26 = 3.85$ relative rejection and 0.9004 relative acceptance. Therefore, the CEX background in table 4.20 is reduced by an additional factor of 3.85, and the $K_{\pi 2}$, $K_{\mu 2}$, single-beam and double-beam backgrounds are reduced by an additional factor of $1/0.9004 = 1.111$. As shown in table 4.21, the contributions from each background type in this tighter golden region are roughly equal, combining for a total of 0.00646 ± 0.00180 background events in the golden region for the complete 1995-7 data set. This is a factor of 10.4 less than the background in the signal region (0.0675 ± 0.0138), at $0.564 \cdot 0.640 \cdot 0.9004 = 33\%$ of the signal region acceptance.

4.8 Search for Signal

From section 4.5, backgrounds are estimated to contribute $\ll 1$ event in the $\pi^+\nu\bar{\nu}(1)$ signal region, namely, 0.08 ± 0.02 events. The outside-the-box tests from section 4.6 revealed no flaws in the background estimation procedure, and signal evaluation criteria have been defined in section 4.7. According to the analysis strategy described in section 4.2, the box can now be opened with the understanding that any events observed in the box are defined to be signal.

Figure 4.29 shows range in scintillator (R) vs. energy (E) for events passing all other cuts

in the complete 1995-7 data set. The rectangular box defined by the RBOX and EBOX cuts therefore indicates the $\pi^+\nu\bar{\nu}(1)$ signal region, where backgrounds are expected to contribute 0.08 ± 0.02 events. One event survives in the box, namely, the same event found in the published 1995 analysis [46]. The events clustered at $E = 108$ MeV are from $K_{\pi 2}$ decays where no photons are detected, the number of which is consistent with that expected from measurements of the photon detection inefficiency. The location of the candidate event in R vs. E with respect to the Monte Carlo (UMC) distribution of $K^+ \rightarrow \pi^+\nu\bar{\nu}$ events is shown in figure 4.30.

A display of the candidate event (event 42251 from run 23271) is shown in figure 4.31. The target, IC, and RS times and energies of this event are shown in figure 4.32. The event passes the tightest cuts defined by the PV, $K_{\pi 2}$ kinematic, $K_{\mu 2}$ kinematic, single-beam, double-beam, and CEX functions, which define $N_{PV} = 0$, $N_{kin,K_{\pi 2}} = 0$, $N_{kin,K_{\mu 2}} = 0$, $N_{BM1} = 0$, $N_{BM2} = 0$, and $N_{CEX} = 0$. The TD function value for this event is $N_{TD} = 0.1343$. Therefore, the event lies in the tight golden region (see tables 4.20 and 4.21). The probability of the event being due to one of the known backgrounds is therefore very small (about 0.6%), so the event is likely due to the decay $K^+ \rightarrow \pi^+\nu\bar{\nu}$.

The kaon decay time of the candidate $K^+ \rightarrow \pi^+\nu\bar{\nu}$ event, defined as the RS track time minus the time of the kaon in the target, $t_{RS} - t_K$, is 24.0 ns (the mean kaon lifetime is 12.386 ns). This large delayed coincidence of the kaon and its decay particle guarantees that the kaon decayed from rest. The pion decay time in the stopping counter, t_μ , is 26.9 ns (the mean pion lifetime = 26.033 ns) and the decay-muon has an energy of 3.20 MeV (the expected scintillator-saturated value is 3.04 ± 0.45 MeV). The decay-muon has a decay time, t_e , of 3252.7 ns (the mean muon lifetime is 2197.03 ns) and the decay-electron has an energy of 50.66 MeV (the Michel spectrum peaks at the endpoint of 53 MeV).

The kinematic quantities associated with the candidate event are $R = 34.75$ cm, $E = 117.73$ MeV and $P = 218.17$ MeV/ c . The uncertainties in these quantities come from a linear interpolation of the R , E , and P resolutions for $K_{\pi 2}$ and $K_{\mu 2}$ decays at rest. From

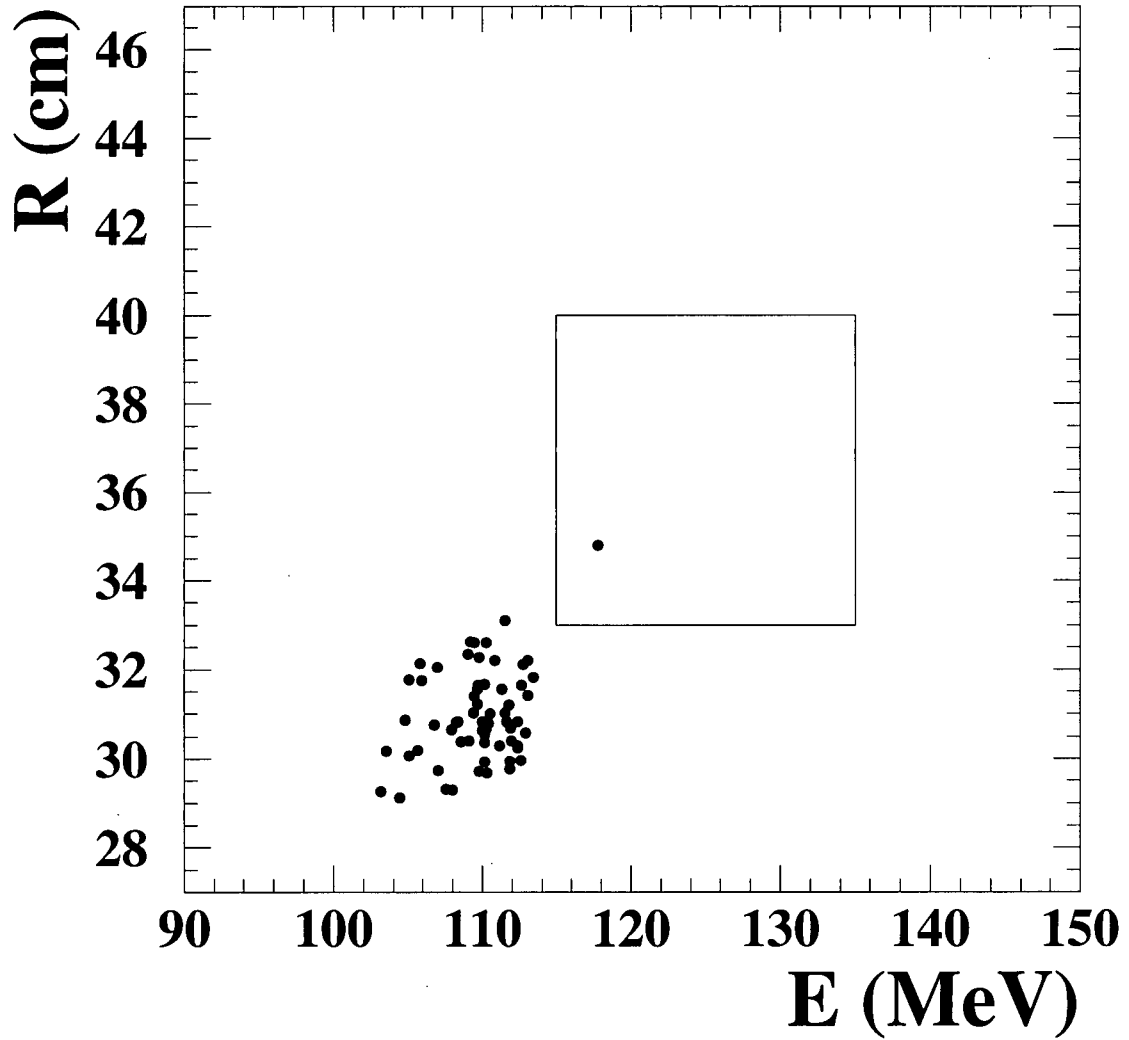


Figure 4.29: Range in scintillator (R) vs. energy (E) for events in the 1995-7 $K^+ \rightarrow \pi^+ \nu \bar{\nu}$ data set passing all other cuts in the analysis. The $\pi^+ \nu \bar{\nu}(1)$ signal region is indicated by a box, and contains a single candidate event.

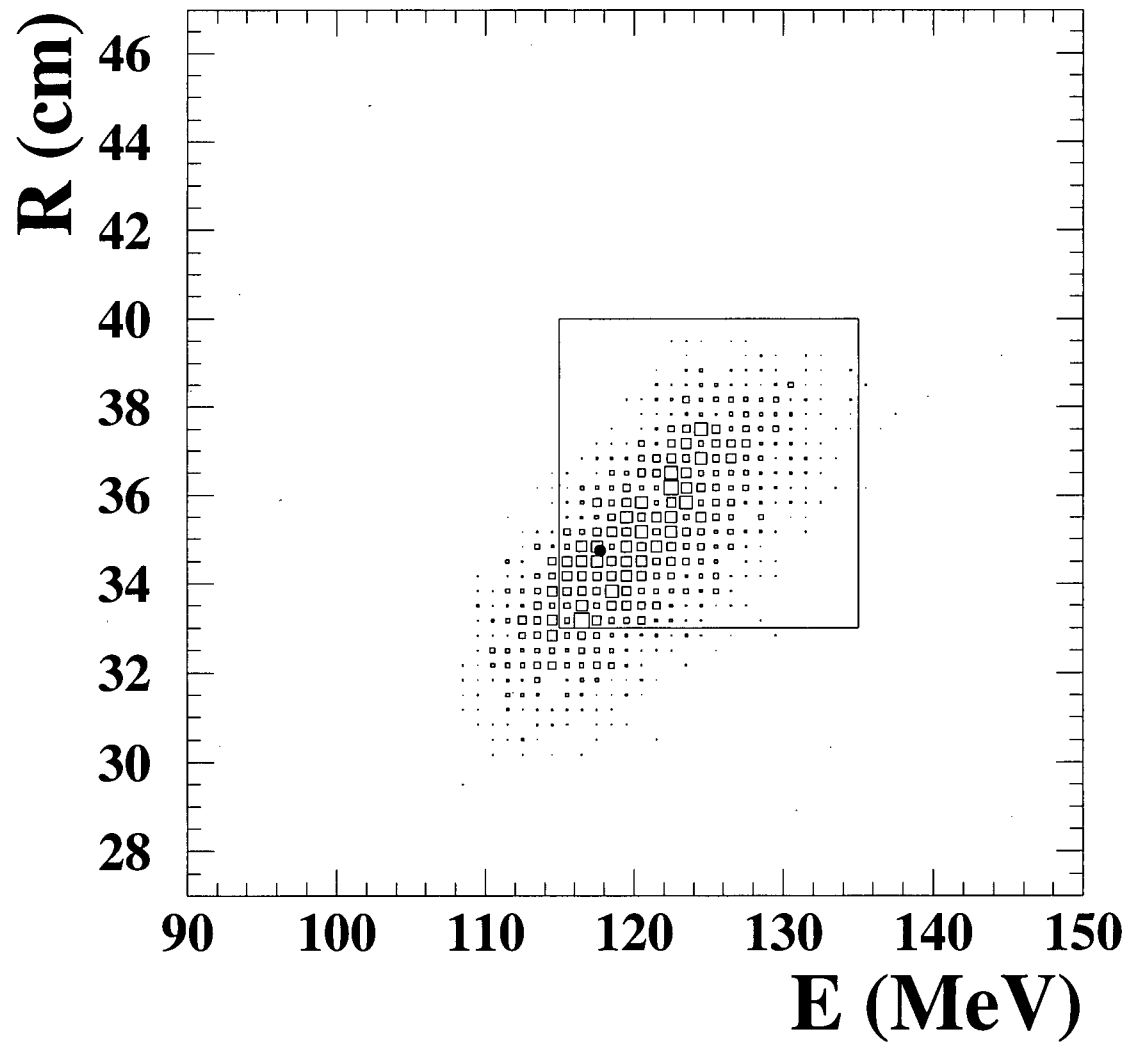


Figure 4.30: Distribution of range in scintillator (R) vs. energy (E) for UMC-generated $K^+ \rightarrow \pi^+ \nu \bar{\nu}$ events (small open squares). Similar to figure 4.29, the $\pi^+ \nu \bar{\nu}(1)$ signal region is indicated by a box, and contains the candidate event from the 1995-7 data, shown as the filled black circle.

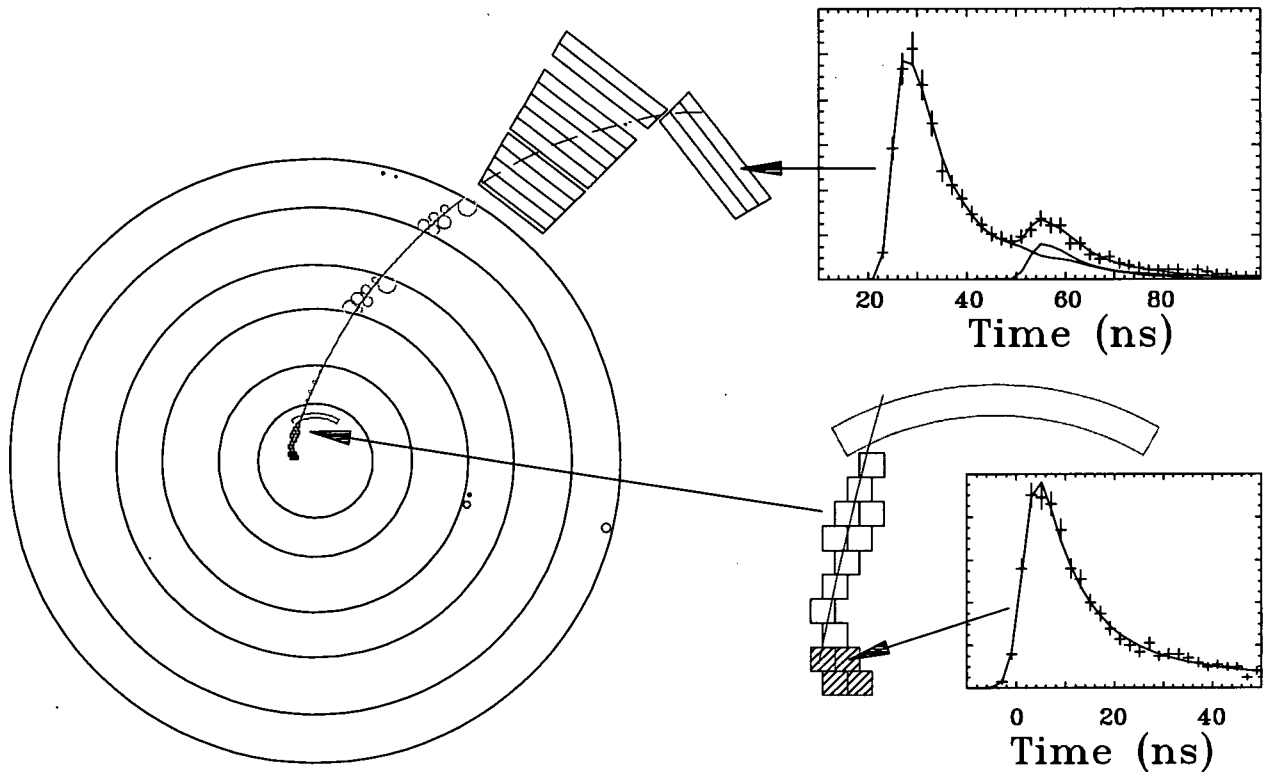


Figure 4.31: Display of the candidate $K^+ \rightarrow \pi^+ \nu \bar{\nu}$ event.

Left: The event is viewed from downstream of the detector, and the pion track is shown to have several hits in the target, an IC hit, anode wire hits in all 3 superlayers of the UTC, and hits in layers 1 – 14 of the RS and the inner RSSC. The extraneous UTC hits in the second and third superlayers, located just below the 3 o'clock position, if fitted to a “track” and propagated back to a radius of 0, indicate that this “track” was produced about 16 cm upstream of the upstream edge of the target, somewhere in the degrader. The fact that the drift circles do not meet indicate that the hits in the second superlayer occurred about 30 ns before the track (i.e., near the time of the kaon). The extraneous UTC hits located just left of the track in the outer superlayer are at about the same z as the extraneous outer superlayer hits near 3 o'clock, and again the drift circles do not meet. The extraneous UTC hit in the second superlayer near 8 o'clock has no ADC value and there is no induced charge on the cathode strips, so it is likely due to electronic noise.

Upper right: TD data in the stopping counter is indicated by crosses, which shows the double-pulse $\pi \rightarrow \mu$ decay signature. Three fits of the TD data to the expected pulse shape are shown: for the first pulse, the second pulse, and the pulses combined.

Lower right: The target region is blown up in order to see the kaon fibers (hatched) and pion fibers (open) more clearly. The CCD data from one of the kaon fibers (not the kaon decay fiber) is indicated by crosses, along with a fit of the data to the expected pulse shape.

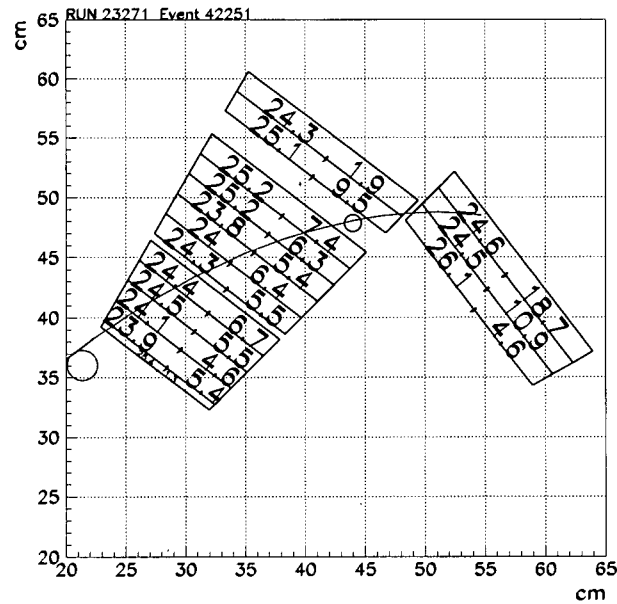
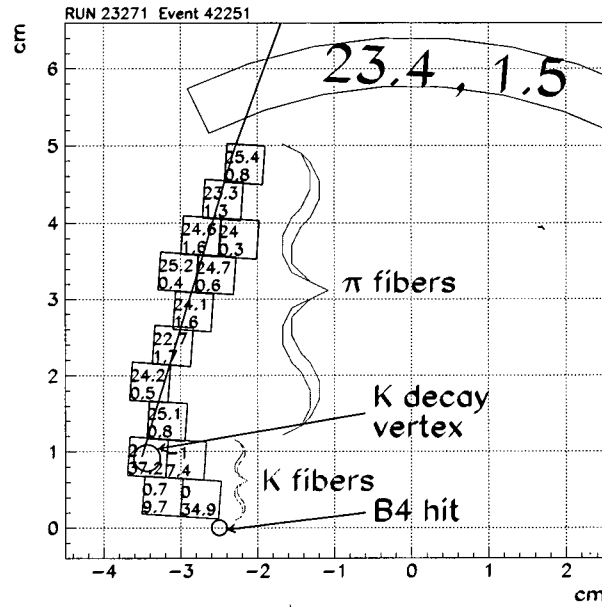


Figure 4.32: Top: Close-up of the target hits for the candidate $K^+ \rightarrow \pi^+ \nu \bar{\nu}$ event. The top and bottom numbers in each target fiber, and the left and right numbers in the IC, are the time (ns) and energy (MeV) of each hit, respectively. The kaon fibers have hits close to $t = 0$ ns, whereas the pion fibers have hits about 24 ns later, ensuring that the kaon decayed from rest. The kaon entered the target near the location of the B4 hit, and left energy in 4 fibers before decaying.

Bottom: Close-up of the RS hits for the candidate $K^+ \rightarrow \pi^+ \nu \bar{\nu}$ event. The left and right numbers in each counter are the time (ns) and energy (MeV) of each hit, respectively.

tables 5.20 and 5.21 of section 5.8 for the 1995 data, the resolutions are given by

$$\sigma(R) = 0.992 + \frac{(R - 30.349)}{(53.988 - 30.349)} \cdot (2.217 - 0.992) = 0.05182 \cdot R - 0.581 \quad (4.4)$$

$$\sigma(E) = 3.295 + \frac{(E - 108.391)}{(154.494 - 108.391)} \cdot (4.336 - 3.295) = 0.02258 \cdot E + 0.848 \quad (4.5)$$

$$\sigma(P) = 0.992 + \frac{(P - 205.177)}{(235.593 - 205.177)} \cdot (2.928 - 2.497) = 0.01417 \cdot P - 0.410 \quad (4.6)$$

Plugging the event kinematics into Eqs. (4.4), (4.5) and (4.6) gives

- $R = 34.75 \pm 1.22$ cm
- $E = 117.73 \pm 3.51$ MeV
- $P = 218.17 \pm 2.68$ MeV/ c

More information about the candidate event can be found elsewhere [55].

The calculations of the $K^+ \rightarrow \pi^+ \nu \bar{\nu}$ and $K^+ \rightarrow \pi^+ f$ branching ratios and $|V_{td}|$ are given in chapter 6, based on observation of this single event and the $K^+ \rightarrow \pi^+ \nu \bar{\nu}$ and $K^+ \rightarrow \pi^+ f$ single-event sensitivities calculated in chapter 5.

Chapter 5

Acceptance and Sensitivity

As shown in the previous chapter, one candidate $K^+ \rightarrow \pi^+ \nu \bar{\nu}$ event was observed in the 1995-7 data. To calculate the branching ratio for $K^+ \rightarrow \pi^+ \nu \bar{\nu}$, the total number of kaons collected must be counted. Also, the “acceptance” of the online and offline cuts must be calculated, which represents the fraction of potential $K^+ \rightarrow \pi^+ \nu \bar{\nu}$ events which survive the online and offline cuts. The “single-event sensitivity” of the analysis is the number of kaons multiplied by the acceptance. The $K^+ \rightarrow \pi^+ \nu \bar{\nu}$ branching ratio is then given by the number of observed $K^+ \rightarrow \pi^+ \nu \bar{\nu}$ events divided by the single-event sensitivity for $K^+ \rightarrow \pi^+ \nu \bar{\nu}$ events.

Because a large sample of $K^+ \rightarrow \pi^+ \nu \bar{\nu}$ events is not available, the acceptances of most cuts are measured using $K_{\mu 2}(1)$, $K_{\pi 2}(2)$, and π_{scat} monitor data (see section 3.3). The acceptances of some cuts must be measured using UMC-generated $K^+ \rightarrow \pi^+ \nu \bar{\nu}$ data because some cuts have specific acceptances for $K^+ \rightarrow \pi^+ \nu \bar{\nu}$ events which can not be estimated using monitor events. The total acceptance is divided into the $K_{\mu 2}$ -based acceptance, the $K_{\pi 2}$ -based acceptance, the π_{scat} -based kinematic acceptance, the π_{scat} -based TD acceptance, the μ -veto acceptance due to accidentals, the T · 2 efficiency, the UMC-based trigger, fiducial, and NIDIF (nuclear interactions and decay in flight) acceptances, and the stopping fraction f_s . The complete measurement of the acceptance and sensitivity is tested by measuring the $K_{\pi 2}$ branching ratio and comparing with the accepted value.

The $K_{\mu 2^-}$, $K_{\pi 2^-}$, π_{scat^-} , and UMC-based acceptance measurements are carefully constructed so that specific types of acceptance loss by every cut are neither omitted nor double-

	1995	1996	1997a	1997b
$K_{Blive}^*(10^{12})$	1.53159	1.16161	0.378020	0.218325
add back bad runs:	—	+0.00324	—	—
multiple scalers:	—	-0.035	—	—
missing TD fiducial pulses, target HV trips:	—	-0.36%	-1.91%	-1.17%
bad stopping counters:	-0.3473%	-0.0468%	-0%	-0.0120%
$K_{Blive}(10^{12})$	1.52627	1.12525	0.370800	0.215745

Table 5.1: K_{Blive} counting in the 1995-7 analysis. The variation in K_{Blive} with each year is primarily due to variation in the data collection time allotted to E787 each year.

counted. Kaons are counted and acceptances are calculated separately for the 1995, 1996, 1997a, and 1997b run periods due to changes in hardware and run conditions (e.g., kaon beam momentum – see section 3.1).

5.1 Counting Kaons

A signal called K_{Blive} is used to count the number kaons entering the detector. It is constructed from the K_B signal (see section 3.3) and a “computer ready” signal. The “computer ready” signal indicates that online data processing and potential readout have been completed, such that all detector systems are ready to accept data. The number of K_{Blive} signals represents the number of kaons that entered the target when the digitizing hardware was available for collection of signals arising from the kaon and its decay products. The K_{Blive} scaler values (see section 3.3) are read and written to tape at the end of each spill. The values on tape are read, summed, and written to logfiles during analysis. The logfiles from the PASS2 analysis, with some bad runs removed (via the BAD_RUN cut – see section C.4), are used to get K_{Blive}^* in table 5.1.

As shown in table 5.1, some runs in 1996 that were supposed to be removed by the BAD_RUN cut were mistakenly included in the PASS3 analysis, so their K_{Blive} is added back in. Also, at the beginning of the 1996 run, scalers were counted in the same way as in 1995, when scaler values were distributed amongst many tapes. The resulting 8-fold multiple

counting of K_{Blive} in early 1996 is removed. The BAD_RUN cut also removes individual events if TD fiducial pulses are missing, and individual spills if target high voltage trips are detected (see section C.4). Note that high voltage trips are, in general, difficult to detect because signals from the high voltage power supplies, which indicate whether or not the high voltage was applied during the spill, are not collected as part of the data. Finally, the BAD_STC cut removes individual events from groups of runs where the TD area-to-MeV calibration fails in the stopping counter (see section C.4). These corrections, and the final K_{Blive} , are shown in table 5.1.

5.2 $K_{\mu 2}$ -based Acceptance

$K^+ \rightarrow \mu^+ \nu_\mu$ events are, in general, single track kaon-decay events with no other activity in the detector. Therefore, they are similar to $K^+ \rightarrow \pi^+ \nu \bar{\nu}$ events with respect to track reconstruction in the target, UTC, and RS; timing and hit patterns in the beamline detectors and target; and photon activity. $K_{\mu 2}$ decays from the $K_{\mu 2}(1)$ monitor data (see section 3.3) are therefore used to measure the acceptances of

- reconstruction cuts;
- beam pathology and function cuts, except those involving track energy and scattering;
- kinematic pathology cuts, except those involving track energy, scattering, and fiducial region;
- all online and offline PV cuts.

The structure and results of the $K_{\mu 2}$ -based acceptance study are shown in table 5.2, which lists the number of surviving $K_{\mu 2}(1)$ monitor events from the 1995, 1996, 1997a, and 1997b data sets after each cut is applied, and the corresponding acceptance of each cut. All setup cuts in table 5.2 are defined in table 5.3. Acceptances are measured using “summary” ntuples (see section 4.3), except for the acceptance loss of the LAYER14 cut due to accidental hits in the outer RSSC, which requires information included only in the

full-record ntuples. After the 1995 PASS1 analysis, some of the PASS1 cuts were modified (STLAY, INTIME, FITPI, UTC/RANGE), so these cuts changed for subsequent passes of the 1995 data. $K_{\mu 2}(1)$ monitor events which pass all other cuts in the $K_{\mu 2}$ -based acceptance study are re-run through the 1995 PASS1 code in order to get the additional acceptance loss from the 1995 PASS1 STLAY, INTIME, and UTC/RANGE cuts. Acceptances are grouped into the quantities A_{RD} , A_{recon} , A_{rest} , A_{PV} , A_{L14}^{acc} , and $A_{K_{\mu 2}}^{P1}$, which are the RS reconstruction, UTC and target reconstruction, beamline and target pattern, PV, LAYER14 accidental, and 1995 PASS1 acceptances, respectively. All of these acceptances are combined into the quantity $A_{K_{\mu 2}}$, which is defined as the $K_{\mu 2}$ -based acceptance.

Note that the ICBIT (online IC requirement) acceptance is 1.0 for all years, because ICBIT is used as a setup cut in the $K_{\mu 2}$ -based acceptance measurement. This is done to make the definition of $A_{K_{\mu 2}}$ equivalent for all years, because the online IC bit was added to the $K_{\mu 2}(1)$ trigger in 1996-7 (as part of T · 2 – see section 3.3). The fiducial and efficiency losses of ICBIT are absorbed into the UMC-based trigger acceptance (section 5.8) and the kaon stopping fraction, f_s (section 5.9). Discussion of the value of $A_{K_{\mu 2}}$ is found in section 5.9.

5.3 $K_{\pi 2}$ -based Acceptance

$K^+ \rightarrow \pi^+\pi^0$ events are similar to $K^+ \rightarrow \pi^+\nu\bar{\nu}$ events in that both involve a roughly minimum-ionizing pion track in the target which arises from kaon decay. Therefore, $K_{\pi 2}$ decays from the $K_{\pi 2}(2)$ monitor data (see section 3.3) are used to measure the acceptances of the beam and kinematic pathology cuts which involve track energy and scattering in the target. The structure and results of the $K_{\pi 2}$ -based acceptance study are shown in table 5.4, which lists the number of surviving $K_{\pi 2}(2)$ monitor events from the 1995, 1996, 1997a, and 1997b data sets after each cut is applied, and the corresponding acceptance of each cut. All setup cuts in table 5.4 are defined in table 5.5. Note that the setup cuts in table 5.5 include the requirement of at least 200 MeV of photon energy in the barrel, EC, and RS combined, such that there is no photon energy in the target (i.e., similar to a $K^+ \rightarrow \pi^+\nu\bar{\nu}$ event in the target, because $K_{\pi 2}$ events have a total of 225 MeV photon energy). Note also that the

Chapter 5. Acceptance and Sensitivity

cut	1995 (acc.)	1996 (acc.)	1997a (acc.)	1997b (acc.)
SETUP _{RD}	45635	119105	39495	23990
RD_TRK	45635 (1.000)	119105 (1.000)	39495 (1.000)	23990 (1.000)
TRKTIM	45635 (1.000)	118849 (0.998)	39492 (1.000)	23990 (1.000)
A_{RD}	1.0000 ± 0.0000	0.9979 ± 0.0001	0.9999 ± 0.0000	1.0000 ± 0.0000
SETUP _{recon}	24749	66786	21386	13805
UTC/RANGE	24749 (1.000)	66786 (1.000)	21386 (1.000)	13805 (1.000)
UTCQUAL	24245 (0.980)	64517 (0.966)	20417 (0.955)	13329 (0.966)
PROBZ	24245 (1.000)	63935 (0.991)	20228 (0.991)	13202 (0.990)
TARGET	24102 (0.994)	63640 (0.995)	20132 (0.995)	13159 (0.997)
A_{recon}	0.9739 ± 0.0010	0.9529 ± 0.0008	0.9414 ± 0.0016	0.9532 ± 0.0018
SETUP _{rest}	36718	96912	30379	20119
ICBIT	36718 (1.000)	96912 (1.000)	30379 (1.000)	20119 (1.000)
TIC	36397 (0.991)	96437 (0.995)	30247 (0.996)	20049 (0.997)
TIMCON	35983 (0.989)	95748 (0.993)	30088 (0.995)	19954 (0.995)
TGCCD	32338 (0.899)	89541 (0.935)	27635 (0.918)	18673 (0.936)
DCBIT	29564 (0.914)	79835 (0.892)	25529 (0.924)	16859 (0.903)
DELCD	26607 (0.900)	71834 (0.900)	22578 (0.884)	14868 (0.882)
CKTRS	26443 (0.994)	71218 (0.991)	22404 (0.992)	14757 (0.993)
CKTAIL	25786 (0.975)	69329 (0.973)	21578 (0.963)	14286 (0.968)
B4DEDX	25535 (0.990)	68424 (0.987)	21384 (0.991)	14159 (0.991)
CPITRS	25484 (0.998)	68339 (0.999)	21353 (0.999)	14132 (0.998)
CPITAIL	25469 (0.999)	68323 (1.000)	21348 (1.000)	14127 (1.000)
PSCUT	25226 (0.990)	67920 (0.994)	21221 (0.994)	14058 (0.995)
TARGF	24406 (0.967)	65836 (0.969)	20544 (0.968)	13617 (0.969)
DTGTP	24403 (1.000)	65830 (1.000)	20544 (1.000)	13617 (1.000)
RTDIF	24157 (0.990)	65142 (0.990)	20286 (0.987)	13493 (0.991)
TQUALT	24157 (1.000)	65142 (1.000)	20286 (1.000)	13493 (1.000)
PIGAP	23869 (0.988)	64483 (0.990)	20063 (0.989)	13393 (0.993)
TGB4	22613 (0.947)	61087 (0.947)	19005 (0.947)	12752 (0.952)
KIC	22405 (0.991)	60484 (0.990)	18854 (0.992)	12659 (0.993)
TGCEO	22361 (0.998)	60362 (0.998)	18823 (0.998)	12644 (0.999)
EIC	22137 (0.990)	59902 (0.992)	18606 (0.988)	12557 (0.993)
EICKIN	21586 (0.975)	58795 (0.982)	18237 (0.980)	12326 (0.982)
B4EKZ	21374 (0.990)	58158 (0.989)	18043 (0.989)	12201 (0.990)
B4EKZ_IC	21308 (0.997)	57935 (0.996)	17954 (0.995)	12160 (0.997)
TGZFOOL	21308 (1.000)	57935 (1.000)	17954 (1.000)	12160 (1.000)
TGCUT	21307 (1.000)	57934 (1.000)	17954 (1.000)	12160 (1.000)
BWTRS	20711 (0.972)	56856 (0.981)	17615 (0.981)	11956 (0.983)
BHTRS	20638 (0.996)	56508 (0.994)	17527 (0.995)	11906 (0.996)
B4TRS	20508 (0.994)	56313 (0.997)	17444 (0.995)	11847 (0.995)
B4TD	20383 (0.994)	56011 (0.995)	17359 (0.995)	11787 (0.995)
PBNRS	19716 (0.967)	55401 (0.989)	16578 (0.955)	11312 (0.960)
A_{rest}	0.5370 ± 0.0026	0.5717 ± 0.0016	0.5457 ± 0.0029	0.5623 ± 0.0035
SETUP _{PV}	10504	29224	8701	5905
HEX	9992 (0.951)	27794 (0.951)	8225 (0.945)	5619 (0.952)
online PV ($BV+EC$)	9721 (0.973)	27177 (0.978)	8018 (0.975)	5523 (0.983)
STLAY	9584 (0.986)	26897 (0.990)	7921 (0.988)	5471 (0.991)
RSHEX	9357 (0.976)	26317 (0.978)	7748 (0.978)	5373 (0.982)
INTIME	9331 (0.997)	26262 (0.998)	7732 (0.998)	5364 (0.998)
PVCUT	9136 (0.979)	25738 (0.980)	7571 (0.979)	5273 (0.983)
TGPPVCUT	9111 (0.997)	25685 (0.998)	7555 (0.998)	5266 (0.999)
TGPVTR	9111 (1.000)	25685 (1.000)	7555 (1.000)	5266 (1.000)
PASS3 PV	8284 (0.909)	23284 (0.907)	6816 (0.902)	4870 (0.925)
A_{PV}	0.7887 ± 0.0040	0.7967 ± 0.0024	0.7834 ± 0.0044	0.8247 ± 0.0049
full-record	24816	23282	6782	4831
LAYER14acc	24644	23129	6740	4805
A_{L14}^{rec}	0.9931 ± 0.0005	0.9934 ± 0.0005	0.9938 ± 0.0010	0.9946 ± 0.0011
SETUP _{$K_{\mu 2}$} ^{P1}	11250	—	—	—
PASS1 STLAY	11239	—	—	—
PASS1 INTIME	11216	—	—	—
PASS1 UTC/RANGE	11165	—	—	—
$A_{K_{\mu 2}}^{P1}$	0.9924 ± 0.0008	—	—	—
$A_{K_{\mu 2}}$	0.4065 ± 0.0029	0.4303 ± 0.0018	0.3999 ± 0.0032	0.4396 ± 0.0039

Table 5.2: $K_{\mu 2}$ -based acceptances of cuts. The quoted uncertainties are purely statistical. Table entries are described in section 5.2 of the text. The ICBIT and DCBIT cuts are the online IC and DC requirements (see section 3.3). The PROBZ cut is not applied to the 1995 data (see section C.3.1). The various SETUP's are defined in table 5.3.

$K_{\mu 2}$ SETUP	component cuts
SETUP _{RD}	BAD_RUN, BAD_STC, $K_{\mu 2}(1)$ trigger, ICBIT, $t_{IC} - t_{Ck} > 5$ ns, B4DEX, UTC, TARGET
SETUP _{recon}	BAD_RUN, BAD_STC, $K_{\mu 2}(1)$ trigger, ICBIT, $t_{IC} - t_{Ck} > 5$ ns, B4DEX, CPITRS, CPITAIL, CKTRS, CKTAIL, BWTRS, BHTRS, A_{RD} cuts, $ t_{IC} - t_{RS} < 5$ ns, PV(noBV), $120 \leq E_{RS} \leq 150$ MeV
SETUP _{rest}	BAD_RUN, BAD_STC, $K_{\mu 2}(1)$ trigger, ICBIT, A_{RD} cuts, A_{recon} cuts, PV(noBV), $120 \leq E_{RS} \leq 150$ MeV, KM2PBOX, COS3D
SETUP _{PV}	BAD_RUN, BAD_STC, $K_{\mu 2}(1)$ trigger, ICBIT, A_{RD} cuts, A_{recon} cuts, A_{rest} cuts, $120 \leq E_{RS} \leq 150$ MeV, KM2PBOX, COS3D, stopping layer < 21
SETUP _{$K_{\mu 2}$} ^{P1}	ICBIT, A_{RD} cuts, A_{recon} cuts, A_{rest} cuts, A_{PV} cuts, $120 \leq E_{RS} \leq 150$ MeV, KM2PBOX, COS3D, stopping layer < 21

Table 5.3: SETUP cuts used in the $K_{\mu 2}$ -based acceptance measurement shown in table 5.2. $K_{\mu 2}(1)$ trigger is an offline reproduction of the $K_{\mu 2}(1)$ trigger (see section 3.3). t_{IC} , t_{Ck} , t_{RS} , and E_{RS} are defined in Appendix D. PV(noBV) is the PV function cut with the requirements in the barrel disabled. KM2PBOX is a 2σ cut on the $K_{\mu 2}$ momentum.

EV5 and TDLIK3 cuts are not part of the setup cuts because they require information on the electron from $\pi \rightarrow \mu \rightarrow e$ decay in the stopping counter, and $K_{\pi 2}(2)$ monitor data only includes TD data in the smaller time range consistent with $\pi \rightarrow \mu$ decay. Acceptances are grouped into the quantities A_{ops} and A_{tgin} , which are the target opposite-side and kinematic acceptances, respectively. These acceptances are combined into the quantity $A_{K_{\pi 2}}$, which is defined as the $K_{\pi 2}$ -based acceptance.

5.4 π_{scat} -based Kinematic Acceptance

Events arising from beam pions scattering into the detector are similar to $K^+ \rightarrow \pi^+ \nu \bar{\nu}$ events in that both involve pion tracks in the RS with range, energy, and momentum roughly uniformly distributed throughout the $\pi^+ \nu \bar{\nu}(1)$ signal region. Therefore, “clean” beam pion scattering events (i.e., with no non-track activity in the RS) from the π_{scat} monitor data (see section 3.3) are used to measure the acceptances of kinematic pathology and function cuts

cut	1995 (acc.)	1996 (acc.)	1997a (acc.)	1997b (acc.)
SETUP _{ops}	15869	49593	12397	8103
OPSVETO	15271 (0.962)	47658 (0.961)	11903 (0.960)	7791 (0.961)
OPSVETO_LKB	15271 (1.000)	47274 (0.992)	11793 (0.991)	7735 (0.993)
A_{ops}	0.9623 ± 0.0015	0.9532 ± 0.0009	0.9513 ± 0.0019	0.9546 ± 0.0023
SETUP _{tgkin}	14558	45273	11297	7441
TGDEDX	14347 (0.986)	44541 (0.984)	11080 (0.981)	7324 (0.984)
TGER	14345 (1.000)	44533 (1.000)	11078 (1.000)	7321 (1.000)
TGLIKE	14090 (0.982)	43597 (0.979)	10860 (0.980)	7191 (0.982)
EPITG	14088 (1.000)	43587 (1.000)	10858 (1.000)	7190 (1.000)
EPIMAXK	13844 (0.983)	42865 (0.983)	10686 (0.984)	7091 (0.986)
TGEDGE	13831 (0.999)	42771 (0.998)	10659 (0.997)	7069 (0.997)
TGCCDPF	13594 (0.983)	42427 (0.992)	10562 (0.991)	7011 (0.992)
PHIVTX	13388 (0.985)	41832 (0.986)	10409 (0.986)	6918 (0.987)
PHIVTX2	13305 (0.994)	41614 (0.995)	10365 (0.996)	6879 (0.994)
DRP	13230 (0.994)	41374 (0.994)	10303 (0.994)	6832 (0.993)
A_{tgkin}	0.9088 ± 0.0024	0.9139 ± 0.0013	0.9120 ± 0.0027	0.9182 ± 0.0032
$A_{K\pi_2}$	0.8745 ± 0.0027	0.8711 ± 0.0015	0.8676 ± 0.0031	0.8765 ± 0.0037

Table 5.4: K_{π_2} -based acceptances of cuts. The quoted uncertainties are purely statistical. Table entries are described in section 5.3 of the text. The OPSVETO_LKB cut is not applied to the 1995 data (see section C.3.2). The various SETUP's are defined in table 5.5.

K_{π_2} SETUP	component cuts
SETUP _{ops}	BAD_RUN, BAD_STC, $K_{\pi_2}(2)$ trigger, all reconstruction cuts, all beam function cuts, all beam and kinematic pathology cuts (except those whose acceptances are being measured in table 5.4), photon energy in barrel+EC+RD > 200 MeV, all TD cuts except TDECON, TDVEL, EV5, and TDLIK3, 2σ cut on the K_{π_2} peak R , E , and P
SETUP _{tgkin}	SETUP _{ops} , A_{ops} cuts, TGPVCUT

Table 5.5: SETUP cuts used in the K_{π_2} -based acceptance measurement shown in table 5.4. $K_{\pi_2}(2)$ trigger is an offline reproduction of the $K_{\pi_2}(2)$ trigger.

which involve the momentum-energy correlation, range-momentum correlation, range-energy correlation, and scattering of pions in the RS. The structure and results of the π_{scat} -based kinematic acceptance study are shown in table 5.6, which lists the number of surviving π_{scat} monitor events from the 1995, 1996, 1997a, and 1997b data sets after each cut is applied, and the corresponding acceptance of each cut. All setup cuts in table 5.6 are defined in table 5.7. Because π_{scat} events do not arise from kaon decay in the target, the reconstruction of the track in the target is poor, leading to uncertainties in R , E , and P which define the $\pi^+\nu\bar{\nu}(1)$ signal region (i.e., the BOX cut). The BOX cut is part of the setup cuts, and the π_{scat} -based kinematic acceptance is a function of how tightly the BOX cut encompasses the pion band, so there is a systematic uncertainty in the acceptance which is estimated by varying the BOX cut. The appropriate variations in R , E , and P are found by comparing π_{scat} and $K_{\pi 2}$ pion mass resolutions. These are found to be 10.4 and 8.6 MeV/ c^2 respectively, where mass is defined by $(P^2 - E^2)/2E$. So the fractional uncertainty in π_{scat} target track reconstruction is roughly $\sqrt{(10.4)^2 - (8.6)^2}/140 = 4.2\%$. The contributions of P and E to the mass resolution are assumed to be roughly equal, so their uncertainties are $4.2\%/\sqrt{2} = 3.0\%$. R scales approximately linearly with E , so the uncertainty in R is also expected to be 3.0%. Expanding and shrinking the BOX cut at the high and low sides by 3.0% define “large” and “small” BOX cuts which, when used in the setup, define lower and upper limits to the π_{scat} -based kinematic acceptance, $A_{\pi_{scat}}^{large}$ and $A_{\pi_{scat}}^{small}$. The systematic uncertainty is given by $\pm 0.5 \cdot (A_{\pi_{scat}}^{large} - A_{\pi_{scat}}^{small})$. The final value for the π_{scat} -based kinematic acceptance, $A_{\pi_{scat}}^{final}$, comes from the measurement where the standard BOX cut is used in the setup. Note that the acceptance of the MASS cut is evaluated only using the final BOX cut in the setup, because the pion mass resolution for $K^+ \rightarrow \pi^+\nu\bar{\nu}$ events is similar to that for $K_{\pi 2}$ events, not π_{scat} events.

5.5 π_{scat} -based TD Acceptance

Events arising from beam pions scattering into the detector are also similar to $K^+ \rightarrow \pi^+\nu\bar{\nu}$ events in that both involve pion tracks which have stopping layers roughly uniformly

cut	1995 (acc.)	1996 (acc.)	1997a (acc.)	1997b (acc.)
large BOX, SETUP $_{\pi_{scat}}$	424	1800	466	438
MASS	746 (1.000)	2807 (0.961)	738 (0.944)	684 (0.961)
RNGMOM	710 (0.952)	2715 (0.967)	719 (0.974)	661 (0.966)
CHIMAX	705 (0.993)	2691 (0.991)	709 (0.986)	655 (0.991)
CL_RSDEDX	688 (0.976)	2622 (0.974)	681 (0.961)	636 (0.971)
RSLIKE	635 (0.923)	2423 (0.924)	638 (0.937)	608 (0.956)
CHIRF(xy)	619 (0.975)	2303 (0.950)	607 (0.951)	570 (0.938)
CHIRF(z)	611 (0.987)	2234 (0.970)	582 (0.959)	558 (0.979)
CHIRF_NHZ	611 (1.000)	2224 (0.996)	577 (0.991)	553 (0.991)
$A_{\pi_{scat}}^{large}$	0.8190 ± 0.0168	0.7615 ± 0.0096	0.7382 ± 0.0197	0.7771 ± 0.0186
final BOX, SETUP $_{\pi_{scat}}$	424	1800	466	438
MASS	424 (1.000)	1730 (0.961)	440 (0.944)	421 (0.961)
RNGMOM	406 (0.958)	1685 (0.974)	429 (0.975)	407 (0.967)
CHIMAX	403 (0.993)	1671 (0.992)	424 (0.988)	404 (0.993)
CL_RSDEDX	396 (0.983)	1637 (0.980)	414 (0.976)	395 (0.978)
RSLIKE	375 (0.947)	1545 (0.944)	389 (0.940)	383 (0.970)
CHIRF(xy)	371 (0.989)	1474 (0.954)	374 (0.961)	362 (0.945)
CHIRF(z)	365 (0.984)	1429 (0.969)	358 (0.957)	359 (0.992)
CHIRF_NHZ	365 (1.000)	1424 (0.997)	355 (0.992)	356 (0.992)
$A_{\pi_{scat}}^{final}$	0.8608 ± 0.0168	0.7911 ± 0.0096	0.7618 ± 0.0197	0.8128 ± 0.0186
small BOX, SETUP $_{\pi_{scat}}$	424	1800	466	438
MASS	102 (1.000)	378 (0.961)	99 (0.944)	70 (0.961)
RNGMOM	99 (0.971)	369 (0.976)	97 (0.980)	69 (0.986)
CHIMAX	99 (1.000)	365 (0.989)	97 (1.000)	69 (1.000)
CL_RSDEDX	98 (0.990)	358 (0.981)	96 (0.990)	67 (0.971)
RSLIKE	96 (0.980)	346 (0.966)	94 (0.979)	67 (1.000)
CHIRF(xy)	94 (0.979)	337 (0.974)	89 (0.947)	64 (0.955)
CHIRF(z)	93 (0.989)	328 (0.973)	86 (0.966)	64 (1.000)
CHIRF_NHZ	93 (1.000)	325 (0.991)	85 (0.988)	62 (0.969)
$A_{\pi_{scat}}^{small}$	0.9118 ± 0.0168	0.8264 ± 0.0096	0.8107 ± 0.0197	0.8513 ± 0.0186
$A_{\pi_{scat}}$	0.8608 $\pm 0.0168^{stat}$ $\pm 0.0464^{syst}$	0.7911 $\pm 0.0096^{stat}$ $\pm 0.0324^{syst}$	0.7618 $\pm 0.0197^{stat}$ $\pm 0.0362^{syst}$	0.8128 $\pm 0.0186^{stat}$ $\pm 0.0371^{syst}$

Table 5.6: π_{scat} -based acceptances of kinematic cuts. Table entries are described in section 5.4 of the text. The MASS and CHIRF_NHZ cuts are not applied to the 1995 data (see section C.3.1). The various SETUP's are defined in table 5.7.

π_{scat} SETUP	component cuts
SETUP $_{\pi_{scat}}$	BAD_RUN, BAD_STC, all PASS1 cuts, $E_{B4} \leq 1.3$ MeV, $ t_{\pi} - t_{RS} < 5$ ns, ICBIT, $ t_{IC} - t_{RS} < 5$ ns, TARGF, DTGTPP, RTDIF, TGQUALT, TGZFOOL, BHTRS, CKTRS, CKTAIL, PV in the RS only, all TD cuts, COS3D, LAYV4
final BOX	$33 \leq R \leq 40$ cm, $115 \leq E \leq 135$ MeV, $211 \leq P \leq 229$ MeV/c
small BOX	$34.0 \leq R \leq 38.8$ cm, $118.4 \leq E \leq 131.0$ MeV, $217.3 \leq P \leq 222.2$ MeV/c
large BOX	$32.0 \leq R \leq 41.2$ cm, $111.6 \leq E \leq 139.0$ MeV, $204.7 \leq P \leq 235.8$ MeV/c

Table 5.7: SETUP cuts used in the π_{scat} -based kinematic acceptance measurement shown in table 5.6. E_{B4} , t_{π} , t_{RS} , and t_{IC} are defined in Appendix D.

distributed between layers 11 and 18, which is the range of stopping layers required by the LAYV4 cut. Therefore, “clean” beam pion scattering events (i.e., with no non-track activity in the RS) from the π_{scat} monitor data (see section 3.3) are used to measure the acceptances of online and offline TD cuts, which require observation of the $\pi \rightarrow \mu \rightarrow e$ decay signature in and around the stopping counter. The structure and results of the π_{scat} -based TD acceptance study are shown in table 5.8, which lists the number of surviving π_{scat} monitor events from the 1995, 1996, 1997a, and 1997b data sets after each cut is applied, and the corresponding acceptance of each cut. All setup cuts in table 5.8 are defined in table 5.9. After the 1995 PASS1 analysis, new TD pulse shape calibration files for 1995 were created, so the FITPI cut (which involves $\pi \rightarrow \mu$ double-pulse fitting in the stopping counter) changed for subsequent passes of the 1995 data. π_{scat} monitor events passing all other cuts in the π_{scat} -based TD acceptance study are re-run through the 1995 PASS1 code in order to get the additional acceptance loss from the 1995 PASS1 FITPI cut.

A concern in the TD acceptance measurement is TD-kinematic correlation. If the kinematic setup cuts are correlated with TD cuts, then the application of these setup cuts will likely result in a TD acceptance which is too high. For example, the RSDEDX cuts (CHIMAX and CL_RSDEDX) may be correlated with the ELVETO cut via muon-time accidentals along the track affecting the track dE/dx , thereby causing events to fail the RSDEDX cut as well as the ELVETO cut. However, this correlation is expected to be small, because the dE/dx values from RS counter energies along the track come from TD PH energies instead

cut	1995 (acc.)	1996 (acc.)	1997a (acc.)	1997b (acc.)
SETUP _{TD} ⁽¹⁾	1153	4002	1124	1027
FITPI(bad data)	1135 (0.984)	3902 (0.975)	1100 (0.979)	996 (0.970)
FITPI(counting)	800 (0.705)	2806 (0.719)	786 (0.715)	731 (0.734)
L11.and.L12	598 (0.748)	2522 (0.899)	664 (0.845)	555 (0.759)
TDCUT	568 (0.950)	2432 (0.964)	643 (0.968)	547 (0.986)
RSHEX2	558 (0.982)	2388 (0.982)	643 (1.000)	547 (1.000)
TDTCON	554 (0.993)	2375 (0.995)	642 (0.998)	544 (0.995)
TDDFA1	554 (1.000)	2207 (0.929)	588 (0.916)	503 (0.925)
EV5	426 (0.769)	1695 (0.768)	449 (0.764)	437 (0.869)
ELVETO	393 (0.923)	1626 (0.959)	436 (0.971)	418 (0.957)
TDFOOL	393 (1.000)	1624 (0.999)	435 (0.998)	418 (1.000)
TDECON	393 (1.000)	1522 (0.937)	410 (0.943)	402 (0.962)
TDVEL	393 (1.000)	1434 (0.942)	386 (0.941)	374 (0.930)
TDLIK2	359 (0.913)	1360 (0.948)	364 (0.943)	346 (0.925)
TDLIK3	356 (0.992)	1345 (0.989)	360 (0.989)	336 (0.971)
TDDFA2	336 (0.944)	1291 (0.960)	344 (0.956)	321 (0.955)
$A_{TD}^{(1)}$	0.2914 ± 0.0134	0.3226 ± 0.0074	0.3060 ± 0.0137	0.3126 ± 0.0145
SETUP _{TD} ⁽²⁾	1055	3481	967	901
FITPI(bad data)	1040 (0.986)	3400 (0.977)	947 (0.979)	878 (0.974)
FITPI(counting)	734 (0.706)	2468 (0.726)	679 (0.717)	649 (0.739)
A_{FITPI}^{count}	0.706 ± 0.014	0.726 ± 0.008	0.717 ± 0.015	0.739 ± 0.015
A_{FITPI}^{area}	0.710 ± 0.028	0.719 ± 0.022	0.730 ± 0.030	
L11.and.L12	553 (0.753)	2224 (0.901)	575 (0.847)	497 (0.766)
TDCUT	525 (0.949)	2147 (0.965)	560 (0.974)	492 (0.990)
RSHEX2	517 (0.985)	2110 (0.983)	560 (1.000)	492 (1.000)
TDTCON	515 (0.996)	2098 (0.994)	559 (0.998)	490 (0.996)
TDDFA1	515 (1.000)	1955 (0.932)	512 (0.916)	454 (0.927)
EV5	401 (0.779)	1504 (0.769)	393 (0.768)	396 (0.872)
ELVETO	370 (0.923)	1443 (0.959)	382 (0.972)	377 (0.952)
TDFOOL	370 (1.000)	1442 (0.999)	381 (0.997)	377 (1.000)
TDECON	370 (1.000)	1349 (0.936)	359 (0.942)	363 (0.963)
TDVEL	370 (1.000)	1269 (0.941)	339 (0.944)	337 (0.928)
TDLIK2	339 (0.916)	1205 (0.950)	321 (0.947)	311 (0.923)
TDLIK3	336 (0.991)	1194 (0.991)	317 (0.988)	304 (0.977)
TDDFA2	317 (0.943)	1146 (0.960)	302 (0.953)	291 (0.957)
$A_{TD}^{(2)}$	0.3005 ± 0.0141	0.3292 ± 0.0080	0.3123 ± 0.0149	0.3230 ± 0.0156
A_{TD}^{low}	0.2914 ± 0.0134	0.3226 ± 0.0074	0.3060 ± 0.0137	0.3126 ± 0.0145
A_{TD}^{high}	0.3047 ± 0.0143	0.3338 ± 0.0081	0.3167 ± 0.0151	0.3275 ± 0.0158
SETUP _{TD} ^{P1}	2464	—	—	—
PASS1 FITPI	2422	—	—	—
A_{TD}^{P1}	0.9830 ± 0.0026	—	—	—
A_{TD}	0.2930 $\pm 0.0096^{stat}$ $\pm 0.0065^{syst}$	0.3282 $\pm 0.0055^{stat}$ $\pm 0.0056^{syst}$	0.3114 $\pm 0.0102^{stat}$ $\pm 0.0054^{syst}$	0.3201 $\pm 0.0107^{stat}$ $\pm 0.0075^{syst}$

Table 5.8: π_{scat} -based acceptances of TD cuts. Table entries are described in section 5.5 of the text. The TDDFA1, TDECON, and TDVEL cuts are not applied to the 1995 data (see section C.3.4). L1.2 became active in 1997b. The various SETUP's are defined in table 5.9.

π_{scat} SETUP	component cuts
SETUP $_{TD}^{(1)}$	SETUP $_{\pi_{scat}}$ from table 5.6, with BOX, LAYV4, RNGMOM, ZFRF, ZUTOOUT, LAYER14, and EICKIN, but without the TD cuts
SETUP $_{TD}^{(2)}$	SETUP $_{TD}^{(1)}$, CL_RSDEDX, CHIMAX, CHIRF, CHIRF_NHZ
SETUP $_{TD}^{P1}$	$E_{B4} < 1.5$ MeV, CPITRS, BWTRS, all PASS1 cuts, PVCUT, TGPVCUT, all $A_{TD}^{low,high}$ cuts, COS3D, LAYV4, and large BOX (as defined in table 5.6)

Table 5.9: SETUP cuts used in the π_{scat} -based TD acceptance measurement shown in table 5.8. E_{B4} is defined in Appendix D.

of ADC energies when the ADC/TD PH energy ratio is found to be bigger than a critical value, thereby indicating the presence of an accidental (see UTC/RANGE/TARGET in section C.1). A correlation may also exist between the CHIRF setup cut and TD pulse-fitting cuts (e.g., TDDFA1, TDDFA2, TDLIK2). As described in section C.3.1, CHIRF is a χ^2 cut which involves the pion energy in the stopping counter, calculated as total pion plus decay-muon ADC energy, minus the muon energy found from a double-pulse fit to the TD data. This stopping counter pion energy could be affected by a poor $\pi \rightarrow \mu$ double-pulse fit, which can happen when the pion decays early and the muon pulse is buried underneath the tail of the pion pulse. This usually makes the pion energy too small which, for example, can cause the event to preferentially fail both the CHIRF and TDDFA1 cuts.

To test these correlations, the TD acceptance is measured without and with the RSD-EDX and CHIRF cuts in the setup, giving rise to the values of $A_{TD}^{(1)}$ and $A_{TD}^{(2)}$, respectively, in table 5.8. The RSD-EDX, CHIRF correlations are shown to be $< 3\%$, which is smaller than the statistical uncertainties in the TD acceptance measurements. In fact, the slightly lower acceptances seen when the RSD-EDX and CHIRF cuts are removed from the setup may not be due to correlations, but rather due to the presence of muons and/or pion absorption and decay in flight (DIF) introduced into the data sample by turning these cuts off. This

	# events	fail UFATE	NIDIF contamination
no setup	23566	2482	10.5%
SETUP1	5451	78	1.4%
SETUP2	5408	71	1.3%
SETUP3	5439	71	1.3%

Table 5.10: Pion-nuclear absorption and decay in flight (NIDIF) contamination in the 1995 $K^+ \rightarrow \pi^+ \nu \bar{\nu}$ UMC data. The total number of $K^+ \rightarrow \pi^+ \nu \bar{\nu}$ events in the UMC data sample, the number that fail the UFATE cut (i.e., the number of events where the pion undergoes NI or DIF), and the resulting NIDIF contamination are listed for 4 different groups of setup cuts applied to the $K^+ \rightarrow \pi^+ \nu \bar{\nu}$ data. “no setup” refers to no setup cuts applied. SETUP1 includes reconstruction, PV, and fiducial cuts, plus a two-sided RNGMOM cut to isolate the pion band, the BOX and CHIRF cuts. SETUP2 is SETUP1 plus the RSDEDX cut. SETUP3 is SETUP2 with the two-sided RNGMOM cut replaced by the standard RNGMOM cut (see section C.3.5). A NIDIF contamination of roughly 1.4% is indicated for $K^+ \rightarrow \pi^+ \nu \bar{\nu}$ events, even after kinematic cuts such as RSDEDX and CHIRF are applied.

contamination is estimated to be as high as 5% [41]. However, it’s not clear whether the 3% change in TD acceptance comes from correlations or contaminations, so a lower limit to the TD acceptance is assigned, $A_{TD}^{low} = A_{TD}^{(1)}$, based on the measurement without RSDEDX and CHIRF in the setup. Furthermore, a study of UMC-generated pions from $K^+ \rightarrow \pi^+ \nu \bar{\nu}$ shows that about 1.4% of these pions which pass all kinematic setup cuts (including RSDEDX and CHIRF) are absorbed or DIF (see table 5.10). Therefore, the π_{scat} data sample used in the TD acceptance measurement may have a 1.4% contamination of pion absorption and DIF, even after the RSDEDX and CHIRF cuts are applied. The acceptance loss from these types of events is measured elsewhere (see section 5.8), so this loss should not be counted here. An upper limit to the TD acceptance is therefore assigned based on the measurement with RSDEDX and CHIRF in the setup, plus 1.4%: $A_{TD}^{high} = 1.014 \cdot A_{TD}^{(2)}$. The systematic uncertainty in the TD acceptance due to contaminations/correlations is given by $\pm 0.5 \cdot (A_{TD}^{high} - A_{TD}^{low})$. The final value for the π_{scat} -based TD acceptance, A_{TD} , is given by the average of the high and low values, as shown in table 5.8.

The FITPI cut is the primary cut which requires a good $\pi \rightarrow \mu$ double-pulse fit in the stopping counter. In table 5.8, the acceptance of the FITPI cut is measured before that of the other TD cuts by simply counting the number of π_{scat} events that pass FITPI. This

method for measuring the acceptance of the FITPI cut is called the “counting” method. It assumes that the π_{scat} data sample has been appropriately selected such that none of the FITPI acceptance loss arises from pion absorption or DIF events (which are accounted for elsewhere – see section 5.8). The only acceptance losses are assumed to arise from early $\pi \rightarrow \mu$ decay (such that the muon pulse is buried underneath the pion pulse), accidentals in the stopping counter (which can cause confusion in the assignment of the pion, muon, and accidental pulses), early $\mu \rightarrow e$ decay (which again can sometimes cause confusion in the assignment of pion, muon, and electron pulses), and muon escape from the stopping counter. Another method for measuring the acceptance of the FITPI cut, called the “area” method, attempts to account for each type of event that fails the FITPI cut separately, such that any potential losses from pion absorption or DIF are explicitly excluded from the acceptance calculation. The area-method acceptance of the FITPI cut is calculated according to

$$A_{FITPI} = \frac{M_P}{M_A + \Delta M_A} \cdot \epsilon_{\mu escape}. \quad (5.1)$$

M_P is the number of events in the π_{scat} data sample that pass the FITPI cut. M_A is the integrated number of events under a pion-lifetime fit to these FITPI-passed events, and accounts for the FITPI acceptance loss that arises from early $\pi \rightarrow \mu$ decays where the muon pulse can't be seen. ΔM_A is the “hand-scan correction”, which is the number of events with good $\pi \rightarrow \mu$ decay signatures which fail the FITPI cut due to the presence of accidental and/or electron pulses, as described above. This number is found from a visual inspection of the TD pulses for events which fail FITPI. $\epsilon_{\mu escape} = 0.982$ [56] is a correction for missed muon pulses because the muon escapes the stopping counter. The area-method acceptance of the FITPI cut is calculated in detail elsewhere [41], and the results are shown in table 5.5. The area-method acceptance agrees with the counting-method acceptance for each of the 1995, 1996, 1997a, and 1997b data sets, so pion absorption and DIF are not likely to significantly contaminate the π_{scat} data sample used to calculate the TD acceptance (perhaps due to the RSDIDX, CHIRF, and BOX cuts which are part of $SETUP_{TD}^{(2)}$ in table 5.8. These cuts select pion tracks which have the expected counter-by-counter energy loss and trajectory for charged pions whose total energy deposit in the RS is consistent with the momentum

measured in the UTC). The agreement of the area-method and counting-method results further suggests that all types of acceptance losses of the FITPI cut have been accounted for. For ease of calculation then, the counting-method results are used in the total TD acceptance calculation shown in table 5.8.

5.6 μ -veto Accidental Loss

The $\pi^+\nu\bar{\nu}(1)$ trigger involves a muon veto which requires that no hit be present at track time in layer 19, 20, or 21 of the RS in a ct sector, defined by $\overline{19_{ct} + 20_{ct} + 21_{ct}}$, where a ct sector is defined as the $T \cdot 2$ sector or within 2 sectors clockwise of the $T \cdot 2$ sector as viewed from downstream of the detector (see section 3.3). Candidate $K^+ \rightarrow \pi^+\nu\bar{\nu}$ events can therefore be lost if an accidental gives rise to one of these hits. To estimate this acceptance loss, $K_{\mu 2}$ decays from the $K_{\mu 2}(1)$ monitor data (see section 3.3) are examined for events which have a hit in layer 19, 20, or 21 in a 10 ns pre-track-time window in any of 12 adjacent sectors opposite the stopping sector. Because this hit occurs before track time and is on the opposite of the detector, it is assumed to be unrelated to the $K_{\mu 2}$ decay and to arise from an accidental. The total number of events in the data sample is denoted by M_{tot} , and the number of events which satisfy the above definition of an accidental hit is denoted M_{acc} . Because the trigger is sensitive to accidentals in a ± 20 ns window around the detector strobe, and because ct in 19_{ct} defines 3 sectors, the accidental muon-veto acceptance, $A_{\bar{\mu}}^{acc}$, is given by

$$A_{\bar{\mu}}^{acc} = \left(M_{tot} - M_{acc} \cdot \frac{40 \text{ ns}}{10 \text{ ns}} \cdot \frac{3 \text{ sectors}}{12 \text{ sectors}} \right) / M_{tot} = (M_{tot} - M_{acc}) / M_{tot}. \quad (5.2)$$

Values of M_{tot} , $M_{tot} - M_{acc}$, and $A_{\bar{\mu}}^{acc}$ are shown in table 5.11.

5.7 $T \cdot 2$ Efficiency

The $\pi^+\nu\bar{\nu}(1)$ trigger requires coincident hits in layers 1 and 2 and a hit in layer 6 or 7 of the RS, defined by $T \cdot 2$ and $6_{ct} + 7_{ct}$ (see section 3.3). Candidate $K^+ \rightarrow \pi^+\nu\bar{\nu}$ events can therefore be lost if one of these counters is “inefficient”, that is, if the scintillation light

	M_{tot}	$M_{tot} - M_{acc}$	A_{μ}^{acc}
1995	106237	105432	0.9924 ± 0.0003
1996	93773	93119	0.9930 ± 0.0003
1997a	29822	29599	0.9925 ± 0.0005
1997b	19517	19400	0.9940 ± 0.0006

Table 5.11: Accidental-induced acceptance of the trigger μ -veto, given by $A_{\mu}^{acc} = (M_{tot} - M_{acc})/M_{tot}$. M_{tot} and M_{acc} are defined in section 5.6 of the text. The quoted uncertainties are purely statistical.

induced by the charged pion track liberates 0 photoelectrons at the RS PMT photocathode, when a mean value of \bar{n} photoelectrons is expected. The probability of seeing n photoelectrons when \bar{n} photoelectrons are expected is given by the Poisson distribution:

$$P(n; \bar{n}) = \frac{\bar{n}^n}{n!} e^{-\bar{n}} \quad (5.3)$$

So the probability of seeing 0 photoelectrons is

$$P(n = 0; \bar{n}) = e^{-\bar{n}} \quad (5.4)$$

Layers 2, 6, and 7 respond to charged tracks with about 12 photoelectrons per MeV [57]. These counters are each about 2 cm thick, so a minimum ionizing particle deposits about 4 MeV per counter, giving rise to about 50 photoelectrons. The T (layer 1) counters, however, only give rise to about 3 photoelectrons per MeV [57], and are only about 0.6 cm thick. A minimum ionizing particle therefore deposits about 1.2 MeV, giving rise to about 4 photoelectrons. The probability of seeing 0 photoelectrons in layers 2, 6, and 7 is very small (e^{-50}), but it is not insignificant for the T counters ($e^{-4} = 2\%$). Therefore, the T · 2 efficiency needs to be calculated in order to find the corresponding acceptance loss for $K^+ \rightarrow \pi^+ \nu \bar{\nu}$ events.

The T · 2 efficiencies for $K^+ \rightarrow \pi^+ \nu \bar{\nu}$ and $K^+ \rightarrow \pi^+ f$ events are found by interpolating the T · 2 efficiencies measured for $K_{\mu 2}$ and $K_{\pi 2}$ decays. Monitor data with the sole trigger requirement of K_B (see section 3.3) is separated into $K_{\mu 2}$ and $K_{\pi 2}$ decays according to the cuts in tables 5.24 and 5.28 of sections 5.9.1 and 5.9.2), respectively. The number of events with a valid T · 2, divided by the total number of events in each of the $K_{\pi 2}$ and $K_{\mu 2}$ data

samples, gives the T · 2 efficiencies for both $K_{\pi 2}$ and $K_{\mu 2}$ decays. The $K_{\pi 2}$ and $K_{\mu 2}$ T · 2 efficiencies, shown as a function of run number in figure 5.1, are both about 93% in 1995, but the $K_{\mu 2}$ efficiency is as low as 83% and is about 5% lower than the $K_{\pi 2}$ efficiency in 1996-7. The T · 2 inefficiency is mainly due to T-counter inefficiency, often when tracks are near the air gap between sectors as shown in figure 5.2. The top and bottom plots in figure 5.2 show the number of $K_{\pi 2}$ and $K_{\mu 2}$ events (1995-7 data combined) with a missing T · 2 as a function of azimuthal angle ϕ of the track at the T counter. The azimuthal angle ϕ is shown in figure 3.7 and defined in Appendix D. The T · 2 efficiencies vary from year to year (see figure 5.1), but figure 5.2 can be used to estimate the T · 2 inefficiency due to gaps between sectors, which is $4.1 \pm 0.2\%$ [41]. Summing over the 1995-7 data, the average $K_{\pi 2}$ and $K_{\mu 2}$ T · 2 inefficiencies from figure 5.1 are about 8.5% and 11.7%, respectively. Excluding the gap inefficiency, the T · 2 inefficiency for $K_{\pi 2}$ decays is therefore about 4.4%, and that for $K_{\mu 2}$ decays is about 7.6%. The $K_{\pi 2}$ and $K_{\mu 2}$ T · 2 inefficiencies are both somewhat higher than the 2% inefficiency estimated above, perhaps due to poorer RS counter quality than expected. They also do not agree with each other, perhaps due to differing energy deposits in the T counters for 109 MeV $K_{\pi 2}$ pions and 152 MeV $K_{\mu 2}$ muons. The run dependence of the T · 2 efficiency, particularly that for $K_{\pi 2}$ decays in 1997 (see figure 5.1) is not understood, though it may be related to the online RS energy calibration and adjustment of RS PMT high voltages.

The T · 2 efficiencies for pion tracks arising from kaon decay into $\pi^+\nu\bar{\nu}$ and πf are found as follows. According to Eq. (5.4), the probability of seeing 0 photoelectrons from the T counter is given by

$$P(0) = e^{-\bar{n}} = 1 - \epsilon_{T,2} - 0.041 \quad (5.5)$$

where $\epsilon_{T,2}$ is the total T · 2 efficiency, and 0.041 is the gap inefficiency discussed above. The expected number of photoelectrons, \bar{n} , is given by

$$\bar{n} = \epsilon_q \cdot \frac{E}{E_{ex}} \cdot e^{-d/L_0} \quad (5.6)$$

where ϵ_q is the photocathode quantum efficiency; E is the energy deposited in the T counter; E_{ex} is the scintillator molecular excitation energy; d is the distance between the photocathode

T · 2 efficiency as a function of run number

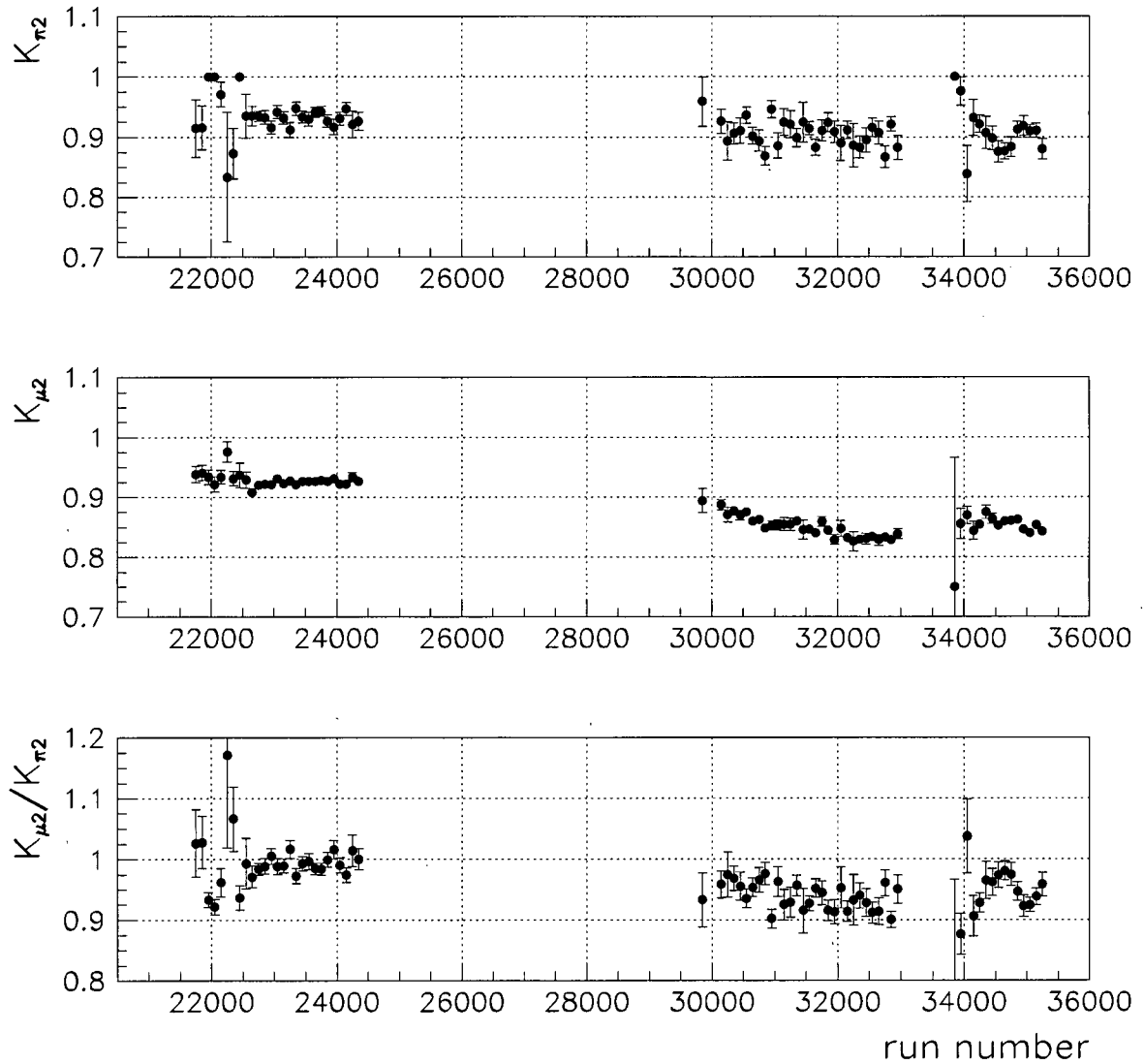


Figure 5.1: T · 2 efficiency as a function of run number for $K_{\pi 2}$ and $K_{\mu 2}$ decays, and the $K_{\mu 2}/K_{\pi 2}$ ratio of efficiencies. The three clusters of data, from left to right, correspond to 1995, 1996, and 1997 data.

ϕ at the T counter for T.2 misses

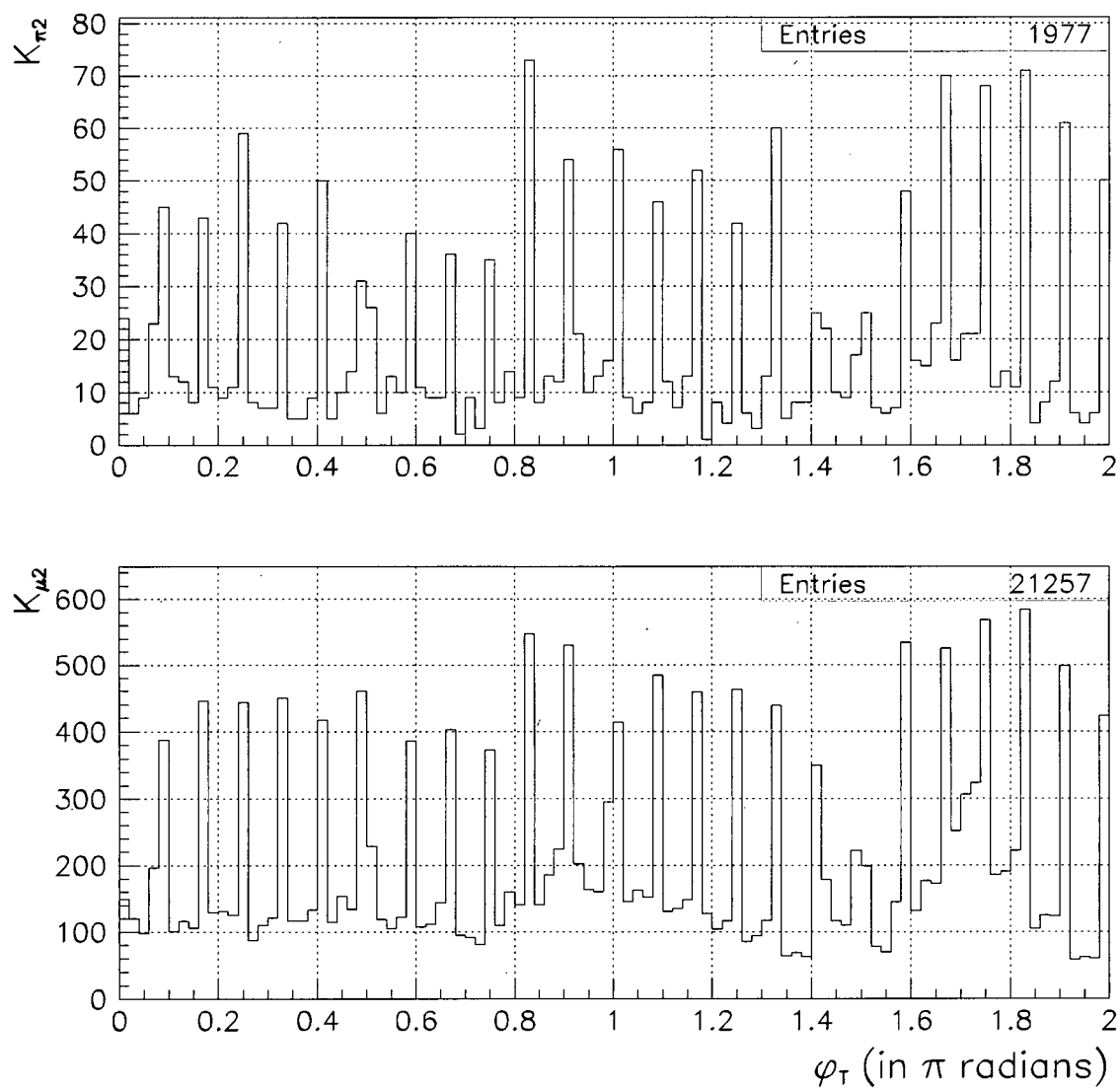


Figure 5.2: Number of T · 2-inefficient events for $K_{\pi 2}$ (top) and $K_{\mu 2}$ (bottom) decays as a function of the azimuthal angle ϕ of the track at the T counter (in π radians).

and the energy deposit; and L_0 is the photon attenuation length in the scintillator. If d is fixed at some value (say, in the middle of the counter of length L such that $d = L/2$), then

$$\bar{n} = kE \quad (5.7)$$

Combining Eqs. (5.5) and (5.7) gives

$$\epsilon_{T \cdot 2} = 1 - 0.041 - e^{-kE} \quad (5.8)$$

From Eq. (5.7), k is the number of photoelectrons per MeV. $\epsilon_{T \cdot 2}(K_{\pi 2}, K_{\mu 2})$ is measured using monitor data (as shown in figure 5.1), whereas E for $K_{\pi 2}$ and $K_{\mu 2}$ decays and kaon decays into $\pi^+\nu\bar{\nu}$ and πf is taken from UMC data. $\epsilon_{T \cdot 2}$ and E for both $K_{\pi 2}$ and $K_{\mu 2}$ decays are plugged into Eq. (5.8) to get 2 independent values of k . This is done by varying k and multiplying by E until the mean of the $1 - 0.041 - e^{-kE}$ distribution gives the measured average value of $\epsilon_{T \cdot 2}$ for each year. The final value of k is the average value of k calculated using $K_{\pi 2}$ and $K_{\mu 2}$ decays.

The E787 detector as simulated by UMC has realistic gaps between T counters, so T · 2 inefficiency due to gaps is accounted for elsewhere (A_{trig} , calculated in section 5.8). Therefore, only the non-gap T · 2 efficiency is calculated here, $\epsilon_{T \cdot 2}^{ng}$, which, in the case of kaon decay into $\pi^+\nu\bar{\nu}$ and πf , is found from the mean of the $1 - e^{-kE}$ distribution, where k is measured as described above, and E comes from UMC data. The systematic uncertainty in $\epsilon_{T \cdot 2}^{ng}(\pi^+\nu\bar{\nu}, \pi f)$ is half the difference of the maximum and minimum values of $\epsilon_{T \cdot 2}^{ng}(\pi^+\nu\bar{\nu}, \pi f)$ as found using the $K_{\pi 2}$ and $K_{\mu 2}$ values of k . The non-gap T · 2 efficiencies for $K_{\pi 2}$ and $K_{\mu 2}$ decays are found by dividing out the gap efficiency ($95.9 \pm 0.2\%$) from the total T · 2 efficiencies measured using monitor data. Results are shown in table 5.12.

5.8 UMC-based Acceptances

The acceptances of several cuts used in the analysis depend on the kinematics of pion tracks, and so cannot be estimated using $K_{\pi 2}$, $K_{\mu 2}$, or beam pion data. Instead, UMC-generated $K^+ \rightarrow \pi^+\nu\bar{\nu}$ and $K^+ \rightarrow \pi^+ f$ data is used to account for

	$\epsilon_{T,2}^{ng}(K_{\pi 2})$	$k_{K_{\pi 2}}$	$\epsilon_{T,2}^{ng}(K_{\mu 2})$	$k_{K_{\mu 2}}$	k	$\epsilon_{T,2}^{ng}(\pi^+\nu\bar{\nu})$	$\epsilon_{T,2}^{ng}(\pi f)$
1995	0.9721 ± 0.0033	2.26	0.9645 ± 0.0022	2.61	2.44	0.976 ± 0.005	0.975 ± 0.005
1996	0.9420 ± 0.0039	1.76	0.8849 ± 0.0024	1.66	1.71	0.930 ± 0.006	0.928 ± 0.006
1997a	0.9326 ± 0.0064	1.66	0.8967 ± 0.0031	1.74	1.70	0.929 ± 0.004	0.927 ± 0.004
1997b	0.9437 ± 0.0072	1.75	0.8821 ± 0.0035	1.64	1.70	0.928 ± 0.008	0.926 ± 0.008

Table 5.12: Non-gap T · 2 efficiencies, $\epsilon_{T,2}^{ng}$, for $K_{\pi 2}$ and $K_{\mu 2}$ decays and kaon decays into $\pi^+\nu\bar{\nu}$ and πf . The uncertainties in $\epsilon_{T,2}^{ng}(K_{\pi 2}, K_{\mu 2})$ are both statistical (counting events with missing T · 2) and systematic (from estimation of the gap inefficiency); the uncertainties in $\epsilon_{T,2}^{ng}(\pi^+\nu\bar{\nu}, \pi f)$ are primarily systematic. k is the average of $k_{K_{\pi 2}}$ and $k_{K_{\mu 2}}$, which are the number of photoelectrons per MeV in the T counters, as found from $K_{\pi 2}$ and $K_{\mu 2}$ decays, respectively.

- the acceptance of the level 0 trigger (see section 3.3), in the absence of accidentals;
- losses due to pion absorption and decay in flight, and pion decay in the gaps between RS counters, because the $\pi \rightarrow \mu \rightarrow e$ decay sequence is not observed in the stopping counter;
- losses due to pion tracks which wrap back around on themselves, such that the trigger assigns the wrong stopping counter;
- the acceptance of cuts sensitive to the length of pion tracks: LAYV4, COS3D, LAYER14, ZFRF, and ZUTOUT;
- the acceptance of cuts on the kinematic phase space: BOX and BOX'.

As described in section 3.2.6, the generation of UMC data involves propagation of kaon decay products into the detector starting from a “real” distribution of kaon stops in the target, as stored in “beam files”. $K^+ \rightarrow \pi^+\nu\bar{\nu}$ and $K^+ \rightarrow \pi^+f$ events are generated with pion-nuclear interactions and pion decay in flight (NIDIF) turned on and off, and acceptances of cuts are measured in both cases. The ratio of the NIDIF-on/NIDIF-off UMC acceptances then gives the acceptance loss due to pion-nuclear interactions and pion decay in flight.

The $\pi^+\nu\bar{\nu}(1)$ level 0 trigger acceptance, A_{trig} , is shown for UMC-generated $K^+ \rightarrow \pi^+\nu\bar{\nu}$ and $K^+ \rightarrow \pi^+f$ events with the 1996 kaon stopping distribution in tables 5.13 and 5.14, respectively, which list the number of surviving events after each trigger condition is applied,

	NIDIF on		NIDIF off	
	# events	(acc.)	# events	(acc.)
KT	200000		100000	
T · 2	77991	(0.3900)	41051	(0.4105)
6 _{ct} + 7 _{ct}	54617	(0.7003)	33600	(0.8185)
μ -veto	54287	(0.9940)	33592	(0.9998)
\overline{BV}	54199	(0.9984)	33592	(1.0000)
\overline{EC}	54166	(0.9994)	33592	(1.0000)
HEX	54099	(0.9988)	33592	(1.0000)
Refined Range	23683	(0.4378)	17991	(0.5356)
$A_{trig}(\pi^+\nu\bar{\nu})$	0.1184 ± 0.0007		0.1799 ± 0.0012	

Table 5.13: UMC-based $K^+ \rightarrow \pi^+\nu\bar{\nu}$ trigger acceptance for 1996 data. The quoted uncertainties are purely statistical. Table entries are described in section 5.8 of the text. KT is the number of $K^+ \rightarrow \pi^+\nu\bar{\nu}$ events generated by UMC. The various trigger conditions are defined in section 3.3, including “ μ -veto” which is defined as $(19_{ct} + 20_{ct} + 21_{ct})$, and “refined range” which is defined as $L0rr1(1) \cdot US + L0rr1(2) \cdot DS$.

and the corresponding acceptance of each condition, for pion NIDIF turned on and off. The acceptance of the online DC requirement is not part of A_{trig} because it is included in the $K_{\mu 2}$ -based acceptance measurement (see table 5.2). Note that A_{trig} for $K^+ \rightarrow \pi^+\nu\bar{\nu}$ is only about half of that for $K^+ \rightarrow \pi^+f$. Pions from $K^+ \rightarrow \pi^+\nu\bar{\nu}$ can have momenta between $P = 0$ and $P = 227$ MeV/ c (see figure 4.3), whereas pions from the two-body decay $K^+ \rightarrow \pi^+f$ always have $P = 227$ MeV/ c (for massless f). Pions from $K^+ \rightarrow \pi^+\nu\bar{\nu}$ are therefore less likely to penetrate layers 1 and 2, layers 6 or 7, and layer 11 of the RS, resulting in lower T · 2, 6_{ct} + 7_{ct}, and refined range acceptances, respectively.

The other, non-trigger UMC-based acceptances are shown for UMC-generated $K^+ \rightarrow \pi^+\nu\bar{\nu}$ and $K^+ \rightarrow \pi^+f$ events with the 1996 kaon stopping distribution in tables 5.15 and 5.16, respectively, which list the number of surviving events after each cut is applied, and the corresponding acceptance of each cut, for pion NIDIF turned on and off. The combined acceptance of the cuts in each of tables 5.15 and 5.16 is called the “fiducial acceptance”, A_{umc} . UFATE, USTMED, and USTOP_HEX are logical bits which are false if: the pion is absorbed or decays in flight; the pion decays in the gap between RS counters; or the pion track wraps back on itself such that the trigger assigns the wrong stopping counter,

	NIDIF on		NIDIF off	
	# events	(acc.)	# events	(acc.)
KT	99998		50000	
T · 2	43877	(0.4388)	22708	(0.4542)
$6_{ct} + 7_{ct}$	36348	(0.8284)	22708	(1.0000)
μ -veto	35613	(0.9798)	22570	(0.9939)
\overline{BV}	35491	(0.9966)	22570	(1.0000)
\overline{EC}	35447	(0.9988)	22570	(1.0000)
HEX	35338	(0.9969)	22570	(1.0000)
Refined Range	24919	(0.7052)	20171	(0.8937)
$A_{trig}(\pi f)$	0.2492 ± 0.0014		0.4034 ± 0.0022	

Table 5.14: UMC-based $K^+ \rightarrow \pi^+ f$ trigger acceptance for 1996 data. The quoted uncertainties are purely statistical. Table entries are described in section 5.8 of the text. KT is the number of $K^+ \rightarrow \pi^+ f$ events generated by UMC. The various trigger conditions are defined in section 3.3, including “ μ -veto” which is defined as $(19_{ct} + 20_{ct} + 21_{ct})$, and “refined range” which is defined as $L0rr1(1) \cdot US + L0rr1(2) \cdot DS$.

respectively. The acceptance of the LAYV4 cut is omitted because it is included in A_{trig} : the refined range and μ -veto requirements ensure that a pion stops in one of RS layers 11 through 18 inclusive. The acceptance of the ZFRF cut (see section C.3.1) is measured after adding 1.0 cm to the UTC-extrapolated z positions of the UMC-generated track in RS counters, because the real UTC and that simulated by UMC are offset by 1.0 cm. The PFBOX cut listed in table 5.16 is the “ πf BOX” cut, defined as a 2σ cut around the pion peak resulting from kaon decay into a pion and a massless familon: $35.5 < R < 40.0$ cm, $120 < E < 135$ MeV and $221 < P < 229$ MeV/ c . The acceptance of the BOX' cut is omitted from table 5.16 because events which pass the PFBOX cut automatically pass the BOX' cut (see section C.3.5). Note that A_{umc} for $K^+ \rightarrow \pi^+ \nu \bar{\nu}$ is only about 2/3 of that for $K^+ \rightarrow \pi^+ f$. This again is due to the different pion momenta spectra for $K^+ \rightarrow \pi^+ \nu \bar{\nu}$ and $K^+ \rightarrow \pi^+ f$, resulting in different acceptances of the BOX cut.

Before measuring the acceptances of the BOX, BOX', and PFBOX cuts, R , E , and P values from UMC-generated events must be scaled and smeared to match the real data. First, values of R , E , and P from the real data are scaled so that the $K_{\pi 2}$ and $K_{\mu 2}$ peak values are the same as the accepted values [16]. The accepted values for $K_{\pi 2}$ decay are

cut	NIDIF on		NIDIF off	
	# events	(acc.)	# events	(acc.)
setup	23636		17977	
UFATE	21157	(0.8951)	17977	(1.0000)
USTMED	21001	(0.9926)	17871	(0.9941)
USTOP_HEX	20608	(0.9813)	17809	(0.9965)
COS3D	19931	(0.9671)	17250	(0.9686)
LAYER14	19862	(0.9965)	17241	(0.9995)
ZFRF	18579	(0.9354)	16054	(0.9312)
ZUTOUT	18578	(0.9999)	16054	(1.0000)
BOX	6914	(0.3722)	6790	(0.4229)
BOX'	6680	(0.9662)	6532	(0.9620)
[BOX' check1]	[6617]	[(0.9570)]	[6453]	[(0.9504)]
[BOX' check2]	[6714]	[(0.9711)]	[6563]	[(0.9666)]
$A_{umc}(\pi^+\nu\bar{\nu})$	0.2826 ± 0.0029		0.3634 ± 0.0036	

Table 5.15: UMC-based $\pi^+\nu\bar{\nu}$ fiducial acceptance for 1996 data. The quoted uncertainties are purely statistical. Table entries are described in section 5.8 of the text. The “# events” after “setup” is the number of UMC-generated $K^+ \rightarrow \pi^+\nu\bar{\nu}$ events remaining at the bottom of table 5.13 after some reconstruction and beam pathology cuts are additionally applied.

cut	NIDIF on		NIDIF off	
	# events	(acc.)	# events	(acc.)
setup	24861		20161	
UFATE	21906	(0.8811)	20161	(1.0000)
USTMED	21701	(0.9906)	19954	(0.9897)
USTOP_HEX	20949	(0.9653)	19902	(0.9974)
COS3D	20059	(0.9575)	18994	(0.9544)
LAYER14	19923	(0.9932)	18961	(0.9983)
ZFRF	18141	(0.9106)	17252	(0.9099)
ZUTOUT	18138	(0.9998)	17249	(0.9998)
BOX	11873	(0.6546)	12285	(0.7122)
PFBOX	10442	(0.8795)	11352	(0.9241)
$A_{umc}(\pi f)$	0.4200 ± 0.0031		0.5631 ± 0.0035	

Table 5.16: UMC-based πf fiducial acceptance for 1996 data. The quoted uncertainties are purely statistical. Table entries are described in section 5.8 of the text. The “# events” after “setup” is the number of UMC-generated $K^+ \rightarrow \pi^+ f$ events remaining at the bottom of table 5.14 after some reconstruction and beam pathology cuts are additionally applied.

$R = 30.37$ cm, $E = 108.55$ MeV and $P = 205.14$ MeV/ c . The accepted values for $K_{\mu 2}$ decay are $R = 54.34$ cm, $E = 152.49$ MeV and $P = 235.53$ MeV/ c . The scaling is performed via

$$X = m_X \cdot X_{raw} + b_X \quad (5.9)$$

where X_{raw} is the peak value of R , E , or P for $K_{\pi 2}$ or $K_{\mu 2}$ decay, measured using SKIM1 (see table 4.5) or $K_{\mu 2}(1)$ monitor data (see section 3.3), respectively; and m_X and b_X are fitted linear scaling constants applied to X_{raw} such that X is the accepted value. The peak values of R , E , and P measured for $K_{\pi 2}$ and $K_{\mu 2}$ decays (i.e., the values of X_{raw}) and the scaling factors m_X and b_X are shown for each of the 1995, 1996, and 1997 data sets in table 5.17. Note in table 5.17 that the peak value of E for $K_{\mu 2}$ decays is anomalously low in 1995. This is because the $K_{\mu 2}(1)$ monitor data was mistakenly analyzed with a ‘‘pion hypothesis’’, where the track is assumed to be that of a pion for the purposes of R , E , and P calculations. Roughly 3 MeV of muon energy in the stopping counter (arising from $\pi \rightarrow \mu$ decay) was mistakenly removed, though this should have no effect on the UMC-based acceptance measurement (see below).

The scaling constants in table 5.17 are also applied to the raw values of R , E , and P from UMC-generated data. The scaled UMC values must be scaled again and smeared so that the peak positions and resolutions of UMC-generated $K_{\pi 2}$ and $K_{\mu 2}$ decays match those of the real data. The UMC scaling is performed via

$$X_{sc} = m_{sc}^X \cdot X + b_{sc}^X \quad (5.10)$$

where X is given by Eq. (5.9) in terms of the scaling factors m_X and b_X and the raw peak value X_{raw} for UMC-generated $K_{\pi 2}$ or $K_{\mu 2}$ decay; and m_{sc}^X and b_{sc}^X are fitted linear scaling constants applied to X such that the doubly-scaled value from UMC-generated data, X_{sc} , agrees with the scaled value from real data, X . The smearing of the UMC variables is performed via

$$\begin{aligned} X_{sc}^{sm} &= X_{sc} + r \cdot \sigma_{X_{sc}}(X_{sc}) \\ &= X_{sc} + r \cdot (m_{sm}^X \cdot X_{sc} + b_{sm}^X) \end{aligned} \quad (5.11)$$

	1995	1996	1997
Range:			
$K_{\pi 2}$ peak (cm)	30.49	30.506	30.539
$K_{\mu 2}$ peak (cm)	54.58	54.506	54.549
m_R	0.9949	0.9988	0.9983
b_R	0.0409	-0.0979	-0.1181
Energy:			
$K_{\pi 2}$ peak (MeV)	105.73	105.80	105.88
$K_{\mu 2}$ peak (MeV)	150.35	152.46	152.78
m_E	0.9845	0.9415	0.9367
b_E	4.4550	8.9402	9.3750
Momentum:			
$K_{\pi 2}$ peak (MeV/c)	205.55	205.49	206.02
$K_{\mu 2}$ peak (MeV/c)	235.85	235.67	236.38
m_P	1.0030	1.0070	1.0010
b_P	-1.0205	-1.7799	-1.0836

Table 5.17: Measured raw values of R , E , and P for the $K_{\pi 2}$ and $K_{\mu 2}$ peaks, and linear scaling factors applied according to Eq. (5.9) such that the scaled values of R , E , and P are the accepted values.

where X_{sc}^{sm} is a Gaussian distribution of R , E , or P with mean X_{sc} and resolution $\sigma_{X_{sc}}$ the same as the mean and resolution of the X distribution in Eq. (5.9) from real $K_{\pi 2}$ or $K_{\mu 2}$ data; m_{sm}^X and b_{sm}^X are fitted linear smearing constants applied to the UMC X_{sc} values such that the kinematic resolutions of UMC-generated and real data agree; and r is a Gaussian random variable with unit variance. The UMC scaling and smearing constants are re-calculated for each of the 1995, 1996, 1997a, and 1997b kaon stopping distributions and are summarized in tables 5.18 and 5.19. Real data typically has worse (larger) kinematic resolutions than UMC-generated data, due to the limited ability of UMC to simulate real processes in the real detector. However, the R resolution from UMC is slightly larger than that from the real data, so no smearing on R is performed. The matching of the R , E , and P peak positions and resolutions for real and UMC-generated $K_{\pi 2}$ and $K_{\mu 2}$ decays is summarized in tables 5.20 and 5.21 for each of the 1995, 1996, 1997a, and 1997b kaon stopping distributions. Note in table 5.21 that the peak value of E for $K_{\mu 2}$ decays is anomalously high in 1995. This is because the 1995 E scaling factors in table 5.17 were calculated using $K_{\mu 2}(1)$ monitor data

year	$m_{sc}^R \cdot R + b_{sc}^R$	$m_{sc}^E \cdot E + b_{sc}^E$	$m_{sc}^P \cdot P + b_{sc}^P$
1995	$1.007 \cdot R - 0.1378$	$1.059 \cdot E - 3.9199$	$1.009 \cdot P - 0.6436$
1996	$1.008 \cdot R - 0.1275$	$1.015 \cdot E + 0.6787$	$1.008 \cdot P - 0.2431$
1997a	$1.013 \cdot R - 0.3192$	$1.012 \cdot E + 1.1894$	$1.009 \cdot P - 0.6247$
1997b	$1.010 \cdot R - 0.2224$	$1.012 \cdot E + 1.0319$	$1.012 \cdot P - 1.3390$

Table 5.18: Scaling factors given in Eq. (5.10) which are applied to R , E , and P values from UMC-generated data, such that the R , E , and P values from UMC-generated data agree with those from real data.

year	$m_{sm}^R \cdot R_{sc} + b_{sm}^R$	$m_{sm}^E \cdot E_{sc} + b_{sm}^E$	$m_{sm}^P \cdot P_{sc} + b_{sm}^P$
1995	No Smearing	$0.02793 \cdot E_{sc} - 0.5525$	$0.00681 \cdot P_{sc} - 0.2493$
1996	No Smearing	$0.02520 \cdot E_{sc} - 0.2827$	$0.01804 \cdot P_{sc} - 2.8055$
1997a	No Smearing	$0.02805 \cdot E_{sc} - 0.6036$	$0.01182 \cdot P_{sc} - 1.5674$
1997b	No Smearing	$0.02746 \cdot E_{sc} - 0.5099$	$0.01521 \cdot P_{sc} - 2.2377$

Table 5.19: Smearing factors given in Eq. (5.11) which are applied to scaled values of R , E , and P from UMC-generated data, such that the resolutions in R , E , and P from UMC-generated data agree with those from real data.

which had an anomalously low value of E (see discussion above). This should not affect the UMC-based acceptance measurement, because the final location of the E peak for $K_{\mu 2}$ decays is the same for UMC-generated and real data.

The R , E , and P peaks from real $K_{\pi 2}$ and $K_{\mu 2}$ data are also measured to be modest functions of the polar angle of the charged track, increasing by almost 1% between $\cos \theta = 0$ and $|\cos \theta| = 0.5$ [58], where the polar (dip) angle is defined in Appendix D. The E and P dip-angle dependences are not modelled by UMC, so the dip-angle dependences of the EBOX' and PBOX' cuts (see section C.3.5) are disabled when measuring the total acceptance of the BOX' cut in table 5.15. The systematic uncertainty in the acceptance of the BOX' cut arising from the dip-angle dependences of the R , E , and P cut positions is estimated by fully enabling (“BOX' check1” in table 5.15) and fully disabling (“BOX' check2”) the dip-angle-dependences of the R , E , and P cut positions. The variation in acceptance is small, and therefore this systematic uncertainty is ignored.

The UMC-based acceptances for the 1995, 1996, 1997a, and 1997b kaon stopping distri-

year	R	E	P
1995 data: mean	30.349 ± 0.002	108.391 ± 0.007	205.177 ± 0.005
σ	0.992 ± 0.002	3.295 ± 0.008	2.497 ± 0.006
UMC: mean	30.331 ± 0.017	108.354 ± 0.059	205.145 ± 0.027
σ	1.019 ± 0.014	3.388 ± 0.046	2.532 ± 0.034
1996 data: mean	30.344 ± 0.002	108.385 ± 0.007	205.183 ± 0.005
σ	0.982 ± 0.003	3.201 ± 0.009	2.508 ± 0.007
UMC: mean	30.330 ± 0.011	108.294 ± 0.055	205.242 ± 0.025
σ	1.057 ± 0.014	3.235 ± 0.041	2.504 ± 0.033
1997a data: mean	30.327 ± 0.004	108.450 ± 0.019	205.177 ± 0.009
σ	0.998 ± 0.005	3.209 ± 0.016	2.450 ± 0.013
UMC: mean	30.308 ± 0.019	108.452 ± 0.056	205.114 ± 0.019
σ	1.034 ± 0.014	3.259 ± 0.043	2.461 ± 0.036
1997b data: mean	30.329 ± 0.005	108.486 ± 0.024	205.142 ± 0.010
σ	0.994 ± 0.006	3.249 ± 0.020	2.430 ± 0.017
UMC: mean	30.318 ± 0.019	108.420 ± 0.058	205.135 ± 0.023
σ	1.047 ± 0.015	3.370 ± 0.045	2.401 ± 0.034

Table 5.20: Means and σ 's of Gaussian fits to kinematic variables from real $K_{\pi 2}$ data, and from UMC $K_{\pi 2}$ data after scaling and smearing.

year	R	E	P
1995 data: mean	53.988 ± 0.006	154.494 ± 0.011	235.593 ± 0.008
σ	2.217 ± 0.006	4.336 ± 0.013	2.928 ± 0.007
UMC: mean	53.929 ± 0.018	154.389 ± 0.046	235.633 ± 0.017
σ	2.282 ± 0.020	4.371 ± 0.040	2.967 ± 0.020
1996 data: mean	54.072 ± 0.006	152.532 ± 0.011	235.676 ± 0.006
σ	2.215 ± 0.007	4.108 ± 0.014	2.984 ± 0.008
UMC: mean	54.004 ± 0.018	152.462 ± 0.032	235.768 ± 0.010
σ	2.303 ± 0.021	4.210 ± 0.039	3.023 ± 0.023
1997a data: mean	54.083 ± 0.011	152.532 ± 0.020	235.679 ± 0.016
σ	2.225 ± 0.013	4.160 ± 0.025	2.914 ± 0.014
UMC: mean	54.014 ± 0.019	152.499 ± 0.031	235.629 ± 0.014
σ	2.332 ± 0.021	4.245 ± 0.040	2.950 ± 0.022
1997b data: mean	54.063 ± 0.014	152.475 ± 0.025	235.632 ± 0.020
σ	2.209 ± 0.016	4.218 ± 0.032	2.932 ± 0.018
UMC: mean	54.020 ± 0.018	152.281 ± 0.033	235.605 ± 0.015
σ	2.306 ± 0.020	4.185 ± 0.039	2.983 ± 0.020

Table 5.21: Means and σ 's of Gaussian fits to kinematic variables from real $K_{\mu 2}$ data, and from UMC $K_{\mu 2}$ data after scaling and smearing.

year	A_{trig}	A_{umc}	A_{nidif}
1995	0.1799 ± 0.0012	0.3650 ± 0.0036	0.5144 ± 0.0086
1996	0.1799 ± 0.0012	0.3634 ± 0.0036	0.5118 ± 0.0086
1997a	0.1780 ± 0.0012	0.3752 ± 0.0036	0.5069 ± 0.0085
1997b	0.1811 ± 0.0012	0.3657 ± 0.0036	0.5126 ± 0.0086

Table 5.22: Summary of UMC-based acceptances for $K^+ \rightarrow \pi^+ \nu \bar{\nu}$ events. The quoted uncertainties are purely statistical.

year	A_{trig}	A_{umc}	A_{nidif}
1995	0.4021 ± 0.0022	0.5698 ± 0.0035	0.4674 ± 0.0058
1996	0.4034 ± 0.0022	0.5631 ± 0.0035	0.4608 ± 0.0057
1997a	0.4018 ± 0.0022	0.5764 ± 0.0035	0.4584 ± 0.0057
1997b	0.4115 ± 0.0022	0.5762 ± 0.0034	0.4598 ± 0.0055

Table 5.23: Summary of UMC-based acceptances for $K^+ \rightarrow \pi^+ f$ events. The quoted uncertainties are purely statistical.

butions are summarized in table 5.22 for $K^+ \rightarrow \pi^+ \nu \bar{\nu}$ events, and in table 5.23 for $K^+ \rightarrow \pi^+ f$ events. The trigger and fiducial acceptances, A_{trig} and A_{umc} , are taken from the NIDIF-off values; the NIDIF acceptance, A_{nidif} , is then taken from the NIDIF-on/NIDIF-off ratio of $A_{trig} \cdot A_{umc}$.

5.9 Kaon Stopping Fraction, f_s

The acceptances of most of the online and offline cuts used in the $K^+ \rightarrow \pi^+ \nu \bar{\nu}$ analysis are found directly through analysis of monitor and UMC-generated data, as described in the previous sections of this chapter. The remaining acceptance losses (e.g. fraction of kaons that stop in the target, and various detector inefficiencies) are lumped into a “fudge factor” called f_s . This factor f_s is found by normalizing the measured $K_{\mu 2}$ branching ratio to the accepted value [16]. The value of f_s , and the $K^+ \rightarrow \pi^+ \nu \bar{\nu}$ acceptance measurement as a whole, are then tested by measuring the $K_{\pi 2}$ branching ratio and comparing with the accepted value [16]. A subset of the same cuts from the $K^+ \rightarrow \pi^+ \nu \bar{\nu}$ analysis, and the same acceptance measurement structure, are used to measure the $K_{\mu 2}$ and $K_{\pi 2}$ branching ratios.

Because many cuts are common to the $K_{\mu 2}$ and $K_{\pi 2}$ analyses, the acceptances of these cuts cancel out in the $K_{\pi 2}$ branching ratio calculation, assuming that these cuts are insensitive to the kaon decay particle (i.e., pion or muon). If an anomalous or unstable value of the $K_{\pi 2}$ branching ratio is measured, this could indicate problems in the $K^+ \rightarrow \pi^+ \nu \bar{\nu}$ acceptance structure, and/or to errors in the assumptions that various acceptances/efficiencies can be measured independent of the type of kaon decay particle, and/or to problems with UMC (e.g., simulation of pion-nuclear interactions). All appropriate $K^+ \rightarrow \pi^+ \nu \bar{\nu}$ cuts are applied when measuring the $K_{\mu 2}$ and $K_{\pi 2}$ branching ratios, in order to test the $K^+ \rightarrow \pi^+ \nu \bar{\nu}$ acceptance measurement as thoroughly as possible.

5.9.1 Measurement of f_s

The $K_{\mu 2}$ branching ratio is measured by analyzing $K_{\mu 2}(1)$ monitor data (see section 3.3). The cuts applied in the analysis are shown in table 5.24, which lists the number of $K_{\mu 2}(1)$ monitor events, $M_{K_{\mu 2}}$, from each of the 1995, 1996, 1997a, and 1997b data sets which remain after each cut is applied. The PV(noBV) cut is the PV function cut, with the requirements in the barrel disabled because many $K_{\mu 2}$ decays have tracks which enter the barrel. The RTOT40 cut requires $R > 40$ cm, and is implemented to remove $K_{\pi 2}$ and radiative $K_{\mu 2}$ decays not removed by PV(noBV). The acceptances of the cuts are measured using $K_{\mu 2}(1)$ monitor data and UMC-generated $K_{\mu 2}$ data, in much the same way way as the $K_{\mu 2}$ - and UMC-based acceptance measurements of sections 5.2 and 5.8. Table 5.25 lists the number of surviving $K_{\mu 2}(1)$ monitor events from the 1995, 1996, 1997a, and 1997b data sets after each cut used in the $K_{\mu 2}$ branching ratio measurement is applied, and the corresponding acceptance of each cut. All setup cuts in table 5.25 are defined in table 5.3. Acceptances in table 5.25 are grouped into the quantities A_{RD} , A_{recon} , A_{rest} , A_{PV} , and $A_{bad}(K_{\mu 2})$, which are the RS reconstruction, UTC and target reconstruction, beamline and target pattern, PV, and bad data acceptances, respectively, for the cuts applied in the $K_{\mu 2}$ branching ratio measurement. All of these acceptances are combined into the quantity $A_{K_{\mu 2}}$, which is analogous to the $A_{K_{\mu 2}}$ quantity from table 5.2. Table 5.26 lists the number of

surviving UMC-generated $K^+ \rightarrow \mu^+ \nu_\mu$ events for the 1995, 1996, 1997a, and 1997b kaon stopping distributions after each trigger condition or cut used in the $K_{\mu 2}$ branching ratio measurement is applied, and the corresponding acceptance of each cut. Acceptances in table 5.26 are grouped into the quantities $A_{trig}^{K_{\mu 2}}$, $A_{K_{\mu 2}, recon}^{umc}$, and $A_{K_{\mu 2}, kin}^{umc}$, which are the $K_{\mu 2}(1)$ trigger, UMC-based reconstruction, and kinematic acceptances, respectively, for the cuts applied in the $K_{\mu 2}$ branching ratio measurement. These acceptances are combined into the quantity $A_{K_{\mu 2}}^{umc}$. $A_{K_{\mu 2}, recon}^{umc}$ is not used in the calculation of the $K_{\mu 2}$ branching ratio, but it is measured here for later use in the $K_{\pi 2}$ branching ratio calculation.

The measured $K_{\mu 2}$ branching ratio, $B(K^+ \rightarrow \mu^+ \nu_\mu)$, is normalized to the accepted value of 0.6351 ± 0.0018 [16] in order to get the kaon “stopping fraction”, f_s , given by

$$f_s = \frac{B(K^+ \rightarrow \mu^+ \nu_\mu)}{0.6351} = \frac{M_{K_{\mu 2}}}{\epsilon_{T \cdot 2}^{ng}(K_{\mu 2}) \cdot (K_{Blive}^{eff})_{K_{\mu 2}} \cdot A_{K_{\mu 2}} \cdot A_{trig}^{K_{\mu 2}} \cdot A_{K_{\mu 2}, kin}^{umc}} \cdot \frac{1}{0.6351}} \quad (5.12)$$

where $\epsilon_{T \cdot 2}^{ng}(K_{\mu 2})$ is the “non-gap” T · 2 efficiency for $K_{\mu 2}$ decays (see section 5.7), and $(K_{Blive}^{eff})_{K_{\mu 2}}$ is K_{Blive} (see section 5.1) corrected for online and offline $K_{\mu 2}(1)$ monitor prescales [41] and shown in table 5.27. Using the numbers in tables 5.12, 5.24, 5.25, 5.26 and 5.27 and Eq. (5.12), the values of f_s for each run period are

$$1995: \quad f_s = 0.681 \pm 0.007^{stat} \pm 0.014^{syst}$$

$$1996: \quad f_s = 0.726 \pm 0.006^{stat} \pm 0.015^{syst}$$

$$1997a: \quad f_s = 0.700 \pm 0.008^{stat} \pm 0.015^{syst}$$

$$1997b: \quad f_s = 0.760 \pm 0.009^{stat} \pm 0.016^{syst}$$

where the systematic uncertainty in f_s comes from the uncertainty in the T · 2 gap inefficiency: $4.1 \pm 0.2\%$ (see section 5.7). The average value of f_s , weighted by $A \epsilon \cdot f_s \cdot K_{Blive}$ (see section 5.10 and table 5.32), is $0.704 \pm 0.004^{stat} \pm 0.009^{syst}$.

5.9.2 Measurement of the $K_{\pi 2}$ Branching Ratio

The $K_{\pi 2}$ branching ratio is measured by analyzing $K_{\pi 2}(1)$ monitor data (see section 3.3). The cuts applied in the analysis are shown in table 5.28, which lists the number of $K_{\pi 2}(1)$ monitor events, $M_{K_{\pi 2}}$, from each of the 1995, 1996, 1997a, and 1997b data sets which

cut	1995	1996	1997a	1997b
BAD_RUN	88989	223363	74999	43727
BAD_STC	87795	210984	69478	41473
BAD_STC	87772	210981	69478	41473
$K_{\mu 2}(1)$ trigger	87772	210981	69478	41473
RD_TRK	87771	210924	69478	41473
TRKTIM	87771	209516	69467	41467
UTC/RANGE	82261	201981	66275	39979
UTCQUAL	78878	191885	62013	38120
PROBZ	78878	190072	61357	37761
TARGET	76702	187146	60439	37284
COS3D	74377	182165	58711	36478
B4DEDX	73254	178520	57910	36110
CPITRS	72621	177574	57599	35924
CPITAIL	72521	177475	57555	35903
ICBIT	67934	176602	57469	35877
TIC	66699	173979	56695	35488
TIMCON	65588	172079	56052	35127
TGCCD	57947	158028	50354	32517
DCBIT	51956	137028	45360	28665
DELC	46258	122262	39662	24998
CKTRS	45822	120490	39172	24692
CKTAIL	44288	116286	37292	23716
BWTRS	41575	111591	35694	22910
BHTRS	41401	110864	35493	22810
TARGF	39877	107039	34248	22010
DTGTP	39867	107010	34246	22008
RTDIF	39434	105751	33775	21785
TGQUALT	39434	105751	33775	21785
PIGAP	38829	104382	33288	21538
TGB4	36803	98986	31536	20498
KIC	36466	98005	31277	20342
TGCEO	36359	97739	31197	20308
B4EKZ	35847	96526	30800	20098
B4EKZ_IC	35623	95881	30602	19959
TGZFOOL	35623	95881	30602	19959
PV(noBV)	30482	81954	25854	17426
RTOT40	30470	81926	25840	17417
$M_{K_{\mu 2}}$	30470	81926	25840	17417

Table 5.24: Cuts applied to $K_{\mu 2}(1)$ monitor data in order to measure the $K_{\mu 2}$ branching ratio. Table entries are described in section 5.9.1 of the text. The PROBZ cut is not applied to the 1995 data, as is the case in the $K^+ \rightarrow \pi^+ \nu \bar{\nu}$ analysis (see section C.3.1).

cut	1995 (acc.)	1996 (acc.)	1997a (acc.)	1997b (acc.)
SETUP _{RD}	45635	119105	39495	23990
RD_TRK	45635 (1.000)	119105 (1.000)	39495 (1.000)	23990 (1.000)
TRKTIM	45635 (1.000)	118849 (0.998)	39492 (1.000)	23990 (1.000)
A_{RD}	1.0000 ± 0.0000	0.9979 ± 0.0001	0.9999 ± 0.0000	1.0000 ± 0.0000
SETUP _{recon}	24749	66786	21386	13805
UTC/RANGE	24749 (1.000)	66786 (1.000)	21386 (1.000)	13805 (1.000)
UTCQUAL	24245 (0.980)	64517 (0.966)	20417 (0.955)	13329 (0.966)
PROBZ	24245 (1.000)	63935 (0.991)	20228 (0.991)	13202 (0.990)
TARGET	24102 (0.994)	63640 (0.995)	20132 (0.995)	13159 (0.997)
A_{recon}	0.9739 ± 0.0010	0.9529 ± 0.0008	0.9414 ± 0.0016	0.9532 ± 0.0018
SETUP _{rest}	36718	96912	30379	20119
ICBIT	36718 (1.000)	96912 (1.000)	30379 (1.000)	20119 (1.000)
TIC	36397 (0.991)	96437 (0.995)	30247 (0.996)	20049 (0.997)
TIMCON	35983 (0.989)	95748 (0.993)	30088 (0.995)	19954 (0.995)
TGCCD	32338 (0.899)	89541 (0.935)	27635 (0.918)	18673 (0.936)
DCBIT	29564 (0.914)	79835 (0.892)	25529 (0.924)	16859 (0.903)
DELC	26607 (0.900)	71834 (0.900)	22578 (0.884)	14868 (0.882)
CKTRS	26443 (0.994)	71218 (0.991)	22404 (0.992)	14757 (0.993)
CKTAIL	25786 (0.975)	69329 (0.973)	21578 (0.963)	14286 (0.968)
B4DEDX	25535 (0.990)	68424 (0.987)	21384 (0.991)	14159 (0.991)
CPITRS	25484 (0.998)	68339 (0.999)	21353 (0.999)	14132 (0.998)
CPITAIL	25469 (0.999)	68323 (1.000)	21348 (1.000)	14127 (1.000)
TARGF	24642 (0.968)	66223 (0.969)	20668 (0.968)	13685 (0.969)
DTGTTP	24639 (1.000)	66217 (1.000)	20668 (1.000)	13685 (1.000)
RTDIF	24392 (0.990)	65526 (0.990)	20410 (0.988)	13561 (0.991)
TGQUALT	24392 (1.000)	65526 (1.000)	20410 (1.000)	13561 (1.000)
PIGAP	24103 (0.988)	64866 (0.990)	20184 (0.989)	13460 (0.993)
TGB4	22801 (0.946)	61397 (0.947)	19098 (0.946)	12803 (0.951)
KIC	22593 (0.991)	60787 (0.990)	18945 (0.992)	12708 (0.993)
TGCEO	22549 (0.998)	60665 (0.998)	18914 (0.998)	12692 (0.999)
B4EKZ	22314 (0.990)	60001 (0.989)	18708 (0.989)	12562 (0.990)
B4EKZ_IC	22244 (0.997)	59765 (0.996)	18616 (0.995)	12516 (0.996)
TGZFOOL	22244 (1.000)	59765 (1.000)	18616 (1.000)	12516 (1.000)
BWTRS	21619 (0.972)	58623 (0.981)	18253 (0.981)	12307 (0.983)
BHTRS	21541 (0.996)	58261 (0.994)	18160 (0.995)	12254 (0.996)
A_{rest}	0.5867 ± 0.0026	0.6012 ± 0.0016	0.5978 ± 0.0028	0.6091 ± 0.0034
SETUP _{PV}	11553	30866	9627	6426
PV(noBV)	10328 (0.894)	27535 (0.892)	8481 (0.881)	5862 (0.912)
A_{PV}	0.8940 ± 0.0029	0.8921 ± 0.0018	0.8810 ± 0.0033	0.9122 ± 0.0035
SETUP _{bad}	79122	221585	74826	43653
BAD.RUN	78066 (0.987)	209267 (0.944)	69315 (0.926)	41405 (0.949)
BAD.STC	78052 (1.000)	209264 (1.000)	69315 (1.000)	41405 (1.000)
$K_{\mu 2}(1)$ trigger	78052 (1.000)	209264 (1.000)	69315 (1.000)	41405 (1.000)
$A_{bad}(K_{\mu 2})$	0.9865 ± 0.0004	0.9444 ± 0.0005	0.9263 ± 0.0010	0.9485 ± 0.0011
$A_{K_{\mu 2}}$	0.5039 ± 0.0028	0.4816 ± 0.0017	0.4592 ± 0.0029	0.5023 ± 0.0036

Table 5.25: $K_{\mu 2}$ -based acceptance of cuts applied in the $K_{\mu 2}$ branching ratio measurement. The quoted uncertainties are purely statistical. Table entries are described in section 5.9.1 of the text. The PROBZ cut is not applied to the 1995 data, as is the case in the $K^+ \rightarrow \pi^+ \nu \bar{\nu}$ analysis (see section C.3.1). The various SETUP's are defined in table 5.3. SETUP_{bad} is simply the online IC requirement (ICBIT).

cut	1995 (acc.)	1996 (acc.)	1997a (acc.)	1997b (acc.)
KT	50000	50000	49999	49999
T · 2	22629 (0.452)	22632 (0.453)	22602 (0.452)	22806 (0.456)
$19_{ct} + 20_{ct} + 21_{ct}$	18777 (0.830)	18737 (0.828)	18674 (0.826)	18967 (0.832)
$A_{trig}^{K_{\mu 2}}$	0.3755 ± 0.0022	0.3747 ± 0.0022	0.3735 ± 0.0022	0.3793 ± 0.0022
UTC/RANGE	18764 (0.999)	18726 (0.999)	18657 (0.999)	18955 (0.999)
UTCQUAL	18761 (1.000)	18717 (1.000)	18649 (1.000)	18949 (1.000)
PROBZ	18761 (1.000)	18684 (0.998)	18621 (0.998)	18915 (0.998)
TARGET	18703 (0.997)	18638 (0.998)	18576 (0.998)	18887 (0.999)
$A_{K_{\mu 2}, recon}^{umc}$	0.9961 ± 0.0005	0.9947 ± 0.0005	0.9948 ± 0.0005	0.9958 ± 0.0005
COS3D	18405 (0.984)	18306 (0.982)	18234 (0.982)	18556 (0.982)
RTOT40	18403 (1.000)	18305 (1.000)	18231 (1.000)	18555 (1.000)
$A_{K_{\mu 2}, kin}^{umc}$	0.9840 ± 0.0009	0.9821 ± 0.0010	0.9814 ± 0.0010	0.9824 ± 0.0010
$A_{K_{\mu 2}}^{umc}$	0.3681 ± 0.0022	0.3660 ± 0.0022	0.3646 ± 0.0022	0.3711 ± 0.0022

Table 5.26: UMC-based acceptances of cuts applied in the $K_{\mu 2}$ branching ratio measurement. The quoted uncertainties are purely statistical. Table entries are described in section 5.9.1 of the text. KT is the number of $K^+ \rightarrow \mu^+ \nu_{\mu}$ events generated by UMC. The various trigger conditions are defined in section 3.3.

year	$(K_{Blive}^{eff})_{K_{\mu 2}}$
1995	392509
1996	1132804
1997a	385261
1997b	218617

Table 5.27: Values of $(K_{Blive}^{eff})_{K_{\mu 2}}$ for each run period.

remain after each cut is applied. The KP2BOX cut is a 3σ cut on the $K_{\pi 2}$ range, energy and momentum. The KP2STOP cut requires the stopping layer to be between layers 8 and 15 inclusive.

Table 5.29 lists the number of surviving $K_{\pi 2}(1)$ monitor events from the 1995, 1996, 1997a, and 1997b data sets after each cut used in the $K_{\pi 2}$ branching ratio measurement is applied, and the corresponding acceptance of each cut, grouped into the quantities A_{RD} , A_{recon} , A_{rest} , and A_{bad} , which are the RS reconstruction, UTC and target reconstruction, beamline and target pattern, and bad data acceptances, respectively, for the cuts applied in the $K_{\pi 2}$ branching ratio measurement. All setup cuts in table 5.29 are similar to those in table 5.25 which are defined in table 5.3, but with the following modifications: all SETUP's include the requirement of at least 200 MeV of photon energy in the barrel and EC combined, such that there is no photon energy in the RS which can adversely affect track reconstruction ($K_{\pi 2}$ decays have a total of 225 MeV of photon energy); $75 < E_{RS} < 105$ MeV is required instead of $120 < E_{RS} < 150$ MeV in order to isolate the $K_{\pi 2}$ energy peak; the PV(noBV) cut is not applied; and the KM2PBOX cut is replaced by the KP2BOX, KP2STOP, and FITPI cuts. $SETUP_{bad}$ is simply the online IC requirement (ICBIT). A_{RD} , A_{recon} , and A_{rest} in table 5.29 are essentially the same quantities as those measured using $K_{\mu 2}(1)$ monitor data, shown in table 5.25). However, the measurements using $K_{\pi 2}(1)$ monitor data are expected to give lower acceptances than the same measurements which use $K_{\mu 2}(1)$ monitor data, because the $K_{\pi 2}(1)$ data sample after setup cuts are applied has a larger component of kaon-rate-dependent background, which can affect the performance of reconstruction and pathology cuts. The larger component of rate-dependent background arises from the fact that the $K_{\pi 2}(1)$ trigger selects tracks which are not required to penetrate far into the RS, and are therefore closer to the beam axis where activity is highest. A_{RD} , A_{recon} , and A_{rest} are therefore most accurately measured using $K_{\mu 2}(1)$ monitor data for both the $K_{\mu 2}$ and $K_{\pi 2}$ branching ratio measurements, and will consequently "cancel out" when using f_s to calculate the $K_{\pi 2}$ branching ratio (see below). They are measured using $K_{\pi 2}(1)$ monitor data and listed in table 5.29 mainly for the sake of investigating the assumption that these acceptances are independent of the type of kaon decay particle. Conversely, $A_{bad}(K_{\pi 2})$ in

cut	1995	1996	1997a	1997b
ALL	88970	104092	34246	19386
BAD_RUN	87677	102375	33438	19304
BAD_STC	87536	102326	33438	19302
$K_{\pi_2}(1)$ trigger	87536	102326	33438	19302
RD_TRK	87527	102266	33437	19302
TRKTIM	87527	101500	33411	19294
UTC/RANGE	72258	91831	30147	17652
UTCQUAL	67318	85934	27712	16575
PROBZ	67318	85045	27378	16409
TARGET	62313	81725	26370	15886
COS3D	55954	74470	23854	14730
B4DEX	54907	72586	23408	14502
CPITRS	54344	72111	23249	14412
CPITAIL	54252	72070	23228	14404
ICBIT	51393	71806	23198	14386
TIC	50247	70499	22790	14161
TIMCON	49371	69564	22501	14009
TGCCD	42531	62233	19700	12701
DCBIT	36678	51733	16956	10790
DELC	32564	46129	14760	9450
CKTRS	32310	45548	14587	9357
CKTAIL	31246	43973	13892	9022
BWTRS	29482	42211	13313	8735
BHTRS	29377	41952	13254	8703
TARGF	27855	39825	12623	8301
DTGTTP	27854	39820	12622	8300
RTDIF	27557	39278	12457	8189
TGQUALT	27557	39278	12457	8189
PIGAP	26998	38560	12203	8041
TGB4	25213	36062	11408	7585
KIC	24538	35162	11184	7452
TGGEO	24343	34874	11086	7409
B4EKZ	23959	34413	10935	7316
B4EKZ_IC	23857	34231	10875	7279
TGZFOOL	23857	34231	10875	7279
FITPI	8067	11534	3617	2522
KP2BOX	7294	10528	3282	2268
KP2STOP	7272	10501	3272	2262
$M_{K_{\pi_2}}$	7272	10501	3272	2262

Table 5.28: Cuts applied to $K_{\pi_2}(1)$ monitor data in order to measure the K_{π_2} branching ratio. Table entries are described in section 5.9.2 of the text. The PROBZ cut is not applied to the 1995 data, as is the case in the $K^+ \rightarrow \pi^+ \nu \bar{\nu}$ analysis (see section C.3.1).

table 5.29 is different from $A_{bad}(K_{\mu 2})$ in table 5.25, and must be explicitly included in the $K_{\pi 2}$ branching ratio measurement, because the BAD_RUN and BAD_STC cuts can be dependent on stopping layer.

A_{FITPI} in table 5.29 is the acceptance of the FITPI cut measured using π_{scat} monitor data, similar to the measurement of the acceptance of the FITPI cut from section 5.5, except that the π_{scat} monitor events here are selected to fall into the $K^+ \rightarrow \pi^+\pi^0$ kinematic region instead of the $K^+ \rightarrow \pi^+\nu\bar{\nu}$ kinematic region. That is, the π_{scat} monitor events must pass the KP2BOX and KP2STOP cuts instead of the BOX and LAYV4 cuts (see tables 5.8 and 5.9). $A_{\bar{\mu}}^{acc}$ in table 5.29 is the μ -veto accidental acceptance measured using $K_{\mu 2}(1)$ monitor data as described in section 5.6 and shown also in table 5.11. A_{RD} , A_{recon} , A_{rest} , $A_{bad}(K_{\pi 2})$, A_{FITPI} , and $A_{\bar{\mu}}^{acc}$ are combined into the quantity $A_{K_{\pi 2}}$ for use in the calculation of the $K_{\pi 2}$ branching ratio.

Table 5.30 lists the number of surviving UMC-generated $K^+ \rightarrow \pi^+\pi^0$ events for the 1995, 1996, 1997a, and 1997b kaon stopping distributions after each trigger condition or cut used in the $K_{\pi 2}$ branching ratio measurement is applied, and the corresponding acceptance of each cut. Acceptances in table 5.30 are grouped into the quantities $A_{trig}^{K_{\pi 2}}$, $A_{K_{\pi 2},recon}^{umc}$, and $A_{K_{\pi 2},kin}^{umc}$, which are the $K_{\pi 2}(1)$ trigger, UMC-based reconstruction, and kinematic acceptances, respectively, for the cuts applied in the $K_{\pi 2}$ branching ratio measurement. These acceptances are combined into the quantity $A_{K_{\mu 2}}^{umc}$. The ratio of the $K_{\mu 2}$ and $K_{\pi 2}$ UMC-based reconstruction acceptances, $A_{K_{\mu 2},recon}^{umc}/A_{K_{\pi 2},recon}^{umc}$ from tables 5.26 and 5.30, is used to account for a potential difference in $K_{\mu 2}$ and $K_{\pi 2}$ event reconstruction due to the presence of photons in $K_{\pi 2}$ decays. The structure of the UMC-based acceptance measurement in table 5.30 is identical to that used in the $K^+ \rightarrow \pi^+\nu\bar{\nu}$ analysis (compare table 5.30 with tables 5.13 and 5.15), specifically with respect to measurement of the acceptances of the $K_{\pi 2}(1)$ and $\pi^+\nu\bar{\nu}(1)$ triggers; the KP2STOP and LAYV4 cuts; and the KP2BOX, BOX, and BOX' cuts. The measurement of the $K_{\pi 2}$ branching ratio is therefore a test of the accuracy of UMC in simulating $\pi^+,^{12}\text{C}$ interactions. Furthermore, similar to measurement of the acceptances of the BOX and BOX' cuts (see section 5.8), the acceptance of the KP2BOX cut is measured after scaling and smearing R , E , and P values from UMC-generated $K_{\pi 2}$ events according

cut	1995 (acc.)	1996 (acc.)	1997a (acc.)	1997b (acc.)
SETUP _{RD}	10368	13829	4343	2719
RD_TRK	10368 (1.000)	13829 (1.000)	4343 (1.000)	2719 (1.000)
TRKTIM	10368 (1.000)	13829 (1.000)	4343 (1.000)	2719 (1.000)
A_{RD}	1.0000 ± 0.0000	1.0000 ± 0.0000	1.0000 ± 0.0000	1.0000 ± 0.0000
SETUP _{recon}	6375	8676	2706	1809
UTC/RANGE	6375 (1.000)	8676 (1.000)	2706 (1.000)	1809 (1.000)
UTCQUAL	6207 (0.974)	8387 (0.967)	2553 (0.943)	1725 (0.954)
PROBZ	6207 (1.000)	8305 (0.990)	2525 (0.989)	1707 (0.990)
TARGET	6110 (0.984)	8195 (0.987)	2487 (0.985)	1688 (0.989)
A_{recon}	0.9584 ± 0.0025	0.9446 ± 0.0025	0.9191 ± 0.0052	0.9331 ± 0.0059
SETUP _{rest}	5936	7917	2414	1581
ICBIT	5936 (1.000)	7917 (1.000)	2414 (1.000)	1581 (1.000)
TIC	5857 (0.987)	7849 (0.991)	2394 (0.992)	1570 (0.993)
TIMCON	5784 (0.988)	7765 (0.989)	2372 (0.991)	1559 (0.993)
TGCCD	5152 (0.891)	7184 (0.925)	2149 (0.906)	1454 (0.933)
DCBIT	4652 (0.903)	6391 (0.890)	1972 (0.918)	1309 (0.900)
DELC	4107 (0.883)	5700 (0.892)	1716 (0.870)	1182 (0.903)
CKTRS	4070 (0.991)	5635 (0.989)	1698 (0.990)	1174 (0.993)
CKTAIL	3924 (0.964)	5407 (0.960)	1608 (0.947)	1132 (0.964)
B4DEX	3898 (0.993)	5330 (0.986)	1594 (0.991)	1121 (0.990)
CPITRS	3866 (0.992)	5309 (0.996)	1586 (0.995)	1116 (0.996)
CPITAIL	3858 (0.998)	5307 (1.000)	1585 (0.999)	1115 (0.999)
TARGF	3679 (0.954)	5079 (0.957)	1528 (0.964)	1073 (0.962)
DTGTTP	3679 (1.000)	5079 (1.000)	1528 (1.000)	1073 (1.000)
RTDIF	3643 (0.990)	5023 (0.989)	1509 (0.988)	1064 (0.992)
TGQUALT	3643 (1.000)	5023 (1.000)	1509 (1.000)	1064 (1.000)
PIGAP	3594 (0.987)	4961 (0.988)	1491 (0.988)	1052 (0.989)
TGB4	3395 (0.945)	4675 (0.942)	1404 (0.942)	1003 (0.953)
KIC	3365 (0.991)	4622 (0.989)	1392 (0.991)	996 (0.993)
TGCEO	3341 (0.993)	4592 (0.994)	1378 (0.990)	986 (0.990)
B4EKZ	3272 (0.979)	4533 (0.987)	1355 (0.983)	974 (0.988)
B4EKZ.IC	3255 (0.995)	4512 (0.995)	1349 (0.996)	968 (0.994)
TGZFOOL	3255 (1.000)	4512 (1.000)	1349 (1.000)	968 (1.000)
BWTRS	3060 (0.940)	4320 (0.957)	1276 (0.946)	939 (0.970)
BHTRS	3052 (0.997)	4295 (0.994)	1269 (0.995)	934 (0.995)
A_{rest}	0.5142 ± 0.0065	0.5425 ± 0.0056	0.5257 ± 0.0102	0.5908 ± 0.0124
SETUP _{bad}	19665	27161	8557	5005
BAD_RUN	19456 (0.989)	26742 (0.985)	8378 (0.979)	4987 (0.996)
BAD_STC	19430 (0.999)	26739 (1.000)	8378 (1.000)	4986 (1.000)
$K_{\pi 2}(1)$ trigger	19430 (1.000)	26739 (1.000)	8378 (1.000)	4986 (1.000)
A_{bad}	0.9880 ± 0.0008	0.9845 ± 0.0008	0.9791 ± 0.0015	0.9962 ± 0.0009
A_{FITPI}	$.7117 \pm .0120$	$.7063 \pm .0069$	$.7111 \pm .0134$	$.7171 \pm .0142$
A_{μ}^{acc}	0.9924 ± 0.0003	0.9930 ± 0.0003	0.9925 ± 0.0005	0.9940 ± 0.0006
$A_{K_{\pi 2}}$	0.3458 ± 0.0074	0.3557 ± 0.0052	0.3358 ± 0.0093	0.3932 ± 0.0116

Table 5.29: Monitor-based acceptances of cuts applied in the $K_{\pi 2}$ branching ratio measurement. The quoted uncertainties are purely statistical. Table entries are described in section 5.9.2 of the text. The PROBZ cut is not applied to the 1995 data, as is the case in the $K^+ \rightarrow \pi^+ \nu \bar{\nu}$ analysis (see section C.3.1).

cut	1995 (acc.)	1996 (acc.)	1997a (acc.)	1997b (acc.)
KT	19999	19999	19999	19996
T · 2	8988 (0.449)	9042 (0.452)	8867 (0.443)	9018 (0.451)
6 _{ct} + 7 _{ct}	7530 (0.838)	7597 (0.840)	7372 (0.831)	7542 (0.836)
μ-veto	7197 (0.956)	7302 (0.961)	7079 (0.960)	7232 (0.959)
UFATE	6063 (0.842)	6156 (0.843)	5980 (0.845)	6097 (0.843)
USTMED	5920 (0.976)	6017 (0.977)	5872 (0.982)	5979 (0.981)
USTOP_HEX	5368 (0.907)	5480 (0.911)	5299 (0.902)	5422 (0.907)
$A_{trig}^{K_{\pi^2}}$	0.2684 ± 0.0031	0.2740 ± 0.0032	0.2650 ± 0.0031	0.2712 ± 0.0031
UTC/RANGE	5355 (0.998)	5448 (0.994)	5268 (0.994)	5396 (0.995)
UTCQUAL	5351 (0.999)	5442 (0.999)	5266 (1.000)	5393 (0.999)
PROBZ	5351 (1.000)	5422 (0.996)	5249 (0.997)	5378 (0.997)
TARGET	5295 (0.990)	5361 (0.989)	5205 (0.992)	5324 (0.990)
$A_{K_{\pi^2},recon}^{umc}$	0.9864 ± 0.0016	0.9783 ± 0.0020	0.9823 ± 0.0018	0.9819 ± 0.0018
KP2STOP	5083 (0.960)	5152 (0.961)	4998 (0.960)	5128 (0.963)
COS3D	4864 (0.957)	4926 (0.956)	4763 (0.953)	4939 (0.963)
KP2BOX	4517 (0.929)	4567 (0.927)	4420 (0.928)	4544 (0.920)
$A_{K_{\pi^2},kin}^{umc}$	0.8531 ± 0.0049	0.8519 ± 0.0049	0.8492 ± 0.0050	0.8535 ± 0.0048
$A_{K_{\pi^2}}^{umc}$	0.2259 ± 0.0029	0.2284 ± 0.0030	0.2211 ± 0.0029	0.2273 ± 0.0029

Table 5.30: UMC-based acceptances of cuts applied in the K_{π^2} branching ratio measurement. The quoted uncertainties are purely statistical. Table entries are described in section 5.9.2 of the text. UFATE, USTMED, and USTOP_HEX are defined in section 5.8. KT is the number of $K^+ \rightarrow \pi^+\pi^0$ events generated by UMC. The various trigger conditions are defined in section 3.3, including “μ-veto” which is defined as $(19_{ct} + 20_{ct} + 21_{ct})$.

to tables 5.18 and 5.19 to match the real data.

The K_{π^2} branching ratio is given by

$$B(K^+ \rightarrow \pi^+\pi^0) = \frac{M_{K_{\pi^2}}}{\epsilon_{T,2}^{ng}(K_{\pi^2}) \cdot (K_{Blive}^{eff})_{K_{\pi^2}} \cdot A_{FITPI} \cdot A_{\mu}^{acc} \cdot A_{K_{\pi^2}} \cdot A_{K_{\pi^2},kin}^{umc} \cdot f_s} \quad (5.13)$$

where $\epsilon_{T,2}^{ng}(K_{\pi^2})$ is the “non-gap” T · 2 efficiency for K_{π^2} decays (see section 5.7), and $(K_{Blive}^{eff})_{K_{\pi^2}}$ is analogous to $(K_{Blive}^{eff})_{K_{\mu 2}}$ from section 5.9.1 and shown in table 5.31. Using Eq. (5.12), Eq. (5.13) becomes

$$\begin{aligned} B(K^+ \rightarrow \pi^+\pi^0) &= 0.6351 \cdot \frac{M_{K_{\pi^2}}}{M_{K_{\mu 2}}} \cdot \frac{\epsilon_{T,2}^{ng}(K_{\mu 2})}{\epsilon_{T,2}^{ng}(K_{\pi^2})} \cdot \frac{(K_{Blive}^{eff})_{K_{\mu 2}}}{(K_{Blive}^{eff})_{K_{\pi^2}}} \cdot \frac{A_{K_{\mu 2}} \cdot A_{K_{\mu 2}}^{umc}}{A_{K_{\pi^2}} \cdot A_{K_{\pi^2}}^{umc}} \cdot \frac{1}{A_{FITPI} \cdot A_{\mu}^{acc}} \quad (5.14) \\ &= 0.6351 \cdot \frac{M_{K_{\pi^2}}}{M_{K_{\mu 2}}} \cdot \frac{\epsilon_{T,2}^{ng}(K_{\mu 2})}{\epsilon_{T,2}^{ng}(K_{\pi^2})} \cdot \frac{(K_{Blive}^{eff})_{K_{\mu 2}}}{(K_{Blive}^{eff})_{K_{\pi^2}}} \cdot \frac{A_{K_{\mu 2}}^{umc}}{A_{K_{\pi^2}}^{umc}} \cdot \frac{A_{PV}}{A_{FITPI} \cdot A_{\mu}^{acc}} \cdot \frac{A_{bad}(K_{\mu 2})}{A_{bad}(K_{\pi^2})}. \end{aligned}$$

The uncertainties in these quantities from tables 5.12, 5.24, 5.25, 5.26, 5.27, 5.28, 5.29, 5.30 and 5.31 are purely statistical, so, from Eq. (5.14), the values of the K_{π^2} branching ratio for

year	$(K_{Blive}^{eff})_{K\pi_2}$
1995	557517
1996	807044
1997a	273726
1997b	155559

Table 5.31: Values of $(K_{Blive}^{eff})_{K\pi_2}$ for each run period.

each run period are

$$1995: \quad B(K^+ \rightarrow \pi^+\pi^0) = 0.218 \pm 0.006^{stat}$$

$$1996: \quad B(K^+ \rightarrow \pi^+\pi^0) = 0.210 \pm 0.004^{stat}$$

$$1997a: \quad B(K^+ \rightarrow \pi^+\pi^0) = 0.212 \pm 0.007^{stat}$$

$$1997b: \quad B(K^+ \rightarrow \pi^+\pi^0) = 0.216 \pm 0.007^{stat}$$

The average value of the K_{π_2} branching ratio, weighted by $A\epsilon \cdot f_s \cdot K_{Blive}$ (see section 5.10 and table 5.32), is 0.214 ± 0.003^{stat} . This agrees with the accepted value of 0.2116 ± 0.0014 [16], which implies that the value of f_s , the UMC simulation of $\pi^+, ^{12}\text{C}$ interactions, and the $K^+ \rightarrow \pi^+\nu\bar{\nu}$ acceptance measurement as a whole are accurate. Further comparisons of $\pi^+, ^{12}\text{C}$ interactions in UMC with real data [41] indicate that UMC simulates these interactions to an accuracy of about $\pm 2\%$. This is a measure of the systematic uncertainty in the measured K_{π_2} branching ratio, given therefore by $0.214 \pm 0.003^{stat} \pm 0.004^{syst}$, which, as mentioned above, agrees with the accepted value.

5.10 Summary

The acceptances for $K^+ \rightarrow \pi^+\nu\bar{\nu}$ and $K^+ \rightarrow \pi^+f$ are combined with the number of kaons entering the target to get the single-event sensitivities shown in tables 5.32 and 5.33. In these tables, monitor- and UMC-based acceptances are combined into the quantity A , detector efficiencies are combined into the quantity ϵ , the kaon stopping fraction is given by f_s , and the number of kaons is given by K_{Blive} , such that the total acceptance is defined by $A\epsilon \cdot f_s$ and the sensitivity is given by $A\epsilon \cdot f_s \cdot K_{Blive}$.

	1995	1996	1997a	1997b
A_{trig}	0.1799 ± 0.0012	0.1799 ± 0.0012	0.1780 ± 0.0012	0.1811 ± 0.0012
A_{μ}^{acc}	0.99242 ± 0.00027	0.99303 ± 0.00027	0.99252 ± 0.00050	0.99401 ± 0.00055
A_{umc}	0.3650 ± 0.0036	0.3634 ± 0.0036	0.3752 ± 0.0036	0.3657 ± 0.0036
A_{nidf}	0.5144 ± 0.0086	0.5118 ± 0.0086	0.5069 ± 0.0085	0.5126 ± 0.0086
$A_{K\mu 2}$	0.4065 ± 0.0029	0.4303 ± 0.0018	0.3999 ± 0.0032	0.4396 ± 0.0039
$A_{K\pi 2}$	0.8745 ± 0.0027	0.8711 ± 0.0015	0.8676 ± 0.0031	0.8765 ± 0.0037
$A_{\pi scat}$	0.8608 $\pm 0.0168^{stat}$ $\pm 0.0464^{syst}$	0.7911 $\pm 0.0096^{stat}$ $\pm 0.0324^{syst}$	0.7618 $\pm 0.0197^{stat}$ $\pm 0.0362^{syst}$	0.8128 $\pm 0.0186^{stat}$ $\pm 0.0371^{syst}$
A_{TD}	0.2930 $\pm 0.0096^{stat}$ $\pm 0.0065^{syst}$	0.3282 $\pm 0.0055^{stat}$ $\pm 0.0056^{syst}$	0.3114 $\pm 0.0102^{stat}$ $\pm 0.0054^{syst}$	0.3201 $\pm 0.0107^{stat}$ $\pm 0.0075^{syst}$
ϵ_{T-2}^{ng}	0.976 $\pm 0.005^{syst}$	0.930 $\pm 0.006^{syst}$	0.929 $\pm 0.004^{syst}$	0.928 $\pm 0.008^{syst}$
f_s	0.6808 $\pm 0.0068^{stat}$ $\pm 0.0142^{syst}$	0.7261 $\pm 0.0057^{stat}$ $\pm 0.0151^{syst}$	0.6997 0.0077^{stat} 0.0146^{syst}	0.7596 0.0095^{stat} 0.0158^{syst}
$A\epsilon$	0.00293 $\pm 0.00013^{stat}$ $\pm 0.00017^{syst}$	0.00301 $\pm 0.00009^{stat}$ $\pm 0.00013^{syst}$	0.00257 $\pm 0.00012^{stat}$ $\pm 0.00013^{syst}$	0.00314 $\pm 0.00015^{stat}$ $\pm 0.00016^{syst}$
$A\epsilon \cdot f_s$	0.00200 $\pm 0.00009^{stat}$ $\pm 0.00012^{syst}$	0.00218 $\pm 0.00007^{stat}$ $\pm 0.00011^{syst}$	0.00180 $\pm 0.00009^{stat}$ $\pm 0.00010^{syst}$	0.00238 $\pm 0.00011^{stat}$ $\pm 0.00013^{syst}$
$K_{Blive}(10^{12})$	1.52627	1.12525	0.37080	0.21574
sensitivity (10^9)	3.0482 $\pm 0.1375^{stat}$ $\pm 0.1894^{syst}$	2.4569 $\pm 0.0751^{stat}$ $\pm 0.1214^{syst}$	0.6666 $\pm 0.0324^{stat}$ $\pm 0.0366^{syst}$	0.5145 $\pm 0.0248^{stat}$ $\pm 0.0288^{syst}$
total sensitivity (10^9)	$6.686 \pm 0.162^{stat} \pm 0.230^{syst}$			
total 1/sensitivity (10^{-10})	$1.496 \pm 0.036^{stat} \pm 0.051^{syst}$			

 Table 5.32: $K^+ \rightarrow \pi^+ \nu \bar{\nu}$ single-event sensitivity of the 1995-7 analysis.

	1995	1996	1997a	1997b
A_{trig}	0.4021 ± 0.0022	0.4034 ± 0.0022	0.4018 ± 0.0022	0.4115 ± 0.0022
A_{μ}^{acc}	0.99242 ± 0.00027	0.99303 ± 0.00027	0.99252 ± 0.00050	0.99401 ± 0.00055
A_{umc}	0.5698 ± 0.0035	0.5631 ± 0.0035	0.5764 ± 0.0035	0.5762 ± 0.0034
A_{nidi}	0.4674 ± 0.0058	0.4608 ± 0.0057	0.4584 ± 0.0057	0.4598 ± 0.0055
$A_{K\mu 2}$	0.4065 ± 0.0029	0.4303 ± 0.0018	0.3999 ± 0.0032	0.4396 ± 0.0039
$A_{K\pi 2}$	0.8745 ± 0.0027	0.8711 ± 0.0015	0.8676 ± 0.0031	0.8765 ± 0.0037
$A_{\pi scat}$	0.8608	0.7911	0.7618	0.8128
	$\pm 0.0168^{stat}$	$\pm 0.0096^{stat}$	$\pm 0.0197^{stat}$	$\pm 0.0186^{stat}$
	$\pm 0.0464^{syst}$	$\pm 0.0324^{syst}$	$\pm 0.0362^{syst}$	$\pm 0.0371^{syst}$
A_{TD}	0.2930	0.3282	0.3114	0.3201
	$\pm 0.0096^{stat}$	$\pm 0.0055^{stat}$	$\pm 0.0102^{stat}$	$\pm 0.0107^{stat}$
	$\pm 0.0065^{syst}$	$\pm 0.0056^{syst}$	$\pm 0.0054^{syst}$	$\pm 0.0075^{syst}$
$\epsilon_{T,2}^{ng}$	0.975	0.928	0.927	0.926
	$\pm 0.005^{syst}$	$\pm 0.006^{syst}$	$\pm 0.004^{syst}$	$\pm 0.008^{syst}$
f_s	0.6808	0.7261	0.6997	0.7596
	$\pm 0.0068^{stat}$	$\pm 0.0057^{stat}$	0.0077^{stat}	0.0095^{stat}
	$\pm 0.0142^{syst}$	$\pm 0.0151^{syst}$	0.0146^{syst}	0.0158^{syst}
$A\epsilon$	0.00929	0.00939	0.00804	0.01006
	$\pm 0.00039^{stat}$	$\pm 0.00024^{stat}$	$\pm 0.00036^{stat}$	$\pm 0.00044^{stat}$
	$\pm 0.00054^{syst}$	$\pm 0.00042^{syst}$	$\pm 0.00041^{syst}$	$\pm 0.00052^{syst}$
$A\epsilon \cdot f_s$	0.00633	0.00682	0.00563	0.00764
	$\pm 0.00027^{stat}$	$\pm 0.00018^{stat}$	$\pm 0.00026^{stat}$	$\pm 0.00035^{stat}$
	$\pm 0.00039^{syst}$	$\pm 0.00034^{syst}$	$\pm 0.00031^{syst}$	$\pm 0.00043^{syst}$
$K_{Blive}(10^{12})$	1.52627	1.12525	0.37080	0.21574
sensitivity (10^9)	9.6544	7.6694	2.0859	1.6488
	$\pm 0.4137^{stat}$	$\pm 0.2075^{stat}$	$\pm 0.0970^{stat}$	$\pm 0.0756^{stat}$
	$\pm 0.5997^{syst}$	$\pm 0.3791^{syst}$	$\pm 0.1145^{syst}$	$\pm 0.0924^{syst}$
total sensitivity (10^9)	$21.059 \pm 0.479^{stat} \pm 0.725^{syst}$			
total 1/sensitivity (10^{-10})	$0.475 \pm 0.011^{stat} \pm 0.016^{syst}$			

 Table 5.33: $K^+ \rightarrow \pi^+ f$ single-event sensitivity of the 1995-7 analysis.

Note, in table 5.32, that the acceptance of the TD cuts, A_{TD} , increases in 1996-7 relative to 1995. This is mostly due to an increased level 1.1 trigger acceptance (see section 3.3), which is offset in large part by losses from additional cuts designed to attack the increase in tail-fluctuation and GDR background (the MASS cut in $A_{\pi_{scat}}$, and the TDDFA1, TDECON, and TDVEL cuts in A_{TD} , which are only applied to the 1996-7 data set – see sections C.3.1 and C.3.4). The increase in these backgrounds is thought to be mainly due to the use of narrower TD pulse shapes for double-pulse fitting by FITPI (see section C.3.4), which is estimated to increase the FITPI acceptance by about 6%. The drop in $\epsilon_{T.2}^{ng}$ in 1996-7 relative to 1995 is thought to be due to deteriorating RS scintillator or light guide quality. f_s and $A\epsilon \cdot f_s$ (i.e., sensitivity per K_{Blive} , which represents the general quality of the data taking and analysis) increase from year to year, except for a drop in 1997a. The increase in f_s is likely due to a gradual lowering of kaon beam momentum between 1995 and 1997 (see section 3.1). The drop in $A\epsilon \cdot f_s$ in 1997a seems to come mainly from a low value of f_s and from acceptance losses of cuts such as UTCQUAL, TGCCD, PBNRS, the PV cuts, MASS, RSLIKE, CHIRF(z), L1.1, and TDDFA1. Also, the target HV problem (part of the BAD_RUN cut) was at its worst in 1997a. Hardware problems and/or higher kaon rate/poorer beam quality may be responsible for the drop in performance in 1997a.

The total $K^+ \rightarrow \pi^+ \nu \bar{\nu}$ single-event sensitivity for the combined 1995-7 analysis is a factor of $4.2/1.5 = 2.8$ greater than the published 1995 sensitivity of $(4.2_{-3.5}^{+9.7}) \times 10^{-10}$ [46].

Chapter 6

Final Results

In this chapter, the number of candidate $K^+ \rightarrow \pi^+ \nu \bar{\nu}$ events from chapter 4 is divided by the $K^+ \rightarrow \pi^+ \nu \bar{\nu}$ single-event sensitivity from chapter 5 to calculate the $K^+ \rightarrow \pi^+ \nu \bar{\nu}$ branching ratio. Similarly, the number of $K^+ \rightarrow \pi^+ f$ events is inferred here and divided by the $K^+ \rightarrow \pi^+ f$ single-event sensitivity from chapter 5 to calculate the $K^+ \rightarrow \pi^+ f$ branching ratio. Finally, the $K^+ \rightarrow \pi^+ \nu \bar{\nu}$ branching ratio is used to calculate a value of the CKM matrix element $|V_{td}|$ (see section 2.1).

6.1 $K^+ \rightarrow \pi^+ \nu \bar{\nu}$ Branching Ratio

As shown in section 4.8, one candidate $K^+ \rightarrow \pi^+ \nu \bar{\nu}$ decay was observed in the 1995-7 data set. The $K^+ \rightarrow \pi^+ \nu \bar{\nu}$ branching ratio is therefore 1.0 divided by the $K^+ \rightarrow \pi^+ \nu \bar{\nu}$ single-event sensitivity from table 5.32, which gives 1.50×10^{-10} .

Uncertainties in measured quantities with Gaussian distributions are typically quoted as $\pm 1\sigma$, which corresponds to a 68% confidence interval. For a Poisson process where 1.0 events are observed, the lower bound of the 68% confidence interval is given by the mean, \bar{n} , of the Poisson distribution for which the probability of observing 1 or more events is $(1 - 0.68)/2 = 0.16$. From Eq. (5.3), this lower bound is found by solving

$$P(n \geq 1; \bar{n}) = 1 - P(n = 0; \bar{n}) = 1 - e^{-\bar{n}} = 0.16 \quad (6.1)$$

which gives $\bar{n} = 0.17435$. The upper bound of the 68% confidence interval is given by the mean, \bar{n} , of the Poisson distribution for which the probability of observing 1 or fewer events is 0.16. Solving

$$P(n \leq 1; \bar{n}) = P(n = 0; \bar{n}) + P(n = 1; \bar{n}) = e^{-\bar{n}} + \bar{n}e^{-\bar{n}} = 0.16 \quad (6.2)$$

gives $\bar{n} = 3.2885$. The 68% confidence interval therefore spans the range [0.17435, 3.2885] events [59]. Dividing this by the $K^+ \rightarrow \pi^+\nu\bar{\nu}$ single-event sensitivity from table 5.32 gives a $K^+ \rightarrow \pi^+\nu\bar{\nu}$ branching ratio range of $[0.261, 4.92] \times 10^{-10}$, or

$$B(K^+ \rightarrow \pi^+\nu\bar{\nu}) = 1.50_{-1.24}^{+3.42} \times 10^{-10} \quad (6.3)$$

6.2 $K^+ \rightarrow \pi^+ f$ Upper Limit

The signal region for kaon decays into a pion and a massless familon, $K^+ \rightarrow \pi^+ f$, defined as the “ πf ” region, is the same as the $\pi^+\nu\bar{\nu}(1)$ signal region with the additional requirement of the PFBOX cut. The PFBOX cut is a 2σ cut around the pion peak resulting from $K^+ \rightarrow \pi^+ f$ decay (see section 5.8), and was defined before looking in the πf region. That is, the search for $K^+ \rightarrow \pi^+ f$, similar to the search for $K^+ \rightarrow \pi^+\nu\bar{\nu}$, was performed blind. The candidate $K^+ \rightarrow \pi^+\nu\bar{\nu}$ event (see section 4.8) does not fall into the πf region.

Results of fits to the R , E , and P peaks of UMC-generated $K^+ \rightarrow \pi^+ f$ decays, where values of R , E , and P from UMC have been scaled and smeared by the quantities in tables 5.18 and 5.19 to match real data, are shown in table 6.1. The R , E , and P values of the candidate event given in section 4.8 are also listed in table 6.1, along with their distances from the $K^+ \rightarrow \pi^+ f$ peak values. The candidate event is located 2.65σ , 2.64σ , and 3.21σ lower than the $K^+ \rightarrow \pi^+ f$ peak in R , E , and P , respectively. To find the probability that a $K^+ \rightarrow \pi^+ f$ event has these values of R , E , and P , presumably due to a pion-nuclear interaction and/or Gaussian resolution, the probability that a $K_{\pi 2}$ event is located this far or farther from the $K_{\pi 2}$ peak is measured. Results of fits to the R , E , and P peaks of $K_{\pi 2}$ decays are shown in table 6.1, along with the number of events $M_{K_{\pi 2}}^{\pi f}$ used to perform the fits, which is the number of $K_{\pi 2}$ decays from the $K_{\pi 2}(1)$ monitor data (see section 3.3) which

	Range	Energy	Momentum
$K^+ \rightarrow \pi^+ f$, mean $\pm\sigma$	37.93 ± 1.201	127.6 ± 3.734	227.0 ± 2.755
Candidate event, mean $\pm\sigma$	34.75 ± 1.22	117.73 ± 3.51	218.17 ± 2.68
Distance to the πf peak	2.65σ	2.64σ	3.21σ
$K_{\pi 2}$ mean $\pm\sigma$	30.43 ± 0.8811	108.7 ± 2.808	205.1 ± 2.258
$M_{K_{\pi 2}}^{\pi f}$	6398		
$M_{K_{\pi 2}}^{\pi f}$ at $R, E, P < [2.65, 2.64, 3.21]\sigma$	16		
Probability that a $K^+ \rightarrow \pi^+ f$ event has candidate values of R, E, P	$0.250 \pm 0.062\%$		

Table 6.1: Calculation of the probability that a $K^+ \rightarrow \pi^+ f$ event, for massless f , has the R , E , and P values of the candidate event. Table entries are described in section 6.2 of the text.

pass all cuts except the PV function cut for detector subsystems outside of the target, the BOX cut, and the LAYV4 cut (see section C.3). Also shown in table 6.1 is the number of $K_{\pi 2}$ decays located as far or farther from the $K_{\pi 2}$ peak as the candidate event is from the $K^+ \rightarrow \pi^+ f$ peak, which, when divided by $M_{K_{\pi 2}}^{\pi f}$, gives the probability that a $K^+ \rightarrow \pi^+ f$ event has the R , E , and P values of the candidate event. As shown in table 6.1, this probability is only 0.3%, which suggests that the candidate event is not due to $K^+ \rightarrow \pi^+ f$ decay. Based on no $K^+ \rightarrow \pi^+ f$ decays observed, the upper limit on the $K^+ \rightarrow \pi^+ f$ branching ratio at the 90% confidence level is given by the mean, \bar{n} , of the Poisson distribution for which the probability of observing 0 events is $1 - 0.90 = 0.10$. From Eq. (5.3), this upper limit is found by solving

$$P(n = 0; \bar{n}) = e^{-\bar{n}} = 0.10 \quad (6.4)$$

which gives $\bar{n} = 2.3026$. Dividing this by the $K^+ \rightarrow \pi^+ f$ single-event sensitivity from table 5.33 gives an upper limit to the $K^+ \rightarrow \pi^+ f$ branching ratio at the 90% confidence level of 1.09×10^{-10} .

6.3 V_{td}

As stated in section 2.3, the measured value of the $K^+ \rightarrow \pi^+ \nu \bar{\nu}$ branching ratio can be used to extract the magnitude of the CKM matrix element V_{td} . From Eq. (2.18), the

$K^+ \rightarrow \pi^+ \nu \bar{\nu}$ branching ratio defines a circle in the (ρ, η) plane (see figure 2.4). This circle has radius r_0 given by Eq. (2.19) which is obtained from

1. the $K^+ \rightarrow \pi^+ \nu \bar{\nu}$ branching ratio range quoted in section 6.1 ($[0.26, 4.92] \times 10^{-10}$);
2. $A = V_{cb}/\lambda^2$ from Eq. (2.2), with $\lambda = 0.22$ and $V_{cb} = 0.040 \pm 0.003$ [18];
3. $X(x_t)$ as defined in Eqs. (2.7) and (2.8), with $\eta_X = 0.994$ and $x_t = m_t^2/M_W^2$, where $m_t = \bar{m}_t(m_t) = (166 \pm 5) \text{ GeV}/c^2$ [18] and $M_W = 80.41 \text{ MeV}/c^2$ [16]; and
4. $\kappa_+ = 4.11 \times 10^{-11}$ [18].

The circle is centered at $(\rho_0, 0)$, where ρ_0 is given by Eq. (2.13) and is obtained using tabulated values of $P_0(X)$ [18] and A and $X(x_t)$ as given above. ρ_0 and r_0 define limits on R_t according to Eq. (2.23), where R_t is the length of one of the sides of the unitarity triangle and is related to V_{td} via Eq. (2.21). Looping over the full ranges of all variables, the limits on V_{td} from the measured $K^+ \rightarrow \pi^+ \nu \bar{\nu}$ branching ratio are

$$0.0024 < |V_{td}| < 0.038 \quad (6.5)$$

These limits on V_{td} are less restrictive than those which follow from assumption of unitarity of the quark mixing matrix, which are given in Eq. (2.3): $0.004 < |V_{td}| < 0.014$.

Chapter 7

Conclusions

The decay $K^+ \rightarrow \pi^+ \nu \bar{\nu}$ involves a flavour-changing neutral weak current, and therefore cannot occur at first order (“tree level”) in the Standard Model (SM). However, flavour symmetry is “broken” as evidenced by the widely different quark masses, which allows $K^+ \rightarrow \pi^+ \nu \bar{\nu}$ to proceed at second order (“one-loop level”). $K^+ \rightarrow \pi^+ \nu \bar{\nu}$ is therefore particularly sensitive to weak interactions of the highest mass quark (in the SM, this is the top quark), and is highly suppressed in the SM with a predicted branching ratio of $(0.8 \pm 0.3) \times 10^{-10}$. The uncertainty in the branching ratio is dominated by measurement uncertainties in the Cabibbo-Kobayashi-Maskawa (CKM) quark mixing matrix elements $|V_{cb}|$ and $|V_{ub}/V_{cb}|$. The theoretical uncertainty is only 7%. Because the predicted branching ratio is so low and lies in a narrow range, measurement of $K^+ \rightarrow \pi^+ \nu \bar{\nu}$ offers a high-precision test of the 2-class, 3-generation, 4-force structure of the SM. It can also be used to hunt for non-SM physics.

Positive identification of $K^+ \rightarrow \pi^+ \nu \bar{\nu}$ requires suppression of potential backgrounds by at least a factor of 10^{10} . The experimental signature for $K^+ \rightarrow \pi^+ \nu \bar{\nu}$ is $K^+ \rightarrow \pi^+$ with nothing else observed. Known background processes which can mimic this signature include the first-order weak decays $K^+ \rightarrow \pi^+ \pi^0$ ($K_{\pi 2}$) and $K^+ \rightarrow \mu^+ \nu_\mu$ ($K_{\mu 2}$), scattering of pions in the beam, and kaon charge exchange. $K_{\pi 2}$ and $K_{\mu 2}$ decays are two-body decays, which means that the charged track from these decays is monochromatic in the kaon rest frame. These decays are therefore suppressed by requiring kaons to stop before they decay, and restricting the search for $K^+ \rightarrow \pi^+ \nu \bar{\nu}$ to the kinematic window between the $K_{\pi 2}$ and $K_{\mu 2}$ peaks. $K_{\pi 2}$ decays are further suppressed by high-efficiency photon detection. $K_{\mu 2}$ decays

are further suppressed by μ^+/π^+ particle separation via the different energy loss rate and range-momentum correlation of muons and pions in detector materials. Also, the detector is constructed such that the π^+ track from $K^+ \rightarrow \pi^+\nu\bar{\nu}$ is confined within, so $K_{\mu 2}$ decays are additionally suppressed by requiring identification of the $\pi \rightarrow \mu \rightarrow e$ decay sequence in the detector. Backgrounds arising from pion scattering in the beam and kaon charge exchange are suppressed by K^+/π^+ particle identification in the beam, and by requiring non-coincident beamline and decay-volume detector activity.

Experiment 787 (E787) at Brookhaven National Laboratory (BNL) has adopted a “blind” approach to the search for $K^+ \rightarrow \pi^+\nu\bar{\nu}$, in an attempt to minimize analysis “bias” which can arise due to small statistics. A small number of $K^+ \rightarrow \pi^+\nu\bar{\nu}$ events is expected in the 1995-7 data, based on the number of collected kaons, the acceptance of data-selection requirements, and the predicted $K^+ \rightarrow \pi^+\nu\bar{\nu}$ branching ratio. Therefore, a signal region, or “box”, is defined where the signal/background ratio is expected to be the highest, and small numbers of events in the box are not used to define the properties of background or signal events. Instead, potential backgrounds are identified *a priori*, and techniques are devised to measure the background level in the box using events which lie outside the box. Events in the box are not examined until the background estimates are final. The goal in the analysis is to reduce the expected background to $\ll 1$ event in the box. Then, if events are observed in the box, they will have a high probability to be signal, in part because they have not previously been examined at any point in the analysis.

To reduce the effects of small-statistics bias on the background measurements, backgrounds are estimated using “bifurcated” analyses. That is, each background is addressed by two uncorrelated cuts or sets of cuts. Each of the two cuts is inverted to provide a high-statistics, outside-the-box background data sample, on which the performance of the other cut is measured. Correlations between the cuts are verified to be small by comparing predicted and observed numbers of background events in regions outside the box, defined by loosening both cuts simultaneously. The degree to which bias has entered the analysis is measured by dividing the data into 1/3 and 2/3 samples. Cuts were designed using the 1/3 data sample, and then verified to perform as expected on the independent 2/3 data sample.

The total number of background events expected in the box for data collected between 1995 and 1997 is 0.08 ± 0.02 events. Opening the box revealed one event inside. This event passed the most stringent cut-tightening criteria, which were designed before examining the event, and further reduce the estimated background in the box to 0.006 ± 0.002 events. Therefore, the observed event is likely a $K^+ \rightarrow \pi^+ \nu \bar{\nu}$ signal event. The probability that a kaon decaying into a pion and a massless familon gives rise to the measured kinematic quantities of the candidate event is 0.3%. Assuming then that the event is due to $K^+ \rightarrow \pi^+ \nu \bar{\nu}$, the $K^+ \rightarrow \pi^+ \nu \bar{\nu}$ branching ratio is $1.5_{-1.2}^{+3.4} \times 10^{-10}$. Based on no $K^+ \rightarrow \pi^+ f$ events observed, the upper limit on the $K^+ \rightarrow \pi^+ f$ branching ratio at the 90% confidence level is 1.1×10^{-11} (for massless f). The $K^+ \rightarrow \pi^+ \nu \bar{\nu}$ branching ratio is sensitive to the weak coupling of top to down quarks which, as parameterized by the CKM quark mixing matrix element V_{td} , is calculated to lie in the range $0.002 < |V_{td}| < 0.04$.

The measured branching ratio for $K^+ \rightarrow \pi^+ \nu \bar{\nu}$, $1.5_{-1.2}^{+3.4} \times 10^{-10}$, agrees with the SM prediction, $(0.8 \pm 0.3) \times 10^{-10}$, although the statistical uncertainty associated with observation of one event makes it difficult to draw any conclusions about the presence or absence of non-SM contributions to the decay. One calculation [18] suggests that if the $K^+ \rightarrow \pi^+ \nu \bar{\nu}$ branching ratio is found to be $> 1.67 \times 10^{-10}$, then this would be compelling evidence for new physics. Again however, the statistical uncertainty of the current measurement does not allow any definitive statements to be made about contributions from non-SM physics.

Nevertheless, the $K \rightarrow \pi$ decay system is unique in that it involves decay of the two lightest SM pseudoscalar (spin 0) particles. By conservation of angular momentum, the other particle in a two-body $K \rightarrow \pi$ decay must also have spin = 0. Therefore, there are no two-body $K \rightarrow \pi$ decays which have a massless SM scalar or non-scalar particle (e.g., the photon) in the final state. The breaking of a global continuous symmetry in nature at a high energy scale gives rise to a massless Goldstone boson (scalar or pseudoscalar), so the $K \rightarrow \pi$ decay system is a clean system for searching for Goldstone bosons associated with the $s \rightarrow d$ flavour/family change (e.g., familons, or axions coupled to this flavour/family change). The upper limit on the $K^+ \rightarrow \pi^+ f$ width is related to a limit on the energy scale

F of the symmetry breaking via [60]

$$\Gamma(K \rightarrow \pi f) = \frac{1}{16\pi} \frac{m_K^3}{F^2} g_V^2 \beta^3 |F_1(0)|^2 \quad (7.1)$$

where $\beta = 1 - m_\pi^2/m_K^2$, g_V is the weak vector coupling constant, and $F_1(q^2)$ is the $K^+ \rightarrow \pi^+$ weak vector form factor. According to the conserved vector current hypothesis, $g_V = 1$, and in the limit of exact flavour SU(3) symmetry, $F_1(0) = 1$ [60]. The branching ratio B is related to the width Γ and mean lifetime τ via $\Gamma = B\hbar/\tau$, so

$$F_{sd}^V = \sqrt{\frac{1}{16\pi} \frac{m_k^3}{B(K^+ \rightarrow \pi^+ f)} \frac{\tau_K}{\hbar} \left(1 - \frac{m_\pi^2}{m_K^2}\right)^3} \quad (7.2)$$

where F_{sd}^V is the energy scale of the symmetry breaking which gives rise to a Goldstone boson that couples vectorially to the $s \rightarrow d$ flavour/family change. Using the $K^+ \rightarrow \pi^+ f$ upper limit of 1.09×10^{-11} , Eq. (7.2) gives $F_{sd}^V > 1.8 \times 10^{12}$ GeV. The energy scale of the symmetry breaking is inversely proportional to the Goldstone boson's coupling to SM particles, or, equivalently, to the Goldstone boson's mass via [16]

$$m = 0.62 \times 10^{-3} \text{ eV} \cdot (10^{10} \text{ GeV}/F) \quad (7.3)$$

So the mass of the familon or axion which couples vectorially to the $s \rightarrow d$ flavour/family change is restricted to be $m < 3.5 \times 10^{-6}$ eV. The allowed window of masses is found to be $(1.0 < m < 3.5) \times 10^{-6}$ eV, using astrophysical constraints on the axion mass [16] shown in figure 7.1.

The experimental progress of the search for $K^+ \rightarrow \pi^+ \nu \bar{\nu}$ is shown in figure 7.2. Data from 1998-9 is currently being analyzed, and has a single-event sensitivity similar to the combined 1995-7 data set. With E949, the successor experiment to E787 at BNL, it is hoped to eventually achieve a $K^+ \rightarrow \pi^+ \nu \bar{\nu}$ single-event sensitivity of $(8 - 15) \times 10^{-12}$ via improved data-taking conditions in 2001-3. This sensitivity should allow for observation of about 10 $K^+ \rightarrow \pi^+ \nu \bar{\nu}$ events, which will reduce the statistical uncertainty in the branching ratio measurement, and allow for a more precise determination of $|V_{td}|$. Specifically, the duty factor of the AGS spill will be increased from about 41% to 64%; the number of protons per spill on the kaon production target will be increased from about 15 Tp/spill to 65 Tp/spill;

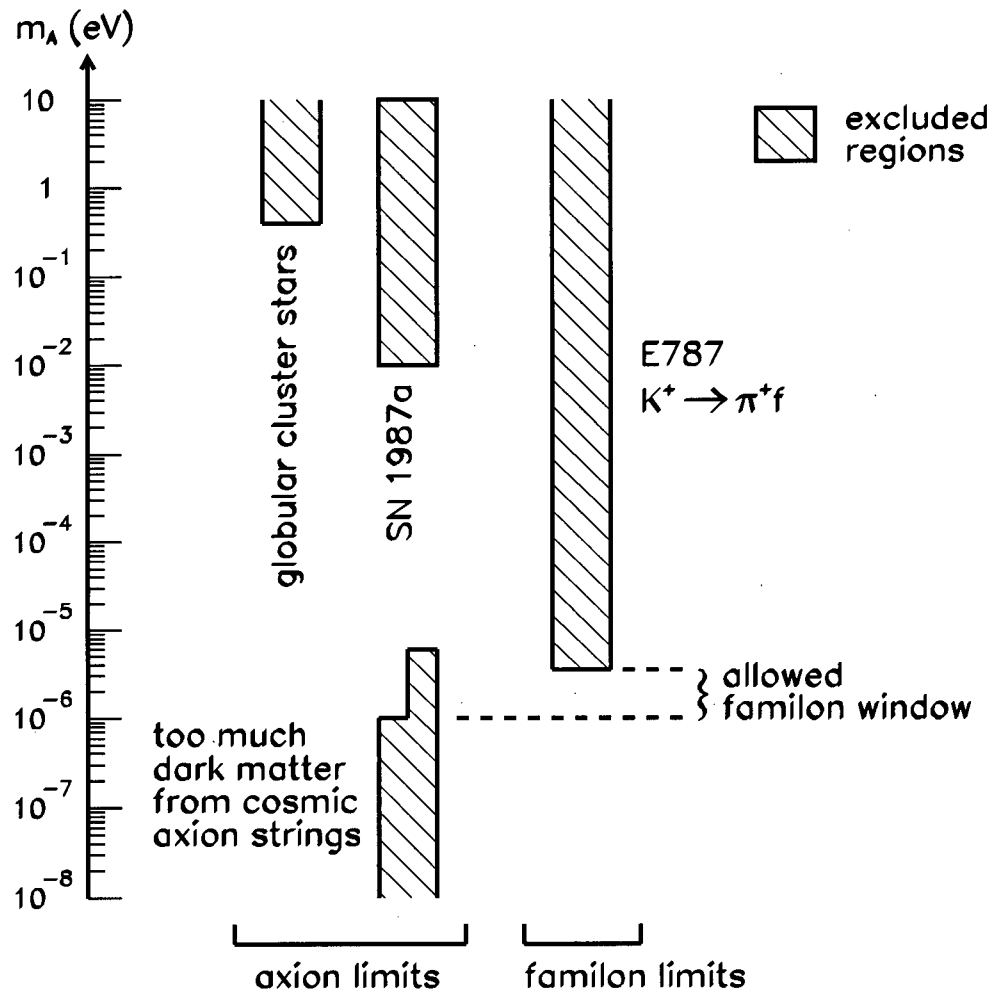


Figure 7.1: Constraints from astrophysics [16] and $K^+ \rightarrow \pi^+ f$ on the masses of the axion and familon. The axion mass limits come from comparisons of predicted and observed energy losses from globular cluster stars and supernova 1987a, and from considerations of axion production in the early universe. The “step” in the mass constraint from dark matter considerations indicates the theoretical uncertainty in this constraint. The familon is a “flavour-coupled axion”, so both astrophysics and $K^+ \rightarrow \pi^+ f$ can be used to set an allowed mass region for the familon.

the kaon beam momentum will be kept low (at about 700 MeV/c, as in 1997) in order to maintain a high kaon stopping fraction in the target; the data acquisition will be improved via reduced trigger and readout deadtimes and online accidental losses; the “barrel veto liner” will replace the outer 3 layers of the RS to provide improved photon detection; new scintillator for layers 1 – 5 of the RS will be installed, which is expected to increase the $T \cdot 2$ efficiency; a new B4 hodoscope with greater segmentation will be installed in order to improve the spatial resolution of beam particles; another active degrader with photon and charged particle detection abilities may replace part of the BeO degrader; and running periods will be extended to ≥ 25 weeks/year, symbiotic with the operation of the AGS, in 2000 and afterwards, as an injector for the “relativistic heavy-ion collider” (RHIC).

The blind analysis technique used by E787 to search for $K^+ \rightarrow \pi^+ \nu \bar{\nu}$ is useful when a small number of $K^+ \rightarrow \pi^+ \nu \bar{\nu}$ events is expected, such that it is desirable to define a signal region which is never probed for the purposes of signal or background event definition, and where backgrounds are estimated to contribute $\ll 1$ event. Because E949 expects to collect on the order of 10 $K^+ \rightarrow \pi^+ \nu \bar{\nu}$ events in a comparably-sized signal region, it may no longer be desirable to define such a signal region. Instead, the background in the signal region could be directly measured, and subtracted from the number of events observed in this region. Or, the signal region could be defined on a sliding scale, and the $K^+ \rightarrow \pi^+ \nu \bar{\nu}$ branching ratio could be found as a function of background level (which should be constant, if the background is well understood). Furthermore, bifurcated analyses become more difficult as the expected signal increases, because this signal will significantly contaminate a background data sample when a single cut is inverted to define the data sample. Therefore, new background estimation techniques may be needed for analysis of E949 data.

In order to measure the $K^+ \rightarrow \pi^+ \nu \bar{\nu}$ branching ratio and $|V_{td}|$ to high precision ($\pm 10\%$), it is necessary to observe on the order of 100 $K^+ \rightarrow \pi^+ \nu \bar{\nu}$ events. To collect this data in a reasonable amount of time, kaon rates would have to be much higher than those used in E787/E949. However, the E787/E949 detector is limited with respect to the kaon rate that it can handle, due to the need for detection of photons in order to suppress $K_{\pi 2}$ decays, and identification of the $\pi \rightarrow \mu \rightarrow e$ decay sequence in order to suppress $K_{\mu 2}$ decays. Both

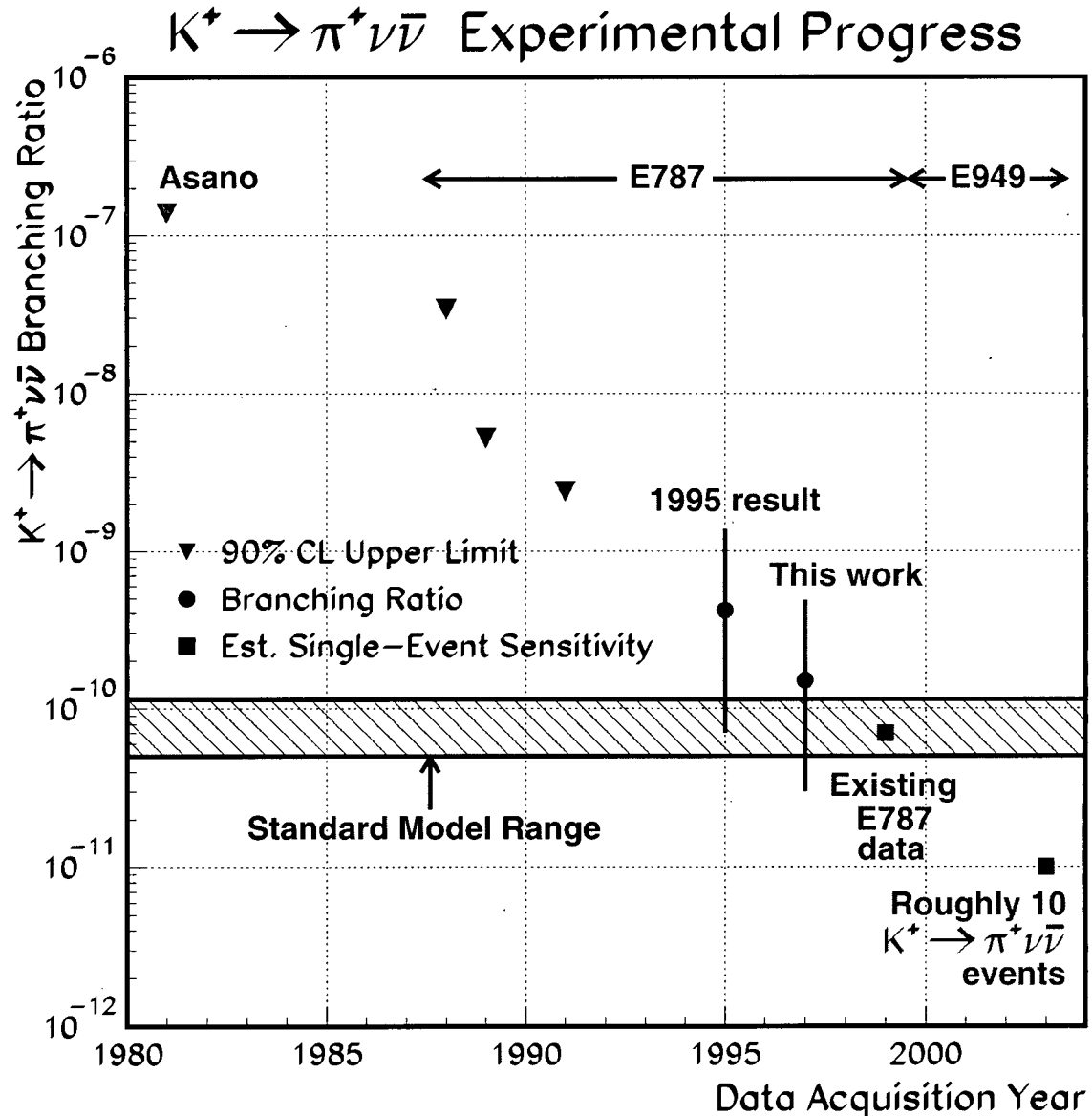


Figure 7.2: Experimental progress of the search for $K^+ \rightarrow \pi^+ \nu \bar{\nu}$. The upper limit on the $K^+ \rightarrow \pi^+ \nu \bar{\nu}$ branching ratio at the 90% confidence level is shown as triangles [61, 62], the measured branching ratio for the 1995 analysis [46] and this work [63] are shown as circles, and the estimated $K^+ \rightarrow \pi^+ \nu \bar{\nu}$ single-event sensitivities for the complete E787 data and the E949 experiment are shown as squares, each as a function of year in which data is acquired. The current theoretical prediction for the $K^+ \rightarrow \pi^+ \nu \bar{\nu}$ branching ratio [18] is shown as the hatched region. The point labelled “Asano” comes from an experiment which pre-dates E787 at BNL [61].

of these requirements can cause large losses in acceptance when a high rate of accidentals is present. A new detector, with better rate capabilities and the ability to collect close to 100 $K^+ \rightarrow \pi^+ \nu \bar{\nu}$ events in 2 years with a background level of about 10 events has been proposed, which would collect kaon decays in flight rather than requiring the kaons to stop before decaying. Because the momentum of a kaon decaying in flight is not known to the near-perfect precision of a stopped kaon, the in-flight technique of the proposed "CKM" experiment at Fermilab [64] may perhaps suffer from worse kinematic resolution of $K_{\pi 2}$ and $K_{\mu 2}$ decays, resulting in worse kinematic suppression of these decays, than the stopped-kaon technique of E787/E949. However, the muon and photon vetos of the CKM detector are better than E787/E949, which allows for the collection of kaon decays at a high rate. Beam-related backgrounds in the CKM experiment are suppressed via use of a high purity kaon beam ($> 70\%$). Backgrounds arising from scattering of kaons, muons, and pions in detector materials can potentially be understood much better in the CKM experiment because the amount of material that these particles traverse can be varied. Furthermore, the CKM detector, similar to the E787/E949 detector, allows for redundant measurements of the kinematics of charged pion tracks, which in turn allows for high background suppression and reliable background estimation. However, while the in-flight technique of the CKM experiment has the potential for making high-precision measurements of the $K^+ \rightarrow \pi^+ \nu \bar{\nu}$ branching ratio and $|V_{td}|$ in a short amount of time, it is not well-tested whereas the stopped-kaon technique of E787/E949 is. Therefore, the in-flight technique may face unanticipated challenges, particularly in the realm of background suppression.

Experiment 787 at Brookhaven National Laboratory has been successful in observing one $K^+ \rightarrow \pi^+ \nu \bar{\nu}$ decay in a sample of 6.7 billion kaon decays. The positive identification of this extremely rare signal is made possible by excellent understanding of the E787 detector, and by excellent understanding and suppression of potential background processes for $K^+ \rightarrow \pi^+ \nu \bar{\nu}$.

Bibliography

- [1] M. Berman, *The Reenchantment of the World*, Fifth printing, Cornell University Press, Ithaca, New York, 1994 (pg. 147).
- [2] M.J. Veltman, *Sci. Amer.* **255**, 76 (1986).
- [3] S. Glashow, *Nucl. Phys.* **22**, 579 (1961).
- [4] S. Weinberg, *Phys. Rev. Lett.* **19**, 1264 (1967).
- [5] A. Salam, *Elementary Particle Physics (Nobel Symp. No. 8)*, Almqvist and Wilsell, Stockholm, 367 (1968).
- [6] G. Arnison *et al.* (UA1 collaboration), *Phys. Lett.* **122B**, 103 (1983).
- [7] cern.web.cern.ch/CERN/Announcements/2000/NewStateMatter
- [8] F. Mandl and G. Shaw, *Quantum Field Theory*, John Wiley and Sons, Toronto, 1993.
- [9] B. Greene, *The Elegant Universe*, W.W. Norton & Company, N.Y., 1999.
- [10] Y. Fukuda *et al.*, *Phys. Rev. Lett.* **81**, 1562 (1998).
- [11] N. Cabibbo, *Phys. Rev. Lett.* **10**, 531 (1963).
- [12] S.L. Glashow, J. Iliopoulos, and L. Maiani, *Phys. Rev. D* **2**, 1285 (1970).
- [13] M. Kobayashi and T. Maskawa, *Prog. Theor. Phys.* **49**, 652 (1973).
- [14] J.H. Christenson *et al.*, *Phys. Rev. Lett.* **13**, 138 (1964).
- [15] L. Wolfenstein, *Phys. Rev. Lett.* **51**, 1945 (1983).

Bibliography

- [16] C. Caso *et al.* (Particle Data Group), “The Review of Particle Physics”, European Physical Journal **C3**, 1 (1998).
- [17] C. Jarlskog, Phys. Rev. Lett. **55**, 1039 (1985).
- [18] G. Buchalla and A.J. Buras, Nucl. Phys. **B548**, 293 (1999).
- [19] G. Buchalla and A.J. Buras, Nucl. Phys. **B412**, 106 (1994).
- [20] J.S. Hagelin and L.S. Littenberg, Prog. Part. Nucl. Phys. **D23**, 1 (1989).
- [21] D. Rein and L.M. Sehgal, Phys. Rev. **D39**, 3325 (1989).
- [22] M. Lu and M.B. Wise, Phys. Lett. **B337**, 133 (1994).
- [23] F. Wilczek, Phys. Rev. Lett. **49**, 1549 (1982).
- [24] L. Silvestrini, e-print hep-ph/9906202.
- [25] www.ags.bnl.gov/~kbrown/seb/sebsetup.html
- [26] www.ags.bnl.gov/~kbrown/seb/overview.html
- [27] J. Doornbos *et al.*, Nucl. Instr. Meth. **A444**, 546 (2000).
- [28] V. Fitch and R. Motley, Phys. Rev. **101**, 496 (1956).
- [29] M.S. Atiya *et al.*, Nucl. Instr. Meth. **A321**, 129 (1992).
- [30] P. Kitching and T. Nakano, “The New Beam Instrumentation”, E787 Technical Note No. 237 (1992). Unpublished.
- [31] D.A. Bryman *et al.*, Nucl. Instr. Meth. **A396**, 394 (1997).
- [32] E.W. Blackmore *et al.*, Nucl. Instr. Meth. **A404**, 295 (1998).
- [33] T.K. Komatsubara, “Brief Summary of the Status of Upgraded-E787 in 1995”, E787 Technical Note No. 305 (1995). Unpublished.

Bibliography

- [34] R.A. McPherson, "Chasing the Rare Decay $K^+ \rightarrow \pi^+ \nu \bar{\nu}$ ", Princeton University, Ph.D. Thesis, November 1995.
- [35] I.-H. Chiang *et al.*, IEEE Trans. Nucl. Sci. **42**, 394 (1995).
- [36] T.K. Komatsubara *et al.*, Nucl. Instr. Meth. **A404**, 315 (1998).
- [37] The version of UMC used in this analysis is version 6.
- [38] P. Meyers, "A Modified Version of the UMC Multiple Scattering Routine MSCAT1", E787 Technical Note No. 77 (1985). Unpublished.
- [39] A.J. Stevens, "Nuclear Interactions in CH revisited", E787 Technical Note No. 140 (1987). Unpublished.
- [40] W.R. Nelson *et al.*, "The EGS4 Code System", SLAC 265, SLAC (1985).
- [41] P.C. Bergbusch *et al.*, " $\pi^+ \nu \bar{\nu}(1)$ Analysis of the 1995-7 Data Set", E787 Technical Note No. 365 (2000). Unpublished.
- [42] H. Brafman *et al.*, IEEE Trans. Nucl. Sci., **32**, 1 (1985).
- [43] M. Burke *et al.*, IEEE Trans. Nucl. Sci., **41**, 131 (1994).
- [44] S. Kettell and T. Komatsubara, "Some Analysis of the 1996 Data Set", E787 Technical Note No. 337 (1997). Unpublished.
- [45] S. Kettell, "Summary of 1997 Pass1", E787 Technical Note No. 338 (1997). Unpublished.
- [46] S. Adler *et al.*, Phys. Rev. Lett. **79**, 2204 (1997).
- [47] J.R. Stone, "Capturing the Rare Decay $K^+ \rightarrow \pi^+ \nu \bar{\nu}$ ", Princeton University, Ph.D. Thesis, November 1998.
- [48] F. Ajzenberg-Selove, Nucl. Phys. **A506**, 1 (1990).
- [49] S.C. Fultz *et al.*, Phys. Rev. **143**, 790 (1966).

Bibliography

- [50] J.B. Birks, Proc. Phys. Soc. **A64**, 874 (1951).
- [51] H-S Ng, "Low Energy (K^+ , ^{12}C) Charge Exchange Cross Section Measurements, University of Alberta, M.Sc. Thesis, 2000.
- [52] A. Konaka *et al.*, " $\pi^+\nu\bar{\nu}$ Analysis Memo No. 4", E787 1995 Analysis Memo-4 (1997). Unpublished.
- [53] O. Couet, "PAW - Physics Analysis Workstation", CERN Program Library entry **Q121**, CERN (1993).
- [54] A. Konaka *et al.*, "A note on the charge exchange background estimate", E787 1995 Analysis Memo-Cex (1997). Unpublished.
- [55] A. Konaka *et al.*, "A note for the analysis checking committee (2): Results of a detailed examination", E787 1995 Analysis Memo-6 (1997). Unpublished.
- [56] A.S. Turcot, "The Search for the Decay $K^+ \rightarrow \pi^+\nu\bar{\nu}$ ", University of Victoria, Ph.D. Thesis, 1994.
- [57] M. Diwan, "E787 Energy Resolution Studies Part 1", E787 Technical Note No. 362 (1998). Unpublished.
- [58] A. Konaka *et al.*, "Background and acceptance studies", E787 1995 Analysis Memo-3 (1996). Unpublished.
- [59] S. Ferneyhough, "Some General Results on Poisson Statistics", E787 Technical Note No. 326 (1997). Unpublished.
- [60] J. Feng *et al.*, Phys. Rev. **D57**, 5875 (1998).
- [61] Y. Asano *et al.*, Phys. Lett. **B107**, 159 (1981).
- [62] S. Adler *et al.*, Phys. Rev. Lett. **76**, 1421 (1996).
- [63] S. Adler *et al.*, Phys. Rev. Lett. **84**, 3768 (2000).

Bibliography

- [64] R. Coleman *et al.*, “A Proposal for a Precision Measurement of the Decay $K^+ \rightarrow \pi^+ \nu \bar{\nu}$ and Other Rare K^+ Decay Processes at Fermilab Using the Main Injector”, www.fnal.gov/projects/ckm/documentation/public/proposal/ckm-proposal.ps.gz
- [65] A. Desjardins, “Study of Range Stack dE/dx Calibrations and Likelihood Analysis”, E787 Technical Note No. 363 (1998). Unpublished.
- [66] S. Wilks, *Mathematical Statistics*, J. Wiley and Sons, 1962.

Appendix A

BNL E787 Collaboration

S. Adler, M.S. Atiya, I-H. Chiang, M.V. Diwan, J.S. Frank, J.S. Haggerty, V. Jain,
S.H. Kettell, T.F. Kycia, K.K. Li, L.S. Littenberg, C. Ng, R.C. Strand, C. Witzig

Brookhaven National Laboratory

M. Kazumori, T.K. Komatsubara, M. Kuriki, N. Muramatsu, A. Otomo, S. Sugimoto

KEK, Tanashi-branch

T. Inagaki, S. Kabe, M. Kobayashi, Y. Kuno, T. Sato, T. Shinkawa, Y. Yoshimura

KEK, Tsukuba

Y. Kishi, T. Nakano, T. Sasaki

Osaka University

M. Ardebili, A.O. Bazarko, M.R. Convery, M.M. Ito, D.R. Marlow, R.A. McPherson,
P.D. Meyers, F.C. Shoemaker, A.J.S. Smith, J.R. Stone

Princeton University

M. Aoki, E.W. Blackmore, P.C. Bergbusch, D.A. Bryman, A. Konaka, J.A. Macdonald,
J. Mildenerger, T. Numao, P. Padley, J.-M. Poutissou, R. Poutissou, G. Redlinger

TRIUMF

P. Kitching and R. Soluk

University of Alberta

Appendix B

Personal Contributions

Due to the highly collaborative nature of particle physics experiments, it has become customary in Ph.D. theses to include some information on the major contributions of the author to the experiment. The duties/contributions of the present author to the E787 experiment in the years 1995-2000 include:

- hardware
 - tuning and maintenance of the full CCD system, including target, EC, barrel, and beam detector CCD's
 - maintenance of the UTC and BWC gas systems
 - maintenance of the UTC post-amps, ADC's, and TDC's
 - maintenance of the BWC post-amps
 - tests of the demultiplexed BWC1
 - feasibility study of implementing TDC's on the RS
- data acquisition
 - maintenance of the SSP's
 - maintenance of the computer system used in data acquisition, and some computer system administration
 - acquisition and storage of monitor data

Appendix B. Personal Contributions

- calibrations
 - all TD time calibrations: RS, RS flags, EC, IC, B4, Čerenkov, and strobes
 - TD pulse height → MeV calibration
 - TD pulse shape calibrations: RS, B4
- processing
 - check of all calibrations required at PASS1
 - development of PASS1 source code and run scripts
 - verification of the quality of PASS1 data reduction
 - tape-loading at TRIUMF, and coordination of parallel PASS1 processing using machines at Princeton, BNL, and in Japan
- analysis
 - elucidation and suppression of TD backgrounds
 - outside-the-box studies → GDR background correlation mechanism
 - all aspects of the acceptance and sensitivity measurements, except UMC
- calculations
 - $K_{\pi 2}$, $K^+ \rightarrow \pi^+ \nu \bar{\nu}$, and $K^+ \rightarrow \pi^+ f$ branching ratios/upper limits
 - V_{td}
 - allowed mass range of the familon

Appendix C

Detailed Cut Descriptions

C.1 PASS1

The PASS1 cuts, in order of application, are described below.

- **TRBIT:** This is an offline reproduction of the online $K^+ \rightarrow \pi^+ \nu \bar{\nu}$ trigger requirement (see section 3.3).
- **RD_TRK:** This track reconstruction cut requires that a track be found in the RS. This is the first reconstruction cut that is applied because accidental hit rates in the detector are lowest farthest from the beamline. Only one positively-charged track is found, beginning at the T · 2 hit closest in time to the detector strobe (i.e., closest in time to the T · 2 hit found by the trigger), and extending at least to layer 6. Gaps between RS layers are allowed at sector crossings occurring up to layer 12. The timing of hits comes from the TD's, and each hit must have a minimum energy (0.1 MeV for the T counters; 0.5 MeV for layers 2 – 21).
- **STLAY:** For the track which satisfies the RD_TRK cut requirements, the stopping layer and hexant as found by the offline track reconstruction must be the same as those found by the trigger. The stopping layer found by the trigger is the outermost layer with a “charged-track” (*ct*) hit (see section 3.3), so this cut rejects highly-curved tracks which cross hexants in the stopping layer. For example, muon tracks from $K_{\mu 2}$

Appendix C. Detailed Cut Descriptions

decays can cross hexants in layer 21, due to high track curvature or re-entrance of the track muon or decay-electron into the RS from the barrel. This cut also rejects $K_{\pi 2}$ decays which have non-contiguous energy deposition in the RS due to a charged track at low layers and a photon splash at higher layers in the ct sectors. Events with undefined TD times in the stopping counter are also rejected.

- **RSHEX:** For the track that satisfies the RD_TRK cut requirements, if there is a hit in the stopping hexant and layer with more than 1 MeV ADC energy which is not part of the track fit, then the event is rejected. This cut rejects $K_{\mu 2}$ decays which may have a false $\pi \rightarrow \mu$ decay signature. This can happen because RS counters in the same hexant and layer are multiplexed together into the same TD (see section 3.2.4), so if the TD flags fail for some reason, the accidental (non-track) hit in the stopping layer could be assigned to a second, later hit the stopping counter, thereby faking the $\pi \rightarrow \mu$ decay signature. This cut also rejects $K_{\pi 2}$ decays where a photon converts near the charged pion track.
- **TRKTIM:** For hits on the RS track that satisfies the RD_TRK cut requirements, TD time information must be available such that an average track time, t_{RS} , can be found. Otherwise the event is rejected.
- **INTIME:** This cut rejects events which have hits in the RS which occur at track time, but are located outside of the track, and sum to more than 10 MeV. This cut primarily rejects $K_{\pi 2}$ decays which have photon energy in the RS.
- **FITPI:** This is the lowest-level muon/pion particle identification cut in the RS, which requires that a crude $\pi \rightarrow \mu$ double-pulse signature be present in the stopping counter. Loose conditions are imposed on the χ^2 of the double-pulse fit; the muon energy recorded on each end of the stopping counter, $E_{1\mu}$ and $E_{2\mu}$, as well as the geometric mean muon energy, $E_{\mu} = \sqrt{E_{1\mu} \cdot E_{2\mu}}$; the pion decay time; and the muon z relative to the pion z , where z comes from end-to-end timing, i.e., $t_1 - t_2$, where t_1 and t_2 are the times of a pulse recorded on the upstream and downstream ends of a RS counter,

respectively. This cut rejects $K_{\mu 2}$ decays.

- **UTC/RANGE/TARGET:** This track reconstruction cut requires that a track be found in the UTC which links up with the track in the RS. Track reconstruction in the target is also attempted in order to refine the track fit in the UTC, but the specific target track reconstruction requirements of the TARGET cut are disabled at PASS1. The (x, y) projection of tracks in the UTC is reconstructed using the times of anode-wire hits which, for a constant electron drift time in the gas, are fit to circular isochrones (see figure 4.11). The polar angles of tracks in the UTC and the z component of the particles' momenta are found from linear fits to the (r, z) coordinates of induced charge on the helical cathode strips. More information on the UTC track-fitting can be found elsewhere [32].

The UTC track that points to the T · 2 sector of the RS track is found, followed by reconstruction of the track in the target, using extrapolation of this UTC track back into the target. Track hits in the target (“pion fibers”) are found in a 2-cm-wide “swath” centered on the UTC extrapolation, and kaon hits in the target (“kaon fibers”) are found in clusters which touch the swath, based on a likelihood function which uses the fiber energy, time, and distance from the UTC-extrapolated track to assign pion fibers (see figure 4.12). The energy, time, and distance likelihoods are assigned based on an empirical calibration. Photon hits in the target (“gamma fibers”) are defined as hits which are not assigned to the track, but lie within ± 6 ns of the average time of the pion fibers (t_{π}), and are closer to t_{π} than they are to the average time of the kaon fibers (t_K). The kaon decay vertex is defined as the center of the kaon fiber on the swath which is farthest from the target-entry kaon fiber. The (x, y) coordinate of target entry is given by the (x, y) coordinate of the kaon in the B4 hodoscope.

If a track is successfully reconstructed in the target, the UTC fit is re-done using the additional (x, y) coordinates of the target pion fibers. If this fit fails, the original fit (without the pion fibers) is re-done.

Detailed range and energy measurements of the track in the RS are performed. The

Appendix C. Detailed Cut Descriptions

ADC energies of RS track counters are compared to TD pulse heights: if the ADC energy/TD PH ratio is anomalously large, this indicates the presence of an accidental hit in the ADC gate, because maximum pulse height (as opposed to total pulse area) is fairly insensitive to the presence of multiple (low energy) pulses. In this case, for all track counters excluding the stopping counter, the PH energy is used in place of the ADC energy. In the stopping counter, a second pulse from the pion-decay muon is expected, so the ADC energy, minus the muon energy as inferred from the $\pi \rightarrow \mu$ double-pulse fit required by the FITPI cut, is always used. These energies are summed, and corrections are made for energy losses in dead material (RS scintillator wrapping and the RSSC's), as well as saturation of ionizing energy in the plastic scintillator, to get the total energy deposited by the track in the RS. The range of the track in the RS is found by fitting the (x, y) coordinates of the track counters, sector crossings, and RSSC hits, and the stopping-counter energy, to a Monte Carlo track (see figure 4.13). The Monte Carlo track is composed of numerous circular segments, found by propagating the track in steps of 3 MeV energy loss through the RS, for given values of track momentum and the angle in the (x, y) plane between the UTC and RS tracks, at the RS entry point. The RS is treated as a solid block of scintillator, and the momentum and relative angle in (x, y) into the RS are treated as free parameters. The Monte Carlo track which gives the best fit to the RS data for given initial momentum and relative angle in (x, y) is used to get the range of the track in the RS up to the stopping counter. The range in the stopping counter is estimated from the measured energy deposit in this counter.

In the above analysis sequence, if no tracks are reconstructed in the UTC (due to failure in finding an isochrone, or an ambiguity in the z fitting), or no match is found between the UTC and RS tracks, or the range calculation in the RS fails for some reason, then the event is rejected.

- **PDC:** Events where the track momentum measured in the UTC is greater than 280 MeV/ c are rejected. These events can arise from beam pions scattering into the de-

Appendix C. Detailed Cut Descriptions

tor, and are very unlikely to arise from $K^+ \rightarrow \pi^+ \nu \bar{\nu}$ (for which the maximum pion momentum is 227 MeV/c).

- **LAY14:** Tracks which stop in layer 14 and are pointed upstream in the polar angle $120^\circ < \theta < 180^\circ$ ($\cos \theta < -0.5$) are rejected. This is because the support structure for the RS lies in this region and could “hide” track energy. It could also hide accidental activity, which may result in an isolated second pulse in the stopping counter causing a fake $\pi \rightarrow \mu$ decay signature.

At PASS1, the total range, energy, and momentum of a track are also calculated. The range in the target is defined as the distance along the UTC-fitted track, extrapolated from the point of closest approach to the kaon decay vertex, to the edge of the target. Similarly, the range in the IC is defined as the pathlength of the UTC track extrapolation through the IC. The total range is then the RS range (as described above), plus the target and IC ranges, plus the equivalent range in plastic scintillator for the track in the UTC (i.e., conversion of the UTC inner wall, cathode foils, gas volume, and outer wall into an equivalent interaction length of plastic scintillator). The total energy of the track comes from the energy in the RS (as described above), the measured ADC energy in the target, the energy in the IC (as described below), plus a correction for energy loss in the dead material of the UTC (inner wall, foils, gas volume, and outer wall). The ADC and TD energies in the IC come from the IC which lies along the UTC track extrapolation. If a second IC close in azimuth to the UTC-extrapolated track ($-0.4 < \Delta\phi < 0.1$ radians) has a hit with less than 3 MeV ADC energy within ± 3 ns of track time, then the track likely hit two adjacent IC’s and the ADC energy from the second IC is added to the ADC and TD energies of the first IC. Also, if a VC close in azimuth to the UTC-extrapolated track ($|\Delta\phi| < 0.55$ radians) has a hit with less than 2 MeV ADC energy within ± 3 ns of track time, and the kaon stopped deep in the target (at $z > 10$ cm, where the center of the UTC is at $z = 0$ cm) giving rise to a UTC track with polar angle near 90° ($-0.1 < \cos \theta < 0.3$), then the track likely hit a VC and the ADC energy from this VC is added to the ADC and TD energies of the track IC. The resulting, corrected ADC energy for the IC is used unless (1) the expected energy in

the IC, from the UTC-extrapolated range in the IC and empirical tables of pion dE/dx in scintillator, differs from the corrected ADC energy by more than 1 MeV, but differs from the corrected TD energy by less than 1 MeV, or (2) t_{RS} differs from the IC TDC time by more than 5 ns, but differs from the IC TD time by less than 5 ns. In either case the corrected TD energy for the IC is used. The total momentum comes from the momentum measured in the UTC, converted to range in scintillator for a particle of this momentum, using empirical tables of pion or muon range in scintillator as a function of total energy. This range is added to the range in the target, IC, inner UTC wall and half the UTC gas volume as calculated from an extrapolation of the UTC track through these materials. This total range is then converted back to total momentum using the same empirical tables of pion or muon range in scintillator as a function of total energy.

C.2 PASS2

- **PVCUT:** This “photon veto” cut primarily rejects $K_{\pi 2}$ decays. Events are rejected that have more than 2 MeV (visible) in the barrel in a ± 2 ns window, or more than 3.5 MeV in the EC or RS (excluding the track energy) in a ± 1 ns window around track time.
- **TGPVCUT:** This “target photon veto” cut primarily rejects $K_{\pi 2}$ decays. Events are rejected that have more than 5 MeV (total) in target gamma fibers in a ± 1 ns window around track time.
- **TGPVTR:** This cut is a loose version of TGPVCUT for study of beam background pathologies in the target. Events are rejected that fail TGPVCUT only if they (1) satisfy the $\pi^+\nu\bar{\nu}(2)$ trigger, or (2) have $t_{\pi} - t_K < 2$ ns but don’t satisfy the $\pi^+\nu\bar{\nu}(2)$ trigger.
- **TGRECON:** This cut is identical to the PASS1 TARGET cut, and requires that a track be reconstructed in the target. The TGRECON cut rejects events that have no

Appendix C. Detailed Cut Descriptions

kaon cluster in the target due to failure in finding the kaon hits, or have more than 5 kaon-like clusters, or have more than 150 fibers in one kaon cluster, or have no kaon clusters connected to the swath. Events are also rejected that have no pion track along the swath if the kaon cluster is away from the target edge.

- **TGCUT:** This “target” cut rejects events which are poorly reconstructed in the target or IC. Events are rejected that fail any one of the TGRECON, TIMCON, EIC, or TIC cuts (see section C.3.2 for a description of the latter 3 cuts).
- **PSCUT:** This “pion scattering” cut primarily rejects events arising from scattering of beam pions. Events are rejected that fail a loose version of any one of the B4DEDX, B4TRS, or CPITRS cuts (see section C.3.6 for a description of the standard versions of these cuts). That is, events are rejected that have small B4 energy deposition (less than 1.2 MeV, which is indicative of a beam pion), B4 activity at track time (within ± 1.5 ns of $t_{RS} - 0.5$ ns), or \check{C}_π activity at track time (within ± 1.0 ns of t_{RS} , with at least 5 pion tubes firing).
- **RSHEX2:** Events are rejected if the track crosses sectors in the stopping layer, where the sectors are in the same hexant and each counter has a hit with more than 1 MeV ADC energy. Similar to the RSHEX cut (see section C.1), this cut rejects $K_{\mu 2}$ decays which may have a false $\pi \rightarrow \mu$ decay signature, because the track hit in the non-stopping counter gets assigned to a second, later hit in stopping counter, thereby faking the $\pi \rightarrow \mu$ decay signature and simultaneously decreasing the track energy.
- **TDCUT:** This “TD” cut is a loose version of the ELVETO cut (see section C.3.4) and rejects $K_{\mu 2}$ decays that pass the FITPI cut (see section C.1) because an accidental hit provided the second pulse in the stopping counter, thereby faking the $\pi \rightarrow \mu$ decay signature. This accidental may be present as a splash of energy in several neighbouring RS counters, so these events are rejected if there is at least one hit within ± 2.5 ns of muon time, in a RS counter within ± 1 sector of the stopping counter, which has good TD data from each end of the counter.

C.3 PASS3

C.3.1 Kinematic Pathology Cuts

For each kinematic pathology cut, the cut position is set by examining the distribution of the cut variable in a sample of events which passes all other kinematic pathology and function cuts. For kinematic pathology cuts attacking $K_{\pi 2}$ decays, SKIM1 events are used which fail the photon veto function cut, and pass the TD function cut and the beam pathology and function cuts (see subsequent sections for descriptions of these cuts). The EBOX cut on the $K_{\pi 2}$ (low) side is not applied in order to enhance statistics, which implicitly assumes that the limiting $K_{\pi 2}$ background events have a correlated mismeasurement of range and momentum, and an uncorrelated upward fluctuation in energy, placing them in the $PNN(1)$ signal region. For kinematic pathology cuts attacking $K_{\mu 2}$ background, SKIM2 events are used which fail the TD function cut, and pass the PV function cut and the beam pathology and function cuts. The PBOX cut on the $K_{\mu 2}$ (high) side is not applied in order to enhance statistics, which implicitly assumes that the limiting $K_{\mu 2}$ background events have a correlated downshift in range and energy, and an uncorrelated mismeasurement of momentum, placing them in the $\pi^+\nu\bar{\nu}(1)$ signal region. The kinematic pathology cuts are described in more detail below.

- **UTCQUAL:** A UTC track-fitting likelihood is formed from the number of (x, y) coordinates (anode wire hits) and number of UTC layers used in the fit, as well as the number of unused anode wire hits which are within 1.5 cm of the UTC track. For 1995 data the likelihood also includes the number of z coordinates (cathode strip clusters) used in the fit. For 1996-7 data, the UTC z coordinates are not input into the UTCQUAL likelihood; instead, they are used in the PROBZ cut (see below). Events are rejected for which the UTCQUAL likelihood value is $< 10^{-5}$.
- **PROBZ:** Events are rejected which have a χ^2 probability $< 10^{-6}$ for the fit of UTC z hits to a straight track. This cut was designed in the late stages of an earlier 1995

Appendix C. Detailed Cut Descriptions

analysis [47], and subsequent investigation revealed that it may have been tuned on a small number of events, leading to a biased cut position. However, the (normalized) $K_{\mu 2}$ background in the 1/3 1996-7 data sample is found to be larger than that in the 2/3 1995 data by almost a factor of 2, presumably due to the use of narrower TD pulse shapes in 1996-7 for the $\pi \rightarrow \mu$ double-pulse fit in the stopping counter, which increases the probability of a successful double-pulse fit (see section C.3.4). Furthermore, the PROBZ cut's performance was confirmed on the untested 2/3 1996-7 data, so any bias in the cut is likely to be small. Therefore, the cut is applied to 1996-7 data to help reduce $K_{\mu 2}$ background, but to be conservative with respect to potential bias, this cut is not applied to the 1995 data.

- **ZUTOOUT:** Events where the UTC-extrapolated track has $|z| > 25$ cm at the outer radius of the UTC (such that the track exits the side of the UTC) are rejected, because these tracks can lose energy in the dead material of the UTC electronics.
- **LAYV4:** The track must stop in one of RS layers 11 through 18 inclusive. Events with lower stopping layers have a high contamination of $K_{\pi 2}$ decays; events with higher stopping layers have a high contamination of $K_{\mu 2}$ decays.
- **COS3D:** Events where the track is pointed downstream or upstream in the polar angle $0^\circ < \theta < 60^\circ$ or $120^\circ < \theta < 180^\circ$ ($|\cos \theta| < 0.5$) are rejected. This is because tracks at these angles are likely to enter the dead material of the RS support structure and therefore have “hidden” energy. Accidentals can also enter from the support structure and leave an isolated pulse in the exit counter, thereby faking the double-pulse $\pi \rightarrow \mu$ decay signature in the stopping counter. $K_{\mu 2}$ decays which fail the COS3D cut are therefore more likely to be downshifted in range and energy towards the $\pi^+ \nu \bar{\nu}(1)$ signal region, and more likely to pass the TD cuts. That is, $K_{\mu 2}$ decays which fail the COS3D cut can correlate TD and kinematic cuts, so these decays must be removed from a data sample before bifurcating the TD and kinematic cuts to measure the $K_{\mu 2}$ background (see sections 4.2 and 4.4.2).

Appendix C. Detailed Cut Descriptions

- **ZFRF**: Events are rejected at large z in the RS, because the track may have entered the dead material of the RS support structure, which is a potential mechanism for correlation between TD and kinematic cuts in the $K_{\mu 2}$ background estimate (similar to the COS3D cut above). Specifically, if the track in the RS has $|z| > 35$ cm (for stopping layer = 11 or 12), $|z| > 40$ cm (stopping layer = 13), $|z| > 30$ cm (stopping layer = 14), or $|z| > 50$ cm (stopping layer = 15, 16, 17 or 18), where z comes from extrapolation of the UTC track to the stopping layer, then the event is rejected.
- **LAYER14**: Events are rejected which appear to stop in layer 14 of the RS, but also have a hit in the outer RSSC in the stopping sector or one sector clockwise. This cut removes events which potentially lose a large amount of energy in the RSSC (this energy is not included in the track energy). It also removes events which potentially curl around and re-enter layer 14, causing a fake double-pulse $\pi \rightarrow \mu$ decay signature in the stopping counter. These events can correlate TD and kinematic cuts, so they must be removed when making the $K_{\mu 2}$ background estimate (similar to the COS3D cut above).
- **CHIRF**: This cut removes events which have “kinked” RS tracks due to scattering in one or both of the (x, y) and (r, z) planes. The (x, y) part of the cut removes events where the Monte Carlo track fit in the RS (see UTC/RANGE/TARGET in section C.1) gives a χ^2 probability < 0.01 (1995 data) or < 0.05 (1996-7 data). The cut was tightened in 1996-7 due to the increase in $K_{\mu 2}$ background in 1996-7 mentioned in the PROBZ cut description above. The 1995 cut position was found using $K_{\mu 2}$ peak events (see figure 4.1) from SKIM2, but it was later found that muon band events have a worse tail in CHIRF (x, y) probabilities, possibly due to the fact that muon band events need undergo less violent scatters than $K_{\mu 2}$ peak events in order to get into the $\pi^+ \nu \bar{\nu}(1)$ signal region. Therefore, the 1996-7 cut position was found using muon band events, which are statistically enhanced in the SKIM2 data sample by loosening the PV function cut. The (r, z) part of the cut comes from the residuals between the z position of the track calculated from end-to-end timing in each counter

Appendix C. Detailed Cut Descriptions

of the RS (excluding the T counter, stopping counter, and counters in a layer where more than one sector is hit) and the z position as extrapolated from the UTC track. These residuals are divided by the end-to-end timing resolution for each RS counter and summed in order to form a χ^2 quantity. For 1995 data, the end-to-end timing resolution of a RS counter, σ , is parameterized by $\sigma = a + e^{b+cE}$, where a, b, c are constants, and E is the geometric mean TD PH energy of the track in that counter. Events with a χ^2 probability < 0.01 are rejected. For 1996-7 data, σ was found to be more appropriately defined as $\sigma = a + b \cdot e^{cE}$ for the same a, b, c from 1995, which resulted in a re-scaling of probabilities, such that to maintain the same acceptance as the 1995 version, the cut in 1996-7 rejected events with probabilities < 0.0001 . Furthermore, the relationship between the z from the UTC-extrapolated track and the z from RS end-to-end timing was found to be non-linear at large z in 1995, so the residuals in z were based on a polynomial fit. However, further investigation showed that the relationship is actually linear, and that the non-linear behaviour was due to selection of events, based on z and polar angle, in the data sample used to calibrate the z residuals. Because a polynomial fit was used to find the χ^2 for 1995 data, the CHIRF z cut is looser for 1996-7 data than it is for 1995 data.

- **CHIRF_NHZ:** This cut involves calculation of another z -fitting probability, this time from the residuals between the z of the UTC-extrapolated track and the z from the cluster in each of the inner and outer RSSC layers which is closest in (x, y) to the UTC-extrapolated track. These residuals are divided by the z resolution for each RSSC and summed in order to form a χ^2 quantity. The z resolution of a RSSC is an empirical function of RSSC layer and the mean time and time difference of hits on the straws. Events are rejected that have < 5 z clusters from the UTC, *and* have either a RS z -fitting χ^2 probability $< 10^{-3.3}$ (see the CHIRF cut above) or a RSSC z -fitting χ^2 probability $< 10^{-7}$. A version of this cut was originally designed in the late stages of an earlier 1995 analysis [47] and, like the PROBZ cut, was believed to be more biased than later observed. Therefore, similar to the PROBZ cut, this cut is applied to 1996-7

Appendix C. Detailed Cut Descriptions

data to help reduce $K_{\mu 2}$ background, but to be conservative with respect to potential bias, this cut is not applied to the 1995 data.

- **RSDEDX:** The differences between the expected and measured energy deposits in each RS counter, assuming the particle is a pion, are divided by the measured energy resolution in each layer and summed to form a χ^2 quantity. The expected energy in each counter is found starting from the stopping counter and moving backwards, using the energy that the pion has entering the counter, the range in the counter calculated by the Monte Carlo propagation of the fitted track (see UTC/RANGE/TARGET in section C.1), and empirical tables of dE/dx for pions in scintillator. The energy resolution in each RS layer is an empirical function of layer and stopping layer. Events are rejected which have $\chi^2 \geq 5$ from any one counter (called the CHIMAX cut), or a combined χ^2 probability ≤ 0.02 (the CL_RSDEDX cut). The logs of the differences between expected and measured energy are also combined into a likelihood, and events are rejected which have a likelihood value $< 10^{-9}$ (the RSLIKE cut [65]). The CHIMAX cut is effective at removing $K_{\pi 2}$ decays which have photon energy on the track. $K_{\pi 2}$ decays which fail the CHIMAX cut are therefore more likely to be upshifted in energy towards the $\pi^+ \nu \bar{\nu}(1)$ signal region, and more likely to pass the PV cuts. That is, $K_{\pi 2}$ decays which fail the CHIMAX cut can correlate PV and kinematic cuts, so these decays must be removed from a data sample before bifurcating the PV and kinematic cuts to measure the $K_{\pi 2}$ background (see sections 4.2 and 4.4.1). The CL_RSDEDX and RSLIKE cuts are effective at rejecting muon tracks from $K_{\mu 2}$ decays.
- **TGDEDX:** This cut rejects events with dE/dx in the target inconsistent with that of a pion. Events are rejected which have (1) $R_{TG} > 12$ cm, or (2) $E_{TG} > 28$ MeV, or (3) $9.5 \cdot E_{TG} > 28 \cdot R_{TG}$, or (4) $10 \cdot E_{TG} < 21.5 \cdot (R_{TG} - 2)$, where R_{TG} is the UTC-extrapolated range from the kaon decay vertex to the edge of the target, and E_{TG} is the total energy of the pion fibers. This cut is effective at removing events with lepton tracks in the target (e.g., $K_{\mu 2}$ and CEX background).
- **PIGAP:** Events are rejected if the track in the target has a gap between neighbouring

Appendix C. Detailed Cut Descriptions

pion fibers greater than 1.5 cm. This cut removes events which may have abnormally large range because the track particle travels in the air gap between rows of target fibers.

- **TGLIKE:** Events are rejected if the combined likelihood value of all pion fibers in the target, based on fiber time, energy, and distance from the UTC-extrapolated track (see UTC/RANGE/TARGET in section C.1) is $< 10^{-3.2}$. Events are also cut if the combined likelihood value using only the distances from the UTC-extrapolated track is $< 10^{-2.3}$.
- **TGB4:** This cut examines the matching of the (x, y) coordinates of the kaon hit in the B4 hodoscope and the kaon cluster in the target. Events are rejected if (1) the distance between the B4 (x, y) coordinate and the nearest kaon fiber is > 2.0 cm, or (2) the distance between the B4 (x, y) coordinate and the tip of the kaon cluster farthest from the kaon decay vertex is > 2.0 cm, or (3) the distance between the kaon decay vertex and the nearest kaon cluster tip is > 0.7 cm, or (4) the distance from the kaon decay vertex to the closest pion fiber is > 1.5 cm. This last condition removes events with ambiguous, incorrect target entrance and kaon decay fiber assignments, which arise when the B4 hit position is located near the middle of the kaon cluster in the target. Kaon cluster “tips”, where the (x, y) coordinate of the B4 hit is at the tip corresponding to the point of target entry, and the kaon decay vertex is at the other tip, can be seen in figure 4.12.
- **EICKIN:** The expected energy deposit of a pion in the IC is calculated using the energy of the pion (from UTC momentum), range in the IC (from a UTC extrapolation), and empirical tables of dE/dx for pions in scintillator. Events with measured IC energy greater than the expected energy by more than 1.5 MeV are rejected. This cut removes $K_{\pi 2}$ decays with photon activity in the IC, thereby causing a correlated upshift in track energy and momentum towards the $\pi^+\nu\bar{\nu}(1)$ signal region. These quantities are bifurcated and therefore assumed to be uncorrelated in the $K_{\pi 2}$ background estimate (see sections 4.2 and 4.4.1).

- **MASS:** This cut attacks $K_{\mu 2}$ decays which can give rise to GDR background due to inelastic scattering of muons in the RS (see section 4.1.1.1). When analyzing $K^+ \rightarrow \pi^+ \nu \bar{\nu}$ data, the momentum of the muon from $K_{\mu 2}$ decay is reconstructed at 238 MeV/c (instead of the accepted value of 236 MeV/c [16]), because the track is assumed to be that of a pion. That is, the total momentum of a track is found using the UTC-extrapolated range of the track in the target, IC, inner UTC wall and half the UTC gas volume, converted to momentum assuming that the track particle is a pion (see section C.1), so the momentum loss in these materials is overestimated, which, when added to the momentum measured in the UTC, causes the total momentum to be overestimated. The kinetic energy of a $K_{\mu 2}$ muon is 152 MeV, which is downshifted to ≤ 130 MeV if the muon excites the GDR in carbon. Therefore, potential GDR background events are rejected if

$$M = ((P^2 - E^2)/(2E)) > (238^2 - 130^2)/(2 \cdot 130) = 153 \text{ MeV}/c^2$$

i.e., $((P^2 - E^2)/(2E)) > 153 \text{ MeV}/c^2$

The MASS cut is applied as a safety cut only to the 1996-7 data for the reasons outlined in section C.3.4.

C.3.2 Beam Pathology Cuts

- **TGCCDPF:** In the CCD data of any kaon target fiber, if a second pulse is found whose time relative to the first pulse is within ± 5 ns of $t_\pi - t_K$ and whose energy is more than 5 MeV, then reject the event. This cut removes events which may have a significant fraction of the track energy hidden in kaon fibers, because the ADC energy of pion fibers is defined as the track energy in the target.
- **EPITG:** Events which have more than 5 MeV ADC energy in any target pion fiber are rejected. These events likely have $K_{\pi 2}$ photon or accidental energy overlapping the track energy in the target.

Appendix C. Detailed Cut Descriptions

- **EPIMAXK:** The circular UTC track defines an azimuthal angle ω in the (x, y) plane about the center of the UTC track, as shown in figure 4.12 and described in Appendix D. The kaon fiber with the maximum value of ω , ω_K^{max} , is likely to be the kaon decay fiber. This cut requires that pion fibers close to this kaon fiber, specifically, with ω in the range ω_K^{max} to $\omega_K^{max} + 0.06$ radians, each have < 3 MeV energy. Otherwise, it is likely that there is kaon energy overlapping the pion (track) energy, and the event is rejected.
- **PHIVTX:** The value of ω_K^{min} (smallest ω for a kaon fiber) minus ω_π^{min} (smallest ω for a pion fiber, which will be negative for any pion fibers on the non-track side of the kaon decay vertex) must be ≤ 0.0028 . Otherwise the event is rejected. This cut rejects events which have back-to-back tracks in the target (e.g., $K_{\pi 2}$ decays with photon conversion in the target, or $K_L^0 \rightarrow \pi^+ l^- \bar{\nu}_l$ events).
- **PHIVTX2:** The value of ω_K^{decay} (ω of the kaon decay fiber) minus ω_π^{min} must be ≤ 0 . Otherwise the event is rejected. ω_K^{decay} is usually close to 0, so, similar to the PHIVTX cut, this cut rejects events with pion fibers on the non-track side of the kaon decay vertex. This cut was designed only after backgrounds had been measured using both the 1/3 and 2/3 1995 data samples, so it is used in the beam background estimate only for 1996-7 data. It is applied purely as a safety cut for 1995 data.
- **OPSVETO:** Target fibers on the non-track side of the kaon decay fiber, which have hits within ± 4 ns of the target pion time, must have a combined energy $E_{TG}^{op} < 2$ MeV. Otherwise the event is rejected. This cut rejects $K_{\pi 2}$ events, similar to the PHIVTX and PHIVTX2 cuts.
- **OPSVETO_LKB:** Events are rejected if $E_{TG}^{op} > 0.5$ MeV and $lkbeam < 200$ (see the B4EKZ cut below). This cut was designed only after backgrounds had been measured using all of the 1/3 and 2/3 1995 and 1996-7 data samples, and addresses a suspected CEX background event found in the 2/3 1996-7 data which only fails the TGDEDX cut (see sections 4.4.4 and 4.6). This cut is therefore not applied to the 1995 data, and

Appendix C. Detailed Cut Descriptions

is applied as a safety cut to the 1996-7 data. The requirement $lkbeam < 200$ includes most of the beam background, and $E_{TG}^{op} > 0.5$ MeV has as low an energy threshold as possible to generalize the cut.

- **TGEDGE**: Events are rejected which have more than 4 MeV energy in any target edge fiber within ± 5 ns of track time. Due to multiplexing, the edge fibers are not used in the target reconstruction or the track energy calculation, which is valid as long as the edge fiber energy is small.
- **TGQUALT**: This cut is identical to the TGRECON cut (see section C.2).
- **TGER**: Events where the pion has small energy but substantial range in the target, $E_{TG} \leq 1$ MeV when $R_{TG} > 2$ cm, are rejected. These target tracks may be muon tracks, or may have energy hidden in target dead material.
- **TARGF**: Events with more than 0.6 cm between the kaon cluster and nearest pion fiber in the target are rejected, because the pion track may not arise from decay of this kaon.
- **DTGTTP**: This cut requires consistency between two slightly different extrapolations of the UTC track to the target edge.
- **RTDIF**: The path length of the pion in the target is calculated twice, using a UTC extrapolation from the two tips of the kaon cluster to the target edge. Half the difference in these two path lengths represents the maximum error in target range due to kaon decay vertex assignment. If this error is ≥ 1.5 cm, the event is rejected.
- **DRP**: The maximum distance spanned by the pion fibers perpendicular to the tangent to the UTC track at $\omega = 0$ can be no more than 30% of the total UTC-extrapolated range in the target. Otherwise the event is rejected. This cut rejects events with kinked tracks in the target due to pion scattering, which can lead to correlated effects in track range, energy and momentum.

Appendix C. Detailed Cut Descriptions

- **TIMCON:** This cut requires consistency between the time of the kaon as detected by the target, t_K , and the time of the kaon as detected by the B4 hodoscope, $t_{B4strobe}$ (must be within ± 4 ns of each other). This cut also requires consistency between the time of the pion as detected by the target, t_π , and the time of the pion as detected by the RS, t_{RS} (must be within ± 5 ns of each other).
- **TIC:** The IC TDC time or the IC TD time must be within ± 5 ns of t_{RS} . Otherwise the event is rejected, because the IC energy may not be due to the track, leading to correlated mismeasurements of track energy and momentum.
- **TGCCD:** This cut rejects events with misassigned kaon fibers, by comparing CCD times of the kaon fibers, t_{KCCD} , to the RS track time and the B4 strobe time. Specifically, for each kaon fiber, $2 \cdot t_{KCCD} - t_{RS} - t_{B4strobe} \leq 0$ ns is required, and t_{KCCD} must be within ± 3.5 ns of $t_{B4strobe}$. Otherwise the event is rejected.
- **EIC:** Similar to the EICKIN cut in section C.3.1, the measured ADC energy in the track IC must be within ± 5 MeV of the expected IC energy, or the measured TD energy must be within ± 4 MeV of the expected energy. Otherwise the event is rejected, because the IC energy may not be due to the track, leading to correlated mismeasurements of track energy and momentum.
- **KIC:** This cut addresses events where the kaon cluster is near an IC, and this IC has a TDC hit at kaon time. These events can arise from a combination of 2 beam particles, where the first particle enters the target and stops in an IC, with no decay products detected, and the second particle enters the target from this same IC and decays in flight or exits the target through a different IC. Because the first particle stops in the IC, it leaves a large energy pulse in the IC which, after discrimination, can be up to 80 ns wide. The IC hit from the second beam particle is therefore “masked out” for up to 80 ns after the IC hit from the first beam particle. These types of events tend to correlate target and B4 cuts, because the second beam particle enters the target through a dead IC, such that it doesn’t go through the B4 hodoscope, and

Appendix C. Detailed Cut Descriptions

is reconstructed as the decay product of the first beam particle in the target. Target and B4 cuts are bifurcated and therefore assumed to be uncorrelated in the double-beam background estimate (see sections 4.2 and 4.4.3), so these events are found and removed if there are IC TDC hits within ± 3 ns of t_K when the kaon fibers are within 3.7 cm of the IC and are located at the edge of the target (at radii > 5.2 cm). If the IC is on the track, then the event is removed only if the IC hit is closer to kaon time than track time, i.e., $t_{IC} \leq (t_K + t_{RS})/2$ ns.

- **TGGEO:** Double-beam background events are rejected which have the following signature: (1) both particles enter the target near the target edge or from an IC, and (2) the first particle or its decay product leaves a large energy pulse in the IC, such that the IC TDC hit of the second target-entering particle is “masked out”. This cut removes events which can correlate target and B4 cuts, similar to the KIC cut above. The events addressed specifically by TGGEO were recognized after background measurements had already been made on both the 1/3 and 2/3 1995 data samples, so this cut is used in the beam background estimate only for 1996-7 data. It is applied purely as a safety cut for 1995 data. Events are rejected if pion fibers which lie within 1.0 cm of the minimum- ω pion fiber are located at the target edge (at radii ≥ 4.5 cm), and the nearest IC to these pion fibers is not related to the RS track and has a hit with $E > 3$ MeV energy at time $t_{IC} < t_{RS} + 5$ ns. The IC condition is also applied to the next-nearest IC if it is within 1.5 cm of the pion fibers (i.e., the pion fibers are near an IC sector boundary). Events are also rejected if kaon fibers which lie within 1.0 cm of the kaon decay fiber are located at the target edge (at radii ≥ 4.5 cm), and the nearest IC to these kaon fibers is (1) not related to the RS track and has a hit with either (a) t_{IC} within ± 3 ns of t_K , or (b) $E > 3$ MeV at $t_{IC} < t_{RS} + 5$ ns; or (2) related to the RS track and has a hit within ± 3 ns of t_K , and is closer to kaon time than track time, i.e., $t_{IC} < (t_K + t_{RS})/2$ ns (this is the same condition as the KIC cut). Conditions (1) and (2) are also applied to the next-nearest IC if it is within 1.5 cm of the kaon fibers (i.e., the kaon fibers are near an IC sector boundary).

- **B4EKZ**: A kaon likelihood is formed from the energy deposited in the B4 hodoscope, the UTC-extrapolated kaon stopping z in the target, and the kaon energy in the target. The likelihood measure $lkbeam$ is calculated using empirical tables of the correlation between these 3 quantities for kaons. Events are rejected if $lkbeam \leq 2$.
- **B4EKZ_IC**: If there are no pion fibers in the target, then the event is rejected if $lkbeam \leq 15$. These events may have kaon energy in the IC, leading to correlated mismeasurements of track energy and momentum.
- **TGZFOOL**: This cut ensures that the kaon enters the target. Events are rejected if the kaon z stopping position (from a UTC extrapolation) is farther upstream than -15 cm. These events can have poor B4 and target information, and therefore potentially correlate B4 and target cuts which are bifurcated and therefore assumed to be uncorrelated in the double beam background estimate (see sections 4.2 and 4.4.3).
- **BHTRS**: Events are rejected which have activity at the beam hole counter within ± 5 ns of track time. This cut rejects double-beam background, where the track-time beam particle may be located in the beam halo, missing the wire chambers, B4 hodoscope, and target.

C.3.3 Photon Veto Function

The PV function cut is optimized for rejection at different values of acceptance using, as far as possible, “pure” data samples of $K_{\pi 2}$ and $K_{\mu 2}$ decays. The $K_{\pi 2}$ data sample is the 1/3 1995 SKIM1 data, with beam and kinematic cuts applied to isolate events in the $K_{\pi 2}$ kinematic peak. The $K_{\mu 2}$ data sample is the 1995 $K_{\mu 2}(1)$ monitor data (see section 3.3), with beam and kinematic cuts applied to isolate the $K_{\mu 2}$ kinematic peak, and a layer 21 veto to remove $K_{\mu 2}$ events which exit the RS and leave energy in the barrel. Because the SKIM1 data already has online, PASS1, and PASS2 PV cuts applied (online $\overline{BV+EC}$, HEX; PASS1 INTIME; and PASS2 RSHEX2, TGPVCUT), these same cuts are also applied to the $K_{\mu 2}(1)$ monitor data.

The optimization consists of an automated search of the parameter space of time windows (around track time) and energy thresholds (minimum energy) for detection of hits, which are grouped into the 17 categories listed in table C.1. Values of rejection for $K_{\pi 2}$ decays are found simultaneously with values of acceptance for $K_{\mu 2}$ decays using the data samples described above, and the time windows and energy thresholds are varied according to an optimization algorithm [58] which selects those that give the maximum rejection at a specified value of acceptance. Figure 4.14 shows the PV background level, N_{PV} , as a function of the acceptance, A_{PV} . Events with $N_{PV} \leq 1.0$, $A_{PV} \leq 1.0$ are defined to pass the PV function cut. This point was chosen to give a total photon veto acceptance of 0.80, including losses from all levels of PV. Measurements using $K_{\mu 2}(1)$ monitor data give a total acceptance of 0.90 from $\overline{BV+EC}$, HEX, INTIME, PVCUT and TGPVCUT (see table 5.2). The $A_{PV} \leq 1.0$ position therefore corresponds to a PV function cut acceptance of 0.89. The 1995 parameters for this cut point are shown in table C.2, which give a PV function cut rejection and acceptance of 50.1 ± 1.1 and 0.893 ± 0.005 , respectively. The PV function is therefore defined for the range $N_{PV} = [0, 50]$ and is tabulated in table C.3. The PV rejection was confirmed with the 2/3 1995 SKIM1 data, and the function was re-optimized for application to 1996-7 data using the 1/3 1996-7 data set, giving slightly more rejection than 1995 at the same acceptance loss point.

C.3.4 TD Function Cuts

The TD background (described in table 4.1) increased significantly in 1996-7 relative to 1995, mainly due to a z -dependent correction to the calibrated TD pulse shapes which are used for $\pi \rightarrow \mu$ double-pulse fitting to TD data. The correction narrowed the shapes, and therefore increased the probability of a successful double-pulse fit at small pion decay times, t_{μ} . The acceptance of the FITPI cut increased by about 6%, but the amount of tail-fluctuation background (resulting from double-pulse fits to a single large or abnormally-shaped pulse) also increased significantly. The narrower shapes may additionally be responsible for the suspected increase in GDR background seen in 1996-7, because the GDR

Appendix C. Detailed Cut Descriptions

detector	cat.	time and energy information
barrel	BV	double-ended TDC, double-ended ADC
	BV1	double-ended TDC, single-ended ADC
	BV2	double-ended TDC, no ADC
	BV3	single-ended TDC, double-ended ADC
	BVS	single-ended TDC, single-ended ADC
endcaps	EC	CCD, excluding upstream inner ring
	EC1	CCD, inner ring of upstream EC only
range stack	RD	double-ended TD
	RD1	double-ended TD time, single-ended energy, not in track hexant
	RD2	double-ended TD time, no ADC energy
	RD3	single-ended TD time, double-ended energy, not in track hexant
	RDS	single-ended TD time, single-ended energy, not in track hexant
target	TG	CCD
I-counters	IC	TDC and ADC
V-counters	VC	TDC and ADC
collars	CO	TDC and ADC
microcollar	CM	TDC and ADC

Table C.1: Definitions of the categories of hits whose time windows and energy thresholds are optimized to get the best PV function cut rejection for a given value of acceptance. A “double-ended” quantity means that the quantity is recorded at both the upstream and downstream ends of a RS or barrel counter. In the RS and barrel, the upstream and downstream times of a pulse must not differ by more than 14 ns in order for the pulse to be defined as having double-ended time information. In the RS, energy comes from the geometric mean of the upstream and downstream TD PH’s. If one end has TD PH = 0 (the TD time on that end can still be valid), then the energy comes from the TD PH on the other end. If both ends have TD PH = 0, then the ADC energy on each end is used. Therefore, single-ended RS energy is defined as single-ended ADC energy, and double-ended RS energy is defined as double-ended TD PH energy, single-ended TD PH energy, or double-ended ADC energy. “No ADC energy” means that there may have been single- or double-ended TD PH energy, but there was no ADC energy.

Appendix C. Detailed Cut Descriptions

cat.	time window (ns)	E_{min} (MeV)	$(M_\pi)_s$	$(M_\pi)_f$	Rej.	$(M_\mu)_s$	$(M_\mu)_f$	Acc.
BV	2.25 ± 5.25	0.20	10977	1914	5.7	35334	34420	0.974
BV1	8.00 ± 8.00	4.00	1923	1914	1.0	34433	34420	1.000
BV2	3.50 ± 0.50	—	1918	1914	1.0	34428	34420	1.000
BV3	-3.50 ± 1.00	5.20	1919	1914	1.0	34426	34420	1.000
BVS	-6.50 ± 2.50	3.60	1914	1914	1.0	34420	34420	1.000
EC	0.25 ± 2.50	2.40	8615	1914	4.5	35089	34420	0.981
EC1	0.25 ± 2.25	1.60	2545	1914	1.3	34756	34420	0.990
RD	1.25 ± 3.25	0.80	4403	1914	2.3	35666	34420	0.965
RD1	-1.50 ± 0.50	4.40	1920	1914	1.0	34436	34420	1.000
RD2	-2.00 ± 0.00	8.20	1914	1914	1.0	34420	34420	1.000
RD3	-3.00 ± 0.50	6.80	1918	1914	1.0	34427	34420	1.000
RDS	-2.00 ± 0.50	4.40	1914	1914	1.0	34421	34420	1.000
TG	-0.75 ± 2.75	3.40	2077	1914	1.1	34605	34420	0.995
IC	-1.00 ± 2.50	1.20	2563	1914	1.3	34577	34420	0.995
VC	-2.50 ± 3.50	1.20	2065	1914	1.1	34511	34420	0.997
CO	1.00 ± 2.00	1.00	2121	1914	1.1	34515	34420	0.997
CM	1.00 ± 2.00	1.00	1925	1914	1.0	34422	34420	1.000

Table C.2: PV function cut parameters and performance at the $N_{PV} \leq 1.0$ cut position. Each cut category is defined in table C.1. Time windows (around track time) and energy thresholds (minimum energy) for detection of hits in each category are listed, along with the rejection and acceptance of each cut category for the time and energy parameters listed. Rejections are given by $(M_\pi)_s/(M_\pi)_f$, where $(M_\pi)_f$ is the “final” number of $K_{\pi 2}$ decays which remain after application of the cut category to a “starting” number of $K_{\pi 2}$ decays, $(M_\pi)_s$. Acceptances are given by $(M_\mu)_s/(M_\mu)_f$, where $(M_\mu)_f$ is the “final” number of $K_{\mu 2}$ decays which remain after application of the cut category to a “starting” number of $K_{\mu 2}$ decays, $(M_\mu)_s$. The listed time windows and energy thresholds result in a total PV function cut rejection and acceptance of 50.1 ± 1.1 and 0.893 ± 0.005 , respectively.

Appendix C. Detailed Cut Descriptions

N_{PV}	A_{PV}	N_{PV}	A_{PV}	N_{PV}	A_{PV}	N_{PV}	A_{PV}
49.8924	1.1195	3.7910	1.0949	1.1134	1.0137	0.5627	0.8568
47.6327	1.1195	3.7764	1.0947	1.1071	1.0130	0.5622	0.8565
45.9331	1.1195	3.7085	1.0941	1.0825	1.0103	0.5502	0.8482
41.6040	1.1193	3.6970	1.0940	1.0810	1.0101	0.5465	0.8456
41.6029	1.1193	3.6829	1.0938	1.0789	1.0099	0.5460	0.8452
33.3129	1.1188	3.6693	1.0937	1.0549	1.0072	0.4645	0.7725
28.5245	1.1184	3.6646	1.0936	1.0475	1.0064	0.4629	0.7713
28.2732	1.1184	3.6635	1.0935	1.0287	1.0040	0.4624	0.7711
27.9650	1.1184	3.6609	1.0935	1.0246	1.0035	0.4608	0.7702
20.9634	1.1176	3.6327	1.0931	1.0047	1.0007	0.4598	0.7694
17.0449	1.1169	3.1938	1.0881	1.0031	1.0005	0.4347	0.7472
16.2894	1.1167	3.1353	1.0874	1.0000	1.0000	0.4326	0.7453
14.7858	1.1162	3.1296	1.0873	0.9744	0.9960	0.4284	0.7417
14.4222	1.1161	3.1233	1.0872	0.9504	0.9922	0.4269	0.7403
14.0993	1.1160	2.9159	1.0841	0.9404	0.9905	0.4154	0.7290
13.8652	1.1158	2.8929	1.0838	0.9242	0.9877	0.4148	0.7285
13.6928	1.1157	2.7764	1.0817	0.8861	0.9800	0.4117	0.7253
12.2868	1.1149	2.7581	1.0813	0.8720	0.9773	0.4002	0.7126
11.8412	1.1146	2.7524	1.0812	0.8710	0.9770	0.3966	0.7089
11.6369	1.1145	2.7487	1.0811	0.8662	0.9760	0.3950	0.7071
10.9676	1.1140	2.7194	1.0804	0.8642	0.9756	0.3595	0.6621
10.9305	1.1140	2.6902	1.0798	0.8417	0.9699	0.3589	0.6614
10.5982	1.1137	2.6160	1.0783	0.8406	0.9696	0.3548	0.6556
10.5178	1.1136	2.5219	1.0763	0.8250	0.9656	0.3516	0.6535
10.2806	1.1134	2.5167	1.0762	0.8224	0.9649	0.3459	0.6471
9.6594	1.1127	2.3798	1.0733	0.8192	0.9641	0.3454	0.6464
9.4979	1.1125	2.3595	1.0728	0.8177	0.9636	0.3443	0.6449
9.2806	1.1123	2.3553	1.0727	0.8135	0.9624	0.3438	0.6441
9.1641	1.1121	2.2738	1.0705	0.7983	0.9579	0.3302	0.6227
9.0120	1.1119	2.0799	1.0640	0.7941	0.9566	0.3281	0.6196
8.3109	1.1110	1.9117	1.0589	0.7884	0.9547	0.3218	0.6108
7.2341	1.1094	1.9049	1.0587	0.7827	0.9529	0.3197	0.6089
7.1834	1.1093	1.8245	1.0558	0.7806	0.9522	0.3177	0.6065
7.1682	1.1093	1.8083	1.0551	0.7680	0.9479	0.3093	0.5925
7.1134	1.1092	1.7900	1.0544	0.7633	0.9464	0.2968	0.5749
6.9817	1.1089	1.5878	1.0462	0.7602	0.9453	0.2821	0.5580
6.9310	1.1087	1.5439	1.0440	0.7372	0.9365	0.2806	0.5555
6.7759	1.1083	1.5204	1.0427	0.7147	0.9285	0.2790	0.5529
6.5475	1.1078	1.5042	1.0419	0.6970	0.9214	0.2727	0.5416
6.4822	1.1076	1.5026	1.0418	0.6959	0.9210	0.2623	0.5261
6.2842	1.1070	1.4838	1.0407	0.6954	0.9208	0.2607	0.5236
5.6149	1.1050	1.4222	1.0373	0.6897	0.9183	0.2602	0.5227
5.4091	1.1043	1.3976	1.0358	0.6604	0.9050	0.2581	0.5189
5.3652	1.1041	1.3772	1.0345	0.6599	0.9048	0.1944	0.3939
4.8015	1.1019	1.3391	1.0321	0.6531	0.9018	0.1823	0.3714
4.7863	1.1017	1.3119	1.0304	0.6202	0.8868	0.1797	0.3671
4.7685	1.1017	1.2931	1.0291	0.6196	0.8865	0.1714	0.3515
4.7508	1.1016	1.2827	1.0282	0.6186	0.8861	0.1390	0.2858
4.7335	1.1015	1.2649	1.0269	0.6176	0.8861	0.1379	0.2852
4.6980	1.1013	1.2382	1.0248	0.6118	0.8836	0.1353	0.2831
4.5617	1.1006	1.2268	1.0239	0.5873	0.8713	0.1338	0.2816
4.5559	1.1006	1.2158	1.0229	0.5841	0.8697	0.1322	0.2791
4.4885	1.1002	1.2064	1.0221	0.5815	0.8683	0.1259	0.2662
4.4284	1.0999	1.1505	1.0173	0.5810	0.8680	0.1243	0.2647
4.2456	1.0987	1.1358	1.0160	0.5763	0.8653	0.1212	0.2591
4.2429	1.0987	1.1338	1.0158	0.5737	0.8638	0.1176	0.2512
4.1630	1.0981	1.1296	1.0153	0.5684	0.8605	0.1160	0.2491
4.0084	1.0968	1.1285	1.0152	0.5643	0.8578		

Table C.3: PV function. N_{PV} is a measure of $K_{\pi 2}$ background level, and A_{PV} is a measure of acceptance, for different time windows (around track time) and energy thresholds (minimum energy) for detection of hits in each category listed in table C.1. Events with $N_{PV} \leq 1.0$ pass the PV function cut. This function is drawn in figure 4.14.

Appendix C. Detailed Cut Descriptions

background, similar to tail-fluctuation background, is concentrated at small t_μ . The GDR background was “discovered” only after backgrounds had been measured using all of the 1/3 and 2/3 1995 and 1996-7 data sets, and the TDECON, TDVEL and MASS cuts were designed to reduce it to a negligible level. Because the GDR background was found after the background measurements on the 2/3 1996-7 data sample had been performed, the MASS cut is applied only as a safety cut to the 1996-7 data. However, to get a potentially more accurate measurement of the TD rejection, the TDECON cut is applied as a pathology cut, and the rejection of the TDVEL cut is used in the calculation of total TD rejection for 1996-7 data. These cuts were designed with large statistics using the 1/3 1996-7 data sample and were found to work as expected when applied to the 2/3 1996-7 data, so any bias in these cuts should be minimal. The PASS3 TD cuts are described in more detail below.

- **TDTCON:** If an accidental hit is present in the stopping counter prior to track time, it’s possible for this accidental to be assigned to pion time, and the track hit to be assigned to muon time, such that the $\pi \rightarrow \mu$ double-pulse decay signature is satisfied. This cut attacks pion-time accidental background by comparing the stopping-counter pion time to t_{RS} . If the stopping-counter pion time is earlier (or later) than t_{RS} by more than 1.5 ns, the event is rejected. Events with pulse misassignment in the stopping counter can correlate TD and kinematic cuts, because these events can have both mismeasured track energy, and a fake $\pi \rightarrow \mu$ decay signature. TD and kinematic cuts are bifurcated and therefore assumed to be uncorrelated in the $K_{\mu 2}$ background estimate (see sections 4.2 and 4.4.2), so the TDTCON cut is applied as a pathology cut when measuring the TD rejection (see figure 4.21).
- **TDDEFA1:** This cut is applied only to the 1996-7 data, in order to remove the extra tail-fluctuation background introduced by the use of narrower pulse shapes for double-pulse fitting to TD data. It is comprised of the weighted sum of three stopping-counter variables: (1) the log of: the product of single-pulse fit χ^2 ’s from the upstream and downstream TD data, divided by that from double-pulse fits; (2) the log of the product of single-pulse fit χ^2 ’s from the upstream and downstream TD data; and (3) second-

Appendix C. Detailed Cut Descriptions

pulse time relative to first-pulse time, t_μ . The weights (0.37522, 0.092414, and 0.07189, respectively) are found from a discriminant function analysis [66] of 1636 pion tracks and 1636 muon tracks in the RS. The pion events are taken from the π_{scat} monitor data (see section 3.3), and the muon events are those that remain in the 1/3 1996-7 SKIM2 data after application of all beam and $K_{\pi 2}$ kinematic cuts, the COS3D, ZFRF, and LAYER14 cuts (see section C.3.1), the EV5, ELVETO, TDFOOL, TDLIK2, and TDLIK3 cuts (see below), and the requirement $t_\mu < 10$ ns. Events are rejected which have TDDFA1 values < 4.2 .

- **EV5:** This cut attacks early muon decay background by looking for accidental activity in the RS at electron time. Electron hits are found within ± 1 sector and ± 2 layers of the stopping counter, and valid electrons must: (1) have a hit in the stopping sector within ± 1 layers of the stopping layer; (2) have at least one hit with at least 1 MeV recorded on both of the upstream and downstream ends; (3) occur at least 20 ns after muon time; and (4) have z within ± 2.7 ns of the pion, where z comes from the end-to-end time difference of the electron hit in the counter closest to the stopping counter. Furthermore, the electron can have no more than 56 MeV summed over all hits in the RS at electron time. Otherwise the event is rejected.
- **ELVETO:** This cut attacks muon-time accidental background by looking for accidental activity in the RS and barrel at muon time. The time windows, energy thresholds, and search region are optimized for rejection and acceptance, similar to the PV optimization described in section C.3.3.
- **TDFOOL:** This cut attacks muon-time accidental background by looking for accidental activity along the track at muon time. A double-pulse fit to the TD data is attempted in the two counters previous to the stopping counter, and if either counter returns a single-pulse fit χ^2 divided by that from a double-pulse fit > 4 on each of the upstream and downstream ends, with the second pulse occurring within ± 5 ns of muon time in the stopping counter and having at least 2.2 MeV energy, then the event is rejected.

Appendix C. Detailed Cut Descriptions

- **TDECON:** This cut requires consistency between TD and ADC pion energies in the stopping counter. The ADC energy is the total gated energy in the stopping counter, minus the fraction of muon energy (found in the TD) lying within the ADC gate (which is about 80 ns wide, starting just before pion time). Kinematic cuts typically use the ADC pion energy in the stopping counter, whereas TD cuts use the TD pion energy. Therefore, events failing TDECON can correlate TD and kinematic cuts if, for example, the calculated fraction of muon energy inside the ADC gate is a function of muon energy. $K_{\mu 2}$ decays with a muon-like accidental pulse in the stopping counter will pass the TD cuts, and may also preferentially pass the kinematic cuts because the calculated fraction of “muon” energy inside the ADC gate, for this muon energy, moves the $K_{\mu 2}$ track energy towards the $\pi^+\nu\bar{\nu}(1)$ signal region. TD and kinematic cuts are bifurcated and therefore assumed to be uncorrelated in the $K_{\mu 2}$ background estimate (see sections 4.2 and 4.4.2), so the TDECON cut is applied as a pathology cut when measuring the TD rejection (see figure 4.21). This cut was designed based on evidence of large TD-kinematic correlations in the 1996-7 data (e.g., arising from GDR background – see section 4.6), so this cut is only applied to the 1996-7 data. Specifically, events are rejected which have $epitc > (37.5 \cdot elast_cor/40. - 0.5)$, where $epitc$ and $elast_cor$ are the geometric means of the TD and ADC pion energies, respectively, from the upstream and downstream ends of the stopping counter. This cut was designed using the 1/3 1996-7 data, and found not to be particularly effective when applied to the 2/3 1996-7 data, so TD-ADC pion energy inconsistency in the stopping counter is unlikely to be a major source of TD-kinematic correlation.
- **TDVEL:** This cut is designed to attack GDR background via the time-energy relation (“velocity”) of emitted neutrons, shown figure 4.5. Specifically, events are rejected which have $t_\mu < (-2.5 \cdot E_\mu + 17.5)$. This cut was designed based on evidence of GDR background in the 1996-7 data, so this cut is only applied to the 1996-7 data.
- **TDLIK2:** This cut attacks muon-time accidental background (as well as tail-fluctuation background) by forming a likelihood out of quantities specific to the muon from $\pi \rightarrow \mu$

Appendix C. Detailed Cut Descriptions

decay. This likelihood is constructed from a sum of the logs of probabilities that the muon has given values of energy, z relative to the pion (where z comes from the end-to-end time difference and from the ratio of energies on each end), and time relative to the pion. The probabilities are taken from signal/background distributions, where the background distributions are measured using the 1368 events in the 1/3 1995 SKIM2 data which remain after application of all beam cuts, except the CKTRS and CKTAIL cuts, cuts specific to 1996-7, and using a loose version of the DELC cut; $t_\pi - t_K \geq 1$ ns; the $K_{\pi 2}$ (low) side of the RBOX and EBOX cuts; the COS3D, ZFRF, and LAYER14 cuts (see section C.3.1); and a subset of the fixed TD cuts (EV5, ELVETO, and TDFOOL, described above). The CKTRS and CKTAIL cuts are turned off, and the DELC cut is loosened, in order to enhance statistics. Meaningful values of this likelihood range from -70 (background-like) to 0 (signal-like). The TD function cut pass condition, $N_{TD} \leq 1.003$, corresponds to events with TDLIK2 likelihood values > -2.128 .

- **TDLIK3:** This cut attacks early muon decay background by forming a likelihood out of quantities specific to the electron from $\pi \rightarrow \mu \rightarrow e$ decay. This likelihood is constructed from a sum of the logs of probabilities that the electron has given values of energy, z relative to the pion (where z comes from the end-to-end time difference in the electron counter closest to the stopping counter), and time relative to the muon. The muon energy and muon time relative to the pion are also part of this likelihood. The probabilities are taken from signal/background distributions, which are measured in the same way as the TDLIK2 distributions. Meaningful values of this likelihood range from -40 (background-like) to 0 (signal-like). The TD function cut pass condition, $N_{TD} \leq 1.003$, corresponds to events with TDLIK3 likelihood values > -2.440 .
- **TD DFA2:** This cut attacks tail-fluctuation background which remains after application of all previous TD cuts. It is comprised of the weighted sum of five stopping-counter variables: (1) the log of: the product of single-pulse fit χ^2 's from the upstream and downstream TD data, divided by that from double-pulse fits; (2) muon energy;

Appendix C. Detailed Cut Descriptions

(3) muon z relative to pion z from end-to-end time differences; (4) the log of the product of single-pulse fit χ^2 's from the upstream and downstream TD data; and (5) the minimum of the muon energy from the upstream and downstream ends. The weights (0.53288, -0.57242 , -0.17664 , 0.42072 , and 0.42446 , respectively) are found from a discriminant function analysis [66] of 52 pion tracks and 52 muon tracks in the RS. The pion events are taken from the π_{scat} monitor data (see section 3.3), and the muon events are those that remain in the 1/3 1995 SKIM2 data with $t_\mu < 10$ ns which remain after application of loose TDLIK2 and TDLIK3 cuts (TDLIK2 > -4 , TDLIK3 > -4) to the TDLIK2 background sample mentioned above. Meaningful values of TDDFA2 range from -1 (background-like) to 4 (signal-like). The TD function cut pass condition, $N_{TD} \leq 1.003$, corresponds to events with TDDFA2 values > 2.605 .

TD background in the $\pi^+\nu\bar{\nu}(1)$ signal region likely comes from some combination of $K_{\mu 2}$ range-tail and muon-band events, because range-tail events already have R and E in the box, and muon-band events can have R , E , and P all in the box (see figure 4.1). Conversely, $K_{\mu 2}$ peak events have R , E , and P well away from the box. Therefore, only $K_{\mu 2}$ range-tail and muon-band events are used to define the TD function. Starting with 381 range-tail and 489 band events from the 1/3 1995 SKIM2 data which pass the EV5, ELVETO, and TDFOOL cuts (i.e., from the TDLIK2 background sample mentioned above), and a larger sample of π_{scat} events from SKIM3 data, the parameter space of possible values of TDLIK2, TDLIK3, and TDDFA2 is scanned to find the optimal value of acceptance for the SKIM3 π_{scat} events, for different values of rejection of the SKIM2 muon events [41]. The TD rejection is required to be the same in the range tail and band at each point on the function, so that TD rejection is uncorrelated (to some degree) with muon track kinematics. Figure 4.15 shows the TD background level, N_{TD} , as a function of the acceptance, A_{TD} , for these events. Events with $N_{TD} \leq 1.003$ are defined to pass the TD function cut. This point was chosen to give a total TD function cut rejection for SKIM2 $K_{\mu 2}$ range-tail and muon-band events of 1000 (using all of the “fixed” and “variable” TD cuts as defined in table 4.9). The TD function is therefore defined for the range $N_{TD} = [0, 1000]$. Events which fail the fixed TD cuts have this maximal TD function value; events which pass the fixed TD function cuts have the smaller N_{TD} values

tabulated in table C.4, depending on their values of TDLIK2, TDLIK3, and TDDFA2. After confirming the TD rejection with the 2/3 1995 SKIM2 data, the function was re-optimized for application to 1995-7 data using the statistics of the full 1995 SKIM2 data sample.

C.3.5 $K_{\pi 2}$ and $K_{\mu 2}$ Kinematic Function Cuts

The $K_{\pi 2}$ and $K_{\mu 2}$ kinematic functions involve loosening/tightening the following cuts.

- **RNGMOM**: The expected RS range, R_{RS}^{exp} , and its resolution, $\sigma(R_{RS})$, are calibrated as a function of momentum in the UTC for muons in the muon band. A χ -like quantity is formed using the measured RS range, and events are rejected that have $\chi(RP) = (R_{RS} - R_{RS}^{exp})/\sigma(R_{RS}) > 2.0$.
- **BOX**: This is a cut on the 3 major kinematic variables of a track (R, E, P), which selects the $\pi^+\nu\bar{\nu}(1)$ kinematic region between the $K_{\pi 2}$ and $K_{\mu 2}$ peaks. Events pass which satisfy the following 3 conditions:
 1. **RBOX**: $33 \leq R \leq 40$ cm.
 2. **EBOX**: $115 \leq E \leq 135$ MeV.
 3. **PBOX**: $211 \leq P \leq 229$ MeV/ c .

The RBOX, EBOX, and PBOX cuts are direct cuts on total range, energy and momentum of a track. Additional cuts on the variables $(X - X_{peak})/\sigma_X$, where X is R, E , or P , and where the $K_{\pi 2}$ peak positions X_{peak} and resolutions σ_X are calibrated as a function of polar angle [41], are imposed on the $K_{\pi 2}$ (low) side of the box:

- **BOX'**: Events pass which satisfy the following 3 conditions:
 1. **RBOX'**: $rdev > 2.80$, where $rdev = (R - R_{peak})/\sigma_R$
 2. **EBOX'**: $edev > 2.453$, where $edev = (E - E_{peak})/\sigma_E$
 3. **PBOX'**: $pdev > 2.625$, where $pdev = (P - P_{peak})/\sigma_P$

Appendix C. Detailed Cut Descriptions

N_{TD}	A_{TD}	TDLIK2	TDLIK3	TDDFA2	N_{TD}	A_{TD}	TDLIK2	TDLIK3	TDDFA2
9.796	1.29630	-59.150	-35.848	-1.726	1.191	1.21127	-2.128	-2.624	2.235
9.242	1.29599	-37.758	-35.848	-1.726	1.139	1.20094	-2.128	-2.440	2.235
8.772	1.29562	-37.758	-17.312	-1.726	1.034	1.17840	-2.128	-2.440	2.550
8.333	1.29524	-36.414	-17.312	-1.726	1.003	1.17126	-2.128	-2.440	2.605
8.265	1.29518	-36.414	-16.040	-1.726	0.987	1.16756	-2.086	-2.440	2.605
8.135	1.29505	-35.868	-16.040	-1.726	0.899	1.14728	-1.918	-2.440	2.605
8.009	1.29493	-35.868	-13.992	-1.726	0.883	1.14665	-1.918	-2.432	2.605
7.048	1.29399	-15.624	-13.992	0.827	0.852	1.14039	-1.876	-2.432	2.605
6.897	1.29392	-15.624	-13.992	1.051	0.836	1.13632	-1.876	-2.352	2.605
6.818	1.29386	-15.624	-13.992	1.171	0.820	1.13218	-1.848	-2.352	2.605
6.771	1.29380	-15.246	-13.992	1.171	0.799	1.12636	-1.820	-2.352	2.605
6.097	1.29280	-11.844	-11.688	1.171	0.773	1.11847	-1.820	-2.352	2.662
6.008	1.29274	-11.844	-9.544	1.171	0.731	1.10213	-1.736	-2.352	2.662
5.925	1.29267	-11.844	-8.568	1.171	0.711	1.09205	-1.694	-2.352	2.662
5.397	1.29198	-9.156	-8.416	1.171	0.705	1.09036	-1.694	-2.328	2.662
5.282	1.29180	-8.652	-8.416	1.171	0.637	1.05072	-1.694	-2.000	2.662
4.974	1.29079	-7.742	-7.808	1.171	0.627	1.04702	-1.694	-2.000	2.691
4.781	1.29023	-7.742	-7.808	1.566	0.564	1.01327	-1.554	-2.000	2.691
4.504	1.28904	-6.916	-7.224	1.566	0.554	1.00983	-1.540	-2.000	2.691
4.028	1.28679	-5.474	-5.928	1.566	0.543	1.00551	-1.526	-2.000	2.691
3.934	1.28666	-5.320	-5.880	1.566	0.538	1.00300	-1.526	-1.984	2.691
3.887	1.28654	-5.320	-5.000	1.566	0.522	0.99324	-1.526	-1.984	2.760
3.866	1.28647	-5.320	-4.840	1.566	0.486	0.96731	-1.526	-1.864	2.760
3.830	1.28635	-5.208	-4.840	1.566	0.465	0.95122	-1.470	-1.864	2.760
3.610	1.28553	-4.746	-4.840	1.566	0.444	0.93613	-1.470	-1.808	2.760
3.600	1.28547	-4.746	-4.696	1.566	0.408	0.89568	-1.470	-1.808	2.958
3.339	1.28359	-4.298	-4.592	1.566	0.392	0.89367	-1.470	-1.800	2.958
3.302	1.28328	-4.228	-4.592	1.566	0.371	0.87395	-1.470	-1.800	3.038
2.973	1.27971	-3.654	-4.568	1.566	0.340	0.85228	-1.470	-1.800	3.112
2.931	1.27959	-3.626	-4.568	1.566	0.334	0.84790	-1.470	-1.800	3.126
2.910	1.27946	-3.626	-4.568	1.621	0.308	0.80820	-1.470	-1.680	3.126
2.894	1.27933	-3.626	-4.304	1.621	0.287	0.78353	-1.470	-1.624	3.126
2.847	1.27883	-3.626	-3.848	1.621	0.266	0.76381	-1.470	-1.584	3.126
2.816	1.27852	-3.584	-3.848	1.621	0.256	0.75848	-1.470	-1.576	3.126
2.800	1.27833	-3.584	-3.848	1.656	0.235	0.75022	-1.470	-1.560	3.126
2.795	1.27827	-3.584	-3.832	1.656	0.214	0.71684	-1.302	-1.560	3.126
2.591	1.27558	-3.332	-3.832	1.656	0.209	0.71296	-1.288	-1.560	3.126
2.414	1.27345	-3.136	-3.832	1.656	0.199	0.70407	-1.260	-1.560	3.126
2.403	1.27339	-3.136	-3.696	1.656	0.183	0.67658	-1.240	-1.520	3.136
2.351	1.27270	-3.108	-3.696	1.656	0.172	0.65554	-1.230	-1.490	3.146
2.330	1.27238	-3.094	-3.696	1.656	0.157	0.61384	-1.160	-1.460	3.156
2.126	1.26900	-2.926	-3.696	1.656	0.141	0.58422	-1.100	-1.450	3.166
2.085	1.26781	-2.926	-3.696	1.848	0.131	0.54665	-1.090	-1.390	3.176
2.074	1.26750	-2.912	-3.696	1.848	0.120	0.52304	-1.080	-1.360	3.186
2.048	1.26662	-2.912	-3.696	1.922	0.110	0.50776	-1.070	-1.340	3.196
1.959	1.26337	-2.786	-3.696	1.922	0.094	0.44665	-0.980	-1.300	3.216
1.766	1.25761	-2.618	-3.696	1.922	0.068	0.40307	-0.900	-1.290	3.226
1.651	1.25141	-2.618	-3.696	2.195	0.063	0.38704	-0.880	-1.280	3.236
1.641	1.25072	-2.618	-3.232	2.195	0.057	0.34890	-0.870	-1.270	3.356
1.620	1.24922	-2.618	-3.232	2.216	0.052	0.33231	-0.860	-1.260	3.386
1.609	1.24846	-2.618	-3.096	2.216	0.047	0.31641	-0.850	-1.250	3.416
1.452	1.23744	-2.380	-3.096	2.216	0.042	0.29656	-0.840	-1.240	3.456
1.437	1.23682	-2.366	-3.096	2.216	0.037	0.28240	-0.830	-1.230	3.476
1.348	1.23037	-2.268	-3.096	2.216	0.031	0.26756	-0.810	-1.220	3.486
1.332	1.22912	-2.268	-2.920	2.216	0.026	0.25667	-0.800	-1.210	3.496
1.322	1.22786	-2.268	-2.920	2.235	0.021	0.24609	-0.790	-1.200	3.506
1.259	1.22016	-2.170	-2.920	2.235	0.016	0.15485	-0.620	-1.190	3.516
1.212	1.21428	-2.170	-2.624	2.235	0.010	0.14402	-0.610	-1.180	3.536
1.202	1.21309	-2.156	-2.624	2.235	0.005	0.12999	-0.590	-1.170	3.546

Table C.4: TD function. N_{TD} is measure of $K_{\mu 2}$ background level, and A_{TD} is a measure of acceptance, for different lower limits on the allowed values of TDLIK2, TDLIK3, and TDDFA2 (see section C.3.4). Events with $N_{TD} \leq 1.003$ pass the TD function cut. This function is drawn in figure 4.15.

Appendix C. Detailed Cut Descriptions

The low sides of the RBOX, EBOX, and PBOX cuts correspond to cuts at 2.4, 2.0, and 2.2 in $rdev$, $edev$, and $pdev$, respectively.

The K_{π_2} kinematic function is based on simultaneous, uniform loosening/tightening of the RBOX', EBOX' and PBOX' cuts. It is measured using K_{π_2} decays from the 1/3 1995 SKIM1 data which fail the PV function cut, pass all beam cuts, pass the TD function cut, and pass the high-side BOX cut (to remove K_{μ_2} decays). For the function at "loose" cut positions ($N_{kin,K_{\pi_2}} > 1.0$), events are first required to fail the low-side RBOX, EBOX, and PBOX cuts. The RBOX', EBOX', and PBOX' cuts are then loosened, and the number of events counted at each step. For the function at "tight" cut positions ($N_{kin,K_{\pi_2}} \leq 1.0$), events are first required to pass the low-side RBOX, EBOX, and PBOX cuts. The RBOX', EBOX', and PBOX' cuts are then tightened to give the same rejection for all 3 kinematic quantities at each step, assuming each quantity has a Gaussian distribution. Note, from section 4.4.1 and figure 4.20, that R and P are bifurcated with E in order to get the K_{π_2} normalization. This "second bifurcation" is valid as long as R and P are not correlated with E for K_{π_2} background. From table C.5, "# events" is the number of events in the SKIM1 data sample described above which pass the listed cuts on R and P , "N(EBOX)" is "# events" divided by the rejection of the cut on E (i.e., the K_{π_2} normalization for the 1/3 1995 data, as described in section 4.4.1), and "N(seen)" is the observed number of events which simultaneously pass the cuts on R , E , and P . The agreement of N(EBOX) with N(seen) verifies the absence of a correlation of R and P with E for K_{π_2} background. Figure 4.16 shows the K_{π_2} kinematic background level, $N_{kin,K_{\pi_2}}$, as a function of the acceptance, $A_{kin,K_{\pi_2}}$. Events with $N_{kin,K_{\pi_2}} \leq 0.3358$ are defined to pass the K_{π_2} kinematic function cut. The function is defined for the range $N_{kin,K_{\pi_2}} = [0, 285.1]$ and is tabulated in table C.5. Note that at the $N_{kin,K_{\pi_2}} = 0.3358$ position in table C.5 that # events = 7 and N(EBOX) = 0.127. In table 4.12 for the 1/3 1995 data however, $B_{RP}^{K_{\pi_2}} = \# \text{ events} = 8$ and $B_{K_{\pi_2}} = \text{N(EBOX)} = 0.16$ for the 1/3 1995 data. This is because some cuts/calibrations were changed slightly between measurement of the K_{π_2} kinematic function, and the measurement of K_{π_2} background in the 1/3 1995 data.

The K_{μ_2} kinematic function is based on the RNGMOM cut and the high side of the

Appendix C. Detailed Cut Descriptions

$\frac{R-R_{peak}}{\sigma_R}$	$\frac{E-E_{peak}}{\sigma_E}$	$\frac{P-P_{peak}}{\sigma_P}$	$N_{kin,K\pi_2}$	$A_{kin,K\pi_2}$	# events	N(EBOX)	N(seen)
1.70	1.157	1.435	285.1200	1.2845	468	104.3	108
1.75	1.220	1.491	221.7600	1.2673	391	80.7	84
1.80	1.283	1.547	190.0800	1.2508	328	63.4	72
1.85	1.345	1.602	142.5600	1.2319	272	49.1	54
1.90	1.407	1.658	102.9600	1.2162	223	37.4	39
1.95	1.468	1.713	81.8400	1.1995	186	28.2	31
2.00	1.529	1.767	66.0000	1.1831	163	22.1	25
2.05	1.589	1.822	55.4400	1.1637	145	17.3	21
2.10	1.649	1.876	42.2400	1.1427	122	13.1	16
2.15	1.708	1.931	36.9600	1.1251	97	9.4	14
2.20	1.767	1.985	31.6800	1.1086	84	7.2	12
2.25	1.826	2.039	21.1200	1.0910	68	5.0	8
2.30	1.884	2.093	10.5600	1.0745	50	2.9	4
2.35	1.942	2.146	7.9200	1.0606	41	1.8	3
2.40	2.000	2.200	1.0996	1.0323	14	0.417	1
2.45	2.057	2.253	1.0512	1.0218	14	0.398	1
2.50	2.115	2.307	0.9306	1.0089	13	0.353	0
2.55	2.171	2.360	0.8868	0.9932	13	0.336	0
2.60	2.228	2.413	0.7772	0.9755	12	0.294	0
2.65	2.285	2.466	0.6745	0.9601	11	0.256	0
2.70	2.341	2.519	0.5792	0.9421	10	0.219	0
2.75	2.397	2.572	0.4364	0.9255	8	0.165	0
2.80	2.453	2.624	0.3358	0.9069	7	0.127	0
2.85	2.508	2.677	0.2893	0.8930	7	0.110	0
2.90	2.564	2.729	0.2418	0.8775	7	0.092	0
2.95	2.618	2.782	0.1708	0.8610	6	0.065	0
3.00	2.673	2.834	0.1175	0.8433	5	0.045	0
3.05	2.728	2.887	0.0742	0.8233	4	0.028	0
3.10	2.783	2.939	0.0541	0.8058	4	0.021	0
3.15	2.838	2.991	0.0436	0.7906	4	0.017	0

Table C.5: K_{π_2} kinematic function. $N_{kin,K\pi_2}$ is a measure of K_{π_2} background level, and $A_{kin,K\pi_2}$ is a measure of acceptance, for different lower limits on the allowed values of $(X - X_{peak})/\sigma_X$ (see section C.3.5). Events with $N_{kin,K\pi_2} \leq 0.3358$ pass the K_{π_2} kinematic function cut. This function is drawn in figure 4.16. “# events”, “N(EBOX)”, and “N(seen)” are defined in section C.3.5 of the text.

Appendix C. Detailed Cut Descriptions

PBOX cut. It is measured using $K_{\mu 2}$ decays from the 1/3 1995 SKIM2 data which fail the TD function cut, pass all beam cuts, pass the PV function cut, and pass the low-side BOX cut (to remove $K_{\pi 2}$ decays). For the function at “loose” cut positions ($N_{kin,K_{\mu 2}} > 0.2681$), events are first required to pass the high-side RBOX and EBOX cuts. The RNGMOM cut and the high side of the PBOX cut are then loosened, and the number of events counted at each step. The two cuts are loosened such that an equal number of $K_{\mu 2}$ range-tail and muon-band events are added at each step. For the function at “tight” cut positions ($N_{kin,K_{\mu 2}} \leq 0.2681$), there are too few events to measure a function. However, there are indications (see section 4.4.2) that the limiting $K_{\mu 2}$ background is dominated by range-tail events, i.e., $K_{\mu 2}$ decays where the muon interacts in the RS, such that range and energy are downshifted, with an uncorrelated momentum mismeasurement placing the muon in the box. The function inside the box can then be measured by tightening the PBOX cut on a large-statistics sample of $K_{\mu 2}$ peak events available from $K_{\mu 2}(1)$ monitor data (see section 3.3), and counting the number of events which remain at each step. The RNGMOM cut is also tightened to define the $K_{\mu 2}$ kinematic function inside the box, but due to lack of a high-statistics sample of muon-band events, the rejection of the RNGMOM cut cannot be measured into the box with any reliability. Therefore, the muon band is assumed to be Gaussian in the quantity $\chi(RP) = (R_{RS} - R_{RS}^{exp})/\sigma(R_{RS})$ (see above), and the RNGMOM cut is tightened to get the same rejection per step for muon-band events as the tightening of the PBOX cut gives for $K_{\mu 2}$ range-tail events. Figure 4.17 shows the $K_{\mu 2}$ kinematic background level, $N_{kin,K_{\mu 2}}$, as a function of the acceptance, $A_{kin,K_{\mu 2}}$. Events with $N_{kin,K_{\mu 2}} \leq 0.2681$ are defined to pass the $K_{\mu 2}$ kinematic function cut. The function is defined for the range $N_{kin,K_{\mu 2}} = [0, 45.15]$ and is tabulated in table C.6.

C.3.6 Beam Function Cuts

Beam functions are measured by loosening/tightening the following cuts:

- **DELIC:** Events are rejected where the kaon decay product is detected soon after the kaon is detected, such that the kaon may have decayed in flight. This cut rejects

Appendix C. Detailed Cut Descriptions

$\chi(RP)$	P	# events	$N_{kin,K_{\mu 2}}$	$A_{kin,K_{\mu 2}}$
7.790	238.00	261	45.1530	1.0757
7.530	237.80	243	42.0390	1.0757
7.450	237.60	234	40.4820	1.0757
7.020	237.30	214	37.0220	1.0757
6.970	237.10	206	35.6380	1.0757
6.900	237.00	198	34.2540	1.0757
6.830	236.90	186	32.1780	1.0757
6.590	236.50	173	29.9290	1.0757
6.450	236.20	157	27.1610	1.0757
6.310	236.00	145	25.0850	1.0756
6.240	235.70	133	23.0090	1.0756
6.170	235.50	123	21.2790	1.0756
6.100	235.10	112	19.3760	1.0756
5.990	234.80	102	17.6460	1.0754
5.880	234.60	90	15.5700	1.0751
5.770	234.50	79	13.6670	1.0749
5.720	234.20	71	12.2830	1.0748
5.650	234.00	65	11.2450	1.0746
5.420	233.60	52	8.9960	1.0740
5.260	233.30	42	7.2660	1.0738
5.170	233.10	38	6.5740	1.0731
5.090	232.80	34	5.8820	1.0727
4.760	232.40	25	4.3250	1.0719
4.690	232.30	21	3.6330	1.0715
4.560	232.10	19	3.2870	1.0712
4.150	231.80	15	2.5950	1.0701
4.060	231.60	13	2.2490	1.0675
3.770	231.20	11	1.9030	1.0643
3.740	230.50	9	1.5570	1.0587
2.900	229.80	5	0.8650	1.0490
2.290	229.30	3	0.5190	1.0351
2.000	229.00	234	0.2681	1.0237
1.852	228.00	142	0.1293	0.9912
1.732	227.00	91	0.0828	0.9500
1.635	226.00	69	0.0628	0.8924
1.534	225.00	47	0.0428	0.8301
1.435	224.00	37	0.0337	0.7541
1.393	223.00	26	0.0237	0.6767
1.320	222.00	22	0.0201	0.5918
1.259	221.00	14	0.0127	0.5093
1.204	220.00	11	0.0100	0.4317
1.121	219.00	9	0.0082	0.3526

Table C.6: $K_{\mu 2}$ kinematic function. $N_{kin,K_{\mu 2}}$ is a measure of $K_{\mu 2}$ background level, and $A_{kin,K_{\mu 2}}$ is a measure of acceptance, for different upper limits on the allowed values of $\chi(RP)$ and P (see section C.3.5). Events with $N_{kin,K_{\mu 2}} \leq 0.2681$ pass the $K_{\mu 2}$ kinematic function cut. This function is drawn in figure 4.17. “# events” is the number of SKIM2 ($N_{kin,K_{\mu 2}} > 0.2681$) or $K_{\mu 2}(1)$ monitor ($N_{kin,K_{\mu 2}} \leq 0.2681$) events which are used to define the $N_{kin,K_{\mu 2}}$ values, which is why # events is discontinuous at $N_{kin,K_{\mu 2}} = 0.2681$ (more details can be found in section C.3.5 of the text).

Appendix C. Detailed Cut Descriptions

single-beam background. Events are rejected unless they satisfy all of the following conditions:

1. $t_\pi - t_K > 2$ ns
 2. $t_\pi - t_K > 5$ ns if $|t_K - t_{B4strobo}| > 1.5$ ns
 3. $t_\pi - t_K > 5$ ns if $|t_\pi - t_{RS}| > 1.5$ ns
 4. $t_\pi - t_K > 5$ ns if there are no pion fibers in the target (in which case t_π comes from the IC)
 5. $t_\pi - t_K > 4$ ns if the kaon energy in the target is small (≤ 50 MeV)
 6. $t_\pi - t_K > 3$ ns if there are less than 4 pion fibers in the target
 7. $t_\pi - t_K > 3$ ns if $lkbeam \leq 200$ (this is primarily intended to attack CEX background)
 8. $t_\pi - t_K > 4$ ns when any kaon fiber has time farther than 2.5 ns from the average kaon time
 9. $t_\pi - t_K > 4$ ns when any pion fiber has time farther than 3.5 ns from the average pion time.
- **BWTRS:** Events are rejected that have hits in BWC1 or BWC2 within ± 5 ns of t_{RS} . This cut rejects double-beam background, where a second beam particle (detected by BWC1 or BWC2) scatters into the RS to produce the apparent decay product of the event kaon.
 - **BWHRs:** Events are rejected where the minimum absolute time of all hits in BWC1 and BWC2 (excluding those due to the event kaon) relative to RS track time is < 0 ns (that is, this cut does nothing). However, this time requirement is tightened to define the double-beam function (see below). This cut rejects double-beam background, where a second beam particle (detected by BWC1 or BWC2) scatters into the RS to produce the apparent decay product of the event kaon.

Appendix C. Detailed Cut Descriptions

- **CKTRS:** Events are rejected that have a \check{C}_K hit within ± 2 ns of t_{RS} , where at least 5 kaon tubes fired. This cut rejects single-beam background, where the event kaon decays in flight, and double-beam background, where a second beam kaon decays in flight to produce the track detected in the RS.
- **CKTAIL:** This cut is similar to CKTRS, but it uses the trailing-edge TDC time to infer the time of a \check{C}_K pulse. \check{C}_K pulses are typically 20 ns wide, so hits occurring up to 20 ns after a previous hit may not have a leading-edge TDC time. This cut therefore attacks double-beam background, where a second beam kaon decays in flight to produce the track detected in the RS, and enters the Čerenkov detector less than 20 ns after the event kaon. Events are rejected depending on the value of $t_\pi - t_K$:
 1. $t_\pi - t_K < 15$ ns: the event is rejected if there are \check{C}_K hits within ± 2 ns of t_{RS} with at least 5 kaon tubes firing
 2. $15 < t_\pi - t_K < 25$ ns: the event is rejected if there are \check{C}_K hits within $+5$ or -2 ns of t_{RS} with at least 1 kaon tube firing
 3. $t_\pi - t_K > 25$ ns: the event is rejected if there are \check{C}_K hits within ± 2 ns of t_{RS} with at least 5 kaon tubes firing.
- **CPITRS:** Events are rejected that have a \check{C}_π hit within ± 2 ns of t_{RS} , where at least 5 pion tubes fired. This cut rejects double-beam background, where a beam pion scatters into the RS to produce the apparent decay product of the event kaon.
- **CPITAIL:** This cut is similar to CPITRS, but it uses the trailing-edge TDC time to infer the time of a \check{C}_π pulse. \check{C}_π pulses are typically 20 ns wide, so hits occurring up to 20 ns after a previous hit may not have a leading-edge TDC time. This cut therefore attacks double-beam background, where a beam pion scatters into the RS to produce the apparent decay product of the event kaon, and enters the the Čerenkov detector less than 20 ns after a previous \check{C}_π hit (presumably due to the event kaon). Events are rejected if there are \check{C}_π hits within ± 2 ns of t_{RS} with at least 5 pion tubes firing.

Appendix C. Detailed Cut Descriptions

- **PBNRS**: Events are rejected that have 2 or more lead glass phototube hits within ± 5 ns of t_{RS} . This cut rejects double-beam background, where a beam pion (detected by the lead glass) scatters into the RS to produce the apparent decay product of the event kaon.
- **B4DEDX**: Events are rejected that have energy in the B4 hodoscope < 1.5 MeV. This cut rejects single- and double-beam background arising from pions in the beam, because pions have smaller dE/dx than kaons of the same momentum.
- **B4TRS**: Events are rejected that have hits in the B4 counter within ± 3 ns of t_{RS} . This cut rejects double-beam background, where a second beam particle is responsible for the apparent decay product of the event kaon.
- **B4TD**: Events are rejected which have second pulses in the TD data of the B4 hodoscope within ± 4 ns of t_{RS} , where the pulse fitting to TD data returns a single-pulse fit χ^2 divided by that of a double-pulse fit > 2.5 , and the energy of the second pulse is more than 20 MeV. This cut removes double-beam background, where a second beam particle is responsible for the apparent decay product of the event kaon.

Individual single- and double-beam normalization and rejection functions are not measured directly due to overlap between the different beam background types. Rather, the beam function cuts which are used in each of the normalization and rejection branches of the bifurcated background estimation structures (see figures 4.22, 4.23, 4.24 and 4.25 of section 4.4.3) are loosened for the purpose of the outside-the-box correlation study (see sections 4.2 and 4.6, and the beam background re-measured at each step. When loosening the beam function cuts associated with the single-beam kaon- and pion-entering rejection branches, the rejections are measured with enhanced statistics, obtained by using a loose BOX cut in the setup (see figures 4.22 and 4.23). When loosening the beam function cuts associated with the double-beam kaon- and pion-entering rejection branches, the rejections are measured with enhanced statistics, obtained by applying only the low side of the BOX cut in the setup (see figures 4.24 and 4.25).

pass condition	M_{BM2K}^{out} (low-side box)	M_{BM2P}^{out} (low-side box)	N_{BM2}	A_{BM2}
$ BWHRs > 0.0$ ns	14	9	1.00	1.0000
$ BWHRs > 1.0$ ns	13	9	0.93	0.9892
$ BWHRs > 2.0$ ns	13	8	0.93	0.9766
$ BWHRs > 3.0$ ns	12	8	0.86	0.9615
$ BWHRs > 4.0$ ns	11	8	0.79	0.9457
$ BWHRs > 5.0$ ns	7	7	0.52	0.9279

Table C.7: Double-beam function “inside the box”. N_{BM2} is a measure of double-beam background level, and A_{BM2} is a measure of acceptance, for different lower limits on the minimum absolute time of all hits in BWC1 and BWC2 (excluding those due to the event kaon) relative to RS track time (see the description of the BWHRs cut in section C.3.6 of the text). This function is drawn in figure 4.18. M_{BM2K}^{out} (low-side box) and M_{BM2P}^{out} (low-side box) are the numbers of surviving events at the bottom of the rejection branches in figures 4.24 and 4.25, respectively, after the BWHRs cut in the table is applied.

Figure 4.18 shows the total double-beam background level, N_{BM2} , as a function of the acceptance, A_{BM2} , for tight cut positions ($N_{BM2} \leq 1.0$). The function is measured using the 2/3 1995 SKIM3 data, by tightening the BWHRs cut and counting the events which survive at the bottom of the rejection branches in figures 4.24 and 4.25. It is defined for the range $N_{BM2} = [0.52, 1.0]$ and is tabulated in table C.7. Figure 4.19 shows the CEX background level, N_{CEX} , as a function of the acceptance, A_{CEX} , for tight cut positions ($N_{CEX} \leq 1.0$). The function is measured using UMC-generated CEX data, by tightening the B4EKZ and DELC cuts and counting the number of events which survive after all other (UMC-appropriate) cuts have been applied (see section 4.4.4). It is defined for the range $N_{CEX} = [0.26, 1.0]$ and is tabulated in table C.8.

C.4 Data Quality Cuts

- **BAD_RUN**: During data-taking, a log is kept of various hardware failures. Runs that are deemed un-analyzable due to hardware problems are omitted from the analysis. Some hardware problems are only found offline: they are removed by imposing various conditions on the data. For example, in 1997 there was a period when the high voltages

pass condition	# events	N_{CEX}	A_{CEX}
$lkbeam > 2$	23	1.00	1.0000
$lkbeam > 3$	21	0.91	0.9934
$lkbeam > 4$	20	0.87	0.9876
$lkbeam > 5$	18	0.78	0.9811
$lkbeam > 6$	14	0.61	0.9763
$lkbeam > 7$	14	0.61	0.9706
$lkbeam > 8$	14	0.61	0.9653
$lkbeam > 9$	13	0.57	0.9612
$lkbeam > 10$	13	0.57	0.9573
$(t_\pi - t_K)/i_{DC} > 1.0$	13	0.57	0.9573
$(t_\pi - t_K)/i_{DC} > 1.1$	10	0.43	0.9373
$(t_\pi - t_K)/i_{DC} > 1.2$	8	0.35	0.9214
$(t_\pi - t_K)/i_{DC} > 1.3$	6	0.26	0.9004

Table C.8: CEX function “inside the box”. N_{CEX} is a measure of CEX background level, and A_{CEX} is a measure of acceptance, for different lower limits on the kaon likelihood ($lkbeam$ – see the description of the B4EKZ cut in section C.3.2) and decay time (see the description of the DELC cut in section C.3.6 of the text). This function is drawn in figure 4.19. i_{DC} is an index which refers to all subconditions of the DELC cut, which are tightened simultaneously. That is, $(t_\pi - t_K)/i_{DC} > 1.0$ refers to the standard DELC cut, and $(t_\pi - t_K)/i_{DC} > 1.1$ means that the veto time window in each subcondition of the DELC cut is widened by 10%, e.g., from $t_\pi - t_K > 2$ ns to $t_\pi - t_K > 2.2$ ns. “# events” is the number of events remaining in the UMC-generated CEX data after all UMC-appropriate cuts and the cuts in the table are applied.

Appendix C. Detailed Cut Descriptions

to the target PMT's were failing. In this case, events are rejected on a spill-by-spill basis by requiring that the number of K_B hits relative to \check{C}_K hits in a spill be ≥ 0.21 (see section 3.3). Other failures found offline include TD failures: if the "fiducial" pulse (a reference pulse for TD timing) is missing from any TD channel, then the event is rejected.

- **BAD_STC**: There are periods of runs for which the TD pulse-area-to-MeV calibration in a particular RS counter fails. If the stopping counter for an event is one of these counters, then the event is rejected. These types of events can preferentially fool both the TD and kinematic cuts, because something is wrong with the pulses in the TD data. TD and kinematic cuts are bifurcated and therefore assumed to be uncorrelated in the $K_{\mu 2}$ background estimate (see sections 4.2 and 4.4.2), so the BAD_STC cut is applied as a pathology cut when measuring backgrounds.

Appendix D

Glossary

- **acceptance** — a measure of a data-selection cut's ability to retain desired events (signal) while removing unwanted events (background) from a data sample. The acceptance of a cut is the fraction of signal events which survive the cut.
- **accidental** — describes an energy deposit in some detector element which arises from a real particle which is not associated with the decay products of the event kaon.
- **ADC** — analog-to-digital converter: hardware used to digitize the energy of a pulse.
- **AGS** — Alternating Gradient Synchrotron: the primary proton accelerator at BNL.
- **azimuthal angle, ϕ** — the angle about the center of the detector, perpendicular to the beam axis, which is the angle of cylindrical symmetry of the detector. That is, ϕ is the angle in the (x, y) plane that a radial line, originating at the center of the detector, makes with respect to the radial line extending horizontally from the center of the detector to the right, as viewed from downstream (see figure 3.7). ϕ ranges from 0° to 360° . A positive increment in ϕ corresponds to a counter-clockwise displacement (as viewed from downstream).
- **azimuthal angle, ω** — the angle in the (x, y) plane that a radial line, originating at the center of the circular UTC track, makes with respect to the radial line extending from the center of the track to the point on the track closest to the kaon decay vertex

Appendix D. Glossary

(see figure 4.12). ω ranges from 0° to 360° . A positive increment in ω corresponds to a displacement in the direction of propagation of the track.

- **B4** — a hodoscope consisting of 2 planes of 8 fingers of plastic scintillator, placed against the upstream face of the target.
- **baryon** — a particle composed of 3 quarks.
- **beam strobe** — a signal used by the trigger which is defined by the time of the beam particle as detected in the Čerenkov counter or B4 hodoscope, whichever is later.
- **bias** — non-reproducible behaviour of an analysis on independent data samples, due to analysis design using a small number of events which may or may not represent a larger population of events.
- **bifurcate** — prepare a data sample by inverting a cut, and use this data sample to evaluate the performance of another uncorrelated cut.
- **blind analysis** — an analysis of data where the true result is hidden from the person analyzing the data, such that the data itself does not influence the analysis. This approach is useful when only a small number of signal events are expected from the data, because it avoids the problem of small-statistics bias. In the E787 analysis of $K^+ \rightarrow \pi^+ \nu \bar{\nu}$ data, a signal region is defined where the signal/background ratio is expected to be highest, and background and signal characteristics are not defined by examining events in this region. Instead, background contamination is estimated using events which lie outside of the signal region, and is suppressed such that the estimated background in the signal region is $\ll 1$ event. Events in the signal region therefore have a high probability to be signal, and are not counted or examined until the background estimates are final.
- **BM1** — single-beam background
- **BM2** — double-beam background

Appendix D. Glossary

- **BNL** — Brookhaven National Laboratory, New York, USA
- **boson** — a particle with integral spin (e.g., spin = 1).
- **box** — a region in a multi-dimensional parameter space where the signal/background ratio is expected to be highest (also known as the “signal region”).
- **BOX** — a cut on the minimum and maximum range, energy, and momentum of a charged track.
- **BR** — branching ratio
- **BV** — barrel veto
- **BWC1, BWPC1, MWPC1** — upstream beam wire chamber
- **BWC2, BWPC2, MWPC2** — downstream beam wire chamber
- \check{C}_K — a signal indicating detection of a beam kaon by the Čerenkov detector
- \check{C}_π — a signal indicating detection of a beam pion by the Čerenkov detector
- **CCD** — charge-coupled device. In the case of E787, the CCD’s are 500 MHz transient digitizers based on a GaAs charge-coupled devices which sample and digitize voltage in 2 ns intervals.
- **Čerenkov detector** — detects charged particles whose speed in a medium is greater than the speed of light, such that a moving dipole is induced in the material, the radiation from which constructively interferes in a cone around the particle’s path. The angle of the cone depends on the particle’s speed in the material.
- **CERN** — European Laboratory for Particle Physics, Geneva, Switzerland
- **CEX** — background arising from kaon charge exchange
- χ^2 — a measure of how well a model fits to data, usually defined by

$$\chi^2 = \sum_{i=1}^N \left(\frac{y_i - y(x_i)}{\sigma_i} \right)^2$$

Appendix D. Glossary

where (x_i, y_i) are data points with standard deviation σ_i , and $y(x_i)$ is the model being fit. If the σ_i are correct, then a good fit is indicated when the χ^2 per degree of freedom, $\chi^2/\text{d.o.f.}$, is equal to 1, where $\text{d.o.f.} = n - m$ with n the number of data points and m the number of model parameters.

- **CKM matrix** — Cabibbo-Kobayashi-Maskawa quark mixing matrix
- **CM** — microcollar detector
- **CO** — collar detector
- **CP** — quantum-mechanical symmetry operation defined by the combination of charge conjugation (C) and parity inversion (P)
- **ct** — charged track: used to denote a RS counter which is in the T · 2 track sector or within 2 sectors clockwise (as viewed from downstream) of the T · 2 track sector.
- **cut** — hardware (online) or software (offline) requirement that an event must satisfy certain criteria. Hardware cuts make up a “trigger” which is used to acquire data, and software cuts are part of a computer program which is used to analyze the data after acquisition. Cuts are used to separate background events from signal events.
- **DC** — “delayed coincidence” trigger requirement
- **delayed coincidence** — requirement that the kaon decay products be detected later than the kaon, such that the kaon decays from rest.
- **dE/dx** — energy loss of a particle per unit distance travelled in a material.
- **detector strobe** — a signal used by the trigger which is defined by the time of coincident hits in the T and 2 counters on the track.
- **DIF** — decay in flight: characterizes a particle which decays while in motion.
- **dip angle** — see polar angle.

- **discriminant function analysis** — an analysis of various parameters associated with two different data sets with the intention of forming a linear combination of the parameters which is maximally different for the two data sets.
- **discriminator** — logic hardware which takes an analog pulse as input, and outputs a constant voltage signal of variable duration when the input pulse is above an adjustable threshold voltage.
- **downstream** — in the direction of the kaon beam momentum
- E — total energy deposited by the track particle in the detector.
- E_μ — energy of the second pulse in the stopping counter (e.g., for pion tracks, this is usually the energy of the muon from pion decay).
- E_{RS} — energy deposited by the track particle in the RS.
- E_{TG} — energy deposited by the track particle in the target.
- E_{TG}^{op} — total energy at kaon decay time in target fibers located on the non-track side of the kaon decay fiber.
- $E1$ — energy of a pulse as recorded on the upstream end of a RS or barrel counter.
- $E2$ — energy of a pulse as recorded on the downstream end of a RS or barrel counter.
- **E787** — Experiment 787 at BNL: search for $K^+ \rightarrow \pi^+ \nu \bar{\nu}$
- **E926** — Experiment 926 at BNL: search for $K_L^0 \rightarrow \pi^0 \nu \bar{\nu}$
- **E949** — Experiment 949 at BNL: successor experiment to E787
- **EC** — CsI endcap detector. Also used to refer to the EC trigger requirement.
- **electromagnetic shower detector** — detects electrons and high-energy photons. High-energy photons (gamma rays) are detected via their conversion into e^+, e^- pairs, which has highest efficiency in the field of atoms of high Z (atomic number). This

is followed by emission of bremsstrahlung photons by the electrons, which in turn convert into more e^+, e^- pairs until all the energy of the original photon is dissipated in a “shower” of electrons. The scintillation light created by the electrons can be converted into an electrical pulse by a PMT.

- **event** — a single kaon entering the target and decaying into the fiducial region of the detector.
- f_s — stopping fraction: a “fudge” factor used to account for the fraction of kaons which stop in the target, and any other cut acceptances/efficiencies that are not calculated explicitly.
- **FCNC** — flavour-changing neutral current
- **Fermilab** — see FNAL
- **fermion** — a particle with half-integral spin (e.g., spin = 1/2).
- **fiducial pulse** — an electronically-generated pulse which is used for reference when finding the times of pulses in TD data.
- **flags** — see TD flags.
- **FNAL** — Fermi National Accelerator Laboratory, Chicago, USA
- **function cut** — an offline cut which is inverted to define a background data sample, on which the performance of another, uncorrelated function cut is evaluated in order to make a bifurcated background estimate. A function cut is designed on a sliding scale in terms of a parameter N (scaled number of background events) or A (acceptance), so that it can be loosened to perform the outside-the-box correlation test (see sections 4.2 and 4.6), and tightened to estimate the “likelihood” of an event to be a signal or background event (see sections 4.2 and 4.7).
- **FWHM** — full width of a peak at the half-maximum value

Appendix D. Glossary

- **gamma fiber** — target fiber with energy at kaon decay time, but located away from the pion track.
- **GDR background** — giant dipole resonance background, whereby positively-charged muons excite the giant dipole resonance in ^{12}C , which de-excites by emitting a single neutron. The neutron travels slowly and leaves an isolated second pulse in the counter where the muon comes to rest, faking the double-pulse $\pi \rightarrow \mu$ decay signature in the stopping counter. The stopping counter information is therefore indicative of a pion track instead of a muon track.
- **geometric mean energy** — $\sqrt{E1 \times E2}$, where $E1$ and $E2$ are upstream and downstream energies, respectively.
- **GIM mechanism** — Glashow-Iliopoulos-Maiani mechanism, whereby flavour-changing neutral weak currents are forbidden.
- **GUT** — grand unified theory: theory which unites the electromagnetic, weak, and strong forces into a single mathematical description.
- **hadron** — any particle which is a bound state of quarks (see meson and baryon).
- **HEX** — trigger requirement for summed hextant energies in the RS.
- **hextant** — a group of 4 adjacent RS sectors, which are multiplexed by layer into the TD's.
- **hodoscope** — a combination of several detector elements arranged in space such that particle tracks can be identified. Hodoscopes are usually constructed from scintillation counters which have short-duration output pulses which can be used for triggering purposes.
- **IC** — I-counter. Also used to refer to the IC trigger requirement.
- **K_B** — a coincidence signal between the \check{C}_K , summed B4, and summed target signals indicating the presence of a beam kaon.

Appendix D. Glossary

- K_{Blive} — K_B signal in coincidence with the “computer ready” signal.
- $K_{\mu 2}$ — $K^+ \rightarrow \mu^+ \nu_\mu$ decay
- $K_{\mu 2}$ peak — kinematic region characterized by range, energy, and momentum values consistent with the μ^+ from $K_{\mu 2}$ decay ($R = 54$ cm, $E = 152$ MeV, $P = 236$ MeV/ c).
- $K_{\mu 2}$ range tail — kinematic region characterized by the expected $K_{\mu 2}$ peak value of momentum, but range (and energy) values smaller than the peak values due to elastic (inelastic) scattering of muons in the detector.
- $K_{\mu 3}$ — $K^+ \rightarrow \pi^0 \mu^+ \nu_\mu$ decay
- $K_{e 3}^0$ — $K_L^0 \rightarrow \pi^+ e^- \bar{\nu}_e$ decay
- $K_{\mu 3}^0$ — $K_L^0 \rightarrow \pi^+ \mu^- \bar{\nu}_\mu$ decay
- $K_{\mu\nu\gamma}$ — $K^+ \rightarrow \mu^+ \nu_\mu \gamma$ decay, also called radiative $K_{\mu 2}$ decay
- $K_{\pi 2}$ — $K^+ \rightarrow \pi^+ \pi^0$ decay
- $K_{\pi 2}$ peak — kinematic region characterized by range, energy, and momentum values consistent with the π^+ from $K_{\pi 2}$ decay ($R = 30$ cm, $E = 108$ MeV, $P = 205$ MeV/ c).
- $K_{\pi 2}$ range tail — kinematic region characterized by the expected $K_{\pi 2}$ peak value of momentum, but range (and energy) values smaller than the peak values due to elastic (inelastic) scattering of pions in the detector.
- kaon fiber — target fiber with pulse time and energy and location consistent with the event kaon.
- KEK — Koh-Enerugii Kasokuki Kenkyu Kikou (High Energy Accelerator Research Organization), Japan
- layer — 1 of 21 radial segments of the RS

- **LESBIII** — low-energy separated beamline III: the kaon beamline at BNL which provides a high intensity and relatively high purity kaon beam for use by E787.
- **LINAC** — linear accelerator: a machine which accelerates charged particles through alternating voltages in a straight path. A LINAC is used at the first stage of particle acceleration at BNL, to accelerate H^- ions.
- **lkbeam** — a kaon likelihood quantity formed from the energy deposited in the B4 hodoscope, the UTC-extrapolated kaon stopping z in the target, and the kaon energy in the target.
- **LLA** — Leading-Order Logarithmic Approximation
- **meson** — a particle composed of a quark, anti-quark pair.
- **minimum ionizing particle** — a moderately relativistic charged particle which loses energy in a medium primarily through ionization at a rate of about $2 \text{ MeV} \cdot \text{cm}^2/\text{g}$, almost independent of the medium. For particles travelling faster than the atomic electrons (i.e., faster than about $c|q|/137$, where c is the speed of light and $|q|$ is magnitude of the particle's charge in units of the proton charge e), the mean rate of energy loss in a medium $|dE/dx|$ is given by the Bethe-Bloch equation [16], and initially falls as $1/\beta^2$, where β is the particle's velocity in units of c . The mean rate of energy loss reaches a broad minimum at $\gamma \approx 3.2$, where $\gamma = (1 - \beta^2)^{-0.5}$. The energy loss rate increases slowly for $\gamma > 4$ so, in practical cases, most relativistic charged particles have energy loss rates close to the minimum, i.e., $2 \text{ MeV} \cdot \text{cm}^2/\text{g}$, almost independent of the medium.
- **Monte Carlo** — see UMC.
- **muon band** — kinematic region in range-momentum space with correlated values of range and momentum consistent with a μ^+ track, and values of range and momentum which are smaller than the $K_{\mu 2}$ peak values. Events in the muon band can arise from

$K^+ \rightarrow \mu^+ \nu_\mu \gamma$ (radiative $K_{\mu 2}$), $K^+ \rightarrow \pi^0 \mu^+ \nu_\mu$ ($K_{\mu 3}$), $K_{\mu 2}$ decay in flight, and/or $K_{\mu 2}$ decay with inelastic scattering in the target.

- **NIDIF** — pion “nuclear interactions and decay in flight”, which can be turned on or off when generating Monte Carlo data (i.e., when propagating pions through the detector).
- **NLLA** — Next-to-Leading-Order Logarithmic Approximation
- **normalization branch** — one of two branches in a bifurcated background estimate. The events in this branch are required to fail a cut whose rejection is measured in the “rejection” branch. All other cuts in the analysis are applied to these events, and the number that remain is referred to as the background “normalization”. This normalization, divided by the rejection calculated in the rejection branch, gives an estimated number of background events.
- **ntuple** — a computer data file containing quantities associated with each event. Ntuples for the E787 analysis are produced and read by PAW.
- **offline** — any system (e.g., software cuts) which operates on data once it has been collected and stored on disk/tape.
- **online** — any system (e.g., digitizing hardware, trigger) that operates on the data as it is being collected.
- **P** — total momentum of a track.
- **PA** — pulse area
- **PASS1** — initial processing of the raw data, with the intention of reducing the total data volume by a factor of about 10 while maintaining high acceptance for $K^+ \rightarrow \pi^+ \nu \bar{\nu}$.
- **PASS2** — separation of the PASS1 output data into background data samples suitable for studying background processes.

- **PASS3** — high-level analysis of the PASS2 output data samples, and storage of various quantities in ntuples for subsequent study using PAW.
- **pathology cut** — an offline cut that is typically applied at the initial stages of a bifurcated analysis in order to remove events which can contaminate the bifurcated data samples with correlations.
- **PAW** — Physics Analysis Workstation: data analysis and plotting program developed at CERN.
- **PH** — pulse height
- **PID** — particle identification
- **PID cuts** — see TD cuts.
- **pion band** — kinematic region in range-momentum space with correlated values of range and momentum consistent with a π^+ track. Events in the pion band can arise from beam pions which scatter into the detector, $K_{\pi 2}$ decay in flight, and/or $K_{\pi 2}$ decay with inelastic scattering in the target.
- **pion fiber** — target fiber with pulse time and energy and location consistent with a charged kaon decay product which is subsequently tracked in the UTC.
- **π_{scat} background** — potential background for $K^+ \rightarrow \pi^+ \nu \bar{\nu}$ due to pions in the beam which scatter into the detector, giving rise to a pion track with similar kinematics as $K^+ \rightarrow \pi^+ \nu \bar{\nu}$ decay.
- **PMT** — photo-multiplier tube: consists of a photocathode and a system of “dynodes”. Scintillation or Čerenkov light (produced by charged particles in a medium) is collected at the photocathode, where the light kicks out electrons via the photoelectric effect. The electrons are accelerated through a sequence of voltages applied to cathodes (dynodes), each acceleration knocking out more electrons at each cathode surface such that the resulting “avalanche” of electrons results in a detectable electrical pulse.

Appendix D. Glossary

- $\pi^+\nu\bar{\nu}(1)$ — refers to the $K^+ \rightarrow \pi^+\nu\bar{\nu}$ signal region kinematically located between the monochromatic $K_{\pi 2}$ and $K_{\mu 2}$ peaks.
- $\pi^+\nu\bar{\nu}(2)$ — refers to the $K^+ \rightarrow \pi^+\nu\bar{\nu}$ signal region kinematically located just below the $K_{\pi 2}$ peak.
- **polar angle, θ** — the angle in the (r, z) plane between the beam axis and the UTC track. θ ranges from 0° (track propagates directly downstream from the kaon decay vertex) to 180° (track propagates directly upstream from the kaon decay vertex).
- **PV** — photon veto
- **QCD** — quantum chromodynamics: quantum field theory which describes the strong force.
- **QED** — quantum electrodynamics: quantum field theory which describes the electromagnetic force.
- **quantum field theory** — see QCD and QED.
- **R** — total range of a track.
- **R_{TG}** — range of a track in the target (as found from an extrapolation of the UTC track from the kaon decay vertex to the outer edge of the target).
- **reconstruction cut** — an offline data-reduction cut that requires an event to have a charged track reconstructed in the target, UTC, and RS, such that the event is worthy of further analysis.
- **rejection** — a measure of a data-selection cut's ability to identify and remove specific types of events from a data sample.
- **rejection branch** — one of two branches in a bifurcated background estimate, in which the rejection of a cut is calculated using events which fail a cut from the normalization branch.

Appendix D. Glossary

- **RHIC** — Relativistic Heavy-Ion Collider at BNL
- **RS** — Range Stack
- **RSSC** — Range Stack Straw Chamber
- **run** — a period of data collection, usually a few hours long, such that the volume of data collected is appropriate for storage on tape and subsequent processing. A “run” can also refer to a collection of runs, e.g., the “1995 run” refers to the collection of all data in 1995.
- **safety cut** — an offline cut used to suppress background, but not used in the background estimates because its performance is difficult to evaluate.
- **scaler** — hardware used to count signals.
- **SCF** — online stopping-counter finder
- **scintillator** — a material (plastic or inorganic crystal) which is used to detect charged particles via excitation of (organic or inorganic) molecules. The molecules de-excite by emitting photons which travel through the material and are converted into an electrical pulse by a PMT.
- **SEB** — slow extracted beam from the AGS at BNL
- **sector** — azimuthal segmentation of the RS or barrel. Sector 1 is located at $\phi = 0$, and numbering of sectors increases with ϕ .
- **SKIM1** — PASS2 output data stream, primarily composed of $K_{\pi 2}$ decays, for use in measuring $K_{\pi 2}$ background at PASS3.
- **SKIM2** — PASS2 output data stream, primarily composed of $K_{\mu 2}$ decays, for use in measuring $K_{\mu 2}$ background at PASS3.
- **SKIM3** — PASS2 output data stream, primarily composed of beam pion scattering events, for use in measuring beam background at PASS3.

Appendix D. Glossary

- **SLAC** — Stanford Linear Accelerator Center, San Francisco, USA
- **SM** — Standard Model of particles and interactions
- **SSP** — SLAC Scanner Processor, used to store and send data to the computer during data-taking.
- **stopping counter** — RS counter (layer/sector/hexant) where the track particle comes to rest.
- **supersymmetry** — see SUSY.
- **SUSY** — supersymmetry: theory that predicts symmetry between fermions and bosons. That is, the fundamental fermions (spin 1/2) have companion bosons (spin 0), and the fundamental bosons (spin 1 or 2) have companion fermions (spin 1/2 or 3/2).
- **swath** — area of the target pointed to by the UTC track where kaon and pion fibers are likely to be found.
- **synchrotron** — a machine which accelerates charged particles through alternating voltages in multiple trips around a circular path. The particles are injected, held, and extracted at a fixed radius using magnets. Two synchrotrons (a “booster” and the AGS) are used at BNL to accelerate protons.
- $t_{B4stroke}$ — time of the kaon as detected by the B4 hodoscope.
- t_{Ck} — time of the kaon as detected by the Čerenkov counter.
- t_K — average time of the kaon as detected by target fibers.
- t_{IC} — time of the track as detected by the IC.
- t_{KCCD} — time of a target kaon fiber pulse as found using CCD data.
- t_μ — second-pulse time relative to first-pulse time in the stopping counter (for pion tracks, this is usually the pion decay time).

Appendix D. Glossary

- t_π — average time of the track as detected by target fibers.
- t_{RS} — average time of the track as detected by RS counters.
- $t1$ — time of a pulse as recorded on the upstream end of a RS or barrel counter.
- $t2$ — time of a pulse as recorded on the downstream end of a RS or barrel counter.
- $T \cdot 2$ — trigger condition requiring coincident hits in the same sector in layers 1 and 2 of the RS.
- **T counter** — (thin) counter in layer 1 of the RS, which defines the fiducial acceptance of the RS.
- **TD** — a 500 MHz transient digitizer based on flash ADC's, which samples and digitizes voltage in 2 ns intervals.
- **TD cuts** — cuts on the second (and third) pulse time, energy, and z in the stopping counter, as well as cuts on the time, energy, and z of pulses in neighbouring counters, which aim to positively identify the signature for $\pi \rightarrow \mu \rightarrow e$ decay in the stopping counter.
- **TD flags** — RS signals used to identify the specific RS counter which gives rise to a TD pulse (the 4 RS counters from the same layer and hexant are multiplexed into a single TD channel).
- **TDC** — time-to-digital converter: hardware used to digitize the time of a pulse.
- **TOE** — theory of everything: theory which unites the electromagnetic, weak, strong, and gravitational forces into a single mathematical description.
- **track time** — time of the track in the RS
- **trigger** — a specific combination of data conditions which signal that good data is available, such that the data is read out, processed, and stored.
- **TRIUMF** — Tri-University Meson Facility, Vancouver, Canada

Appendix D. Glossary

- **UMC** — “Universal” Monte Carlo: code used to simulate the E787 detector and particle interactions therein, so that simulated kaon decay data can be generated for the purposes of acceptance measurements and modelling of background processes to $K^+ \rightarrow \pi^+ \nu \bar{\nu}$.
- **upstream** — in the direction opposite the kaon beam momentum
- **UTC** — ultra thin chamber: a wire chamber used for momentum analysis of charged kaon decay products.
- **VC** — V-counter
- **wire chamber** — a series of high-voltage wires in a volume of gas which detects particles via ionization of the gas. Particles traversing the gas volume ionize the atoms of the gas, liberating electrons which are accelerated by the electric field of the wires towards the wires themselves. The electric field is strongest near the wires, so as the electrons approach the wires, they acquire more and more energy and liberate additional ionization electrons. This “avalanche” of electrons results in a detectable electrical pulse on a wire.